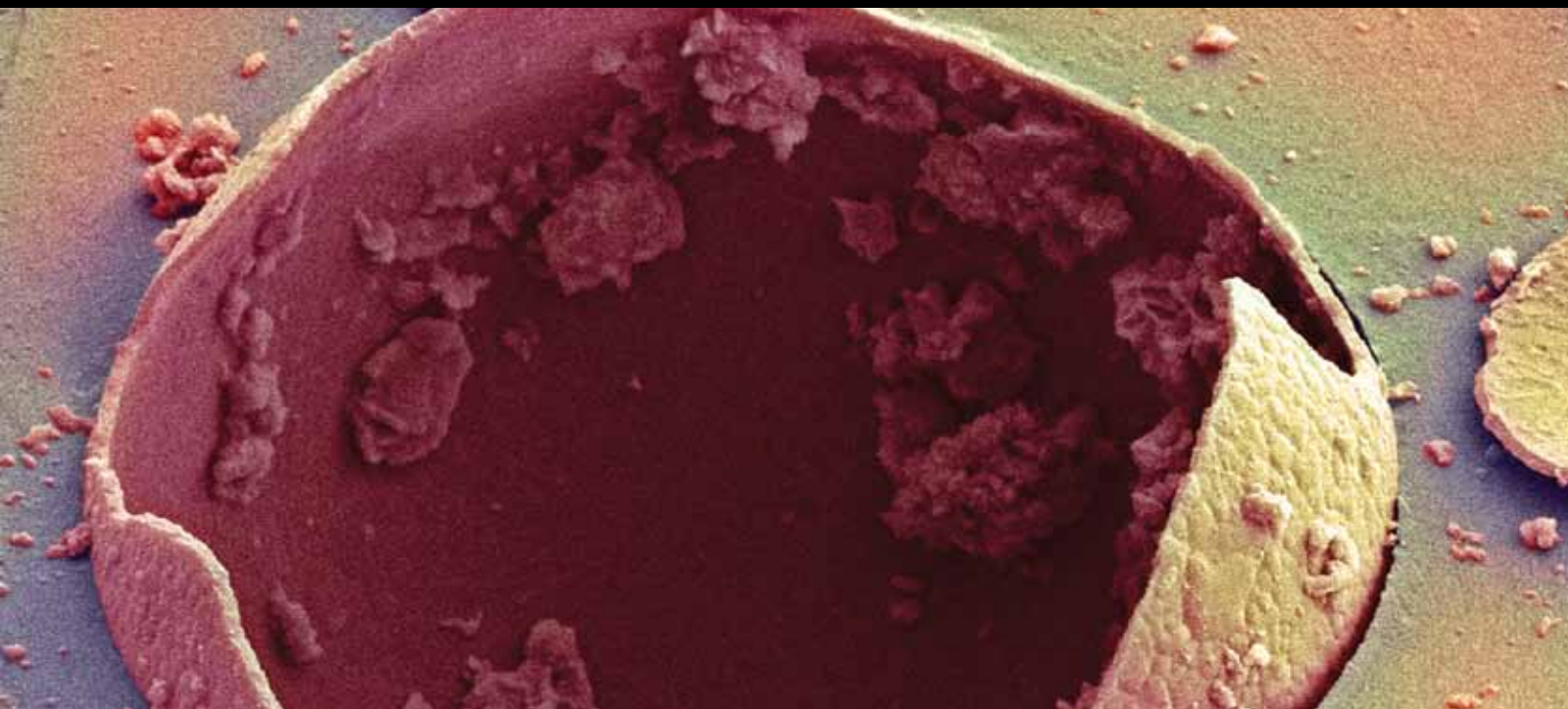


# ADVANCED PIEZOELECTRICS: MATERIALS, DEVICES, AND THEIR APPLICATIONS

GUEST EDITORS: TAO LI, JAN MA, MOHAMMED ES-SOUNI, AND PETER WOIAS





---

# **Advanced Piezoelectrics: Materials, Devices, and Their Applications**

Smart Materials Research

---

# **Advanced Piezoelectrics: Materials, Devices, and Their Applications**

Guest Editors: Tao Li, Jan Ma, Mohammed Es-Souni,  
and Peter Woias



---

Copyright © 2012 Hindawi Publishing Corporation. All rights reserved.

This is a special issue published in "Smart Materials Research." All articles are open access articles distributed under the Creative Commons Attribution License, which permits unrestricted use, distribution, and reproduction in any medium, provided the original work is properly cited.

## Editorial Board

Mehdi Ahmadian, USA

O. J. Aldraihem, Saudi Arabia

Sedat Alkoy, Turkey

Chris Bowen, UK

F. M. B. Fernandes, Portugal

Lin Chi Chen, Taiwan

Ali Cirpan, Turkey

Corneliu Craciunescu, Romania

Gerard F. Fernando, UK

Benoit Guiffard, France

Daniel Guyomar, France

Klaus Hackl, Germany

H. Hosoda, Japan

Bjørn Petter Jelle, Norway

K. S. C. Kuang, Singapore

Weihua Li, Australia

Yong Liu, Singapore

Giovanni Mazzolai, Italy

Xianglong Meng, China

Hoon Cheol Park, Korea

Manas C. Ray, India

Ricardo Romero, Argentina

Annette Schmidt, Germany

Zhifei Shi, China

Norio Shinya, Japan

Outi Söderberg, Finland

Gangbing Song, USA

Marcelo A. Trindade, Brazil

Stefano Vidoli, Italy

David Vokoun, Czech Republic

Shih-Ming Yang, Taiwan

Yaowen Yang, Singapore

Kelvin Yeung, Hong Kong

Yanjun Zheng, China

# Contents

**Advanced Piezoelectrics: Materials, Devices, and Their Applications**, Tao Li, Jan Ma, Mohammed Es-Souni, and Peter Woias  
Volume 2012, Article ID 259275, 2 pages

**Exact Solution for an Anti-Plane Interface Crack between Two Dissimilar Magneto-Electro-Elastic Half-Spaces**, Bogdan Rogowski  
Volume 2012, Article ID 786190, 8 pages

**Epitaxial Piezoelectric  $\text{Pb}(\text{Zr}_{0.2}\text{Ti}_{0.8})\text{O}_3$  Thin Films on Silicon for Energy Harvesting Devices**, A. Sambri, D. Isarakorn, A. Torres-Pardo, S. Gariglio, Pattanaphong Janphuang, D. Briand, O. Stéphan, J. W. Reiner, J.-M. Triscone, Nico F. de Rooij, and C. H. Ahn  
Volume 2012, Article ID 426048, 7 pages

**Synthesis and Characterization of  $\text{Pb}(\text{Zr}_{0.53}\text{Ti}_{0.47})\text{O}_3$ - $\text{Pb}(\text{Nb}_{1/3}\text{Zn}_{2/3})\text{O}_3$  Thin Film Cantilevers for Energy Harvesting Applications**, E. M. A. Fuentes-Fernandez, W. Debray-Mechtaly, M. A. Quevedo-Lopez, B. Gnade, E. Leon-Salguero, P. Shah, and H. N. Alshareef  
Volume 2012, Article ID 872439, 9 pages

**Solid State Adaptive Rotor Using Postbuckled Precompressed, Bending-Twist Coupled Piezoelectric Actuator Elements**, Ronald M. Barrett and Ryan Barnhart  
Volume 2012, Article ID 832939, 10 pages

**Infra-Through Ultrasonic Piezoelectric Acoustic Vector Sensor Particle Rejection System**, Scott E. Cravens and Ronald M. Barrett  
Volume 2012, Article ID 356190, 6 pages

**Static Electric Force and Measurement Principle of Material Constants in Electrostrictive Material**, Zhen-Bang Kuang  
Volume 2012, Article ID 712103, 8 pages

**Active Vibration Control of a Microactuator for the Hard Disk Drive Using Self-Sensing Actuation**, Minoru Sasaki, Yoshihiro Inoue, and Hiroyuki Yamada  
Volume 2012, Article ID 920747, 7 pages

**Comparison of Analog and Digital Self-Powered Systems in Multimodal Vibration Suppression**, Shigeru Shimose, Kanjuro Makihara, and Junjiro Onoda  
Volume 2012, Article ID 287128, 9 pages

**Modeling Hysteresis with Inertial-Dependent Prandtl-Ishlinskii Model in Wide-Band Frequency-Operated Piezoelectric Actuator**, Vahid Hassani, Tegoeh Tjahjowidodo, and Albert D. Soetarto  
Volume 2012, Article ID 164062, 15 pages

**Fabrication of Simple and Ring-Type Piezo Actuators and Their Characterization**, B. Sahoo and P. K. Panda  
Volume 2012, Article ID 821847, 4 pages

**Electromechanical and Dynamic Characterization of In-House-Fabricated Amplified Piezo Actuator**, P. K. Panda, B. Sahoo, S. Raja, Vijaya Kumar M. P., and V. Shankar  
Volume 2012, Article ID 203625, 8 pages



---

**Damping Analyses of Structural Vibrations and Shunted Piezoelectric Transducers**, Saber Mohammadi and Akram Khodayari

Volume 2012, Article ID 431790, 5 pages

**Redirection of Lamb Waves for Structural Health Monitoring**, W. H. Ong and W. K. Chiu

Volume 2012, Article ID 718686, 9 pages

**A Surface Acoustic Wave Ethanol Sensor with Zinc Oxide Nanorods**, Timothy J. Giffney, Y. H. Ng, and K. C. Aw

Volume 2012, Article ID 210748, 4 pages

**Local Fatigue Evaluation in PZT Thin Films with Nanoparticles by Piezoresponse Force Microscopy**, B. S. Li

Volume 2012, Article ID 391026, 9 pages

## Editorial

# Advanced Piezoelectrics: Materials, Devices, and Their Applications

Tao Li,<sup>1</sup> Jan Ma,<sup>1</sup> Mohammed Es-Souni,<sup>2</sup> and Peter Woias<sup>3</sup>

<sup>1</sup> School of Materials Science and Engineering, Nanyang Technological University, Singapore 639798

<sup>2</sup> Institute for Materials and Surface Technology, University of Applied Sciences Kiel, 24149 Kiel, Germany

<sup>3</sup> Department of Microsystems Engineering, IMTEK, University of Freiburg, 79110 Freiburg, Germany

Correspondence should be addressed to Tao Li, tli@ntu.edu.sg

Received 18 March 2012; Accepted 18 March 2012

Copyright © 2012 Tao Li et al. This is an open access article distributed under the Creative Commons Attribution License, which permits unrestricted use, distribution, and reproduction in any medium, provided the original work is properly cited.

After decades of research and development, piezoelectric materials have been applied in a wide range of applications, ranging from household appliances to industrial equipments. In areas such as precision and acoustic engineering, piezoelectric material is well accepted to be one of the leading functional materials. Today, due to the high demand, particularly from the electronic, energy, and biomedical industries, researchers are driven to the exploration of new materials and device configurations for new applications. At the same time, engineers are making continuous effort to improve the existing technologies. As the scope of the area is vast, it is necessary to provide an overview on different branches of piezoelectric materials. We would like to thank all the authors who submitted their papers to this special issue. We also hope that this special issue can give an insight on the current research and development status of piezoelectric materials community. We further expect that this issue could stimulate the generation of new ideas and technologies for advanced future applications.

This special issue accepted sixteen papers from industries, research institutes, and universities worldwide. The topics touched include failure analysis, thin film, nanotechnologies, materials synthesis, fabrication technique, modeling, nondestructive testing, sensors, actuators, transducers, ultrasonics, cleaning, vibration suppression, energy harvesting, and characterization techniques.

In the paper “*Local fatigue evaluation in PZT thin films with nanoparticles by piezoresponse force microscopy*,” a PZT film was fabricated and the local switching polarization behavior of the film during fatigue was investigated using scanning piezoelectric microscopy. It was found that the

introducing of barium titanate (BT) nanoseeds has significantly improved the fatigue performance.

In the paper “*Redirection of Lamb waves for structural health monitoring*,” Lamb wave based structural health monitoring was proposed and its benefits were explored. This technique can potentially be used to improve the detectability of defects in difficult-to-inspect locations.

In the paper “*A surface acoustic wave ethanol sensor with zinc oxide nanorods*,” a surface acoustic wave ethanol sensor using ZnO nanorods was developed and tested. It has shown that the nanorod structure can increase the frequency shift of the sensor.

In the paper “*Damping analyses of structural vibrations and shunted piezoelectric transducers*,” an experimental method was used to calculate the damping energy in a mechanical system. Both piezoelectric damping and structural damping were analyzed. This method is meaningful for vibration suppression and control.

In the paper “*Static electric force and measurement principle of material constants in electrostrictive material*,” a model regarding the electric force acting on the material and method to measure the electrostrictive coefficients were proposed. Factors affecting the measurement accuracy were also discussed based on the proposed model.

In the paper “*Electromechanical and dynamic characterization of in-house-fabricated amplified piezo actuator*,” a diamond-shaped amplified piezo actuator was fabricated and tested. Essential parameters such as displacement and block force were measured.

In the paper “*Fabrication of simple and ring-type piezo actuators and their characterization*,” the fabrication and

characterization of a piezoelectric multilayer structure were illustrated. The procedure was introduced in detail. The obtained actuator can be used for fluid flow control in space vehicles.

In the paper “*Modeling hysteresis with inertial-dependent Prandtl-Ishlinskii model in wide-band frequency-operated piezoelectric actuator*,” the hysteresis and nonlinear effect of a piezoelectric actuator was modeled and characterized. The results are useful for enhancing the controlling capability of an actuator.

In the paper “*Comparison of analog and digital self-powered systems in multimodal vibration suppression*,” the methods of digital and analog vibration suppression were proposed and compared. It shows that both methods are effective in improving damping performance. Also, the self-powering feature makes the methods useful in various applications.

In the paper “*Active vibration control of a microactuator for the hard disk drive using self-sensing actuation*,” a microactuator was combined with sensing function, which can then be used for hard disk vibration control. The work has also demonstrated that the method is effective in suppressing the vibrational modes.

In the paper “*Infra-through ultrasonic piezoelectric acoustic vector sensor particle rejection system*,” an ultrasonic cleaning system was developed to remove the dust from a sensor filament. Therefore, it helps to improve the cleanness and hence maintain the measurement accuracy of the sensor.

In the paper “*Solid state adaptive rotor using postbuckled precompressed, bending-twist coupled piezoelectric actuator elements*,” a piezoelectric actuator was developed, which can be integrated on a solid stator adaptive helicopter rotor. This method is promising on the performance enhancement of the helicopter by reducing part count, increasing reliability, and allowing for decoupled individual blade control of rotor blades.

In the paper “*Synthesis and characterization of  $Pb(Zr_{0.53}Ti_{0.47})O_3$ - $Pb(Nb_{1/3}Zn_{2/3})O_3$  thin film cantilevers for energy harvesting applications*,” a PZT-PZN thin film cantilever was fabricated for the purpose of energy harvesting. The dielectric properties of the film were characterized. The generated electric signal of the cantilever harvester was studied and simulated under various conditions.

In the paper “*Epitaxial piezoelectric  $Pb(Zr_{0.2}Ti_{0.8})O_3$  thin films on silicon for energy harvesting devices*,” PZT thin film was fabricated. Its microstructure and electrical properties were investigated. As an energy harvester, it was compared with other devices and its energy harvesting potential was examined.

In the paper “*Time-dependent piezo-electro-magneto-elastic fracture behavior of conducting cracks in a half-space under anti-plane mechanical and in-plane electric and magnetic impact*,” piezo-electro-magneto-elastic materials under transient loads were modeled and discussed. One of the important findings in this paper is that there exists a strong coupling between stress and electrical and magnetic field near crack tips.

In the paper “*Exact solution for an anti-plane interface crack between two dissimilar magneto-electro-elastic*

*half-spaces*,” the fracture behavior of a piezo-electro-magneto-elastic composite was modeled. Fourier transform was applied. Some important parameters, such as electric displacement and magnetic induction, were determined and discussed.

Tao Li

Jan Ma

Mohammed Es-Souni

Peter Woias

## Research Article

# Exact Solution for an Anti-Plane Interface Crack between Two Dissimilar Magneto-Electro-Elastic Half-Spaces

**Bogdan Rogowski**

*Department of Mechanics of Materials, Technical University of Lodz, Al. Politechniki 6, 93-590 Lodz, Poland*

Correspondence should be addressed to Bogdan Rogowski, bogdan.rogowski@p.lodz.pl

Received 27 October 2011; Accepted 10 February 2012

Academic Editor: Ma Jan

Copyright © 2012 Bogdan Rogowski. This is an open access article distributed under the Creative Commons Attribution License, which permits unrestricted use, distribution, and reproduction in any medium, provided the original work is properly cited.

This paper investigated the fracture behaviour of a piezo-electro-magneto-elastic medium subjected to electro-magneto-mechanical loads. The bimaterial medium contains a crack which lies at interface and is parallel to their poling direction. Fourier transform technique is used to reduce the problem to three pairs of dual integral equations. These equations are solved exactly. The semipermeable crack-face magneto-electric boundary conditions are utilized. Field intensity factors of stress, electric displacement, magnetic induction, cracks displacement, electric and magnetic potentials, and the energy release rate are determined. The electric displacement and magnetic induction of crack interior are discussed. Obtained results indicate that the stress field and electric and magnetic fields near the crack tips exhibit square-root singularity.

## 1. Introduction

Mechanics of magneto-electro-elastic solid has gained considerable interest in the recent decades with increasable wide application of piezoelectric/piezomagnetic composite materials in engineering, particularly in aerospace and automotive industries. Recently, much attention has been paid to dislocation crack and inclusion problems in magneto-electro-elastic solids, which simultaneously possess piezoelectric, piezomagnetic, and magnetoelectric effects. Therefore, it is of vital importance to investigate the magneto-electro-elastic fields as a result of existence of defects, such as cracks, in these solids.

The mode III interface crack solution for two dissimilar half-planes has been analyzed by Li and Kardomateas [1] while for two dissimilar layers by Wang and Mai [2] and by Li and Wang [3]. Li and Kardomateas [1] solved corresponding plane problem by means of Stroh's formalism and complex variable methods. Li and Wang [3] investigated the problems involving an antiplane shear crack perpendicular to and terminating at the interface of a bimaterial piezo-electro-elastic ceramics. Wang and Mai [2] investigated the mode III-crack problem for a crack at the interface between two dissimilar magneto-electro-elastic layers. Extension of

those investigation problems interested in fracture theory, on dielectric and magnetostrictive crack behaviour, is very important, and results and conclusions could have applications in the failure of PEMO-elastic devices and in smart intelligent structures [4].

However, to the authors' best knowledge, no researches dealing with the interface-dielectric crack in PEMO-elastic two-phase composite have been reported in literature. When subjected to mechanical, electrical, and magnetic loads in service, these magneto-electro-elastic composites can fail prematurely due to some defects, namely, cracks, holes and others, arising during their manufacturing process. Therefore, it is of great importance to study the magneto-electro-elastic interaction and fracture behaviours of PEMO-elastic materials.

In mechanic where two-phase composites have twelve material constants only exact solutions are useful. This is motivation for this study. For electrical, magnetic, and mechanical loads (two cases of electrical and magnetic excitations) and semipermeable electrical and magnetic boundary conditions at the interface crack, exact analytical solutions are obtained here for full field interesting in fracture mechanics.

## 2. Basic Equations

For a linearly magneto-electro-elastic medium under antiplane shear coupled with in-plane electric and magnetic fields, there are only the nontrivial antiplane displacement  $w$

$$u_x = 0, \quad u_y = 0, \quad u_z = w(x, y) \quad (1)$$

strain components  $\gamma_{xz}$  and  $\gamma_{yz}$

$$\gamma_{xz} = \frac{\partial w}{\partial x}, \quad \gamma_{yz} = \frac{\partial w}{\partial y} \quad (2)$$

stress components  $\tau_{xz}$  and  $\tau_{yz}$ , in-plane electrical and magnetic potentials  $\phi$  and  $\psi$ , which define electrical and magnetic field components  $E_x, E_y, H_x$  and  $H_y$

$$\begin{aligned} E_x &= -\frac{\partial \phi}{\partial x}, & E_y &= -\frac{\partial \phi}{\partial y}, \\ H_x &= -\frac{\partial \psi}{\partial x}, & H_y &= -\frac{\partial \psi}{\partial y} \end{aligned} \quad (3)$$

and electrical displacement components  $D_x, D_y$ , and magnetic induction components  $B_x, B_y$  with all field quantities being the functions of coordinates  $x$  and  $y$ .

The generalized strain-displacement relations (2) and (3) have the form

$$\gamma_{\alpha z} = w_{,\alpha}, \quad E_\alpha = -\phi_{,\alpha}, \quad H_\alpha = -\psi_{,\alpha}, \quad (4)$$

where  $\alpha = x, y$  and  $w_{,\alpha} = \partial w / \partial \alpha$ .

For linearly magneto-electro-elastic medium, the coupled constitutive relations can be written in the matrix form

$$[\tau_{\alpha z}, D_\alpha, B_\alpha]^T = C[\gamma_{\alpha z}, -E_\alpha, -H_\alpha]^T, \quad (5)$$

where the superscript  $T$  denotes the transpose of a matrix, and

$$C = \begin{bmatrix} c_{44} & e_{15} & q_{15} \\ e_{15} & -\varepsilon_{11} & -d_{11} \\ q_{15} & -d_{11} & -\mu_{11} \end{bmatrix} \quad (6)$$

is the material property matrix, where  $c_{44}$  is the shear modulus along the  $z$ -direction, which is direction of poling and is perpendicular to the isotropic plane  $(x, y)$ ,  $\varepsilon_{11}$  and  $\mu_{11}$  are dielectric permittivity and magnetic permeability coefficients, respectively,  $e_{15}$ ,  $q_{15}$ , and  $d_{11}$  are piezoelectric, piezomagnetic, and magneto-electric coefficients, respectively.

The mechanical equilibrium equation (called as Euler equation), the charge and current conservation equations (called as Maxwell equations), in the absence of the body force electric and magnetic charge densities, can be written as

$$\tau_{z\alpha,\alpha} = 0, \quad D_{\alpha,\alpha} = 0, \quad B_{\alpha,\alpha} = 0, \quad \alpha = x, y. \quad (7)$$

Subsequently, the Euler and Maxwell equations take the form

$$C[\nabla^2 w, \nabla^2 \phi, \nabla^2 \psi]^T = [0, 0, 0]^T, \quad (8)$$

where  $\nabla^2 = \partial^2 / \partial x^2 + \partial^2 / \partial y^2$  is the two-dimensional Laplace operator.

Since  $|C| \neq 0$ , one can decouple(8)

$$\nabla^2 w = 0, \quad \nabla^2 \phi = 0, \quad \nabla^2 \psi = 0. \quad (9)$$

If we introduce, for convenience of mathematics in some boundary value problems, two unknown functions

$$[\chi - e_{15}w, \eta - q_{15}w]^T = C_0[\phi, \psi]^T, \quad (10)$$

where the matrix  $C_0$ , a principal submatrix of  $C$ , is

$$C_0 = \begin{bmatrix} -\varepsilon_{11} & -d_{11} \\ -d_{11} & -\mu_{11} \end{bmatrix}, \quad (11)$$

then

$$[\phi, \psi]^T = C_0^{-1}[\chi - e_{15}w, \eta - q_{15}w]^T, \quad (12)$$

where

$$C_0^{-1} = \frac{1}{\varepsilon_{11}\mu_{11} - d_{11}^2} \begin{bmatrix} -\mu_{11} & d_{11} \\ d_{11} & -\varepsilon_{11} \end{bmatrix} = \begin{bmatrix} c_1 & c_2 \\ c_2 & c_3 \end{bmatrix}. \quad (13)$$

The relevant field variables are

$$\begin{aligned} \tau_{zk} &= \tilde{c}_{44}w_{,k} - \alpha D_k - \beta B_k, \\ \phi &= \alpha w + c_1\chi + c_2\eta, \\ \psi &= \beta w + c_2\chi + c_3\eta, \\ D_k &= \chi_{,k}, \\ B_k &= \eta_{,k}, \quad k = x, y, \end{aligned} \quad (14)$$

$$\nabla^2 w = 0, \quad \nabla^2 \chi = 0, \quad \nabla^2 \eta = 0. \quad (15)$$

The two last equations (15) are equivalent to (9) since  $c_1c_3 - c_2^2 = 1/(\varepsilon_{11}\mu_{11} - d_{11}^2) \neq 0$ . In (14) the material parameters are defined as follows:

$$\begin{aligned} \tilde{c}_{44} &= c_{44} + \alpha e_{15} + \beta q_{15}, \\ \alpha &= \frac{\mu_{11}e_{15} - d_{11}q_{15}}{\varepsilon_{11}\mu_{11} - d_{11}^2} = -(c_1e_{15} + c_2q_{15}), \\ \beta &= \frac{\varepsilon_{11}q_{15} - d_{11}e_{15}}{\varepsilon_{11}\mu_{11} - d_{11}^2} = -(c_3q_{15} + c_2e_{15}). \end{aligned} \quad (16)$$

Note that  $\tilde{c}_{44}$  is the piezo-electro-magnetically stiffened elastic constant.

Note also that the inverse of a matrix  $C$  is defined by parameters  $\alpha, \beta, \tilde{c}_{44}$  and  $c_1, c_2, c_3$  as follows:

$$C^{-1} = \frac{1}{\tilde{c}_{44}} \begin{bmatrix} 1 & \alpha & \beta \\ \alpha & \alpha^2 + \tilde{c}_{44}c_1 & \alpha\beta + \tilde{c}_{44}c_2 \\ \beta & \alpha\beta + \tilde{c}_{44}c_2 & \beta^2 + \tilde{c}_{44}c_3 \end{bmatrix} \quad (17)$$

and is the matrix generalized compliances of PEMO-elastic material. These material parameters will be appear in our solutions.

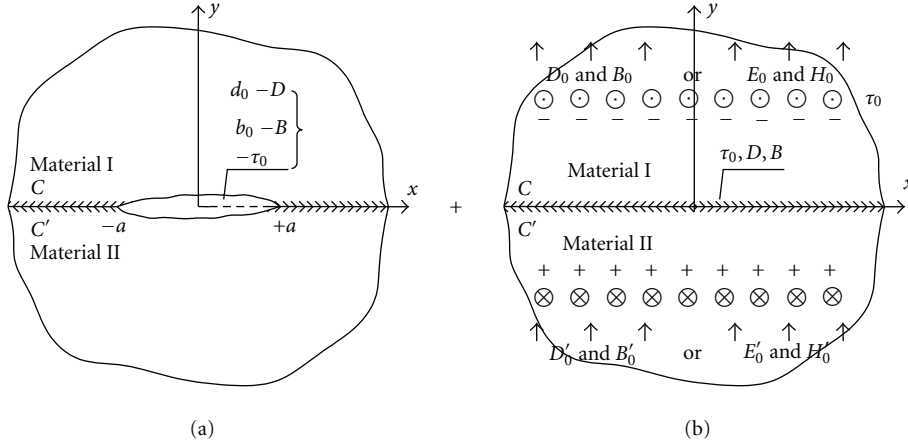


FIGURE 1: The interface crack under antiplane mechanical and in-plane electric and magnetic load. Inside the crack the unknown electromagnetic fields  $d_0$  and  $b_0$  appear. (a) Perturbation problem, (b) Elementary solution for bimaterial without the crack (19) and (20).

### 3. Formulation of the Crack Problem

Let the medium I occupy the upper half-space and medium II be in the lower half-space; the interface crack is assumed to be located in the region from  $-a$  to  $+a$  along the  $x$ -axis. The two-phase composite is subjected to electric, magnetic, and mechanical loads applied at infinity. These are  $(\tau_0, D_0, B_0)$  or  $(\tau_0, E_0, H_0)$ . Under applied external loading, the crack, filled usually by vacuum or air, accumulated an electric and magnetic field, denoted by  $d_0$  and  $b_0$ , would be built up. By the superposition principle, the interface crack problem is equivalent to the one under the applied loading on the upper surface (Figure 1):

$$\begin{aligned} \tau_{zy}(x, 0\pm) &= -\tau_0, & D_y(x, 0\pm) &= -D + d_0, \\ B_y(x, 0\pm) &= -B + b_0; & |x| < a, \end{aligned} \quad (18)$$

where

$$\begin{aligned} D_y &= D \\ &= \begin{cases} D_0, & \text{case I} \\ \frac{e_{15}}{c_{44}}\tau_0 + \left(\varepsilon_{11} + \frac{e_{15}^2}{c_{44}}\right)E_0 + \left(d_{11} + \frac{e_{15}q_{15}}{c_{44}}\right)H_0, & \text{case II} \end{cases} \end{aligned} \quad (19)$$

$$\begin{aligned} B_y &= B \\ &= \begin{cases} B_0, & \text{case I} \\ \frac{q_{15}}{c_{44}}\tau_0 + \left(d_{11} + \frac{e_{15}q_{15}}{c_{44}}\right)E_0 + \left(\mu_{11} + \frac{q_{15}^2}{c_{44}}\right)H_0, & \text{case II.} \end{cases} \end{aligned} \quad (20)$$

Similarly is for lower crack surface, where the material parameters and electro-magnetic loadings are denoted by prime.

To guarantee the continuity of physical quantities at the perfectly bonded interface, applied electro-magnetic loadings  $E$  and  $H$  must obey the relations from which the

loadings of upper material, namely,  $E_0$  and  $H_0$  may be determined by means of loading of lower material, namely,  $E'_0$  and  $H'_0$ , using (19) and (20). Of course,  $D_0 = D'_0$  and  $B_0 = B'_0$  in Case I of loading and  $E_0 = E'_0$  and  $H_0 = H'_0$  for homogeneous medium only.

At the interface  $y = 0\pm$ , we have the conditions

$$\begin{aligned} [|\tau_{zy}|] &= 0, & [D_y] &= 0, & [B_y] &= 0, & |x| < \infty, \\ [w] &= 0, & [|\phi|] &= 0, & [|\psi|] &= 0, & |x| \geq a, \end{aligned} \quad (21)$$

where the notation  $[|f|] = f^+ - f^-$  and  $f^+$  denotes the value for  $0^+$  while  $f^-$  for  $0^-$ .

The electric displacement  $d_0$  and magnetic induction  $b_0$  inside the crack are obtained from semipermeable crack-face boundary conditions [5]. For two different magnetoelastic media: PEMO-elastic material I and notch space, we have the continuity condition of electric and magnetic potential in both materials at interfaces, similarly for interface between second PEMO-elastic material and crack interior. The semipermeable crack-face magnetoelastic boundary conditions are expressed as follows:

$$d_0 = -\varepsilon_c \frac{[|\phi|]}{2\delta(x)}, \quad b_0 = -\mu_c \frac{[|\psi|]}{2\delta(x)}, \quad (22)$$

where  $\delta(x)$  describes the shape of the notch, and  $\varepsilon_c, \mu_c$  are the dielectric permittivity and magnetic permeability of crack interior. If we assume the elliptic notch profile such that

$$\delta(x) = \frac{\delta_0}{a} \sqrt{a^2 - x^2}, \quad (23)$$

where  $\delta_0$  is the half-thickness of the notch at  $x = 0$ , we obtain that

$$\begin{aligned} 2d_0 \frac{\delta_0}{a\varepsilon_c} \sqrt{a^2 - x^2} &= -[|\phi|], \\ 2d_0 \frac{\delta_0}{a\mu_c} \sqrt{a^2 - x^2} &= -[|\psi|]; \quad |x| \leq a. \end{aligned} \quad (24)$$

Equations (24) form two coupling linear equations with respect to  $d_0$  and  $b_0$  since  $[\phi]$  and  $[\psi]$  depend linearly on these quantities as shown boundary conditions (18) and (21).

#### 4. The Solution for Two-Phase Medium with the Discontinuity at Interface

Define the Fourier transform pair by the equations

$$\hat{f}(s) = \int_0^\infty f(x) \cos(sx) dx, \quad f(x) = \frac{2}{\pi} \int_0^\infty \hat{f}(s) \cos(sx) ds. \quad (25)$$

Then (15) are converted to ordinary differential equations and their solutions

$$\begin{aligned} \hat{w}(s, y) &= A(s)e^{-sy}, & y \geq 0, \\ \hat{w}(s, y) &= B(s)e^{sy}, & y \leq 0, \\ \hat{\chi}(s, y) &= C(s)e^{-sy}, & y \geq 0, \\ \hat{\chi}(s, y) &= -C(s)e^{sy}, & y \leq 0, \\ \hat{\psi}(s, y) &= D(s)e^{-sy}, & y \geq 0, \\ \hat{\psi}(s, y) &= -D(s)e^{sy}, & y \leq 0. \end{aligned} \quad (26)$$

These solutions satisfy the regularity conditions at infinity and the conditions of vanishing jumps of electric displacement and magnetic induction at interface and crack surfaces.

From (21)<sub>1</sub> we obtain that

$$B(s) = -\frac{\tilde{c}_{44}}{\tilde{c}_{44}} A(s) + \frac{\alpha - \alpha'}{\tilde{c}_{44}} C(s) + \frac{\beta - \beta'}{\tilde{c}_{44}} D(s). \quad (27)$$

The material parameters of the lower material are denoted by prime.

The mixed boundary conditions on the crack plane and outside lead to

$$\int_0^\infty s \begin{Bmatrix} A(s) \\ C(s) \\ D(s) \end{Bmatrix} \cos(sx) ds = \begin{Bmatrix} \tau_0 + \alpha(D - d_0) + \beta(B - b_0) \\ \tilde{c}_{44} \\ D - d_0 \\ B - b_0 \end{Bmatrix}, \quad |x| < a$$

$$\int_0^\infty s \begin{Bmatrix} A(s) \\ C(s) \\ D(s) \end{Bmatrix} \cos(sx) ds = \begin{Bmatrix} 0 \\ 0 \\ 0 \end{Bmatrix}, \quad |x| \geq a. \quad (28)$$

Using the integrals

$$\begin{aligned} \int_0^\infty J_1(as) \cos(sx) ds &= \frac{1}{a} \begin{cases} 1; & |x| < a \\ a - \frac{|x|}{\sqrt{x^2 - a^2}}, & |x| \geq a \end{cases} \\ \int_0^\infty \frac{J_1(as)}{s} \cos(sx) ds &= \begin{cases} 0; & |x| \geq a \\ \frac{\sqrt{x^2 - a^2}}{a}, & |x| \leq a \end{cases} \end{aligned} \quad (29)$$

we see that the solutions of (28) are

$$\begin{Bmatrix} A(s) \\ C(s) \\ D(s) \end{Bmatrix} = \frac{a}{s} J_1(as) \begin{Bmatrix} \tau_0 + \alpha(D - d_0) + \beta(B - b_0) \\ \tilde{c}_{44} \\ D - d_0 \\ B - b_0 \end{Bmatrix}. \quad (30)$$

We calculate that

$$\begin{aligned} [ [w], [\phi], [\psi] ]^T &= \frac{2}{\pi} \sqrt{a^2 - x^2} [C^{-1} + C'^{-1}] \\ &\quad \times [\tau_0, D - d_0, B - b_0]^T, \end{aligned} \quad (31)$$

where  $C^{-1}$  is defined by the matrix (17) and  $C'^{-1}$  by the same matrix with material parameters of second material.

From the condition (24), we obtain that

$$[d_0, b_0]^T = -\frac{1}{2} \begin{bmatrix} \epsilon_0 & 0 \\ 0 & \mu_0 \end{bmatrix} [C_1^{-1} + C_1'^{-1}] [\tau_0, D - d_0, B - b_0]^T, \quad (32)$$

where

$$\epsilon_0 = \frac{2}{\pi} \frac{a}{\delta_0} \epsilon_c, \quad \mu_0 = \frac{2}{\pi} \frac{a}{\delta_0} \mu_c, \quad (33)$$

$$C_1^{-1} = \frac{1}{\tilde{c}_{44}} \begin{bmatrix} \alpha & \alpha^2 + \tilde{c}_{44}c_1 & \alpha\beta + \tilde{c}_{44}c_2 \\ \beta & \alpha\beta + \tilde{c}_{44}c_2 & \beta^2 + \tilde{c}_{44}c_3 \end{bmatrix} \quad (34)$$

and similarly for  $C_1'^{-1}$  (second material).

#### 5. Field Intensity Factors

The singular behaviour of  $\tau_{zy}$ ,  $D_y$ , and  $B_y$  at  $y = 0$ ,  $|x| \rightarrow a^+$  are:

$$[\tau_{zy}, D_y, B_y]^T = \frac{2}{\pi} \frac{|x|}{\sqrt{x^2 - a^2}} [\tau_0, D - d_0, B - b_0]^T. \quad (35)$$

Defining the stress, electric displacement and magnetic induction intensity factors as follows:

$$[K_\tau, K_D, K_B]^T = \lim_{|x| \rightarrow a^+} \sqrt{2(|x| - a)} [\tau_{zy}, D_y, B_y]^T, \quad (36)$$

we obtain that

$$[K_\tau, K_D, K_B]^T = \frac{2}{\pi} \sqrt{a} [\tau_0, D - d_0, B - b_0]^T. \quad (37)$$

Furthermore, we obtain the displacement, electric and magnetic potentials intensity factors

$$[K_w, K_\phi, K_\psi]^T = \lim_{|x| \rightarrow a} \frac{1}{2\sqrt{2(a-|x|)}} [ [|w| ], [ |\phi| ], [ |\psi| ] ]^T. \quad (38)$$

In view of results (31) and (37), we have

$$[K_w, K_\phi, K_\psi]^T = \frac{1}{2} [C^{-1} + C'^{-1}] [K_\tau, K_D, K_B]^T. \quad (39)$$

The energy release rate is defined as

$$G = \frac{1}{2} (K_\tau K_w + K_D K_\phi + K_B K_\psi) \quad (40)$$

and is the following:

$$G = \frac{1}{4} [K_\tau, K_D, K_B] [C^{-1} + C'^{-1}] [K_\tau, K_D, K_B]^T \quad (41)$$

or in explicit form

$$\begin{aligned} G &= \frac{1}{\pi^2} a \left\{ \left( \frac{1}{\tilde{c}_{44}} + \frac{1}{\tilde{c}'_{44}} \right) \tau_0^2 \right. \\ &\quad + \left( \frac{\alpha^2}{\tilde{c}_{44}} + \frac{\alpha'^2}{\tilde{c}'_{44}} + c_1 + c'_1 \right) (D - d_0)^2 \\ &\quad + \left( \frac{\beta^2}{\tilde{c}_{44}} + \frac{\beta'^2}{\tilde{c}'_{44}} + c_3 + c'_3 \right) (B - b_0)^2 \\ &\quad + 2 \left( \frac{\alpha}{\tilde{c}_{44}} + \frac{\alpha'}{\tilde{c}'_{44}} \right) \tau_0 (D - d_0) \\ &\quad + 2 \left( \frac{\beta}{\tilde{c}_{44}} + \frac{\beta'}{\tilde{c}'_{44}} \right) \tau_0 (B - b_0) \\ &\quad \left. + 2 \left( \frac{\alpha\beta}{\tilde{c}_{44}} + \frac{\alpha'\beta'}{\tilde{c}'_{44}} + c_2 + c'_2 \right) (D - d_0)(B - b_0) \right\}. \quad (42) \end{aligned}$$

For fully impermeable case, we have  $d_0 = 0$  and  $b_0 = 0$ , and the solutions are obtained from (37) and (39). For fully permeable case, we have  $\varepsilon_0 \rightarrow \infty$  and  $\mu_0 \rightarrow \infty$  and

$$D - d_0 = \frac{1}{2} \left( \frac{e_{15}}{c_{44}} + \frac{e'_{15}}{c'_{44}} \right) \tau_0, \quad B - b_0 = \frac{1}{2} \left( \frac{q_{15}}{c_{44}} + \frac{q'_{15}}{c'_{44}} \right) \tau_0. \quad (43)$$

The energy release rate is

$$G = \frac{1}{\pi^2} \left( \frac{1}{c_{44}} + \frac{1}{c'_{44}} \right) \tau_0^2 a. \quad (44)$$

Note that energy release rate (44) for fully permeable crack problem is defined by the harmonic mean of the shear moduli of both materials, that is,

$$G = \frac{2}{\pi^2} \frac{\tau_0^2 a}{c_{44}^*}; \quad \frac{1}{c_{44}^*} = \frac{1}{2} \left( \frac{1}{c_{44}} + \frac{1}{c'_{44}} \right). \quad (44a)$$

The remaining field intensity factors are obtained, in this case, as follows:

$$K_\tau = \frac{2}{\pi} \tau_0 \sqrt{a}, \quad K_D = \frac{1}{\pi} \left( \frac{e_{15}}{c_{44}} + \frac{e'_{15}}{c'_{44}} \right) \tau_0 \sqrt{a}, \quad (45)$$

$$K_B = \frac{1}{\pi} \left( \frac{q_{15}}{c_{44}} + \frac{q'_{15}}{c'_{44}} \right) \tau_0 \sqrt{a}.$$

In particular, for fully permeable crack between two PEMO-elastic materials polarized in opposite directions, we have  $K_D = 0$  and  $K_B = 0$ , since  $e_{15} = -e'_{15}$  and  $q_{15} = -q'_{15}$  in this case.

For electrically impermeable and magnetically permeable crack, the solutions are independent of the applied magnetic field ( $d_0 = 0$  and  $B - b_0$  is independent on  $B$  for  $\varepsilon_0 \rightarrow 0$  and  $\mu_0 \rightarrow \infty$  as shown in (32)).

Alternatively, the solutions for the electrically permeable and magnetically impermeable crack are independent on the applied electric displacement.

In practical applications the following cases appear:

(i) Let  $\varepsilon_0$  tends to infinity and  $\mu_0$  is finite.

Then

$$\begin{aligned} K_D^{\text{perm} \cdot \mu_c} &= K_D^{\text{perm} \cdot \text{imp}} [1 - f_1(\bar{\mu})] + K_D^{\text{perm} \cdot \text{perm}} f_1(\bar{\mu}), \\ K_B^{\text{perm} \cdot \mu_c} &= K_B^{\text{imp} \cdot \text{imp}} [1 - f_1(\bar{\mu})] + K_B^{\text{perm} \cdot \text{perm}} f_1(\bar{\mu}), \end{aligned} \quad (46)$$

where

$$f_1(\bar{\mu}) = \frac{1}{1 + \bar{\mu}}, \quad \bar{\mu} = \frac{\pi \delta_0}{2} \frac{1}{a} \frac{1}{\mu_c} \frac{1}{2} \left( \mu_{11} + \frac{q_{15}^2}{c_{44}} + \mu'_{11} + \frac{q'^2_{15}}{c'_{44}} \right). \quad (47)$$

(ii) Let  $\mu_0$  tends to infinity and  $\varepsilon_0$  is finite.

Then

$$\begin{aligned} K_D^{\varepsilon_c \cdot \text{perm}} &= K_D^{\text{imp} \cdot \text{imp}} [1 - f_2(\bar{\varepsilon})] + K_D^{\text{perm} \cdot \text{perm}} f_2(\bar{\varepsilon}), \\ K_B^{\varepsilon_c \cdot \text{perm}} &= K_B^{\text{imp} \cdot \text{perm}} [1 - f_2(\bar{\varepsilon})] + K_B^{\text{perm} \cdot \text{perm}} f_2(\bar{\varepsilon}), \end{aligned} \quad (48)$$

where

$$f_2(\bar{\varepsilon}) = \frac{1}{1 + \bar{\varepsilon}}, \quad \bar{\varepsilon} = \frac{\pi \delta_0}{2} \frac{1}{a} \frac{1}{\varepsilon_c} \frac{1}{2} \left( \varepsilon_{11} + \frac{e_{15}^2}{c_{44}} + \varepsilon'_{11} + \frac{e'^2_{15}}{c'_{44}} \right). \quad (49)$$

The functions of permittivity ( $\varepsilon_c$ ) and permeability ( $\mu_c$ ) approaches zero as  $\varepsilon_c$  and  $\mu_c$  tend to zero and are unity as  $\varepsilon_c$  and  $\mu_c$  tend to infinity. The solution perfectly matches exact solution in both limiting cases, namely, permeable and/or impermeable electric and/or magnetic boundary conditions.

In above equations the notation  $K^{\text{perm} \cdot \text{imp}}$  denotes the intensity factor for electrically permeable and magnetically impermeable crack boundary conditions.

The electric displacement  $d_0$  and magnetic induction  $b_0$  in the crack region depend on the matrix

$$\bar{C}_1^{-1} = \frac{1}{2} (C_1^{-1} + C_1'^{-1}) \quad (50)$$

as well as  $K_D$ ,  $K_B$ ,  $K_\phi$ ,  $K_\psi$ , and  $K_w$  depend on the matrix

$$\bar{C}^{-1} = \frac{1}{2}(C^{-1} + C'^{-1}), \quad (51)$$

where again “ $-1$ ” denotes the inverse matrix.

Thus,

$$\bar{C} = \begin{bmatrix} \bar{c}_{44} & \bar{e}_{15} & \bar{q}_{15} \\ \bar{e}_{15} & -\bar{\epsilon}_{11} & -\bar{d}_{11} \\ \bar{q}_{15} & -\bar{d}_{11} & -\bar{\mu}_{11} \end{bmatrix} = \left[ \frac{1}{2}(C^{-1} + C'^{-1}) \right]^{-1} \quad (52)$$

is the matrix of material property of equivalent homogeneous material after homogenization in our problem. The generalized effective electroelastic compliances of bi-material system are obtained as arithmetically mean of compliances of single materials constituents. If the lower medium and the upper medium have the same properties but are poled in opposite directions, then  $\alpha = -\alpha'$  and  $\beta = -\beta'$  (see (16)). In consequence from (17), we have

$$\bar{C}^{-1} = \frac{1}{\tilde{c}_{44}} \begin{bmatrix} 1 & 0 & 0 \\ 0 & \alpha^2 + c_1 \tilde{c}_{44} & \alpha\beta + c_2 \tilde{c}_{44} \\ 0 & \alpha\beta + c_2 \tilde{c}_{44} & \beta^2 + c_3 \tilde{c}_{44} \end{bmatrix}. \quad (53)$$

Then

$$\bar{C} = \frac{\tilde{c}_{44}}{\Delta} \begin{bmatrix} \Delta & 0 & 0 \\ 0 & \beta^2 + c_3 \tilde{c}_{44} & -(\alpha\beta + c_2 \tilde{c}_{44}) \\ 0 & -(\alpha\beta + c_2 \tilde{c}_{44}) & \alpha^2 + c_1 \tilde{c}_{44} \end{bmatrix}, \quad (54)$$

$$\Delta = (\alpha^2 + c_1 \tilde{c}_{44})(\beta^2 + c_3 \tilde{c}_{44}) - (\alpha\beta + c_2 \tilde{c}_{44})^2.$$

Magneto-electro-elastic materials usually comprise alternating piezoelectric material and piezomagnetic material. If upper material is piezomagnetic and lower material is piezoelectric (or otherwise), we have

$$C = \begin{bmatrix} c_{44} & 0 & q_{15} \\ 0 & -\infty & 0 \\ q_{15} & 0 & -\mu_{11} \end{bmatrix}, \quad C' = \begin{bmatrix} c'_{44} & e'_{15} & 0 \\ e'_{15} & -\epsilon'_{11} & 0 \\ 0 & 0 & -\infty \end{bmatrix}. \quad (55)$$

The bi-material matrix  $\bar{C}^{-1}$  defined by (51) has the form

$$\bar{C}^{-1} = \frac{1}{2} \begin{bmatrix} \mu_{11} & 0 & q_{15} \\ 0 & 0 & 0 \\ q_{15} & 0 & -c_{44} \end{bmatrix} + \frac{1}{2} \begin{bmatrix} e'_{15} & e'_{15} & 0 \\ e'_{15} & -\epsilon'_{11} & 0 \\ 0 & 0 & 0 \end{bmatrix}. \quad (56)$$

In the solutions also appears electric and magnetic field components

$$\begin{aligned} [E_y, H_y]^T &= -C_1^{-1}[\tau_0, D, B]^T \quad \text{in case I,} \\ E_y &= E_0, \quad H_y = H_0 \quad \text{in case II,} \end{aligned} \quad (57)$$

where the matrix  $C_1^{-1}$  is defined by (34). Of course, for lower material, we have  $C_1^{-1}$  matrix (the material parameters are denoted by prime). This states that, in general, electric and magnetic fields are also singular. The electric and magnetic field intensity factors  $K_E$  and  $K_H$  are related to  $K_\tau$ ,  $K_D$ , and  $K_B$ , as shown (57)<sub>1</sub>. In particular, for a fully permeable crack between two materials polarized in opposite directions, we have  $K_D = 0 = K_B$  and

$$K_E = \frac{\alpha}{\tilde{c}_{44}} K_\tau, \quad K_H = \frac{\beta}{\tilde{c}_{44}} K_\tau. \quad (58)$$

The particular solutions

$$\begin{aligned} w(y) &= \gamma y, & w'(y) &= \gamma' y, \\ \phi(y) &= -E_y y, & \phi'(y) &= -E'_y y, \\ \psi(y) &= -H_y y, & \psi'(y) &= -H'_y y \end{aligned} \quad (59)$$

with

$$\gamma = \frac{1}{\tilde{c}_{44}}(\tau_0 + \alpha D + \beta B), \quad \gamma' = \frac{1}{\tilde{c}'_{44}}(\tau_0 + \alpha' D + \beta' B) \quad (60)$$

complete the full fields in both materials.

## 6. Numerical Results

The basic data for the material properties selected here are similar to those in Sih and Song [6, 7]. These constants read as:  $c_{44} = 43,7 \times 10^9 \text{ N/m}^2$ ,  $e_{15} = 8,12 \text{ C/m}^2$ ,  $\epsilon_{11} = 7,86 \times 10^{-9} \text{ C/Vm}$ ,  $d_{11} = 0,0$ ,  $q_{15} = 165,0 \text{ N/Am}$ , and  $\mu_{11} = 180,5 \times 10^{-6} \text{ N/A}^2$  for first material and  $c_{44} = 44,6 \times 10^9 \text{ N/m}^2$ ,  $e_{15} = 3,48 \text{ C/m}^2$ ,  $\epsilon_{11} = 3,42 \times 10^{-9} \text{ C/Vm}$ ,  $d_{11} = 0,0$ ,  $q_{15} = 385,0 \text{ N/Am}$ ,  $\mu_{11} = 414,5 \times 10^{-6} \text{ N/A}^2$  for second material.

Using these properties of both materials, the material property matrix  $\bar{C}^{-1}$  is obtained as (the matrix of generalized “compliances”):

$$\bar{C}^{-1} = \begin{bmatrix} 19,88 \times 10^{-12} \text{ m}^2/\text{N} & 20,38 \times 10^{-3} \text{ m}^2/\text{C} & 18,33 \times 10^{-6} \text{ Am/N} \\ 20,38 \times 10^{-3} \text{ m}^2/\text{C} & -1,89 \times 10^8 \text{ Vm/C} & 18,78 \times 10^3 \text{ Am/C} \\ 18,33 \times 10^{-6} \text{ Am/N} & 18,78 \times 10^3 \text{ Am/C} & -3,96 \times 10^3 \text{ A}^2/\text{N} \end{bmatrix}. \quad (61)$$

The matrix of generalized stiffness is obtained as follows:

$$\bar{C} = \begin{bmatrix} 45,08 \times 10^9 \text{ N/m}^2 & 4,89 \text{ C/m}^2 & 231,8 \text{ N/Am} \\ 4,89 \text{ C/m}^2 & -4,77 \times 10^{-9} \text{ C/Vm} & 1,36 \times 10^{-12} \text{ C/Am} \\ 231,8 \text{ N/Am} & 1,36 \times 10^{-12} \text{ C/Am} & -251 \times 10^{-6} \text{ N/A}^2 \end{bmatrix}. \quad (62)$$

Therefore, the properties of composite, obtained by averaging the properties of single-phase materials using its

volume fractions, as in the literature (see [8]) gives erroneous result, since give (if ratio is roughly 50 : 50)

$$\bar{C}_{\text{aver}} = \begin{bmatrix} 44,15 \times 10^9 \text{ N/m}^2 & 5,80 \text{ C/m}^2 & 275 \text{ N/Am} \\ 5,80 \text{ C/m}^2 & -5,64 \times 10^{-9} \text{ C/Vm} & 0 \\ 275 \text{ N/Am} & 0 & -297,5 \times 10^{-6} \text{ N/A}^2 \end{bmatrix}. \quad (63)$$

The nonzero material constants for BaTiO<sub>3</sub>-piezoelectric and CoFe<sub>2</sub>O<sub>4</sub>-magnetostrictive medium are given in Table 1 [9].

The bi-material matrix  $\bar{C}^{-1}$  defined by (51) is ("compliance" matrix)

$$\bar{C}^{-1} = \begin{bmatrix} 20,00 \times 10^{-12} \text{ m}^2/\text{N} & 94,13 \times 10^{-4} \text{ m}^2/\text{C} & 10,17 \times 10^{-6} \text{ Am/N} \\ 94,13 \times 10^{-4} \text{ m}^2/\text{C} & -6,28 \times 10^9 \text{ Vm/C} & 0 \\ 10,17 \times 10^{-6} \text{ Am/N} & 0 & -1,01 \times 10^5 \text{ A}^2/\text{N} \end{bmatrix}. \quad (64)$$

The matrix  $\bar{C}$  is obtained as follows: ("stiffness" matrix)

$$\bar{C} = \begin{bmatrix} 49,96 \times 10^9 \text{ N/m}^2 & 74,82 \times 10^{-3} \text{ C/m}^2 & 5,04 \text{ N/Am} \\ 74,82 \times 10^{-3} \text{ C/m}^2 & -1,59 \times 10^{-10} \text{ C/Vm} & 7,55 \times 10^{-12} \text{ C/Am} \\ 5,04 \text{ N/Am} & 7,55 \times 10^{-12} \text{ C/Am} & -9,91 \times 10^{-6} \text{ N/A}^2 \end{bmatrix}. \quad (65)$$

Using the mixture rule [6],  $\kappa^c = \kappa V_f + \kappa'(1 - V_f)$ , for  $V_f = 0,5$ , where  $\kappa$  with superscripts  $c$  without prime or prime denotes the corresponding constants  $c_{44}$ ,  $e$ ,  $\varepsilon$ ,  $q$ ,  $\mu$ ,  $d$

of the composite, first and second material, respectively, and  $V_f$  is the volume fraction of the first material (piezoelectric), we obtain that

$$\bar{C}^* = \begin{bmatrix} 44,15 \times 10^9 \text{ N/m}^2 & 5,80 \text{ C/m}^2 & 275 \text{ N/Am} \\ 5,80 \text{ C/m}^2 & -5,64 \times 10^{-9} \text{ C/Vm} & 0 \\ 275 \text{ N/Am} & 0 & -297,5 \times 10^{-6} \text{ N/A}^2 \end{bmatrix}. \quad (66)$$

which completely differs from  $\bar{C}$ .

Note that in both examples the sums of corresponding material parameters are constant. In consequence the matrix,  $\bar{C}_{\text{aver}}$  and  $\bar{C}^*$  have the same elements. Of course, the matrices of generalized stiffness are dissimilar in both bi-material composites.

Due to the absence of magnetoelectric coupling coefficient in a single-phase piezoelectric and piezomagnetic material, the magnetoelectric constant  $d_{11}$ , existing only in the piezoelectric/piezomagnetic composite as a significant new feature, cannot be determined by the above mixture rule. Therefore, based on the analysis of micromechanics,

TABLE 1: The material constants for BaTiO<sub>3</sub> and CoFe<sub>2</sub>O<sub>4</sub>.

properties	BaTiO <sub>3</sub> piezoelectric	CoFe <sub>2</sub> O <sub>4</sub> piezomagnetic
$c_{44}$ ( $10^9$ N/m <sup>2</sup> )	43,00	45,30
$e_{15}$ (C/m <sup>2</sup> )	11,60	0,00
$\epsilon_{11}$ ( $10^{-9}$ C/Vm)	11,20	0,08
$q_{15}$ (N/Am)	0,00	550,00
$\mu_{11}$ ( $10^{-6}$ N/A <sup>2</sup> )	5,00	590,00
$d_{11}$ ( $10^{-9}$ C/Am)	0,00	0,00

this coefficient is obtained as  $d_{11} = 1,36 \times 10^{-12}$  C/Am for first combination of materials and  $7,55 \times 10^{-12}$  C/Am for barium titanate-cobalt iron oxide bi-material. This is magnetoelectric coupling effect in composite of piezoelectric and piezomagnetic phases.

## 7. Conclusions

The mode III interface crack in a bi-material magneto-electro-elastic medium subjected to mechanical, electrical, and magnetic loads on the surfaces is studied in this paper, and the following points are noted.

- (i) Closed form solution has been obtained for a crack between two dissimilar PEMO-elastic materials. Expressions for the crack-tip field intensity factors, the electromagnetic fields inside the crack, are given. The semipermeable crack-face magneto-electric boundary conditions are investigated.
- (ii) The energy release rate can be explicitly expressed in terms of the external loadings (by (42)). It is affected by electric-magnetic properties of the two constituents of the bi-material media.
- (iii) Applications of electric and magnetic fields do not alter the stress intensity factor of mode III. The values of SIF are identical for any kind of crack-face electric and magnetic boundary condition assumptions. In other words, the crack-face electric and magnetic boundary conditions have no effects on SIF.
- (iv) For electrically impermeable and magnetically permeable crack, the solutions for field intensity factors are independent of the applied magnetic field. Alternatively, these solutions for the electrically permeable and magnetically impermeable crack are independent on the applied electric displacement.
- (v) For fully permeable crack between two PEMO-elastic materials polarized in opposite directions, the electric displacement and magnetic induction intensity factors vanish. In this case electric and magnetic field intensity factors  $K_E$  and  $K_B$  are related to  $K_\tau$  (by (58)).
- (vi) The matrices of “generalized” compliances or stiffness cannot be determined by the mixture rule since it is a significant new feature in interface crack problem considered in this paper.

- (vii) From the reviewing of literature dealing with interface crack, problem may be concluded that the characterization of bonded dissimilar materials with interface crack is still an open problem.

## References

- [1] R. Li and G. A. Kardomateas, “The mode III interface crack in piezo-electro-magneto-elastic dissimilar bimaterials,” *Journal of Applied Mechanics*, vol. 73, no. 2, pp. 220–227, 2006.
- [2] B. L. Wang and Y. W. Mai, “Closed-form solution for an antiplane interface crack between two dissimilar magneto-electroelastic layers,” *Journal of Applied Mechanics*, vol. 73, no. 2, pp. 281–290, 2006.
- [3] X. F. Li and B. L. Wang, “Anti-plane shear crack normal to and terminating at the interface of two bonded piezoelectric ceramics,” *International Journal of Solids and Structures*, vol. 44, no. 11-12, pp. 3796–3810, 2007.
- [4] B. Rogowski, “The mode III cracks emanating from an elliptical hole in the piezo-electro-magneto-elastic materials,” *Archive of Applied Mechanics*, vol. 81, no. 11, pp. 1607–1620, 2011.
- [5] B. Rogowski, “The limited electrically permeable crack model in linear piezoelectricity,” *International Journal of Pressure Vessels and Piping*, vol. 84, no. 9, pp. 572–581, 2007.
- [6] G. C. Sih and Z. F. Song, “Magnetic and electric poling effects associated with crack growth in BaTiO<sub>3</sub>-CoFe<sub>2</sub>O<sub>4</sub> composite,” *Theoretical and Applied Fracture Mechanics*, vol. 39, no. 3, pp. 209–227, 2003.
- [7] Z. F. Song and G. C. Sih, “Crack initiation behavior in magneto-electroelastic composite under in-plane deformation,” *Theoretical and Applied Fracture Mechanics*, vol. 39, no. 3, pp. 189–207, 2003.
- [8] B. L. Wang and Y. W. Mai, “Applicability of the crack-face electromagnetic boundary conditions for fracture of magneto-electroelastic materials,” *International Journal of Solids and Structures*, vol. 44, no. 2, pp. 387–398, 2007.
- [9] J. H. Huang and W. S. Kuo, “The analysis of piezoelectric/piezomagnetic composite materials containing ellipsoidal inclusions,” *Journal of Applied Physics*, vol. 81, no. 3, pp. 1378–1386, 1997.

## Research Article

# Epitaxial Piezoelectric $\text{Pb}(\text{Zr}_{0.2}\text{Ti}_{0.8})\text{O}_3$ Thin Films on Silicon for Energy Harvesting Devices

**A. Sambri,<sup>1,2</sup> D. Isarakorn,<sup>3</sup> A. Torres-Pardo,<sup>4</sup> S. Gariglio,<sup>1</sup> Pattanaphong Janphuang,<sup>3</sup>  
D. Briand,<sup>3</sup> O. Stéphan,<sup>4</sup> J. W. Reiner,<sup>5</sup> J.-M. Triscone,<sup>1</sup> Nico F. de Rooij,<sup>3</sup> and C. H. Ahn<sup>5</sup>**

<sup>1</sup> *Department of Condensed Matter Physics, (DPMC), University of Geneva, 24 Quai Ernest-Ansermet, 1211 Geneva 4, Switzerland*

<sup>2</sup> *Dipartimento di Scienze Fisiche & CNR-SPIN, Università degli Studi di Napoli Federico II, Complesso Universitario di Monte S. Angelo, Via Cintia, 80126 Napoli, Italy*

<sup>3</sup> *The Sensors, Actuators and Microsystems Laboratory, Institute of Microengineering (IMT), Ecole Polytechnique Fédérale de Lausanne (EPFL), Rue Jaquet-Droz 1, P.O. Box 526, 2002 Neuchâtel, Switzerland*

<sup>4</sup> *Laboratoire de Physique des Solides, Université Paris-Sud, CNRS-UMR 8502, 91405 Orsay, France*

<sup>5</sup> *Department of Applied Physics, Yale University, P.O. Box 208284, New Haven, CT 06520-8284, USA*

Correspondence should be addressed to A. Sambri, sambri@fisica.unina.it

Received 20 December 2011; Accepted 27 January 2012

Academic Editor: Mohammed Es-Souni

Copyright © 2012 A. Sambri et al. This is an open access article distributed under the Creative Commons Attribution License, which permits unrestricted use, distribution, and reproduction in any medium, provided the original work is properly cited.

We report on the properties of ferroelectric  $\text{Pb}(\text{Zr}_{0.2}\text{Ti}_{0.8})\text{O}_3$  (PZT) thin films grown epitaxially on (001) silicon and on the performance of such heterostructures for microfabricated piezoelectric energy harvesters. In the first part of the paper, we investigate the epitaxial stacks through transmission electron microscopy and piezoelectric force microscopy studies to characterize in detail their crystalline structure. In the second part of the paper, we present the electrical characteristics of piezoelectric cantilevers based on these epitaxial PZT films. The performance of such cantilevers as vibration energy transducers is compared with other piezoelectric harvesters and indicates the potential of the epitaxial approach in the field of energy harvesting devices.

## 1. Introduction

In the last decade, studies on epitaxial ferroelectric thin films have led to many interesting results and exciting discoveries [1]. The possibility of tailoring or even enhancing some physical parameters via epitaxial strain engineering [2–4] has suggested the idea of the exploitation of such thin films for several technological applications [5]. Nevertheless, the benefits of the epitaxial approach on the performances of ferroelectric thin film-based devices have to compensate the hurdles related to the epitaxial growth on industrial substrates such as silicon, the modern technological platform. It is in fact well known that the basic requirements for the epitaxy, that is, a good lattice match between substrate and film and a reciprocal chemical stability, are not easily fulfilled in the case of oxide growth on silicon. Beside the difference in lattice parameters and thermal expansion coefficients, the main problem is the surface reactivity of silicon to oxygen,

with the formation of an amorphous layer of silicon dioxide that hinders any further epitaxy. Moreover, the cations of most ferroelectric compounds interdiffuse into the silicon substrate, forming spurious extra phases at the interface [6]. In order to overcome such difficulties, a suitable buffer layer is needed that acts as a barrier for cations migration and as a structural template for the growth of the ferroelectric epitaxial film [7–9].

PZT is one of the most investigated ferroelectric materials, due to its high values of remnant polarization and piezoelectric coefficients. In the bulk form, it displays a complex phase diagram versus the Ti/Zr content: for the stoichiometry of our choice, that is,  $\text{Pb}(\text{Zr}_{0.2}\text{Ti}_{0.8})\text{O}_3$  (PZT 20/80), it is ferroelectric with a tetragonal structure up to a transition temperature of 460°C [10]. It is worth stressing that for ferroelectric materials the mechanical boundary conditions may affect substantially the ferroelectric properties because of the strong strain-polarization coupling present in these

compounds [11–13]. Thus, the epitaxial strain often makes the properties of ferroelectric thin films substantially different from the bulk counterpart.

## 2. Heterostructure Growth and Characterization

The investigated epitaxial heterostructure is composed of a ferroelectric PZT layer grown on top of a metallic SrRuO<sub>3</sub> (SRO) film, used as bottom electrode. This bilayer is deposited onto a thin SrTiO<sub>3</sub> (STO) film epitaxially grown on a 2-inch (001) silicon wafer. The choice of STO as buffer layer is determined by the fact that it has the same crystalline structure (perovskite) and a good lattice match with SRO and PZT. STO also acts as a barrier for Pb diffusion into the silicon wafer [14–16]. The STO layer can reach a very high degree of crystalline perfection on silicon when the growth is performed by molecular beam epitaxy through a complex multistep process, where fixed amounts of the elemental materials have to be carefully deposited at specific conditions of substrate temperature and pressure. The deposition process we used is detailed in [17, 18]. *In situ* Reflection High Energy Electron Diffraction (RHEED) is the key tool in order to monitor and control the whole deposition procedure, since every step of the deposition corresponds to a specific diffraction pattern linked to a particular surface reconstruction. Figure 1 shows the evolution of the RHEED pattern during the growth of a STO film on silicon.

The SRO and PZT layers are subsequently grown by rf magnetron sputtering as described in [19]. In the following, a detailed investigation of the crystalline structure of a PZT(100 nm)/SRO(30 nm)/STO(6 nm)/Si stack is given. X-ray structural characterization of the heterostructure has been performed with a high-resolution PANalytical X'Pert diffractometer, equipped with a four-bounce asymmetric Ge(220) monochromator for Cu K $\alpha$ <sub>1</sub> radiation. Through  $\theta$ -2 $\theta$  and  $\phi$ -scan diffractograms, the following out-of-plane orientation and cube-on-cube arrangement of the oxides stack on silicon have been determined: PZT[001]//SRO[001]//STO[001]//Si[001] and PZT[100]//SRO[100]//STO[100]//Si[110] (see also [13]).

Transmission electron microscopy (TEM) characterization, performed on a JEOL JEM2010 microscope, shows at the silicon-STO interface the presence of an amorphous layer of SiO<sub>2</sub>, which clearly did not affect the epitaxy of the oxides multilayer (Figure 2).

Most likely then, the formation of this SiO<sub>2</sub> layer occurs after the growth of the STO/Si interface template through oxygen diffusion, thus not hindering the epitaxy [20–22].

Interestingly, the TEM investigation also revealed the presence in the PZT layer of crystallographic domains with the *c*-axis aligned in the plane of the film, so-called *a*-domains. Figure 3 shows that their width is about 20 nm. We note that the overlap of the more intense (00*l*) SRO reflections with the diffraction peaks of the PZT *a*-domains most probably prevents their detection in the X-ray  $\theta$ -2 $\theta$  scans. The origin of the formation of these domains can be related to the strain arising from the lattice and thermal mismatch

of the film with the substrate during the cool-down across the ferroelectric transition [23, 24]. Figure 3(a) shows a pattern of domains in the PZT layer: they repeat periodically every  $\sim$ 105 nm. The domain wall between *a* and *c* domains runs along the diagonal of the tetragonal unit cell and the difference between the *a* and *c* axis ( $c/a = 1.046$ ) [13] gives rise to a distortion of the neighboring lattices on each side of a 90° domain wall. The misalignment of the growth planes between *a* and *c* domains is clearly visible in Figure 3(c) and can be estimated to be  $\sim$ 3°, in good agreement with the calculated value of  $\sim$ 2.6°.

Due to the different polarization orientations of the *c* and *a* domains, respectively, perpendicular and parallel to the film-substrate interface, we can detect their presence by piezoelectric force microscopy (PFM). In PFM, a conducting tip is scanned in contact with the surface while an ac voltage, lower than the coercive field of the material, is applied between the tip and the sample. From the detection of the in-phase and out-of-phase deformation signals in the vertical (V) and lateral (L) PFM modes [25], it is possible to map the presence of *a* and *c* domains.

Figure 4(a) shows a topography scan of a PZT surface, revealing a nRMS roughness of 5 nm. The V-PFM scan shown in the middle panel is sensitive to the polarization direction of the *c*-domains of the film, here shown as reddish area, while the yellowish lines correspond to *a*-domains, with zero contrast. Conversely, through L-PFM it is possible to detect the piezoelectric response of *a*-domains, with the restriction that domains parallel to the scan direction cannot be detected, as clearly shown in Figure 4(c). Combining the V-PFM and L-PFM measurements, the PZT film appears to be a very dense network of small *a*-domains embedded in a matrix of *c*-axis domains. As can be seen, the phase response detected in the V-PFM and L-PFM is unrelated to the topographic features detected simultaneously by the AFM scan. Figure 5 shows a detail of the PZT *a*-domains network, on a  $1 \times 1 \mu\text{m}^2$  area.

According to some reports, applying an electric field induces a lateral motion of thin *a*-domains [26–33]. Even though some of these results are still under debate, such a motion would give rise to an extrinsic contribution to the piezoelectric response of the material and an enhancement of the conversion coefficients. *a*-domains switching would indirectly enhance the strain state in the film and its piezoelectric response. Indeed, while the estimation of the PZT  $d_{33}$  coefficient by PFM measurement yields a value of about 50 pm/V (in agreement with the data reported for bulk PZT 20/80), the indirect estimation of  $d_{31}$  from the deflection of a microfabricated piezoelectric cantilever gives a higher value (details in the next section).

We investigated the ferroelectric behavior of these epitaxial films grown on silicon through a series of polarization hysteresis measurements, performed by a TF analyzer 2000. To perform the measurements, Cr/Au top electrodes were prepared with a size of  $100 \times 100 \mu\text{m}^2$ . The polarization versus voltage loop, shown in Figure 6(a), reveals a remnant polarization of about  $70 \mu\text{C cm}^{-2}$  and no significant leakage current up to 16 V. Figure 6(b) displays the measurement of the capacitance versus applied bias, revealing the dielectric

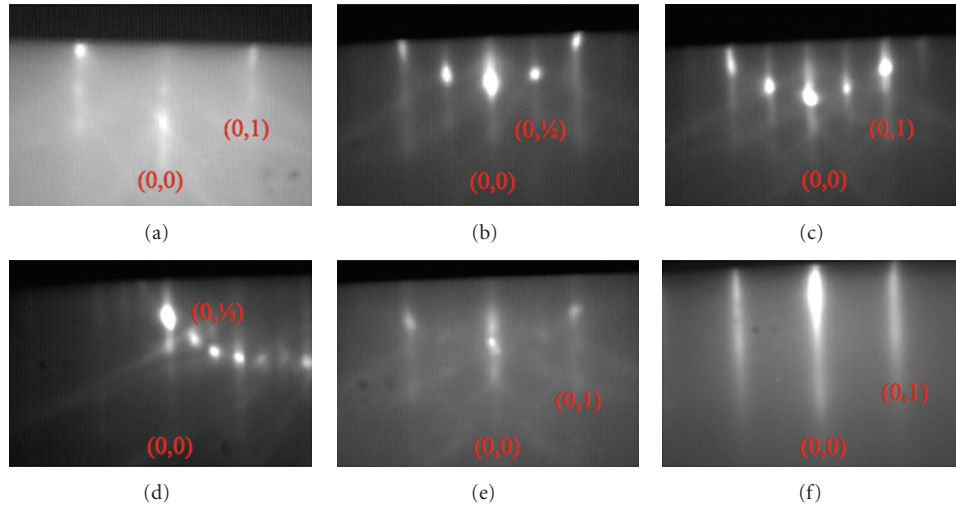


FIGURE 1: Evolution of RHEED pattern during the growth of a STO layer. The patterns shown are taken with the electron beam along the [100] direction. (a) As-received Si wafer (001), the diffuse background indicates the presence of a native amorphous layer of  $\text{SiO}_2$ ; (b) crystalline Si surface after a thermal treatment in vacuum: the appearance of fractional spots  $(0,1/2)$  due to Si dimers indicates the complete removal of  $\text{SiO}_2$ ; (c)  $2\times$  surface reconstruction corresponding to the deposition of half monolayer (ML) of Sr in vacuum at high temperature, (d)  $3\times$  reconstruction corresponding to the deposition of half ML of Sr in vacuum at low temperature, (e) 1 ML of SrO, (f) 3 ML of crystalline STO.

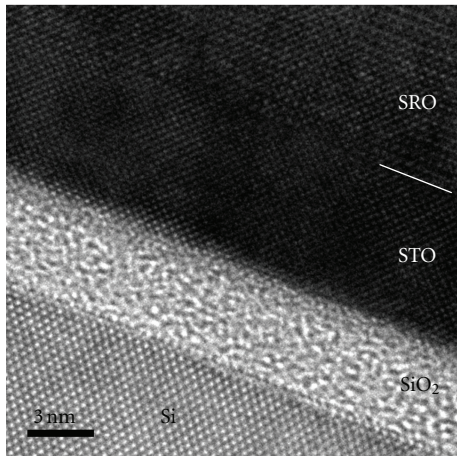


FIGURE 2: Cross-sectional TEM image, revealing the presence of 4.5 nm of amorphous  $\text{SiO}_2$  located between the silicon substrate and the epitaxial oxide stack.

tunability of our epitaxial PZT. In the approximation of a plane capacitor, we estimate a dielectric constant at zero field to be about 150.

### 3. Energy Harvesting Devices

The development of transducers allowing energy from mechanical vibrations to be generated has advanced rapidly during the past few years. Several review articles [34, 35] discuss the principles and advantages of each conversion method. Among these, piezoelectricity based devices have received large attention due to their high power density and

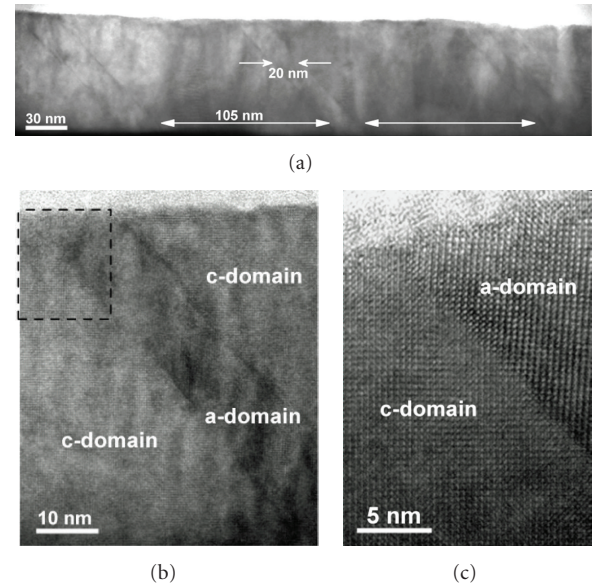


FIGURE 3: (a) Cross-sectional TEM image, revealing the presence of periodic *a*-domains, (b) HRTEM of a single *a*-domain surrounded by a *c*-axis oriented regions. (c) Details of the  $90^\circ$  domain wall.

ease of integration compared to other transduction techniques [36–38]. Several piezoelectric silicon micromachined energy scavengers have been proposed so far, most of these devices being based on polycrystalline PZT (poly-PZT) or aluminum nitride (AlN) films. Energy harvesting devices involving epitaxial PZT thin films are however less common [39–41]. In this study we report on the characteristics of

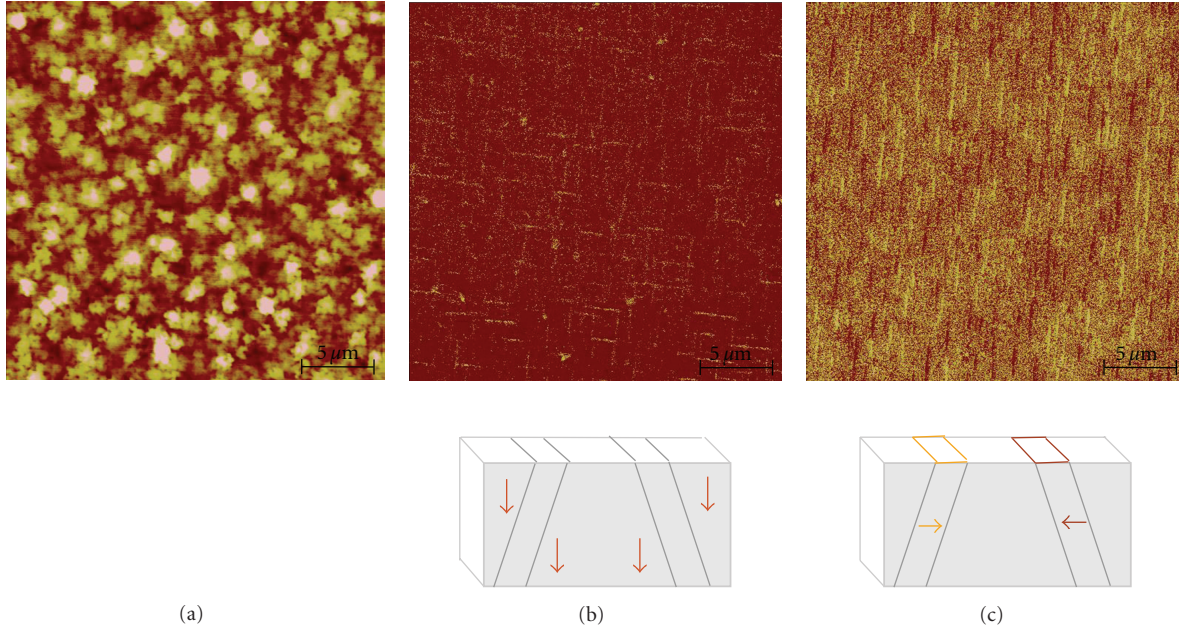


FIGURE 4: (a) Topography scan on a  $20 \times 20 \mu\text{m}^2$  area, (b) V-PFM and (c) L-PFM: phase response of the vertical and lateral PFM measurements on the same area and schematic of the corresponding detected domains.

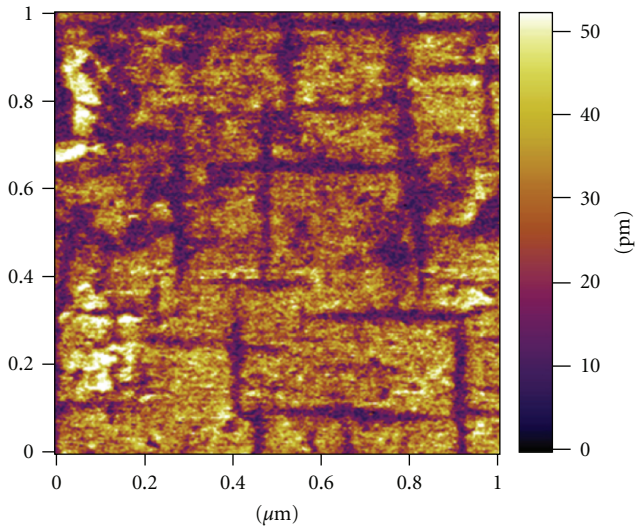


FIGURE 5: V-PFM scan on a  $1 \times 1 \mu\text{m}^2$  area: zoom of the *a*-domains network.

MEMS based vibrations energy scavengers made of an epitaxial PZT film on silicon cantilevers.

A typical device is shown in Figure 7: it is based on a cantilever fabricated using micropatterning techniques optimized for the oxide layers deposited on silicon. The details of the microfabrication process are presented in [19].

The  $d_{31}$  piezoelectric coefficient has been estimated from the displacement at the free end of a cantilever. The deflection of this cantilever, coated with 100 nm thick epi-PZT films, has been measured as a function of dc voltage using an interferometric profiler (Wyko NT110). The piezoelectric

coefficient value is estimated to be  $135.4 \pm 7.1 \text{ pm/V}$  [19]. For a PZT thickness of about 500 nm, we measure a residual stress after the film growth of about 60 MPa, according to stress measurement performed using a Tencor FLX-2320A system. In order to evaluate the performance of our device, the cantilever's resonant frequency has been determined using a Polytec MVS-400 laser Doppler vibrometer, obtaining a value of  $2.3 \pm 0.1 \text{ kHz}$ . The power generation performance of the device has been investigated with a shaker (Bruel and Kjaer type 4811) driven by a vibration exciter control (type 1050) and a power amplifier (type 2712) by applying an acceleration as a mechanical input. The device is connected with various resistive loads ( $R_L$ ) and the current generated under different acceleration levels is recorded with a multimeter (Agilent 34411A). The corresponding average power is calculated by the relation:  $P_{\text{ave}} = I_{\text{rms}}^2 R_L$ . The output current, average power, and voltage as a function of resistive loads are shown in Figure 8.

In order to compare this performance with other MEMS energy harvesters, these output data are normalized as following: the output power per square acceleration ( $\text{g}^2$ ), the current and voltage per acceleration ( $\text{g}$ ). From a single device with an optimal resistive load of  $4.7 \text{ k}\Omega$ , a maximum output power of  $14 \mu\text{W}/\text{g}^2$  with  $60 \mu\text{A}/\text{g}$  output current is obtained, thus resulting in an output voltage of  $0.28 \text{ V}/\text{g}$ . The maximum power density is as high as  $105 \mu\text{W}/(\text{g}^2 \text{ mm}^3)$ . As shown in details in [41], the comparison of the electrical output characteristics between this epitaxial-PZT energy harvester and other piezo-harvesting devices based on poly-PZT and AlN films [42–46] shows that the former provides higher current at smaller resistive load. Usually, energy harvesting devices with a low optimal load resistance are highly desirable because they can generate high output current,

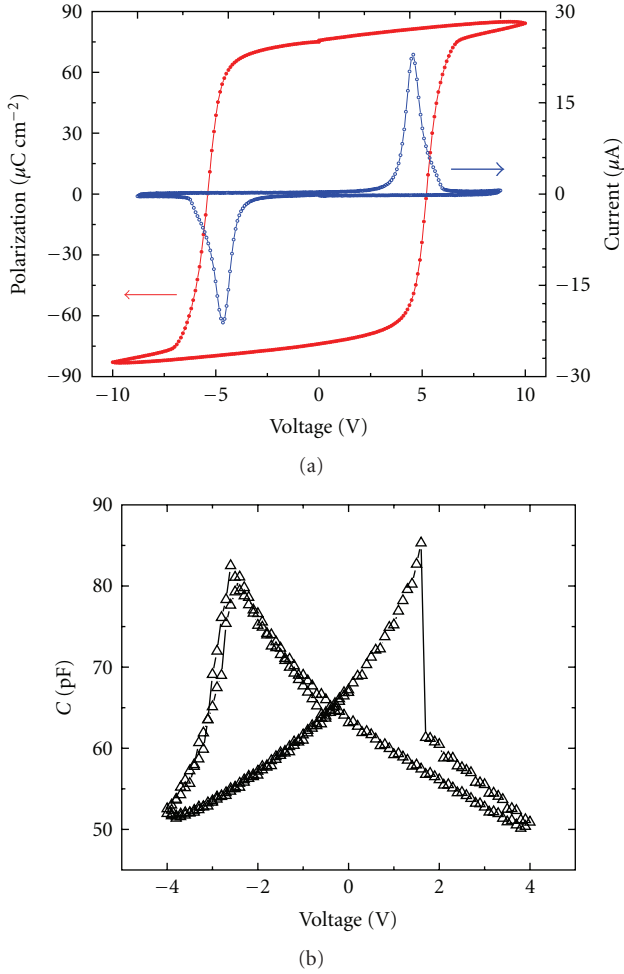


FIGURE 6: (a) Polarization versus applied voltage (PE loop) (full red circle) and corresponding switching current (empty blue circle). (b) Plot of the capacitance versus applied bias. The difference in the coercive field in the PE loop measurement and in the capacitance cycle is due to a different electrical configuration, top-top contacts for PE loops while top-bottom for the capacitance.

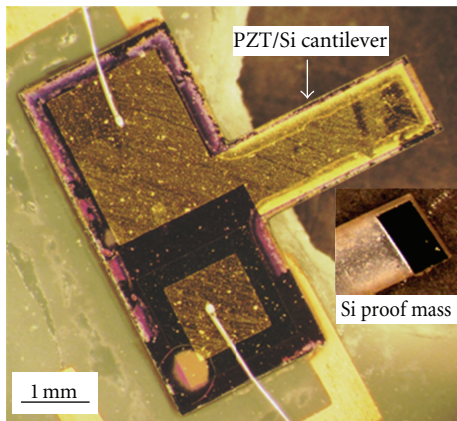


FIGURE 7: Optical image of an epi-PZT cantilever ( $1000 \times 2500 \times 7 \mu\text{m}^3$ ) with a Si proof mass ( $1000 \times 500 \times 230 \mu\text{m}^3$ ). The inset shows the Si proof mass on the back side of the cantilever. The effective volume of the final device is  $0.1325 \text{ mm}^3$ .

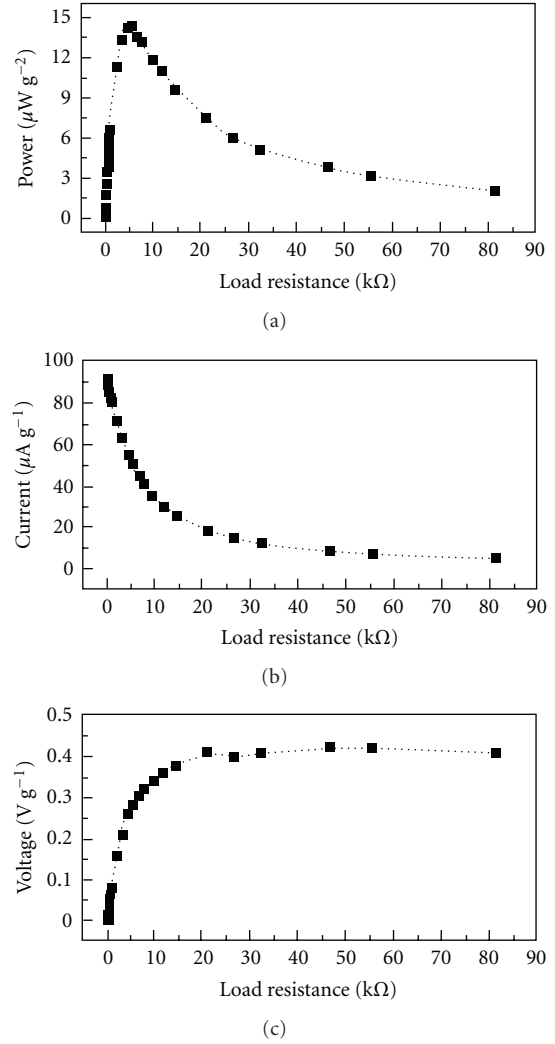


FIGURE 8: (a) Average power, (b) output current, and (c) corresponding output voltage of an epi-PZT harvester versus resistive load.

and also because their impedance can be easily matched to standard electronic devices. Energy harvesting devices based on poly-PZT and AlN films demonstrated useful power generation, but their high impedance limits the output current. Moreover, even though the power generated by the epi-PZT is similar to that of AlN, the epi-PZT harvester exhibits the highest power density, which is of high interest when realizing miniaturized devices. Unlike the polycrystalline film based devices, the device reported here can generate high power and current with usable voltage, while maintaining low optimal resistive load. For piezoelectric energy harvesters, the expressions for the figure of merit for the power, voltage and current are, respectively:  $P_F = e_{31,f}^2/\epsilon_r$ ,  $V_F = e_{31,f}/\epsilon_r$ ,  $I_F = e_{31,f}^2$ , where  $e_{31,f}$  is the effective piezoelectric coefficient. From the measured piezoelectric coefficient  $d_{31}$ , it is possible to estimate a value of  $18.2 \pm 0.9 \text{ C m}^{-2}$  [47], a value which is significantly higher than what has been reported in the past [48]. Such large piezoelectric coefficient

together with a low dielectric constant is among the key parameters to realize high performance piezoelectric energy harvesters.

#### 4. Conclusions

This paper reports on the structural and physical properties of epitaxial PZT thin films deposited on silicon and on the electrical performance of cantilevers microfabricated from such heterostructures. We have shown that the PZT thin films exhibit excellent ferroelectric characteristics with a remnant polarization of  $70 \mu\text{C cm}^{-2}$ . The structural microscopic investigation by TEM and PFM has revealed the presence of *a*-domains embedded in a mostly oriented *c*-axis film. This coexistence of domains with different crystallographic orientation could be at the origin of the large piezoelectric response estimated from the electromechanical behavior of the cantilevers. The performances of our epitaxial piezo-transducers fabricated for energy harvesting indicate that these generate higher power and current with usable voltage requiring lower optimal resistive load as compared to piezoelectric harvesters realized with polycrystalline PZT or AlN films.

#### Acknowledgments

The authors would like to thank M. Lopes for his technical assistance and P. Zubko for many fruitful discussions. This work was supported by the Swiss National Science Foundation through the National Center of Competence in Research, Materials with Novel Electronic Properties, MaNEP and Division II, and by European Union through the project "Nanoxide." D. Isarakorn and P. Janphuang are grateful to the Ministry of Science and Technology, Thailand, for the financial support for their Ph.D. studies at EPFL IMT-NE SAMLAB. A. Torres-Pardo is grateful to the Spanish Ministry of Education and Science for the support through MEC/Fulbright postdoctoral grant. Work at Yale was supported by NSF DMR 1006256 and MRSEC DMR 1119826.

#### References

- [1] M. Dawber, K. M. Rabe, and J. F. Scott, "Physics of thin-film ferroelectric oxides," *Reviews of Modern Physics*, vol. 77, no. 4, pp. 1083–1130, 2005.
- [2] J. H. Haeni, P. Irvin, W. Chang et al., "Room-temperature ferroelectricity in strained  $\text{SrTiO}_3$ ," *Nature*, vol. 430, no. 7001, pp. 758–761, 2004.
- [3] K. J. Choi, M. Biegalski, Y. L. Li et al., "Enhancement of ferroelectricity in strained  $\text{BaTiO}_3$  thin films," *Science*, vol. 306, no. 5698, pp. 1005–1009, 2004.
- [4] P. Zubko, N. Stucki, C. Lichtensteiger, and J. M. Triscone, "X-ray diffraction studies of  $180^\circ$  ferroelectric domains in  $\text{PbTiO}_3/\text{SrTiO}_3$  superlattices under an applied electric field," *Physical Review Letters*, vol. 104, no. 18, Article ID 187601, 2010.
- [5] N. Setter, D. Damjanovic, L. Eng et al., "Ferroelectric thin films: Review of materials, properties, and applications," *Journal of Applied Physics*, vol. 100, no. 10, Article ID 109901, 2006.
- [6] P. Revesz, J. Li, N. Szabo Jr., W. Mayer, D. Caudillo, and E. R. Myers, "PZT interaction with metals and oxides studied by RBS," *Materials Research Society Symposium Proceedings*, vol. 243, pp. 101–106, 1991.
- [7] R. A. McKee, F. J. Walker, and M. F. Chisholm, "Crystalline oxides on silicon: the first five monolayers," *Physical Review Letters*, vol. 81, no. 14, pp. 3014–3017, 1998.
- [8] J. W. Reiner, A. M. Kolpak, Y. Segal et al., "Crystalline oxides on silicon," *Advanced Materials*, vol. 22, no. 26–27, pp. 2919–2938, 2010.
- [9] Z. Yu, Y. Liang, C. Overgaard et al., "Advances in heteroepitaxy of oxides on silicon," *Thin Solid Films*, vol. 462–463, pp. 51–56, 2004.
- [10] B. Jaffe, W. R. Cook, and H. Jaffe, *Piezoelectric Ceramics*, Academic Press, London, UK, 1971.
- [11] N. A. Pertsev, A. G. Zembilgotov, and A. K. Tagantsev, "Effect of mechanical boundary conditions on phase diagrams of epitaxial ferroelectric thin films," *Physical Review Letters*, vol. 80, no. 9, pp. 1988–1991, 1998.
- [12] D. G. Schlom, L. Q. Chen, C. B. Eom, K. M. Rabe, S. K. Streiffer, and J. M. Triscone, "Strain tuning of ferroelectric thin films," *Annual Review of Materials Research*, vol. 37, pp. 589–626, 2007.
- [13] A. Sambri, S. Gariglio, A. Torres Pardo et al., "Enhanced critical temperature in epitaxial ferroelectric  $\text{Pb}(\text{Zr}_{0.2}\text{Ti}_{0.8})\text{O}_3$  thin films on silicon," *Applied Physics Letters*, vol. 98, no. 1, Article ID 012903, 3 pages, 2011.
- [14] D. S. Shin, S. T. Park, H. S. Choi, I. H. Choi, and J. Y. Lee, "Characteristics of  $\text{Pt}/\text{SrTiO}_3/\text{Pb}(\text{Zr}_{0.52}\text{Ti}_{0.48})\text{O}_3/\text{SrTiO}_3/\text{Si}$  ferroelectric gate oxide structure," *Thin Solid Films*, vol. 354, no. 1, pp. 251–255, 1999.
- [15] Ø. Nordseth, C. C. You, E. Folven et al., "Growth and characterization of  $(\text{Pb},\text{La})(\text{Zr},\text{Ti})\text{O}_3$  thin film epilayers on  $\text{SrTiO}_3$ -buffered  $\text{Si}(001)$ ," *Thin Solid Films*, vol. 518, no. 19, pp. 5471–5477, 2010.
- [16] E. Tokumitsu, K. Itani, B. K. Moon, and H. Ishiura, "Crystalline quality and electrical properties of  $\text{PbZr}_x\text{Ti}_{1-x}\text{O}_3$  thin films prepared on  $\text{SrTiO}_3$ -covered Si substrates," *Japanese Journal of Applied Physics*, vol. 34, no. 9, pp. 5202–5206, 1995.
- [17] J. W. Reiner, K. F. Garrity, F. J. Walker, S. Ismail-Beigi, and C. H. Ahn, "Role of strontium in oxide epitaxy on silicon (001)," *Physical Review Letters*, vol. 101, no. 10, Article ID 105503, 2008.
- [18] J. Lettieri, J. H. Haeni, and D. G. Schlom, "Critical issues in the heteroepitaxial growth of alkaline-earth oxides on silicon," *Journal of Vacuum Science and Technology A*, vol. 20, no. 4, pp. 1332–1340, 2002.
- [19] D. Isarakorn, A. Sambri, P. Janphuang et al., "Epitaxial piezoelectric MEMS on silicon," *Journal of Micromechanics and Microengineering*, vol. 20, no. 5, Article ID 055008, 2010.
- [20] G. J. Norga, C. Marchiori, C. Rossel et al., "Solid phase epitaxy of  $\text{SrTiO}_3$  on  $(\text{Ba},\text{Sr})\text{O}/\text{Si}(100)$ : the relationship between oxygen stoichiometry and interface stability," *Journal of Applied Physics*, vol. 99, no. 8, Article ID 084102, 7 pages, 2006.
- [21] L. V. Goncharova, D. G. Starodub, E. Garfunkel et al., "Interface structure and thermal stability of epitaxial  $\text{SrTiO}_3$  thin films on  $\text{Si}(001)$ ," *Journal of Applied Physics*, vol. 100, no. 1, Article ID 014912, 2006.
- [22] V. Shutthanandan, S. Thevuthasan, Y. Liang, E. M. Adams, Z. Yu, and R. Droopad, "Direct observation of atomic disordering at the  $\text{SrTiO}_3/\text{Si}$  interface due to oxygen diffusion," *Applied Physics Letters*, vol. 80, no. 10, Article ID 1803, 3 pages, 2002.

- [23] J. S. Speck and W. Pompe, "Domain configurations due to multiple misfit relaxation mechanisms in epitaxial ferroelectric thin films. I. Theory," *Journal of Applied Physics*, vol. 76, no. 1, pp. 466–476, 1994.
- [24] B. S. Kwak, A. Erbil, J. D. Budai, M. F. Chisholm, L. A. Boatner, and B. J. Wilkens, "Domain formation and strain relaxation in epitaxial ferroelectric heterostructures," *Physical Review B*, vol. 49, no. 21, pp. 14865–14879, 1994.
- [25] S. V. Kalinin, B. J. Rodriguez, S. Jesse et al., "Vector piezoresponse force microscopy," *Microscopy and Microanalysis*, vol. 12, no. 3, pp. 206–220, 2006.
- [26] Z. Ma, F. Zavaliche, L. Chen et al., "Effect of 90° domain movement on the piezoelectric response of patterned  $\text{PbZr}_{0.2}\text{Ti}_{0.8}\text{O}_3/\text{SrTiO}_3$  Si heterostructures," *Applied Physics Letters*, vol. 87, no. 7, Article ID 072907, 3 pages, 2005.
- [27] N. Bassiri-Gharb, I. Fujii, E. Hong, S. Trolier-Mckinstry, D. V. Taylor, and D. Damjanovic, "Domain wall contributions to the properties of piezoelectric thin films," *Journal of Electroceramics*, vol. 19, no. 1, pp. 47–65, 2007.
- [28] G. Le Rhun, I. Vrejoiu, L. Pintilie, D. Hesse, M. Alexe, and U. Gösele, "Increased ferroelastic domain mobility in ferroelectric thin films and its use in nano-patterned capacitors," *Nanotechnology*, vol. 17, no. 13, article 013, pp. 3154–3159, 2006.
- [29] V. Nagarajan, A. Roytburd, A. Stanishevsky et al., "Dynamics of ferroelastic domains in ferroelectric thin films," *Nature Materials*, vol. 2, no. 1, pp. 43–47, 2003.
- [30] R. J. Zednik, A. Varatharajan, M. Oliver, N. Valanoor, and P. C. McIntyre, "Mobile ferroelastic domain walls in nanocrystalline PZT films: the direct piezoelectric effect," *Advanced Functional Materials*, vol. 21, no. 16, pp. 3104–3110, 2011.
- [31] I. Vrejoiu, G. Le Rhun, L. Pintilie, D. Hesse, M. Alexe, and U. Gösele, "Intrinsic ferroelectric properties of strained tetragonal  $\text{PbZr}_{0.2}\text{Ti}_{0.8}\text{O}_3$  obtained on layer-by-layer grown, defect-free single-crystalline films," *Advanced Materials*, vol. 18, no. 13, pp. 1657–1661, 2006.
- [32] L. J. Klein, C. Dubourdieu, M. M. Frank, J. Hoffman, J. W. Reiner, and C. H. Ahn, "Domain dynamics in epitaxial  $\text{Pb}(\text{Zr}_{0.2}\text{Ti}_{0.8})\text{O}_3$  films studied by piezoelectric force microscopy," *Journal of Vacuum Science and Technology B*, vol. 28, no. 4, article C5A20, 4 pages, 2010.
- [33] H. Morioka, K. Saito, H. Nakaki, R. Ikariyama, T. Kurosawa, and H. Funakubo, "Impact of 90°-domain wall motion in  $\text{Pb}(\text{Zr}_{0.43}\text{Ti}_{0.57})\text{O}_3$  film on the ferroelectricity induced by an applied electric field," *Applied Physics Express*, vol. 2, no. 4, Article ID 041401, 3 pages, 2009.
- [34] S. P. Beeby, M. J. Tudor, and N. M. White, "Energy harvesting vibration sources for microsystems applications," *Measurement Science and Technology*, vol. 17, no. 12, pp. R175–R195, 2006.
- [35] P. D. Mitcheson, E. K. Reilly, T. Toh, P. K. Wright, E. M. Yeatman, and J. Micromech, "Performance limits of the three MEMS inertial energy generator transduction types," *Journal of Micromechanics and Microengineering*, vol. 17, supplement 9, pp. S211–S216, 2007.
- [36] S. R. Anton and H. A. Sodano, "A review of power harvesting using piezoelectric materials (2003–2006)," *Smart Materials and Structures*, vol. 16, no. 3, article R01, pp. R1–R21, 2007.
- [37] S. Roundy and P. K. Wright, "A piezoelectric vibration based generator for wireless electronics," *Smart Materials and Structures*, vol. 13, no. 5, pp. 1131–1142, 2004.
- [38] P. Muralt, R. G. Polcawich, and S. Trolier-Mckinstry, "Piezoelectric thin films for sensors, actuators, and energy harvesting," *MRS Bulletin*, vol. 34, no. 9, pp. 658–664, 2009.
- [39] E. K. Reilly and P. K. Wright, "Modeling, fabrication and stress compensation of an epitaxial thin film piezoelectric microscale energy scavenging device," *Journal of Micromechanics and Microengineering*, vol. 19, no. 9, Article ID 095014, 2009.
- [40] T. Harigai, H. Adachi, and E. Fujii, "Vibration energy harvesting using highly (001)-oriented  $\text{Pb}(\text{Zr,Ti})\text{O}_3$  thin film," *Journal of Applied Physics*, vol. 107, no. 9, Article ID 096101, 3 pages, 2010.
- [41] D. Isarakorn, D. Briand, P. Janphuang et al., "The realization and performance of vibration energy harvesting MEMS devices based on an epitaxial piezoelectric thin film," *Smart Materials and Structures*, vol. 20, no. 2, Article ID 025015, 2011.
- [42] R. Elfrink, T. M. Kamel, M. Goedbloed et al., "Vibration energy harvesting with aluminum nitride-based piezoelectric devices," *Journal of Micromechanics and Microengineering*, vol. 19, no. 9, Article ID 094005, 2009.
- [43] Y. B. Jeon, R. Sood, J. H. Jeong, and S. G. Kim, "MEMS power generator with transverse mode thin film PZT," *Sensors and Actuators, A*, vol. 122, no. 1, pp. 16–22, 2005.
- [44] B. S. Lee, S. C. Lin, W. J. Wu, X. Y. Wang, P. Z. Chang, and C. K. Lee, "Piezoelectric MEMS generators fabricated with an aerosol deposition PZT thin film," *Journal of Micromechanics and Microengineering*, vol. 19, no. 6, Article ID 065014, 2009.
- [45] H.-B. Fang, J.-Q. Liu, Z.-Y. Xu et al., "Fabrication and performance of MEMS-based piezoelectric power generator for vibration energy harvesting," *Microelectronics Journal*, vol. 37, no. 11, pp. 1280–1284, 2006.
- [46] D. Shen, J. H. Park, J. Ajitsaria, S. Y. Choe, H. C. Wickle III, and D. J. Kim, "The design, fabrication and evaluation of a MEMS PZT cantilever with an integrated Si proof mass for vibration energy harvesting," *Journal of Micromechanics and Microengineering*, vol. 18, no. 5, Article ID 055017, 2008.
- [47] P. Muralt, "Piezoelectric thin film for MEMS," *Integrated Ferroelectrics*, vol. 17, no. 1, pp. 297–307, 1997.
- [48] S. Trolier-Mckinstry and P. Muralt, "Thin film piezoelectrics for MEMS," *Journal of Electroceramics*, vol. 12, no. 1-2, pp. 7–17, 2004.

## Research Article

# Synthesis and Characterization of $\text{Pb}(\text{Zr}_{0.53}, \text{Ti}_{0.47})\text{O}_3$ - $\text{Pb}(\text{Nb}_{1/3}, \text{Zn}_{2/3})\text{O}_3$ Thin Film Cantilevers for Energy Harvesting Applications

E. M. A. Fuentes-Fernandez,<sup>1</sup> W. Debray-Mechtaly,<sup>1</sup> M. A. Quevedo-Lopez,<sup>1</sup> B. Gnade,<sup>1</sup>  
E. Leon-Salguero,<sup>2</sup> P. Shah,<sup>3</sup> and H. N. Alshareef<sup>4</sup>

<sup>1</sup> Department of Materials Science and Engineering, University of Texas at Dallas, 800 W. Campbell Road, Richardson, TX 75080, USA

<sup>2</sup> Department of Materials Science, Research Center for Advanced Materials, 120 Avenue Miguel de Cervantes, Chihuahua 31109, CHIH, Mexico

<sup>3</sup> Materials Science, Texas MicroPower Inc., 7920 Beltline Road, Suite 1005, Dallas, TX 75254, USA

<sup>4</sup> Department of Materials Science and Engineering, King Abdullah University of Science and Technology, Thuwal 23955, Saudi Arabia

Correspondence should be addressed to B. Gnade, gnade@utdallas.edu

Received 16 December 2011; Accepted 18 January 2012

Academic Editor: Ma Jan

Copyright © 2012 E. M. A. Fuentes-Fernandez et al. This is an open access article distributed under the Creative Commons Attribution License, which permits unrestricted use, distribution, and reproduction in any medium, provided the original work is properly cited.

A complete analysis of the morphology, crystallographic orientation, and resulting electrical properties of  $\text{Pb}(\text{Zr}_{0.53}, \text{Ti}_{0.47})\text{O}_3$ - $\text{Pb}(\text{Nb}_{1/3}, \text{Zn}_{2/3})\text{O}_3$  (PZT-PZN) thin films, as well as the electrical behavior when integrated in a cantilever for energy harvesting applications, is presented. The PZT-PZN films were deposited using sol-gel methods. We report that using 20% excess Pb, a nucleation layer of  $\text{PbTiO}_3$  (PT), and a fast ramp rate provides large grains, as well as denser films. The PZT-PZN is deposited on a stack of  $\text{TiO}_2$ /PECVD  $\text{SiO}_2/\text{Si}_3\text{N}_4$ /thermal  $\text{SiO}_2$ /Poly-Si/Si. This stack is designed to allow wet-etching the poly-Si layer to release the cantilever structures. It was also found that the introduction of the poly-Si layer results in larger grains in the PZT-PZN film. PZT-PZN films with a dielectric constant of 3200 and maximum polarization of  $30 \mu\text{C}/\text{cm}^2$  were obtained. The fabricated cantilever devices produced  $\sim 300$ – $400$  mV peak-to-peak depending on the cantilever design. Experimental results are compared with simulations.

## 1. Introduction

The ability to retrofit systems with power consuming electronics without having to consider issues associated with providing an independent power source offers a significant advantage for devices in hard to reach locations [1].

In the past few years there has been an increase in research on small wireless electronic devices [1–3]. Mechanical vibrations have received attention as a potential source of power for sensors and wireless electronics in a wide variety of applications [4]. To accomplish this, improving the piezoelectric material used in the cantilever is of paramount importance [5].

Piezoelectric materials are widely used for various devices, including multilayer capacitors, sensors, and actuators

[2, 3, 6]. By the 1950s, the ferroelectric solid solution  $\text{Pb}(\text{Zr}_{1-x}\text{Ti}_x)\text{O}_3$  (PZT) was found to have exceptionally high dielectric and piezoelectric properties for compositions close to the morphotropic phase boundary (MPB) [7, 8].

Research to improve the PZT properties, from the material and electrical standpoint, has been mainly accomplished by doping conventional PZT with different elements to “relax” the material [5, 9]. Previous investigations on the dielectric and electrical properties of many ceramic systems, such as barium titanate (BT), lead zirconate titanate (PZT), lead magnesium niobate (PMN), lead titanate (PT), PMN-PT, PZT-BT, and PMN-PZT have demonstrated the importance of the subject [10–13]. Recently, there has been a great deal of interest in the lead zirconate titanate-lead zinc niobate  $\text{Pb}(\text{Zr}_{0.53}\text{Ti}_{0.47})\text{O}_3$ - $\text{Pb}(\text{Zn}_{1/3}\text{Nb}_{2/3})\text{O}_3$  or

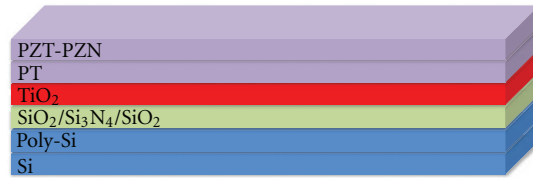


FIGURE 1: Schematic cross-section of PZT-PZN thin film on the cantilever stack.

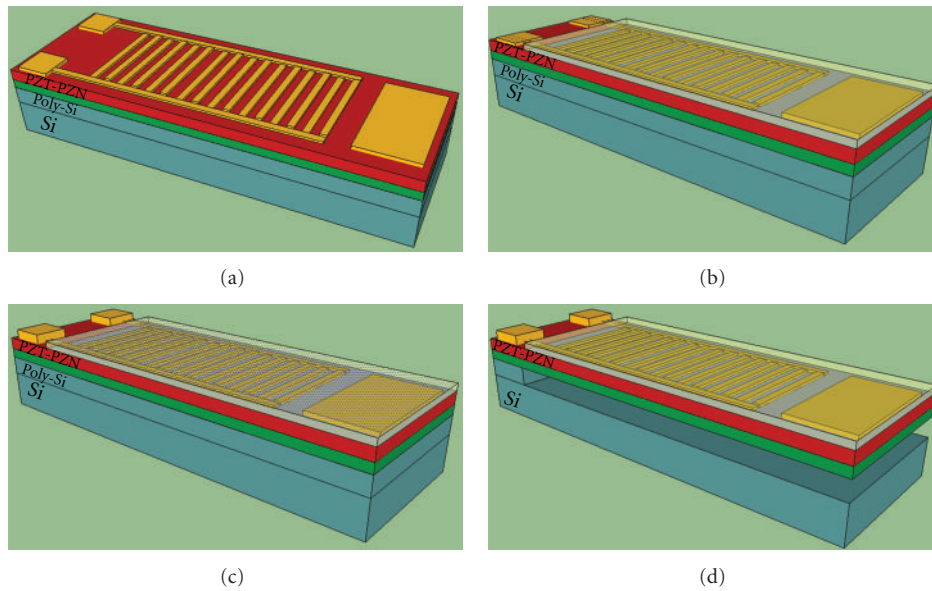


FIGURE 2: Schematics showing the cross-section of the PZT-PZN thin film stack subjected to the 4-step photolithography process, (a) metal deposition (50 nm Cr/500 nm Au), (b) PECVD  $\text{SiO}_2$  encapsulation, (c) deposition of 50 nm Cr/500 nm Au for packaging-bonding, and (d) release step. The cantilever is operating in the  $d_{33}$  mode.

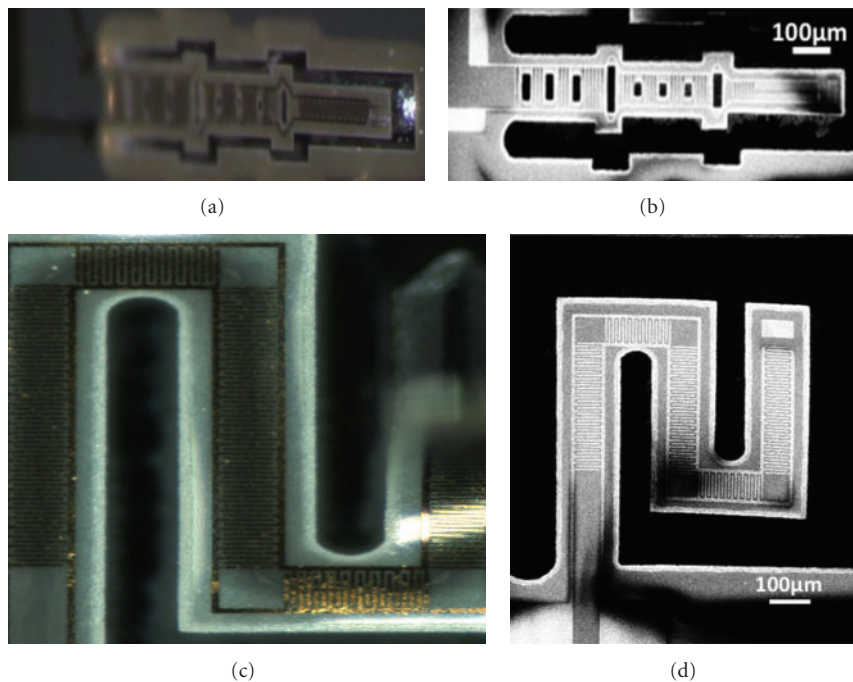


FIGURE 3: Optical micrographs and SEM pictures of; (a) and (b) “linear-shaped” cantilever, respectively, and (c) and (d) “snake-shaped” cantilever.

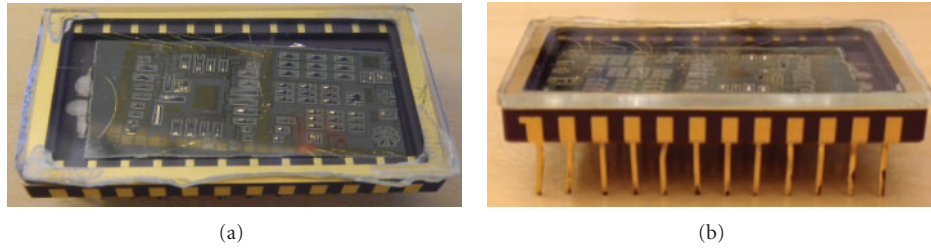


FIGURE 4: Micrographs of the cantilever device mounted and wire-bonded to the chip carrier.

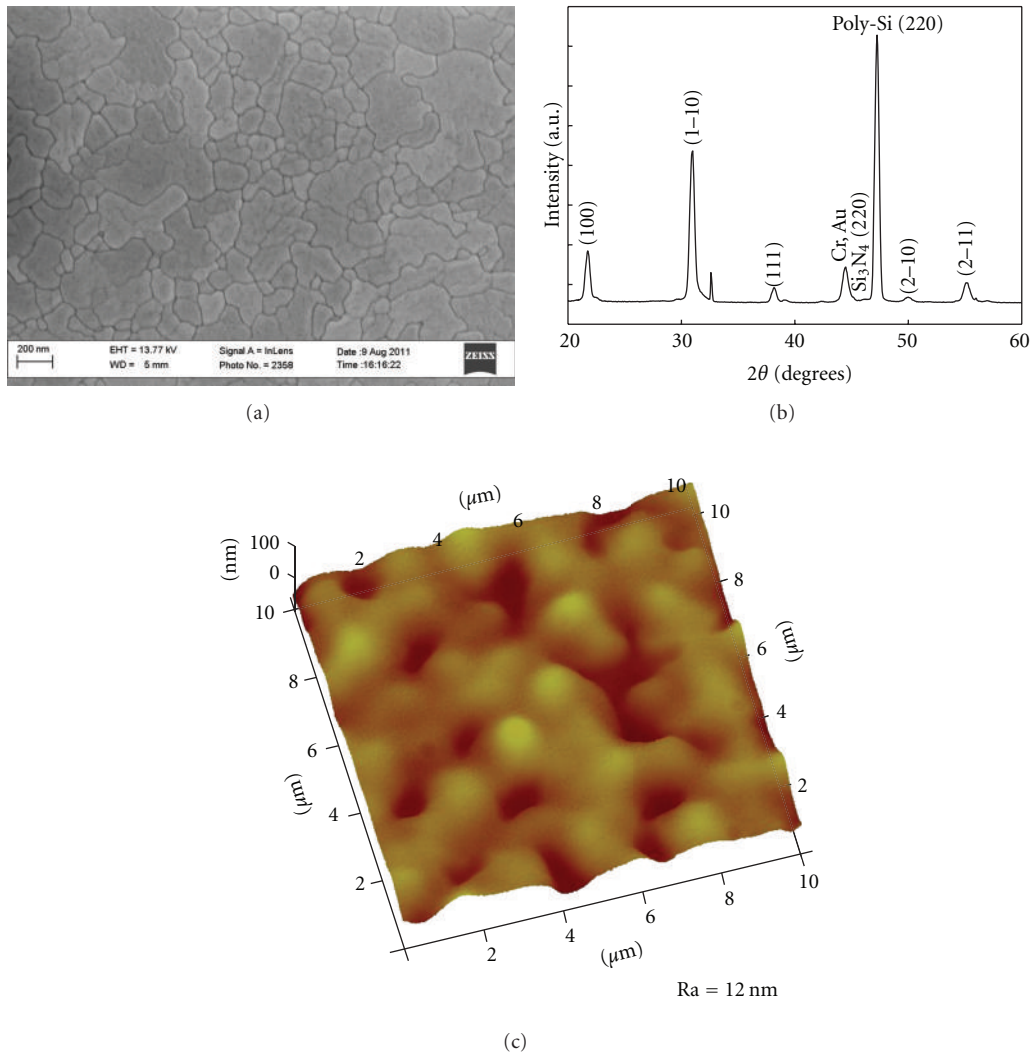


FIGURE 5: (a) SEM picture showing a dense PZT-PZN film with large grain size using optimum conditions (20% excess Pd, fast ramp rate, and PT nucleation layer), (b) X-ray diffraction pattern of the PZT-PZN film on the cantilever stack, and (c) AFM image of the PZT-PZN thin film on the cantilever stack having a roughness of 12 nm, due to the poly-Si layer needed for wet-etch processing.

(PZT-PZN) system because of its high dielectric, piezoelectric, and ferroelectric properties [14–16]. It is important to have not only a good material, but also a device design that matches the material properties. For this reason, the search for different device designs is of great interest. The

cantilever structure is the most efficient structure that has been reported to date [2, 4].

In this paper, the synthesis and characterization of the PZT-PZN thin films for energy harvesting applications are presented. The films were subsequently integrated using

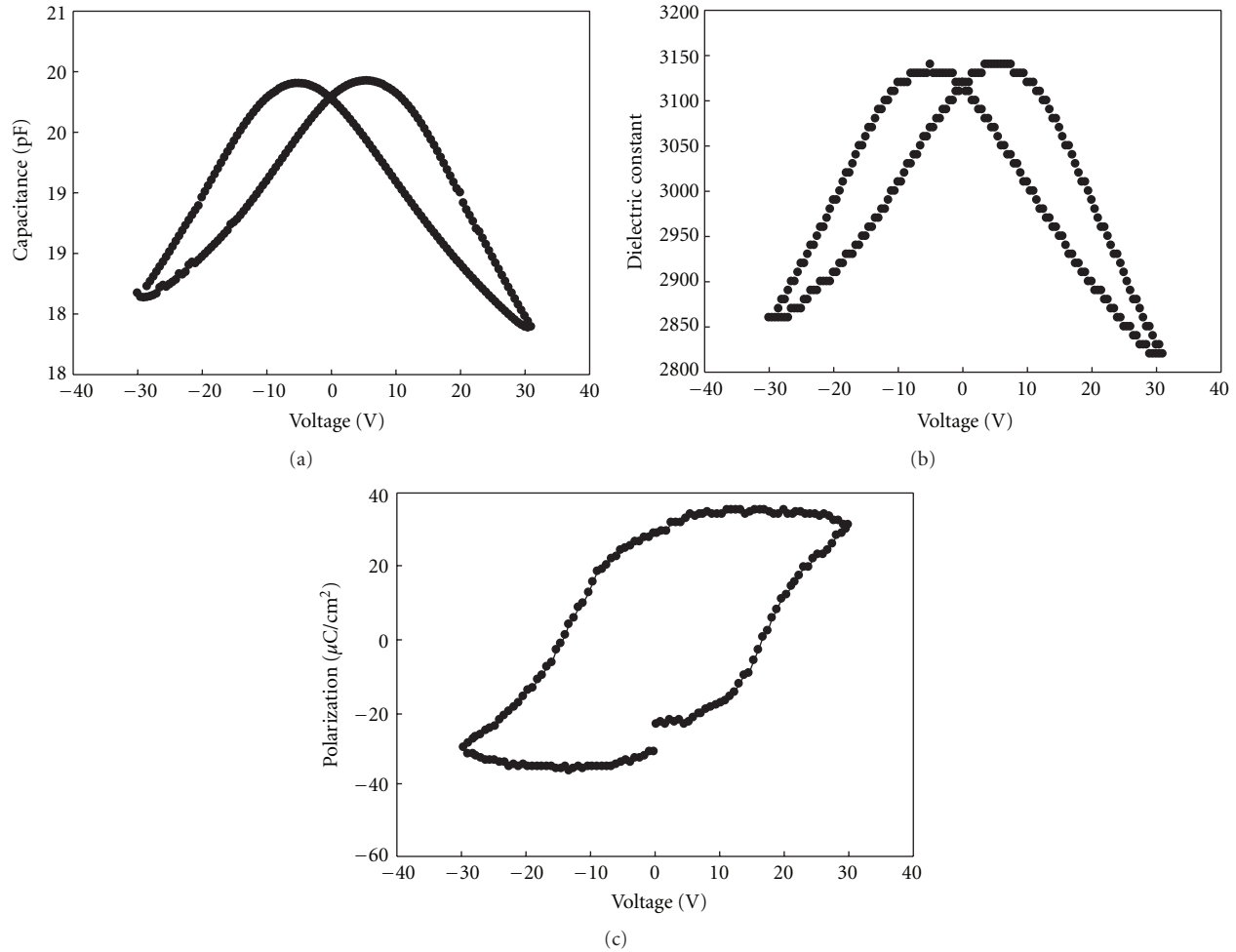


FIGURE 6: Electrical characterization of the PZT-PZN film on the released cantilever. (a) Capacitance versus Voltage curve, (b) calculated dielectric constant versus voltage curve, and (c) polarization versus voltage hysteresis curve.

silicon-compatible microfabrication techniques to fabricate cantilevers using a wet-etch release process.

Additionally, packaging and electrical characterization such as capacitance, polarization, and dielectric constant versus voltage were performed. Experimental voltage output at the resonance frequencies of the cantilevers is compared with simulations.

## 2. Experimental

The solutions used for the fabrication of PZT-PZN films were prepared using a sol-gel process that we previously described for  $\text{Pb}(\text{Zr}_{1-x}\text{Ti}_x)\text{O}_3$  [17, 18]. The starting precursors, zirconium (IV) butoxide, titanium (IV) isopropoxide, and niobium (V) ethoxide, were reacted in acetic acid (95%) and methanol. Lead (IV) acetate and zinc acetate dihydrate were added, and the solution was heated to 85°C to dissolve the acetates. The final PZT-PZN solution has a concentration of 0.4 M. A nucleation  $\text{PbTiO}_3$  (PT) layer was also prepared in a similar manner, but with using titanium (IV) isopropoxide and lead (IV) acetate. The  $\text{Pb}_{1.2}(\text{Zr}_{0.53}\text{Ti}_{0.47})\text{O}_3$ - $\text{Pb}(\text{Zn}_{1/3}\text{Nb}_{2/3})\text{O}_3$  films were deposited from the solution

using a spin-coating technique at 3000 rpm for 30 s, followed by a soft bake on a hot plate at 300°C for 10 min to evaporate the solvents. Finally, the crystallization step is done at 675°C for 30 min in a tube furnace in an air atmosphere, as previously described [9].

The PZT-PZN polycrystalline thin film was grown on a stack consisting of 3 μm of poly-Si, 100 nm of thermal  $\text{SiO}_2$  and 350 nm of  $\text{Si}_3\text{N}_4$  deposited using LPCVD, 500 nm of PECVD  $\text{SiO}_2$  and 50 nm of sputtered Ti (Figure 1). The entire stack is annealed at 1000°C for 30 min in  $\text{O}_2$  to completely oxidize the Ti to  $\text{TiO}_2$ . Next, the stack is subjected to a 4-step photolithography process to fabricate the cantilevers. The first step is the metallization shown in Figure 2(a). The second step is the encapsulation of the device with 100 nm of PECVD  $\text{SiO}_2$ , Figure 2(b); the third step is the deposition of 50 nm Cr/500 nm Au for packaging-bonding purposes, shown schematically in Figure 2(c). Finally the fourth step is the release of the cantilever as shown in Figure 2(d). The release is carried out using 20% HF to etch the PZT-PZN,  $\text{TiO}_2$  and  $\text{SiO}_2$  layers. Next, a RIE plasma-etch step is used to remove the  $\text{Si}_3\text{N}_4$  and the poly-Si layer is etched using 20% KOH at 50°C. This last step releases the cantilever. Images

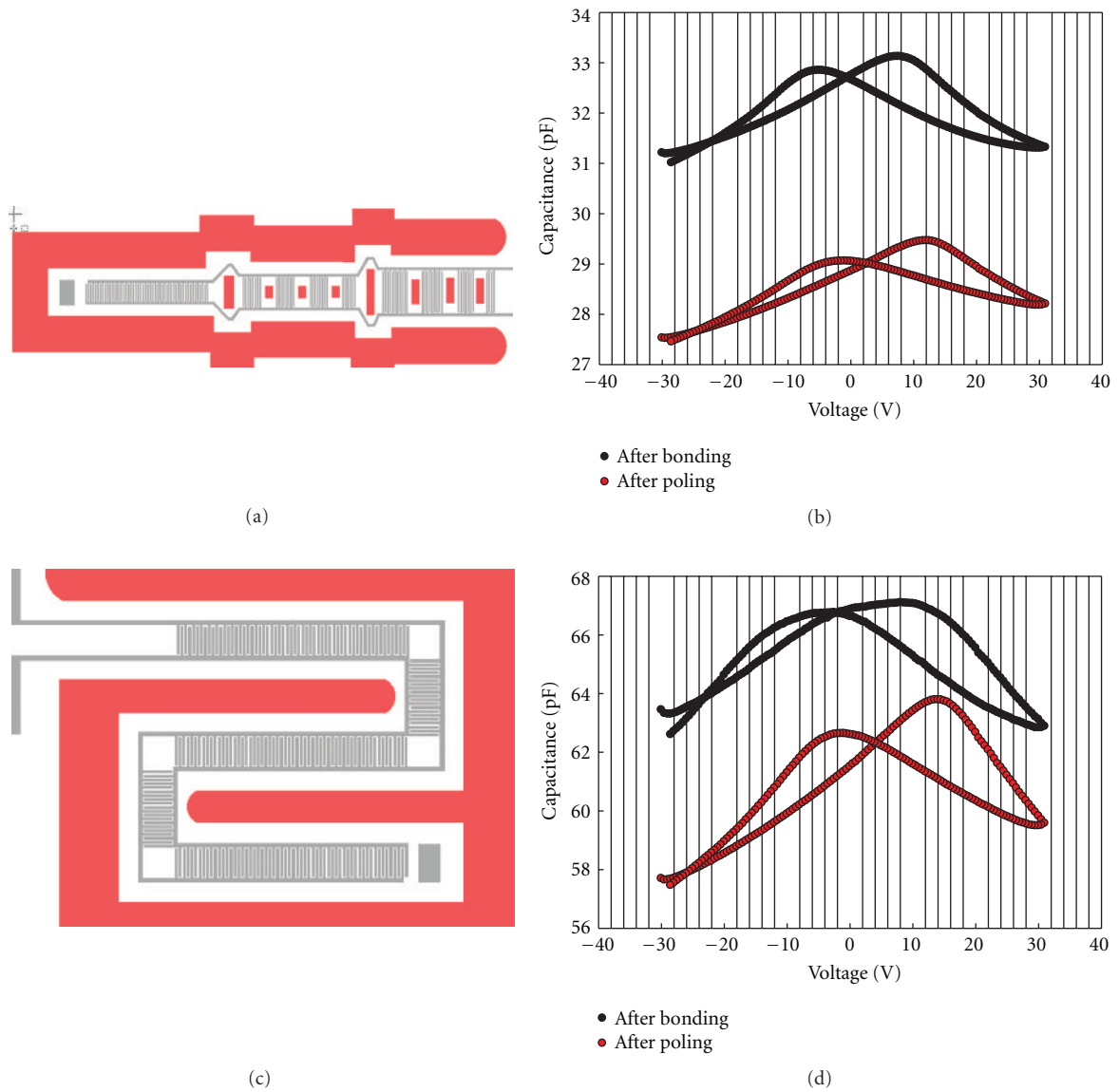


FIGURE 7: (a) Schematic of the "linear-shaped" cantilever, (b) C-V curves of the cantilever device mounted on the chip carrier, showing the results before and after poling. (c) Schematic of the "snake-shaped" cantilever, (d) C-V curves of the cantilever device mounted on the chip carrier, showing the results before and after poling.

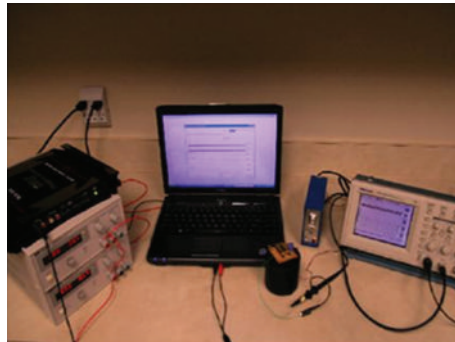


FIGURE 8: Picture of the shaker setup used to measure the voltage-output from the cantilever device.

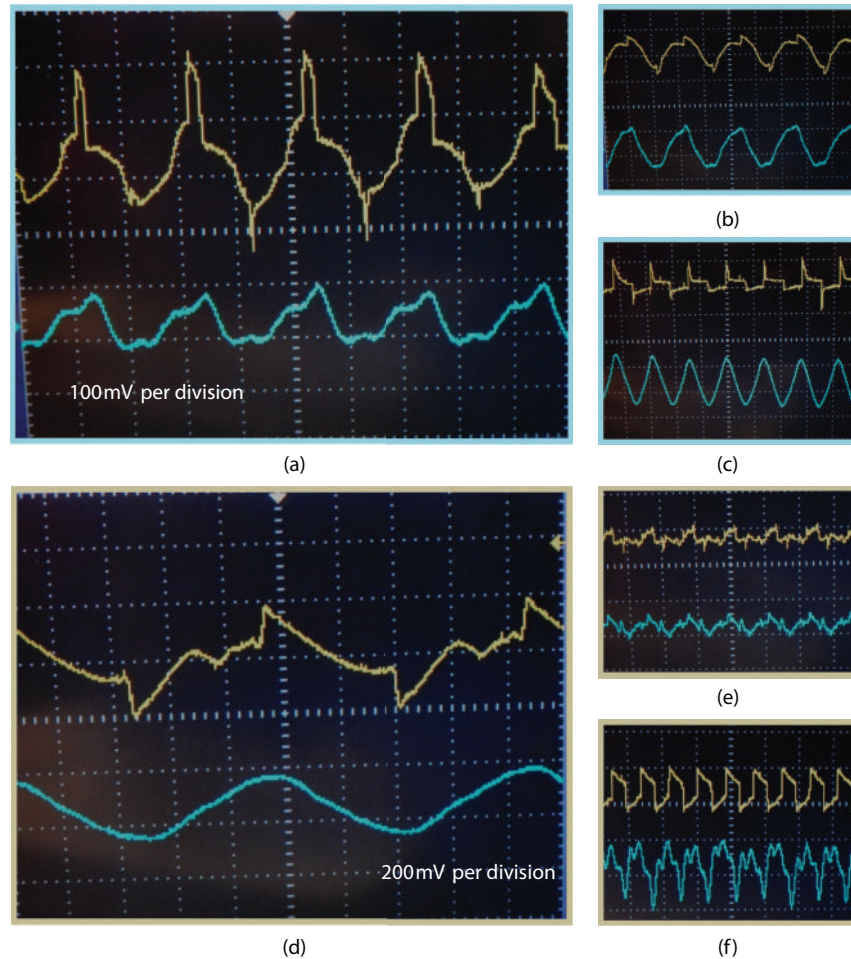


FIGURE 9: Oscilloscope images showing the voltage-output of (a) “linear-shaped” cantilever at its resonance frequency (960 Hz), (b) same structure but at a frequency below the resonance frequency (869 Hz), (c) same “linear-shaped” structure at a frequency above the resonance frequency (1400 Hz), (d) “snake-shaped” cantilever at resonance frequency (875 Hz), (e) same structure at a frequency below the resonance frequency (800 Hz), and (f) same “snake-shaped” structure at a frequency above the resonance frequency (1200 Hz). The yellow signal, or top trace, is the voltage output from the cantilever, and the blue signal, or bottom trace, is the frequency sensor output signal showing the time correlation between the shaker and the cantilever.

of the resulting cantilevers are shown in Figure 3, where (a) and (c) are optical microscopic images of two different cantilever designs, and Figures 3(b) and 3(d) are SEM micrographs of the same cantilever designs. The released cantilevers were mounted and wire-bonded to a chip carrier for poling and output voltage measurements, as show in Figure 4.

### 3. Results and Discussion

**3.1. Material Characterization.** The deposition of PZT-PZN films on the  $\text{TiO}_2$  buffer layer was optimized by varying the lead content, ramp rate, and insertion of a nucleation layer between the film and the underlying  $\text{TiO}_2$ , as shown in Figure 1. Optimum conditions were 20% excess of Pb, direct sample insertion into the furnace previously heated to  $675^\circ\text{C}$  using what we call “a fast ramp rate” (a few seconds to insert the samples manually into the preheated furnace), and the use of a  $\text{PbTiO}_3$  (PT)

nucleation layer between  $\text{TiO}_2$  and the PZT-PZN [9, 19, 20].

SEM results shown in Figure 5(a) indicate a dense film and large grains size (150 nm), which is a difficult characteristic to achieve in PZT-PZN thin films, but is essential for optimal electrical performance. A typical XRD diffraction pattern for the PZT-PZN is shown in Figure 5(b). XRD results demonstrate the absence of pyrochlore, but show a preferred perovskite orientation in the (110) plane.

AFM results (Figure 5(c)) show that the average roughness of the PZT-PZN films is 12 nm. The increased roughness is due to the poly-Si layer. However, the poly-Si layer is required for the wet-etch release of the cantilever. The results using the optimum conditions could be understood as a competition between two effects: lead loss and perovskite phase crystallization [9].

**3.2. Electrical Characterization.** The electrical characterization of the PZT-PZN thin film was done using interdigitated

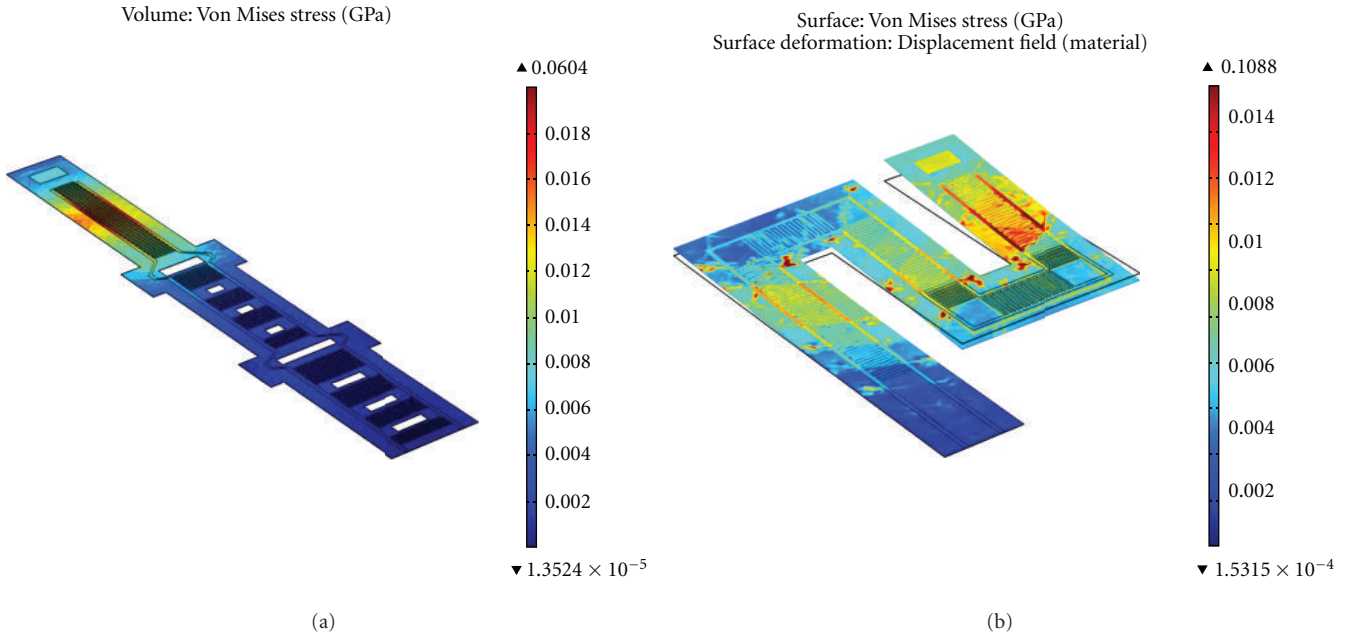


FIGURE 10: Simulation images based on the finite element method (FEM) (COMSOL package) showing the areas of highest stress in the film of (a) “linear-shaped” cantilever and (b) “snake-shaped” cantilever.

electrodes (IDE) on the released cantilevers. Capacitance versus voltage (C-V) measurements were performed on the PZT-PZN films to calculate the dielectric constant. C-V results are shown in Figure 6(a), where the maximum capacitance (20 pF) is observed at 5 V. The calculated dielectric constant for PZT-PZN is shown in Figure 6(b). These calculations were based on studies previously reported [21, 22]. The maximum dielectric constant calculated was 3200 at 5 V. Polarization measurements were also performed on the relaxor thin film and the results are shown in Figure 6(c). The films show a maximum polarization value of  $31.2 \mu\text{C}/\text{cm}^2$  and a remnant polarization of  $28.5 \mu\text{C}/\text{cm}^2$ .

It is well known that a larger grain size can improve the dielectric constant of perovskite materials [23]. Therefore, the high dielectric constant and polarization results are attributed to the larger grain size observed in the PZT-PZN thin films.

In order to measure the output voltage due to vibrational excitation, the films were exposed to a poling step. The poling is accomplished by applying an electric field across the material at elevated temperatures; for thin films, longer poling times are typically required compared to bulk ceramics [24, 25].

The poling was performed after mounting and wire-bonding the devices to a chip carrier, as shown in Figure 4. The poling conditions were  $200 \text{ kV}/\text{cm}$  at  $200^\circ\text{C}$  for 50 min. C-V measurements before and after poling are shown in Figure 7. Two device structures are shown in this figure, “linear-shaped” (Figure 7(a)) and “snake-shaped” (Figure 7(c)) cantilevers. C-V results from both cantilevers increased after wire bonding because of an increase in contact area. If we compare both C-V measurements, we find that the capacitance for the “snake-shaped” cantilever is higher than for the “linear-shaped” cantilever. This may be

explained because the contact area is higher in the “snaked-shape” cantilever.

The C-V curve after poling shifted by an average of 5 V from the original position, as shown in Figures 7(b) and 7(d).

The cantilevers were subsequently tested by mounting the packaged device to a mechanical shaker (Bruel and Kjaer Instruments Inc. Model Type 4810). The force generated by the shaker is proportional to the acceleration, which is controlled by the applied voltage to a power amplifier (Pyle PLA2200). The amplifier was driven by a 12-V power supply and signals from the PC frequency generator. The output voltage from the cantilever was monitored using a Tektronix digital oscilloscope (TDS 210), as shown in Figure 8.

Voltage-output results for the two cantilever designs shown in Figure 7 are presented in Figure 9, where (a) is for the “linear-shaped”  $2000 \mu\text{m}$  long cantilever, and (b) is for the “snake-shaped” cantilever. The “snake-shaped” cantilever shows an output voltage value of 400 mV peak-to-peak while the “linear-shaped” cantilever shows a 300 mV p-p output voltage at the resonant frequencies of 875 Hz and 960 Hz, respectively. The differences are consistent with simulation-based results using the finite element method (FEM). The results shown in Figure 10 show that for the “linear-shaped” cantilever (a), the area of highest stress is near the tip area, while for the “snake-shaped” cantilever (b), there is more stress distributed across the structure.

The FEM (COMSOL) package was used also to model the structural deformation and the voltage output at the resonant frequency, as determined from experimental analysis of the tested cantilevers. Results are shown in Figure 11, where (a) and (c) are the results of the simulated deformation at the respective resonant frequencies; for the “linear-shaped” cantilever a deformation of  $104.6 \mu\text{m}$  at 960 Hz and  $47.1 \mu\text{m}$  at 875 Hz for the “snake-shaped” cantilever.

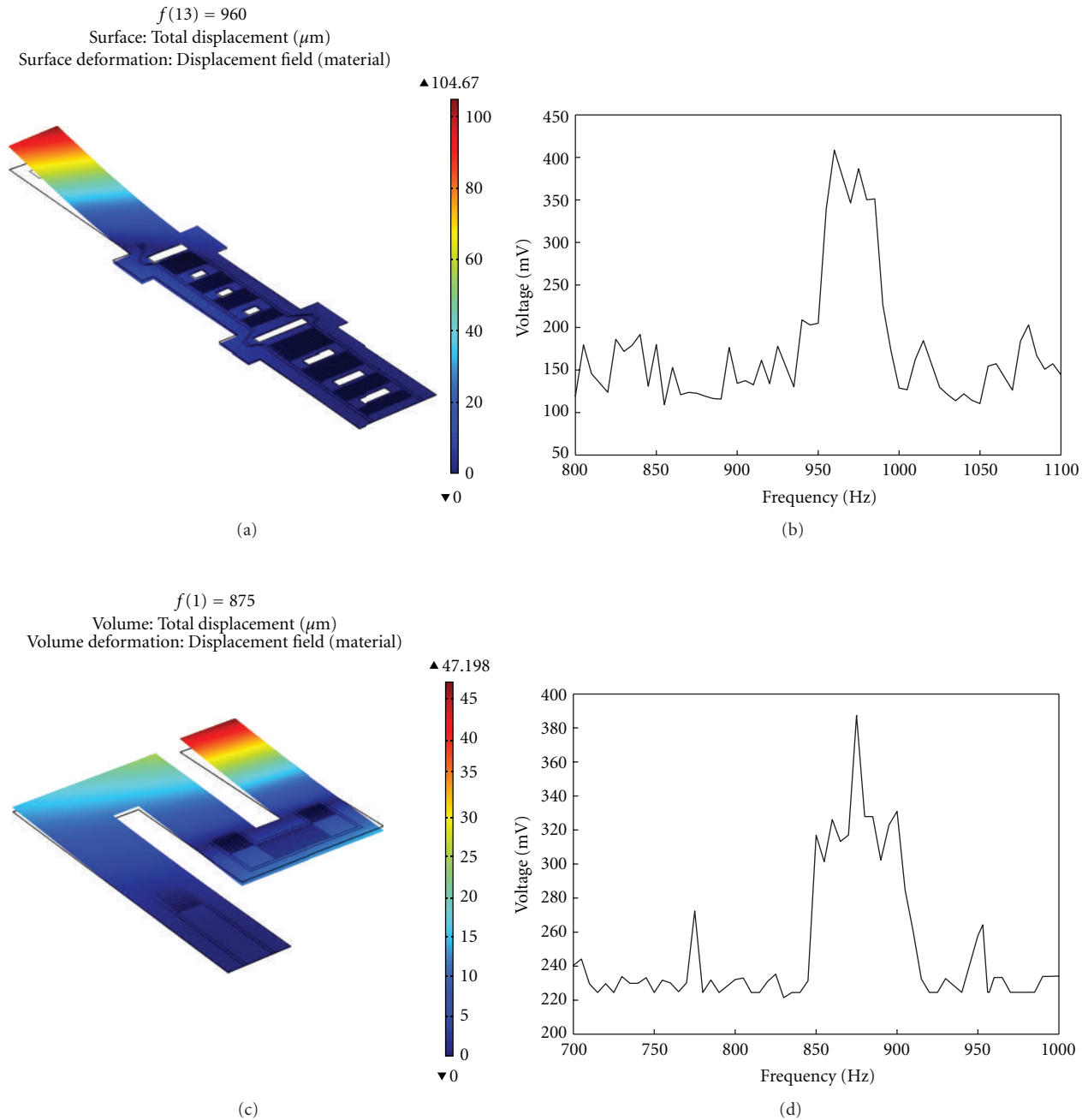


FIGURE 11: Simulation results using the finite element method (FEM), (COMSOL package). (a) Schematic showing the deformation of the “linear-shaped” cantilever, (b) simulated voltage versus frequency plot for the “linear-shape” cantilever, (c) Schematic showing the deformation of the “snake-shaped” cantilever, and (d) simulated voltage versus frequency plot for the “snake-shaped” cantilever.

For the “linear-shaped” cantilever the experimental results show an output voltage of 300 mV over a range of frequencies of 983 to 1053 Hz. Comparing this result to the simulation shown in Figure 10(b), we find that there is a 2% of difference between the experimental and calculated results. For the “snake-shaped” cantilever the experimental result showed a maximum voltage of 400 mV from 858 to 890 Hz with a difference of 2% between the simulated and experimental results, as shown in Figure 11(d). We believe that the voltage output can be improved by adding

a weight at the end of the cantilever to reduce the resonant frequency and improve the deflection of the cantilevers, and consequently increase the voltage output [26].

#### 4. Conclusions

PZT-PZN thin film and microcantilever fabrication processes have been developed to harvest vibrational energy. Integrated cantilevers were successfully fabricated using a wet-etch process to release the cantilevers. The properties of

the relaxor films were optimized to yield the desired phase on the cantilever devices. A dielectric constant of 3200 and polarization of  $30 \mu\text{C}/\text{cm}^2$  were obtained. A 300 to 400 mV p-p output voltage, depending on the cantilever design tested, was obtained. Simulations are in good agreement with experimental data.

## Acknowledgments

The authors would like to thank to NSF Phase I SBIR grant and the Texas Emerging Technology Fund for partial financial support.

## References

- [1] S. P. Beeby, M. J. Tudor, and N. M. White, "Energy harvesting vibration sources for microsystems applications," *Measurement Science and Technology*, vol. 17, no. 12, article R01, pp. R175–R195, 2006.
- [2] S. Roundy, P. K. Wright, and J. Rabaey, "A study of low level vibrations as a power source for wireless sensor nodes," *Computer Communications*, vol. 26, no. 11, pp. 1131–1144, 2003.
- [3] S. Roundy and P. K. Wright, "A piezoelectric vibration based generator for wireless electronics," *Smart Materials and Structures*, vol. 13, no. 5, pp. 1131–1142, 2004.
- [4] A. Hajati and S.-G. Kim, "Ultra-wide bandwidth piezoelectric energy harvesting," *Applied Physics Letters*, vol. 99, no. 8, Article ID 083105, 2011.
- [5] R. Yimnirun, N. Triamnak, M. Unruan, A. Ngamjarurojana, Y. Laosiritaworn, and S. Ananta, "Ferroelectric properties of  $\text{Pb}(\text{Zr}_{1/2}\text{Ti}_{1/2})\text{O}_3$ - $\text{Pb}(\text{Zn}_{1/3}\text{Nb}_{2/3})\text{O}_3$  ceramics under compressive stress," *Current Applied Physics*, vol. 9, no. 1, pp. 249–252, 2009.
- [6] N. M. White and J. D. Turner, "Thick-film sensors: past, present and future," *Measurement Science and Technology*, vol. 8, no. 1, pp. 1–20, 1997.
- [7] A. J. Bell, "Factors influencing the piezoelectric behaviour of PZT and other "morphotropic phase boundary" ferroelectrics," *Journal of Materials Science*, vol. 41, no. 1, pp. 13–25, 2006.
- [8] B. Jaffe, W. R. Cook, and H. Jaffe, *Piezoelectric Ceramics*, Academic Press, 1971.
- [9] E. Fuentes-Fernandez, W. Debray-Mechtaly, M. A. Quevedo-Lopez et al., "Fabrication and characterization of  $\text{Pb}(\text{Zr}_{0.53}\text{Ti}_{0.47})\text{O}_3$ - $\text{Pb}(\text{Nb}_{1/3}\text{Zn}_{2/3})\text{O}_3$  thin films on cantilever stacks," *Journal of Electronic Materials*, vol. 40, no. 1, pp. 85–91, 2011.
- [10] Q. M. Zhang, J. Zhao, K. Uchino, and J. Zheng, "Change of the weak-field properties of  $\text{Pb}(\text{ZrTi})\text{O}_3$  piezoceramics with compressive uniaxial stresses and its links to the effect of dopants on the stability of the polarizations in the materials," *Journal of Materials Research*, vol. 12, no. 1, pp. 226–234, 1997.
- [11] R. Yimnirun, S. Ananta, A. Ngamjarurojana, and S. Wongsanmai, "Effects of uniaxial stress on dielectric properties of ferroelectric ceramics," *Current Applied Physics*, vol. 6, no. 3, pp. 520–524, 2006.
- [12] G. Yang, S. F. Liu, W. Ren, and B. K. Mukherjee, "Uniaxial stress dependence of the piezoelectric properties of lead zirconate titanate ceramics," in *Symposium on Smart Structures and Materials*, vol. 3992 of *Proceedings of the SPIE*, pp. 103–113, June, 2000.
- [13] R. Yimnirun, "Contributions of domain-related phenomena on dielectric constant of lead-based ferroelectric ceramics under uniaxial compressive pre-stress," *International Journal of Modern Physics B*, vol. 20, no. 23, pp. 3409–3417, 2006.
- [14] N. Vittayakorn, G. Rujijanagul, T. Tunkasiri, X. Tan, and D. P. Cann, "Perovskite phase formation and ferroelectric properties of the lead nickel niobate-lead zinc niobate-lead zirconate titanate ternary system," *Journal of Materials Research*, vol. 18, no. 12, pp. 2882–2889, 2003.
- [15] H. Fan and H.-E. Kim, "Perovskite stabilization and electromechanical properties of polycrystalline lead zinc niobate-lead zirconate titanate," *Journal of Applied Physics*, vol. 91, no. 1, pp. 317–322, 2002.
- [16] N. Vittayakorn, G. Rujijanagul, X. Tan, H. He, M. A. Marquardt, and D. P. Cann, "Dielectric properties and morphotropic phase boundaries in the  $x\text{Pb}(\text{Zn}_{1/3}\text{Nb}_{2/3})\text{O}_3$ - $(1-x)\text{Pb}(\text{Zr}_{0.5}\text{Ti}_{0.5})\text{O}_3$  pseudo-binary system," *Journal of Electroceramics*, vol. 16, no. 2, pp. 141–149, 2006.
- [17] T. Schneller and R. Waser, "Chemical modifications of  $\text{Pb}(\text{Zr}_{0.3}\text{Ti}_{0.7})\text{O}_3$  precursor solutions and their influence on the morphological and electrical properties of the resulting thin films," *Journal of Sol-Gel Science and Technology*, vol. 42, no. 3, pp. 337–352, 2007.
- [18] H. N. Al-Shareef, K. R. Bellur, O. Auciello, X. Chen, and A. I. Kingon, "Effect of composition and annealing conditions on the electrical properties of  $\text{Pb}(\text{Zr}_x\text{Ti}_{1-x})\text{O}_3$  thin films deposited by the sol-gel process," *Thin Solid Films*, vol. 252, no. 1, pp. 38–43, 1994.
- [19] E. Fuentes-Fernandez, L. Baldenegro-Perez, M. Quevedo-Lopez et al., "Optimization of  $\text{Pb}(\text{Zr}_{0.53}\text{Ti}_{0.47})\text{O}_3$  films for micropower generation using integrated cantilevers," *Solid-State Electronics*, vol. 63, no. 1, pp. 89–93, 2011.
- [20] L. A. Baldenegro-Perez, W. Debray-Mechtaly, E. Fuentes-Fernandez et al., "Study on the microstructure and electrical properties of  $\text{Pb}(\text{Zr}_{0.53}\text{Ti}_{0.47})\text{O}_3$  thin-films," *Materials Science Forum*, vol. 644, pp. 97–100, 2010.
- [21] H. N. Al-Shareef, D. Dimos, M. V. Raymond, R. W. Schwartz, and C. H. Mueller, "Tunability and calculation of the dielectric constant of capacitor structures with interdigital electrodes," *Journal of Electroceramics*, vol. 1, no. 2, pp. 145–153, 1997.
- [22] G. W. Farnell, I. A. Cermak, P. Silvester, and S. K. Wong, "Capacitance and field distributions for interdigital surface-wave transducers," *IEEE Transactions on Sonics and Ultrasonics*, vol. 17, no. 3, pp. 188–195, 1970.
- [23] G. Arlt, D. Hennings, and G. De With, "Dielectric properties of fine-grained barium titanate ceramics," *Journal of Applied Physics*, vol. 58, no. 4, pp. 1619–1625, 1985.
- [24] G. Yi, Z. Wu, and M. Sayer, "Preparation of  $\text{Pb}(\text{Zr,Ti})\text{O}_3$  thin films by sol gel processing: electrical, optical, and electro-optic properties," *Journal of Applied Physics*, vol. 64, no. 5, pp. 2717–2724, 1988.
- [25] S. Watanabe, T. Fujiu, and T. Fujii, "Effect of poling on piezoelectric properties of lead zirconate titanate thin films formed by sputtering," *Applied Physics Letters*, vol. 66, pp. 1481–1483, 1995.
- [26] Q.-M. Wang, X.-H. Du, B. Xu, and L. Eric Cross, "Electromechanical coupling and output efficiency of piezoelectric bending actuators," *IEEE Transactions on Ultrasonics, Ferroelectrics, and Frequency Control*, vol. 46, no. 3, pp. 638–646, 1999.

## Research Article

# Solid State Adaptive Rotor Using Postbuckled Precompressed, Bending-Twist Coupled Piezoelectric Actuator Elements

**Ronald M. Barrett and Ryan Barnhart**

*Department of Aerospace Engineering, University of Kansas, 2120 Learned Hall, 1530 W 15th Street, Lawrence, KS 66045-7621, USA*

Correspondence should be addressed to Ronald M. Barrett, barrettr@ku.edu

Received 15 November 2011; Accepted 16 January 2012

Academic Editor: Tao Li

Copyright © 2012 R. M. Barrett and R. Barnhart. This is an open access article distributed under the Creative Commons Attribution License, which permits unrestricted use, distribution, and reproduction in any medium, provided the original work is properly cited.

This paper is centered on a new actuation mechanism which is integrated on a solid state rotor. This paper outlines the application of such a system via a Post-Buckled Precompression (PBP) technique at the end of a twist-active piezoelectric rotor blade actuator. The basic performance of the system is handily modeled by using laminated plate theory techniques. A dual cantilevered spring system was used to increasingly null the passive stiffness of the root actuator along the feathering axis of the rotor blade. As the precompression levels were increased, it was shown that corresponding blade pitch levels also increased. The PBP cantilever spring system was designed so as to provide a high level of stabilizing pitch-flap coupling and inherent resistance to rotor propeller moments. Experimental testing showed pitch deflections increasing from just  $8^\circ$  peak-to-peak deflections at 650 V/mm field strength to more than  $26^\circ$  at the same field strength with design precompression levels. Dynamic testing showed the corner frequency of the linear system coming down from 63 Hz (3.8/rev) to 53 Hz (3.2/rev). Thrust coefficients manipulation levels were shown to increase from 0.01 to 0.028 with increasing precompression levels. The paper concludes with an overall assessment of the actuator design.

## 1. Introduction

For more than two decades, adaptive rotors, flaps and helicopter flight and vibration control systems have been actively pursued by a small army of technologists scattered around the world. The work of Crawley and his team at MIT in the mid-1980s laid the foundations of adaptive aerostructures by investigating the properties of bending and twist-active plates [1–3]. These early studies lead to several broad reviews which examined material properties and their associated energy and power densities when used as actuator elements [4, 5].

*1.1. Adaptive Flaps.* The earliest twist, camber, and bending active aerodynamic plates were followed by the first of the adaptive flap studies [6]. A host of adaptive flaps flowed into the technical literature at a steady rate from the early 1990s through their implementation in a full-scale rotor test bed (right) [7–19]. Through much effort it was shown that blade loads could indeed be manipulated as fast as 4/rev with

appreciable deflection levels. However, the weight, cost, and complexity issues still prevent full transition to prototype flying aircraft and serial production aircraft. Efforts with “Smart Active Blade Tips” (SABT) showed good results, but fell prey to the same issues as conventional flaps, but with exacerbated propeller moments. Given that for every 1 unit of mass added at the 75% radius (and further out) it takes on the order of 3 units (or more) of structural mass to distribute the load into the airframe, the weight penalty alone of active flap systems is considerable. Because rotor blades are some of the most expensive items on any given rotorcraft, a sizable cost penalty because of the integration of expensive adaptive actuators is quite daunting. Still, much research regularly appears in scattered literature with new flap and actuator configurations (Figure 1).

*1.2. Twist-Active Rotors.* Just after the twist-active plates of Crawley, De Luis, and Lazarus were published, a series of studies were put forth on twist-active missile fins, wings,

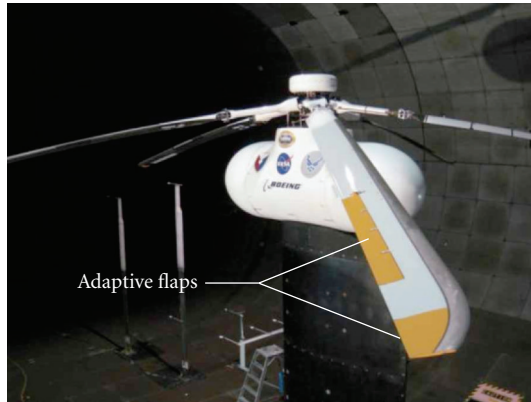


FIGURE 1: “Smart” rotor equipped with active flaps [18].

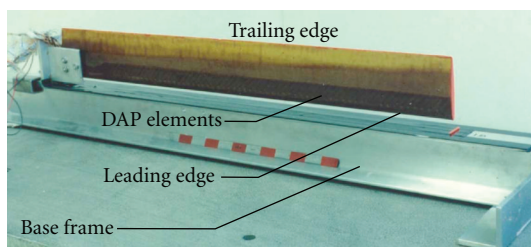


FIGURE 2: First twist-active rotor (1989) [20].

and rotor blades [20–25]. These 20+-year-old studies also included the first patent (which was also the first IP royalty-generating patent) on adaptive aerostructures to be issued. The earliest work of 1989 showed that essentially “microscopic” twist deflections could be generated [21, 22]. Clearly, these  $\pm 0.2^\circ$  deflections were not enough for full cyclic or collective. However, they were enough to kick off the field. Twist active rotor research continued through the 1990s with expansions of the Directionally Attached Piezoelectric (DAP) elements from the first 35% of the chord (for proper blade balance as seen in Figure 2), to much greater distances along the chord. Although destabilizing because they shift the center of gravity aft of the aerodynamic center, they did increase the  $\pm 0.2$  degree deflections substantially to roughly  $\pm 0.3^\circ$  at the same field strength [23]. Twist-active rotor research reached a zenith in 1999 when the largest model to date was wind tunnel tested [24]. Although large-scale experimentation with twist-active rotors has come to a grinding halt, there are occasional technologists who revisit this technology [25]. As with the adaptive flap designs, the weight, cost, and complexities have been shown to be simply prohibitive.

**1.3. Solid State Adaptive Rotor.** One concept that was intended to skirt the “show stopping” issues associated with adaptive materials mounted on the blades was the Solid State Adaptive Rotor (SSAR) (Figure 4). This design employed DAP torque plates mounted at the root of the rotor system between the hub and the lag hinge [20, 26, 27]. Because no extra weight was added to the blade itself, the mass,

lock number, cost, and complexity of the blade systems themselves would be no higher than conventional rotor blades. Because the actuator was designed to actively pitch the rotor about the aerodynamic center which was collocated with the line of centers of gravity and counterbalanced with Chinese weights, the only appreciable attached flow moments were inertial. Because the feathering moments were balanced, respectable pitch deflections of  $8^\circ$  peak to peak could be commanded by the small torque plates. These considerable pitch deflections then translated into nontrivial thrust coefficient manipulation levels as seen in Figure 3. Because they were so high, eventually they were woven into the first rotorcraft to fly using adaptive aerostructures for all flight control, Gamara (Figure 5), (below).

The successes in flight test were matched by several overview papers describing the feasibility of adaptive rotors [28–31]. These overview papers described many approaches and listed several different techniques and approaches for achieving flight control. One of the later overview papers summarized not only rotorcraft, but missile, munition, and UAV successes which were numerous by 2004 [32].

**1.4. VTOL Microaerial Vehicles, Ultrahigh Performance and Convertible UAVs.** Given the very public successes of the SSAR program, the DoD contracted to have a subscale rotorcraft built which actually needed adaptive materials to achieve flight control on the subscale. The “Kolibri” VTOL Coleopter was commissioned by the DoD Counterdrug Technology Office to explore tunnels and stay airborne for 24 hrs [33–37]. It was later understood that these studies were actually the very first Micro Aerial Vehicle (MAV) contracts let by the DoD. These studies eventually enabled free-flight MAVs which used piezoelectric elements extensively in their GNC packages. From 2001 through 2010 a completely new type of UAV has evolved. These new aircraft, first flown under the designation of XQ-138, is capable of hovering in more places than helicopters while pitching over (or converting) to missile mode flight to fly out at tactical missile speeds. Although major DoD elements declined funding, private sources were found and test ranges at Eglin AFB, Florida, Redstone Arsenal, AL and Fort Benning, Georgia gladly hosted the aircraft during some extreme flight tests and demos. It should also be noted that the superior performance of the aircraft also induced all competing UAV manufacturers and Government sponsors to decline *all* flyoff challenges and offers. The US Army’s first exercise with a remote-controlled armored vehicle launching a UAV took place at Redstone Arsenal, AL when an XQ-138 was launched from the turret of an FCS prototype vehicle. Eglin AFB, FL saw the first tandem flights of a Javelin Missile followed closely by an XQ-138 ultrahigh performance UAV flying a Battle Damage Assessment (BDA) mission. Parallel IFF and conversion-stalking missions were also flown for the first time in history by convertible UAVs. 40 mm submunitions were fired from the XQ-138 at Ft. Benning and a Mother-ship drop from 1000 ft AGL was demonstrated. Clearly, the forefront of UAV technology is



FIGURE 3: Solid state adaptive rotor (1996) [20, 26, 27].

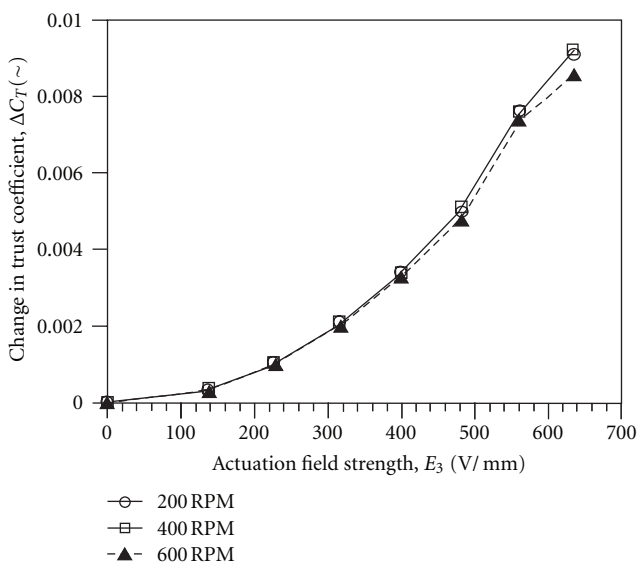


FIGURE 4: SSAR thrust coefficient change levels,  $\Delta C_T(\sim)$ .

being spearheaded by adaptive aerostructures through this class of aircraft (Figure 6).

**1.5. New Discoveries in Structural Mechanics.** Although flight on a 1 m scale was concretely demonstrated as significantly helped by adaptive aerostructures, a new branch of structural mechanics evolved from the mid-1990s through today. In 1997 the first paper describing the superior nature of a new form of structural arrangement was published [38]. Lesieutre et al. showed that by mounting a bending beam, properly the passive stiffness of the actuator, could be nulled. By nulling the passive stiffness the deflections and ultimately the electrical-to-mechanical and mechanical-to-electrical conversion efficiencies could be driven close to 100% [39]. Although Lesieutre et al. primarily used this basic discovery in electrical energy converter, the philosophy of nulling passive stiffnesses is directly transferrable to mechanical actuators. Several related studies were conducted on structures which exhibited negative stiffnesses through

buckling effects associated with snap-through events [40–42]. These were followed by actuator studies on bistable piezoelectric composites which used energy techniques to estimate performance [43–45]. Both the snap-through and bistable studies showed that small amounts of energy invested in piezoelectric actuators could be used to trigger much more energetic processes if the structure and surrounding materials were designed properly.

**1.6. Postbuckled Precompression (Pbp) Techniques and Analysis.** In 2004 a fundamental discovery was made with respect to piezoelectric actuation. The principles of piezoelectric actuation described in [38] were refined for flight control. Rather than pushing the structure through to a bistable situation, a highly controlled axial force could be used to induce a postbuckling effect. This effect would be seen to drive actuator deflections to very high values, but not sacrifice moment generation capability [46–54]. These PBP structures outperformed any other piezoelectrically driven actuators by factors of 3 and 4. Figure 7 shows the basic arrangement of the bending version of the actuator.

Because the performance of PBP-based bending actuators is shown to be so significantly superior with respect to conventional linear techniques a new incarnation of the above model is explored in this paper. By combining the methods of using Zero-Net Passive Stiffness (ZNPS) structural design (also above), it is possible to null the passive torsional stiffness of the SSAR rotor root actuators of Figure 3. By doing so, it will be shown that otherwise huge deflections can be generated by these “old” actuators if they are just mounted properly between negative spring mechanisms.

## 2. PBP SSAR Root Actuator Design

Because PBP techniques call for more of a change in actuator design philosophy as much as a change in how adaptive actuators are handled, the rotor of Figure 3 was simply retrofitted with a pair of stiffness nulling springs so as to generate high deflections with simultaneous high moment generations. Figure 8 shows the root section following retrofit.

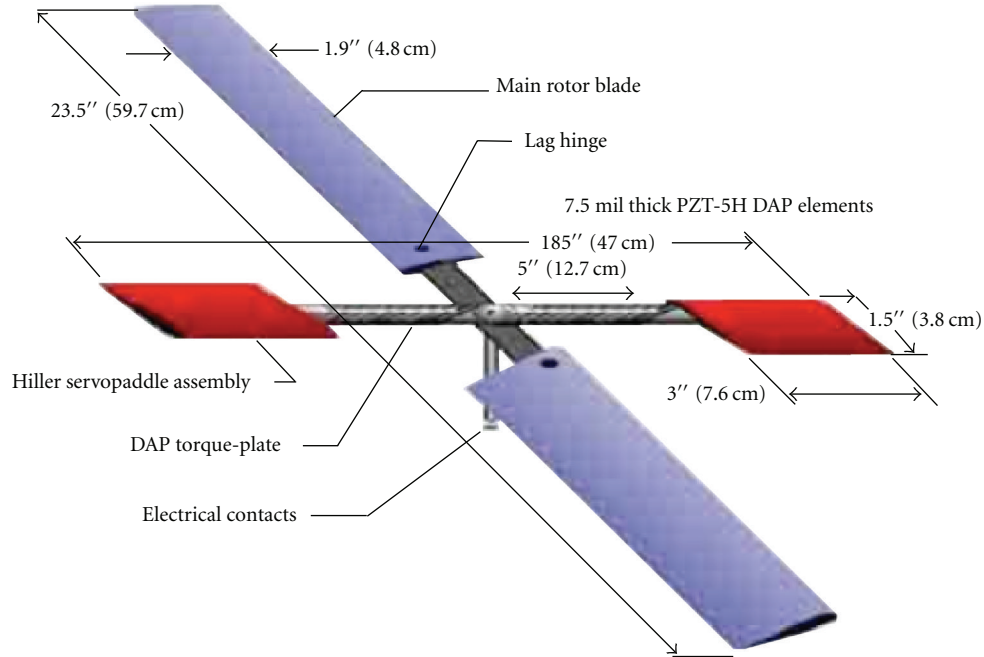


FIGURE 5: Gamara, the first helicopter to use adaptive materials for all flight control (1996) [27].

The spring stiffnesses and prestress levels were set by analytical modeling and fine tuning during whirl-stand testing. The analytical models called upon were established in [46–52] to determine the amount of axial forces required to fundamentally null the net passive stiffness of the piezoelectric actuator element. The overall PBP assembly design was laid out to provide several overarching properties:

- (i) magnify pitch deflections without adversely affecting moment generation properties of the torque plate;
- (ii) provide a stabilizing effective  $\partial_3$  pitch-flap coupling;
- (iii) balance out attached flow aerodynamic, propeller and passive torque-plate stiffnesses;

- (iv) not significantly impact the weight and hub drag of the assembly;
- (v) allow for easy adjustment during testing to fine-tune the assembly.

The overall design takes advantage of destabilizing spring moments applied at the tip of the torque plate. Figure 9 shows the negative torsional spring arrangement. As the piezoelectric torque plate induces pitch deflections, the two springs generate a nose-up pitching moment which is structurally destabilizing, but when properly “tuned” can be balanced exactly against the passive stiffness of the torque plate laminate. By doing so, the deflections are seen to grow by factors of 3 or more while maintaining the moment resistance capability of the laminate.

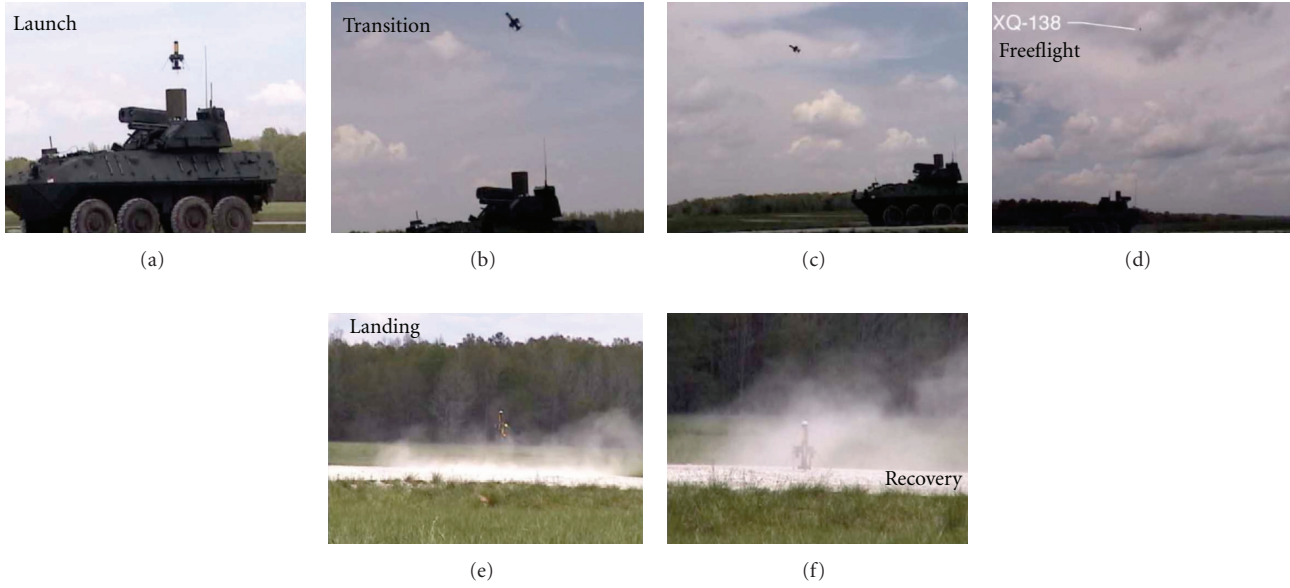


FIGURE 6: The XQ-138 ultrahigh performance UAV using piezoelectric elements in the FCS undergoing conversion to missile mode flight, Redstone Arsenal, AL [55].

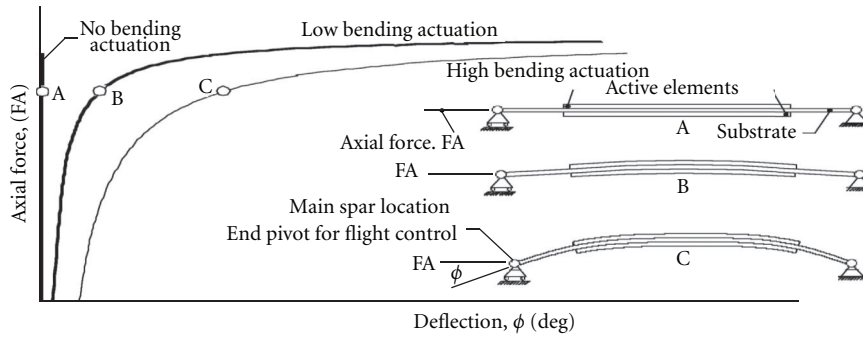


FIGURE 7: Basic arrangement of a linear postbuckled precompressed piezoelectric beam [46–54].

### 3. PBP SSAR Root Actuator Modeling

The overall design philosophy described above can be fairly easily implemented by simply balancing out forces. If one performs a simple accounting, it can be seen that actuator (a), passive laminate (l), aerodynamic (aero), propeller (prop), inertia, and damping moments about the feather axis should be nulled

$$M_a + M_l + M_{aero} + M_{prop} + M_{inertia} + M_{damping} = 0. \quad (1)$$

3.1. *Actuator Modeling.* If one considers the first two terms above, they relate to the laminate. By using a simple

linear classical laminated plate theory (CLPT) model, the overall behavior of the symmetrical actuator can be seen in [26, 27]. The techniques of [56] capture the moment balance, considering forces external (ex) to the laminate:

$$\begin{Bmatrix} N \\ M \end{Bmatrix}_{ex} + \begin{Bmatrix} N \\ M \end{Bmatrix}_a + \begin{Bmatrix} N \\ M \end{Bmatrix}_t = \begin{bmatrix} A & B \\ B & D \end{bmatrix}_1 \begin{Bmatrix} \epsilon \\ k \end{Bmatrix}_1. \quad (2)$$

By expanding (2), the exact structure of the stiffness matrices above can be seen, considering external forces and moments represented by a simple vector

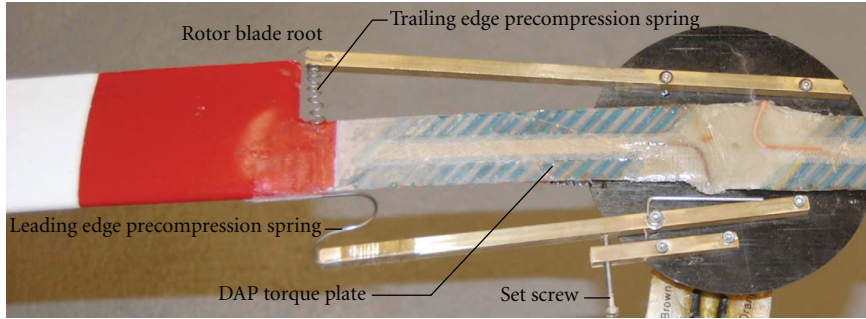


FIGURE 8: Retrofitted SSAR assembly with PBP feather (Pitch) stiffness-nulling springs.

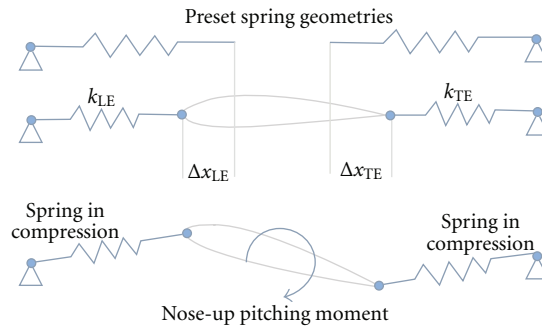


FIGURE 9: Destabilizing compression spring arrangement.

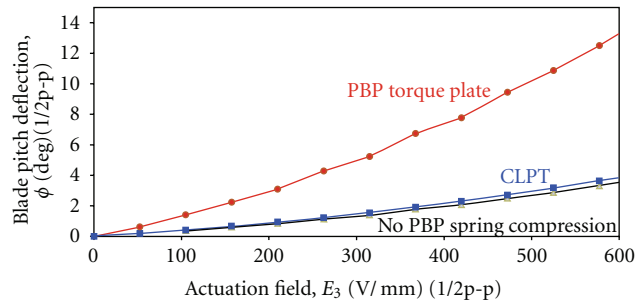
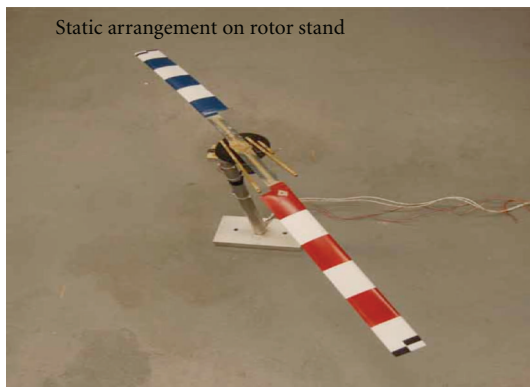


FIGURE 10: Blade pitch results with and without PBP spring compression.



(a)



(b)

FIGURE 11: Solid state adaptive rotor on whirl-stand.

$$\begin{Bmatrix} N_{11} \\ N_{22} \\ N_{12} \\ M_{11} \\ M_{22} \\ M_{12} \end{Bmatrix}_{\text{ex}} + \begin{bmatrix} A_{11} & A_{12} & 2A_{16} & 0 & 0 & 0 \\ A_{12} & A_{22} & 2A_{26} & 0 & 0 & 0 \\ A_{16} & A_{26} & 2A_{66} & 0 & 0 & 0 \\ 0 & 0 & 0 & B_{11} & B_{12} & 2B_{16} \\ 0 & 0 & 0 & B_{12} & B_{22} & 2B_{26} \\ 0 & 0 & 0 & B_{16} & B_{26} & 2B_{66} \end{bmatrix}_a \begin{Bmatrix} \alpha_a \Delta T \\ \alpha_a \Delta T \\ 0 \\ \frac{\Lambda_1 + \Lambda_2}{2} \\ \frac{\Lambda_1 + \Lambda_2}{2} \\ \frac{\Lambda_1 - \Lambda_2}{2} \end{Bmatrix} + \begin{bmatrix} (A_{11} + A_{12})_s \alpha_s \Delta T \\ (A_{11} + A_{12})_s \alpha_s \Delta T \\ 0 \\ 0 \\ 0 \\ 0 \end{bmatrix} = \begin{bmatrix} A_{11} & A_{12} & 2A_{16} & B_{11} & B_{12} & 2B_{16} \\ A_{12} & A_{22} & 2A_{26} & B_{12} & B_{22} & 2B_{26} \\ A_{16} & A_{26} & 2A_{66} & B_{16} & B_{26} & 2B_{66} \\ B_{11} & B_{12} & 2B_{16} & D_{11} & D_{12} & 2D_{16} \\ B_{12} & B_{22} & 2B_{26} & D_{12} & D_{22} & 2D_{26} \\ B_{16} & B_{26} & 2B_{66} & D_{16} & D_{26} & 2D_{66} \end{bmatrix}_l \begin{Bmatrix} \varepsilon_{11} \\ \varepsilon_{22} \\ \varepsilon_{12} \\ k_{11} \\ k_{22} \\ k_{12} \end{Bmatrix}. \quad (3)$$

Considering a laminate constrained in curvature by high centripetal forces, the laminate twist can be solved as

$$k_{12} = \frac{(E_L(1 - \nu_{TL})\Lambda_1 - E_T(1 - \nu_{LT})\Lambda_2)((t_s + 2t_b)t_a + t_a^2)}{(E_s t_s^3(1 - \nu_{LT}\nu_{TL}))/6(1 - \nu_s) + (E_L + E_T - 2E_L\nu_{TL})(((t_s + 2t_b)^2 t_a)/2) + (t_s + t_b)t_a^2 + (2t_a^3/3)}. \quad (4)$$

The actuator moment which can be applied by full hard-over pitch commands considering a bending-constrained laminate is shown in

$$M_a = \frac{E_{La} - E_{Ta}}{4(1 - \nu_{LT}\nu_{TL})} (t_s t_a + t_a^2) W_a \Lambda. \quad (5)$$

**3.2. External Moments.** If one examines the aerodynamic moments, then a simple offset between integrated centers of pressure, elastic axis, and line of centers of gravity can be seen:

$$M_{\text{aero}} = \frac{1}{2} \rho \Omega^2 R_{sp}^2 C_{sp} B_{sp} (x_{cg} - x_{cp}) c_{l\alpha} \phi. \quad (6)$$

Of course, the easy (and logical) design decision is simply to collocate the c.g., c.p. and e.a. so as to null those moments. One set of moments which require a bit of orthogonal design stems from propeller moments:

$$M_{\text{prop}} = -m_{sp} \Omega^2 r_g^2 \phi. \quad (7)$$

From (6) and (7) it is easy to see that aerodynamic and propeller moments are both proportional to blade pitch angle,  $\phi$ . Through proper design, it is possible to balance out these two terms by judiciously prescribing the distance between the c.g. and c.p. Of course this is actually a comparatively dangerous move as the system can become dynamically unstable. In the interest of safety, the blade static margin will be set to zero or slightly positive.

#### 4. Rotor Fabrication, Testing, and Results

Because the geometry of the 122 cm rotor model, its fabrication methods and materials are described in [26, 27], the reader is simply referred to those documents. The modified rotor, equipped with destabilization springs is shown in

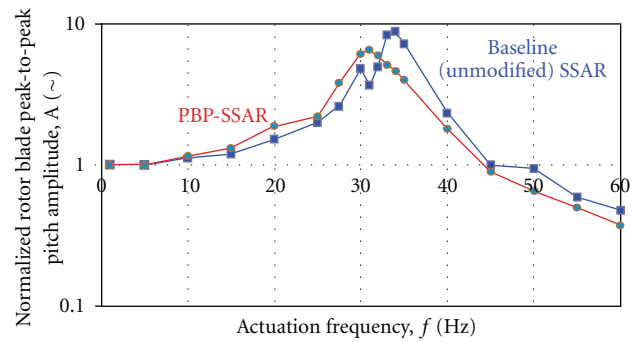


FIGURE 12: Dynamic response of SSAR and PBP-SSAR Systems.

Figure 8. Two series of tests were conducted: static bench tests and dynamic whirl-stand testing. Laser reflection techniques were employed to measure blade pitch deflections. Quasi-static excitation voltages were passed through the rotor hub at 1 Hz. From Figure 10 it can be seen that both the laminated plate theory and the raw piezoelectric performance line up well (as shown in [26, 27]). As the spring compression levels were increased, deflection levels were seen to grow and grow till the edge of structural stability was reached. Figure 10 shows the results from that “edge.” By employing the practical experience and modeling techniques of [46–52], it can be seen that amplification ratios (AR) on the order of 3.5–3.8 are most generally achieved by bidirectional piezoelectric control actuation. Accordingly, the measured AR of 3.8 is seen to be an excellent achievement for the world’s first torsionally amplified low-net passive stiffness piezoelectric actuator. It should be noted that the amplification ratio of 3.8 is essentially constant over the entire range of deflections commanded and measured.

In addition to amplification of static deflections, the thrust coefficient manipulation levels were also increased

dramatically. Figure 11 shows the rotor undergoing whirl-stand testing, demonstrating thrust coefficient manipulation levels 3.8 times higher than measured in the baseline SSAR laid out 15 years ago.

The dynamic testing showed an interesting trend: a slight reduction in both natural frequency and bandwidth, but maintenance of a high resonance peak as well as good frequency response. Figure 12 shows the dynamic response of the rotor system. The corner frequency of the unmodified SSAR blades and actuators was approximately 63 Hz, while the low-net passive stiffness PBP incarnation of the system achieved a corner frequency of 53 Hz.

## 5. Conclusions and Recommendations

It can be concluded that zero-net passive stiffness structural modification techniques can be successfully applied to torque-plate-driven rotors. Such successful application leads to dramatically higher deflections with no adverse effects on moment-generation capabilities, indicating higher total work levels available from such a Postbuckled Precompressed (PBP) Solid State Adaptive Rotor (SSAR) design. Pitch deflection levels were shown to be magnified by up to 3.8 times in static bench tests while thrust coefficient manipulation levels increased 2.8-fold during whirl-stand testing. Dynamic testing showed a reduction in corner frequency from 63 to 53 Hz by the use of PBP techniques, which represent 3.8 and 3.2/rev, respectively.

Given the continued success of the SSAR design, it is recommended that such techniques be implemented in larger scale rotors and flying UAVs. The tremendous promise of this technique has the ability to make feasible now what was deemed “infeasible” many years ago.

## Acknowledgment

The authors would like to acknowledge the University of Kansas Transportation Research Institute (TRI) for providing vital funding and support without which this research would not have been possible.

## References

- [1] E. F. Crawley and J. de Luis, “Use of piezoelectric actuators as elements of intelligent structures,” *AIAA Journal*, vol. 25, no. 10, pp. 1373–1385, 1987.
- [2] E. F. Crawley, K. B. Lazarus, and D. J. Warkentin, “Embedded actuation and processing in intelligent materials,” in *Proceedings of the 2nd international Workshop on Composite Materials and Structures for Rotorcraft*, Troy, New York, NY, USA, September 1989.
- [3] E. F. Crawley and E. H. Anderson, “Detailed models of piezoceramic actuation of beams,” in *Proceedings of the 30th Structures, Structural Dynamics and Materials Conference*, Mobile, Ala, USA, April 1989.
- [4] S. M. Ehlers and T. A. Weisshaar, “Effect of material properties on static aeroelastic control,” in *Proceedings of the 33rd SDM Conference*, Dallas, Tex, USA, April 1992.
- [5] V. Giurgiutiu, Z. Chaudhry, and C. Rogers, “Energy-based comparison of solid state actuators,” Center for Intelligent Material Systems and Structures Report No. CIMSS 95-101, Virginia Polytechnic Institute and State University, Blacksburg, Va, USA, 1995.
- [6] R. L. Spangler and S. R. Hall, “Piezoelectric actuators for helicopter rotor control,” in *Proceedings of the 31st AIAA/ASME/ASCE/AHS/ASC Structures, Structural Dynamics and Materials Conference*, pp. 1589–1599, April 1990.
- [7] C. Walz and I. Chopra, “Design, fabrication, and testing of a helicopter rotor model with smart trailing edge flaps,” in *Proceedings of the AIAA/ASME/ASCE/AHS/ASC 35th Structures, Structural Dynamics, and Materials Conference, Adaptive Structures Forum*, pp. 298–319, Hilton Head, SC, USA, April 1994.
- [8] O. Ben-Zeev and I. Chopra, “Continued development of a helicopter rotor model employing smart trailing-edge flaps for vibration suppression,” in *The International Society for Optical Engineering*, vol. 2443 of *Proceedings of SPIE*, pp. 2–19, February 1995.
- [9] F. K. Straub and D. J. Merkley, “Design of a smart material actuator for rotor control,” in *The International Society for Optical Engineering*, vol. 2443 of *Proceedings of SPIE*, pp. 89–104, San Diego, Ca, USA, February 1995.
- [10] F. K. Straub and R. J. King, “Application of smart materials to control of a helicopter rotor,” in *Symposium on Smart Structures and Materials*, Proceedings of SPIE, San Diego, Ca, USA, February 1996.
- [11] F. K. Straub, M. A. Ealey, and L. M. Schetky, “Application of smart materials to helicopter rotor active control,” in *Smart Structures and Materials 1997: Industrial and Commercial Applications of Smart Structures Technologies*, vol. 3044 of *Proceedings of SPIE*, San Diego, Ca, USA, March 1997.
- [12] F. K. Straub, “Development of a full scale smart rotor system,” in *Proceedings of the 8th ARO Workshop on Aeroelasticity of Rotorcraft Systems*, Penn State University, October 1999.
- [13] N. A. Koratkar and I. Chopra, “Analysis and testing of a Mach-scaled helicopter rotor in hover with piezoelectric bender-actuated trailing-edge flaps,” in *The International Society for Optical Engineering*, vol. 3329 of *Proceedings of SPIE*, pp. 321–332, San Diego, Ca, USA, March 1998.
- [14] T. Lee and I. Chopra, “Design and static testing of a trailing-edge flap actuator with piezostacks for a rotor blade,” in *Smart Structures and Materials 1998: Smart Structures and Integrated Systems*, vol. 3329 of *Proceedings of SPIE*, pp. 321–332, San Diego, Ca, USA, February 1998.
- [15] F. K. Straub, “Development of a full scale smart rotor system,” in *Proceedings of the 8th ARO Workshop on Aeroelasticity of Rotorcraft Systems*, Penn State University, October 1999.
- [16] N. A. Koratkar and Chopra, “Hover testing of a Mach-scaled rotor with piezoelectric bender actuated trailing-edge flaps,” in *Smart Structures and Materials: Smart Structures and Integrated Systems*, N. W. Wereley, Ed., vol. 3985 of *Proceedings of SPIE*, Newport Beach, Ca, USA, March 2000.
- [17] T. Lee and I. Chopra, “Development of a smart trailing-edge flap actuator with multi-stage stroke amplifier for a rotor blade,” in *Smart Structures and Materials: Smart Structures and Integrated Systems*, N. W. Wereley, Ed., vol. 3985 of *Proceedings of SPIE*, pp. 11–25, Newport Beach, Ca, USA, March 2000.
- [18] Anon., “Future Helicopters Get SMART,” *Science Daily*, March 2009.
- [19] D. K. Kennedy, F. K. Straub, L. M. Schetky, Z. Chaudhry, and R. Roznoy, “Development of a SMA actuator for in-flight rotor blade tracking,” in *Smart Structures and Materials 2000: Smart Structures and Integrated Systems*, vol. 3985 of *Proceedings of SPIE*, pp. 62–75, Newport Beach, Ca, USA, 2000.

- [20] R. M. Barrett, "Method and Apparatus for Structural Actuation and Sensing in a Desired Direction," U. S. Patent 5,440,193, Invention Disclosure: November, 1989.
- [21] R. M. Barrett, "Intelligent rotor blade actuation through directionally attached piezoelectric crystals," in *Proceedings of the Proceedings of 46th American Helicopter Society National Conference and Forum*, Washington, DC, USA, May 1990.
- [22] R. Barrett, *Active rotor blade and structures development using directionally attached piezoelectric crystals*, M.S. thesis, The University of Maryland, College Park, Md, USA, 1990.
- [23] P. C. Chen and I. Chopra, "Hover testing of a smart rotor with induced-strain actuation of blade twist," in *Proceedings of the 36th AIAA/ASME/ASCE/AHS/ASC Structures, Structural Dynamics, and Materials Conference and AIAA/ASME Adaptive Structures Forum*, vol. 5, pp. 2836–2853, New Orleans, La, USA, April 1995.
- [24] M. L. Wilbur, W. K. Wilkie, W. T. Yeager Jr. et al., "Hover testing of a NASA APL/MIT active twist rotor," in *Proceedings of the 8th ARO Workshop on Aeroelasticity of Rotorcraft Systems*, Penn State University, October 1999.
- [25] E. Barkanov, S. Gluhiih, and A. Kovalov, "Optimal design of the active twist for helicopter rotor blades with C-spar," *Mechanics of Advanced Materials and Structures*, vol. 15, no. 3-4, pp. 325–334, 2008.
- [26] R. Barrett and G. Cook, "The solid state adaptive rotor, design, development and implications for future rotorcraft," in *Proceedings of the AGARD Flight Vehicle Integration Panel Symposium on Advances in Rotorcraft Technology*, Ottawa, Canada, May 1996.
- [27] R. Barrett, P. Frye, and M. Schliesman, "Design, development and testing of a solid state adaptive rotor," in *1996 Symposium on Smart Materials, Structures, and MEMS*, vol. 3321 of *Proceedings of SPIE*, pp. 424–435, Bangalore, India, December 1996.
- [28] F. K. Straub, "A feasibility study of using smart materials for rotor control," in *Proceedings of the 49th Annual Forum of the American Helicopter Society*, St. Louis, M, USA, May 1996.
- [29] F. K. Straub and R. J. King, "Application of smart materials to control of a helicopter rotor," in *Smart Structures and Materials 1996: Industrial and Commercial Applications of Smart Structures Technologies*, vol. 2721 of *Proceedings of SPIE*, pp. 66–77, San Diego, Ca, USA, February 1996.
- [30] F. K. Straub, M. A. Ealey, and L. M. Schetky, "Application of smart materials to helicopter rotor active control," in *Smart Structures and Materials 1997: Industrial and Commercial Applications of Smart Structures Technologies*, Proceedings of SPIE, pp. 99–113, San Diego, Ca, USA, March 1997.
- [31] F. K. Straub and D. J. Merkley, "Design of a smart material actuator for rotor control," in *Smart Structures and Materials 1995: Smart Structures and Integrated Systems*, vol. 2443 of *Proceedings of SPIE*, pp. 89–104, San Diego, Ca, USA, 1995.
- [32] R. Barrett, "Adaptive aerostructures: the first decade of flight on uninhabited aerial vehicles," in *Smart Structures and Materials 2004: Industrial and Commercial Applications of Smart Structures Technologies*, Proceedings of SPIE, pp. 190–201, San Diego, Ca, USA, March 2004.
- [33] G. Lee, "Design and testing of the kolibri vertical take-off and landing micro aerial vehicle," Final Report for the Department of Defense CounterDrug Technology Office, November 1997.
- [34] R. Barrett, "Wind tunnel report on the LuMAV rotary-wing micro aerial vehicle," Final Program Report for Lutronix Corporation for the DARPA Micro Aerial Vehicle Program, November 1999.
- [35] R. Barrett and N. Howard, "Adaptive aerostructures for subscale aircraft," in *Proceedings of the 20th Southeastern Conference on Theoretical and Applied Mechanics*, Pine Mountain, Ga, USA, April 2000.
- [36] R. Barrett and G. Lee, "Design criteria, aircraft design, fabrication and testing of sub-canopy and urban micro-aerial vehicles," in *Proceedings of the AIAA/AHS International Powered Lift Conference*, Alexandria, Va, USA, November 2000.
- [37] R. Barrett, "Convertible Vertical Take-Off and Landing Miniature Aerial Vehicle," US Patent 6,502,787, 2002.
- [38] G. A. Lesieutre and C. L. Davis, "Can a coupling coefficient of a piezoelectric device be higher than those of its active material?" *Journal of Intelligent Material Systems and Structures*, vol. 8, no. 10, pp. 859–867, 1997.
- [39] G. A. Lesieutre and C. L. Davis, "Transfer Having a Coupling Coefficient Higher than its Active Material," US Patent 6,236,143, May 2001.
- [40] M. R. Schultz and M. W. Hyer, "Snap-through of unsymmetric cross-ply laminates using piezoceramic actuators," *Journal of Intelligent Material Systems and Structures*, vol. 14, no. 12, pp. 795–814, 2003.
- [41] M. R. Schultz, *Use of piezoelectric actuators to effect snap-through behavior of unsymmetric composite laminates*, Ph.D. Dissertation, Engineering Science and Mechanics, Virginia Polytechnic Institute and State University, Blacksburg, Va, USA, 2003.
- [42] M. R. Schultz and M. W. Hyer, "A morphing concept based on unsymmetric composite laminates and piezoceramic MFC actuators," in *Proceedings of the 45th AIAA/ASME/ASCE/AHS/ASC Structures, Structural Dynamics and Materials Conference*, pp. 3192–3204, Springs, San Diego, Ca, USA, April 2004.
- [43] G. Giannopoulos, J. Monreal, and J. VanTomme, "High displacement nonlinear asymmetrically designed piezoelectric actuators," in *Proceedings of the Active and Passive Smart Structures and Integrated Systems Conference*, San Diego, Ca, USA, March 2006.
- [44] J. Monreal, G. Giannopoulos, and J. VanTomme, "Analysis, construction and testing of a large displacement bistable piezoelectric actuator," in *Proceedings of the Active and Passive Smart Structures and Integrated Systems Conference*, San Diego, Ca, USA, March 2007.
- [45] C. Maurini, J. Pouget, and S. Vidoli, "Bistable buckled beam: modelling and piezoelectric actuation," in *Proceedings of the 3rd International Conference on Smart Materials, Structures and Systems—Smart Materials and Micro/Nanosystems (CIMTEC '08)*, vol. 54, pp. 281–286, September 2008.
- [46] R. Barrett and P. Tiso, "PBP adaptive actuator device and embodiments," International Patent Application number PCT/NL2005/000054, via Technische Universiteit Delft, The Netherlands, 2005.
- [47] R. Vos, R. Barrett, L. Krakkers, and M. Van Tooren, "Post-Buckled Precompressed (PBP) piezoelectric actuators for UAV flight control," in *Smart Structures and Materials 2006: Smart Structures and Integrated Systems*, San Diego, Ca, USA, March 2006.
- [48] R. De Breuker, P. Tisot, R. Vos, and R. Barrett, "Nonlinear semi-analytical modeling of Post-Buckled Precompressed (PBP) piezoelectric actuators for UAV flight control," in *Proceedings of the 47th AIAA/ASME/ASCE/AHS/ASC Structures, Structural Dynamics and Materials Conference*, pp. 2461–2473, May 2006.
- [49] R. Barrett, R. McMurtry, R. Vos, P. Tiso, and R. De Breuker, "Post-buckled precompressed piezoelectric flight

- control actuator design, development and demonstration,” *Smart Materials and Structures*, vol. 15, no. 5, pp. 1323–1331, 2006.
- [50] R. Vos, R. De Breuker, R. Barrett, and P. Tiso, “Morphing wing flight control via postbuckled precompressed piezoelectric actuators,” *Journal of Aircraft*, vol. 44, no. 4, pp. 1060–1068, 2007.
- [51] R. Vos, R. Barrett, R. D. Breuker, and P. Tiso, “Post-buckled precompressed elements: a new class of control actuators for morphing wing UAVs,” *Smart Materials and Structures*, vol. 16, no. 3, pp. 919–926, 2007.
- [52] R. Barrett, R. Vos, and R. De Breuker, “Post-Buckled Pre-compressed (PBP) subsonic micro flight control actuators and surfaces,” in *Active and Passive Smart Structures and Integrated Systems 2007*, Proceedings of SPIE, San Diego, Ca, USA, March 2007.
- [53] R. Vos and R. Barrett, “Dynamic elastic axis shifting: an important enhancement of postbuckled precompressed (PBP) actuators,” in *Proceedings of the 48th AIAA/ASME/ASCE/AHS/ASC Structures, Structural Dynamics, and Materials Conference*, pp. 47–60, April 2007.
- [54] R. Vos and R. Barrett, “Post-buckled precompressed techniques in adaptive aerostructures: an overview,” *Journal of Mechanical Design*, vol. 132, no. 3, Article ID 031004, 11 pages, 2010.
- [55] R. Barrett, “Hypermaneuverability and visual cloaking; new adaptive aerostructures technologies for uninhabited aerial vehicles (UAVs),” in *Proceedings of the Bristol International Unmanned Air Vehicle Systems (UAVS) Conference*, Bristol, UK, April 2008.
- [56] R. M. Jones, “Micromechanical behavior of a lamina,” in *Mechanics of Composite Materials*, Hemisphere, New York, NY, USA, 1975.

## Research Article

# Infra-Through Ultrasonic Piezoelectric Acoustic Vector Sensor Particle Rejection System

**Scott E. Cravens and Ronald M. Barrett**

*Aerospace Engineering Department, University of Kansas, Lawrence, KS 66045, USA*

Correspondence should be addressed to Ronald M. Barrett, barrettr@ku.edu

Received 15 November 2011; Accepted 16 January 2012

Academic Editor: Tao Li

Copyright © 2012 S. E. Cravens and R. M. Barrett. This is an open access article distributed under the Creative Commons Attribution License, which permits unrestricted use, distribution, and reproduction in any medium, provided the original work is properly cited.

Sensor elements which employ fine filaments are often vulnerable to particulate fouling when used in certain operational field conditions. Depending on the size, attraction level, thermal and electrical conduction, and charge accumulation properties of the particles, erroneous readings can be easily generated in such “dirty” environments. This paper describes the design, development, and testing of an ultrasonic system which dynamically rejects highly tenacious electrostatically charged particles of a wide variety of sizes and even water. The paper starts with a brief introduction to the field of acoustic vector sensing, outlining its outstanding characteristics and history. Operational challenges including a statistical analysis of typical Middle-Eastern wind-blown desert sand and charge density are laid out. Several representative subscale hot-wire filaments were fouled with calibrated dust representing desert sand. The fouled elements were then exposed to airflows of 13 ft/s (4 m/s) and showed highly erratic shifted conduction levels with respect to baseline (clean) levels. An ultrasonic cleaning system was designed specifically resonate the filament and cantilever so as to mechanically reject foulants. When operated at resonance, the ultrasonic cleaning system showed 98.6% particulate rejection levels and associated restoration of uncorrupted filament resistance levels to within 2% of baseline resistance measurements.

## 1. Introduction

Over the past decade, a new class of acoustic sensors has evolved. Conventional microphone technologies simply measure pressure as a function of time. These scalar measuring devices must be used in sizable clusters with powerful computers detangling this limited information [1]. A new approach using acoustic vector sensors (AVSs) employs fundamentally different sensor physics. These AVS elements are capable of not only determining pressure as a function of time (as do conventional microphones), but they can divide acoustic source directionality by measuring particle velocity in  $x$ ,  $y$ , and  $z$  coordinates with time at very high rates and phenomenal dynamic range [2]. Acoustic vector sensors use a number of different techniques to determine acoustic source direction. One of the leading acoustic vector sensors employs an advanced dual hot-wire anemometry setup to measure particle movement in multiple directions. The device is used in many applications ranging from acoustic holography to

tracking airborne vehicles as well as aquatic applications. Most of the applications currently employing these AVS devices are limited to clean environments, meaning free of dust particles, and other small environmental debris. Testing in dirty environments is limited at best to date. Fouling by particulate adherence or even complete particle blockage of measurement channels is a very distinct possibility given the small scale of the devices. The primary vulnerability comes from the very geometry and size of the sensor filaments which when compared to the size of airborne particulates are such that the largest airborne particles are an exact fit between the substrate and the sensor elements, which indicates that the devices could actually “trap” airborne particles. Figure 1 shows an interesting comparison of typical Appalachian quartz-based beach sand and sand from the Ash Shuqqan in the Empty Quarter (Rub al Khali) of the Arabian Peninsula.

The reader will note a profound difference between the two types of sand as the beach sand is quite rounded and



FIGURE 1: Beach sand from Destin, Florida (for reference) and windblown sand from the Rub al Khali, Arabian Peninsula.

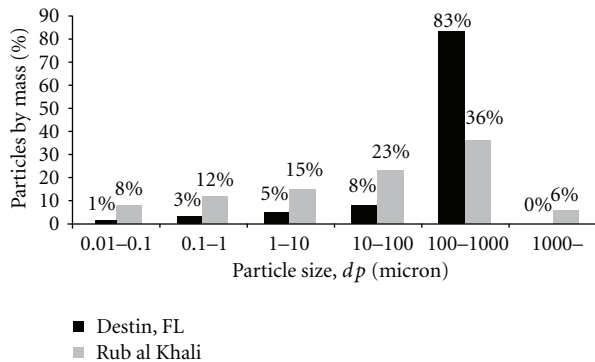


FIGURE 2: Particulate sand size distribution by percentage of sample mass of beach sand and Middle-Eastern windblown sand.

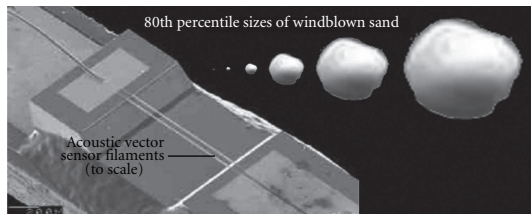


FIGURE 3: Advanced AVS sensing wires [2].

fairly even in size distribution with more than 80% of the grains falling between 130 and 640  $\mu\text{m}$  in diameter. The wind blown sand, on the other hand, is quite different with a wide distribution of sizes ranging widely from less than 1  $\mu\text{m}$  to 1100  $\mu\text{m}$  in diameter in statistically significant numbers by weight and volume. Another interesting characteristic is also seen in Figure 1: Static electric attraction. Wind blown sand from the Arabian Peninsula on the other hand behaves very differently and possesses different properties. Because most beach sand has been completely coated by salt water for a very long time, it is more resistant to holding large static charges. Indeed, single grain electrical resistance levels in 30% humidity were measured at 300–500  $\Omega/\text{mm}$  for the beach sand and more than 20  $\text{M}\Omega/\text{mm}$  for the wind blown sand. Similarly, the capacitance levels (i.e., ability to hold a charge) were 7 orders of magnitude greater for wind-blown sand. Figure 1 shows a comparatively tight dome distribution with mostly only larger grains falling past the edges of the pile. This is because electrostatic attraction generally holds the pile, especially the smaller particles, together. Figure 2 shows a statistical distribution of sizes from the two samples.

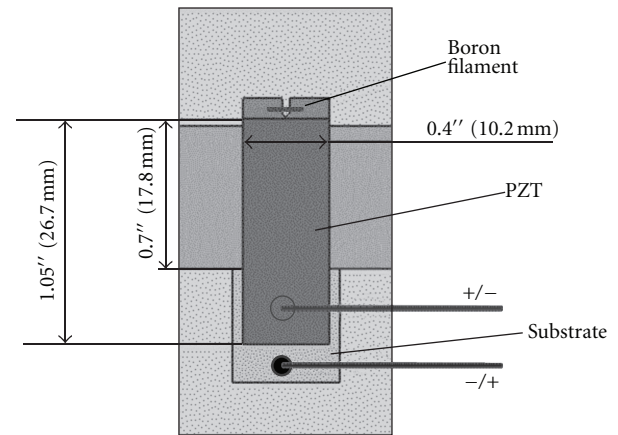


FIGURE 4: Piezoelectric cleaning device dimensions (in inches).

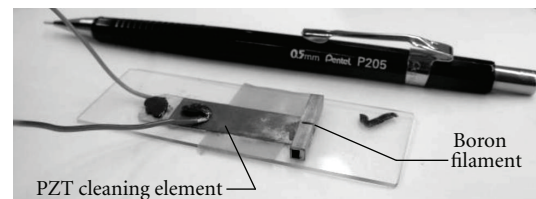


FIGURE 5: Assembled cleaning device.

The biggest challenge posed by windblown sand can be seen when compared to the physical size of an advanced AVS sensor element. Considering 1 mm long platinum sensor elements with a  $5\ \mu\text{m} \times 200\ \text{nm}$  cross-section, it is easy to see that the wide distribution of sizes of windblown sand presents not only a great threat of electrostatic cling, but physical entrapment between the filaments and the substrate itself. From Figure 3, it is easy to see that as air flows from lower left to upper right and back if it were bearing particles with size distributions laid out in Figure 2, serious challenges could be posed to the sensors. Figure 3 shows that the size of the desert sand goes well into the “dust” range with particles ranging down to fractions of a filament diameter, leading to cling of charged particles to filaments.

Because such atmospheric particles can render this remarkable sensor ineffective, this study is centered on making a system which can skirt these problems by effectively and safely cleaning the filaments of all foulants. References [3–5] highlight the point that there is relatively little in the open literature on infra-through-ultrasonic particle rejection known in the open literature.

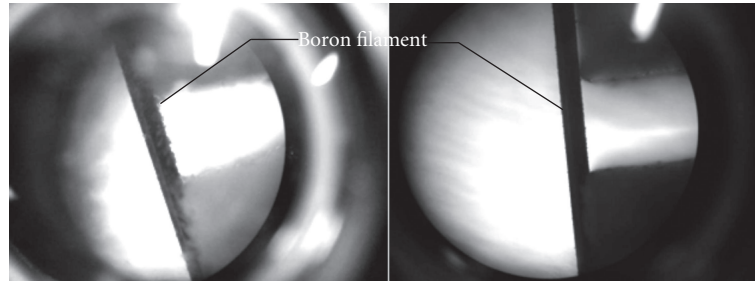


FIGURE 6: Boron fiber before and after cleaning with 20 kHz ultrasonic vibrations.

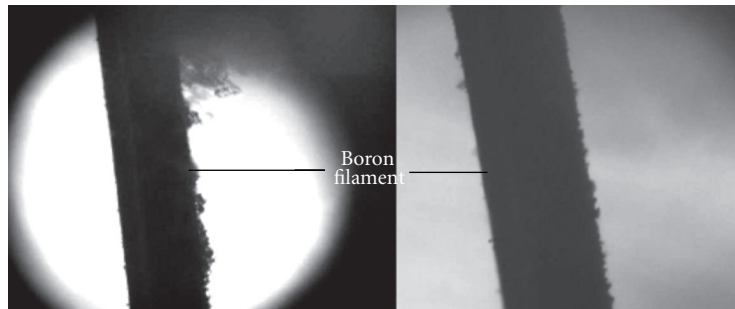


FIGURE 7: Boron fiber before and after cleaning—calibrated 5–30  $\mu\text{m}$  diameter particles.

## 2. Proof-of-Concept Testing on Boron Filaments

The chosen method of cleaning the AVS sensor is to use piezoelectric elements to induce infrasonic, sonic, and ultrasonic vibrations to mechanically knock off particulate contaminants. As a proof-of-concept exercise, Lead-Zirconate Titanate (PZT) was designed into a “micro-shaker.”

To test the concept in a variety of environments a range of filament diameters were chosen as well as a range of particle sizes. The first filament tested represented a large-scale analog to the AVS sensor. A 127  $\mu\text{m}$  diameter boron fiber was fixed to a brass substrate and PZT extensional actuator element. The basic dimensions (in inches) of the device constructed are shown in Figure 4 and the finished device is shown in Figure 5. Teflon tape was used to allow for low friction longitudinal motion.

To observe the fiber, the assembled device was placed under a microscope. Excitation of the PZT strip was achieved using a signal generator and a linear voltage amplifier. Figure shows a fiber which was coated with 5–30  $\mu\text{m}$  diameter dust particles under the microscope before and after the PZT strip was excited. A 20 kHz sine wave with a peak to peak voltage of 20 V was used to excite the PZT, generating local filament accelerations in excess of 350  $g$ 's. Although no deflections were visible during the cleaning event, the effect was pronounced.

Although not clearly visible in Figure 6, the dust used for the first test was microscopically fibrous in nature. Still, it possessed conductivity, capacitance levels and charge accretion properties which were within 20% of the Rub al Khali desert sand sample. Figure 7 shows the Boron fiber which had been dusted with nonfibrous silicate particles

before and after cleaning. As with the fibrous foulants, the conductivity, capacitance levels and charge accretion properties which were within 20% of the Rub al Khali desert sand sample.

## 3. Anemometer Wire Fouling and Cleaning

It has been shown that debris can be successfully removed from a small diameter Boron filament using PZT to vibrate the wire. The following sections extend this result to a hot wire anemometer, which is more representative of AVS elements. Two different anemometers were constructed, one using a copper sensing wire and another using a nickel titanium alloy wire.

**3.1. Nickel Titanium Alloy Filament Anemometer.** Nickel titanium alloy (NiTiNol) was used for the second type of anemometer constructed. This selection was chosen due to its ideally small diameter of only 38  $\mu\text{m}$ . For this anemometer, copper-conducting posts were soldered to a circuit board and the NiTiNOL was fixed to the ends of the posts. Figure 8 shows the basic configuration of the NiTiNOL anemometer. The guide posts were later discarded when it was determined that they would not affect the results.

To vibrate the NiTiNOL anemometer, a small stand was built that supported a PZT bending element. The bending element consisted of PZT strips bonded to either side of an aluminum substrate. This configuration resulted in vertical deflections of the anemometer when the actuator is parallel to the ground. Figures 9 and 10 show the NiTiNOL filament mounted on the PZT bending element.

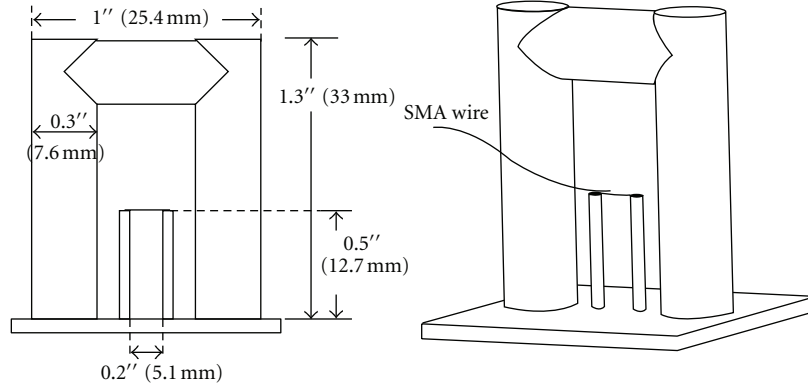


FIGURE 8: Nickel titanium alloy anemometer.

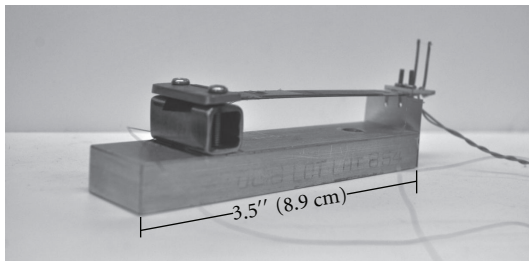


FIGURE 9: NiTiNOL anemometer mounted on PZT bending actuator.

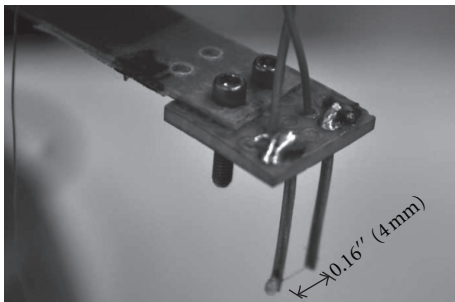


FIGURE 10: NiTiNOL anemometer.

**3.2. Experimental Setup.** A small blowdown type wind tunnel of 2" inner diameter was built to test the properties of the AVS cleaning system as shown in Figure 11. This setup provided a consistent airflow at a velocity of up to 4 m/s. Data was collected using a laptop computer with LABView data acquisition software. This was only used to record the time history of the resistance or current running through the anemometer.

A 1F capacitor arranged in parallel with the power supply provided clean power. For the NiTiNOL tests, a constant voltage was applied across the circuit. Testing was conducted from 50 to 250 mA (with filament failure being experienced at 270 mA. Current was measured by tracking voltage drop across a 1  $\Omega$  power resistor as shown in Figure 12.

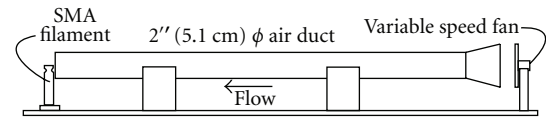


FIGURE 11: Wind tunnel setup.

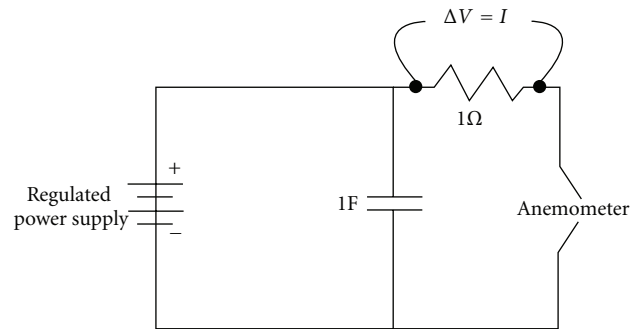


FIGURE 12: NiTiNOL anemometer circuit.

**3.3. Baseline NiTiNOL Anemometer Testing and Results.** As a baseline for the performance of the anemometer, the fan was cycled on and off several times without any cleaning excitation. The actuator was then excited at 200 Hz and the fan was cycled on and off again. Figure 13 shows the current flow through the filament during the fan cycles for the static and vibrating case. The peak voltage for the vibrating case drops a small amount during the cycles, but the amplitude of voltage change is approximately the same over each cycle. This indicates that the vibrations have little effect on the performance of the anemometer.

Figure 13 shows the overall peak-to-peak performance of the actuator by two phase shifted signals. The reader is asked to note that the measurements that are most important from Figure 13 are the peak-to-peak values and intermediate signal ripple, not the degree of phase shift.

After testing the performance of the clean anemometer, calibrated 5–30  $\mu\text{m}$  diameter nonfibrous dust was then applied to the wire and the performance was checked again. Figures 14, 15, and 16 show the resulting change in

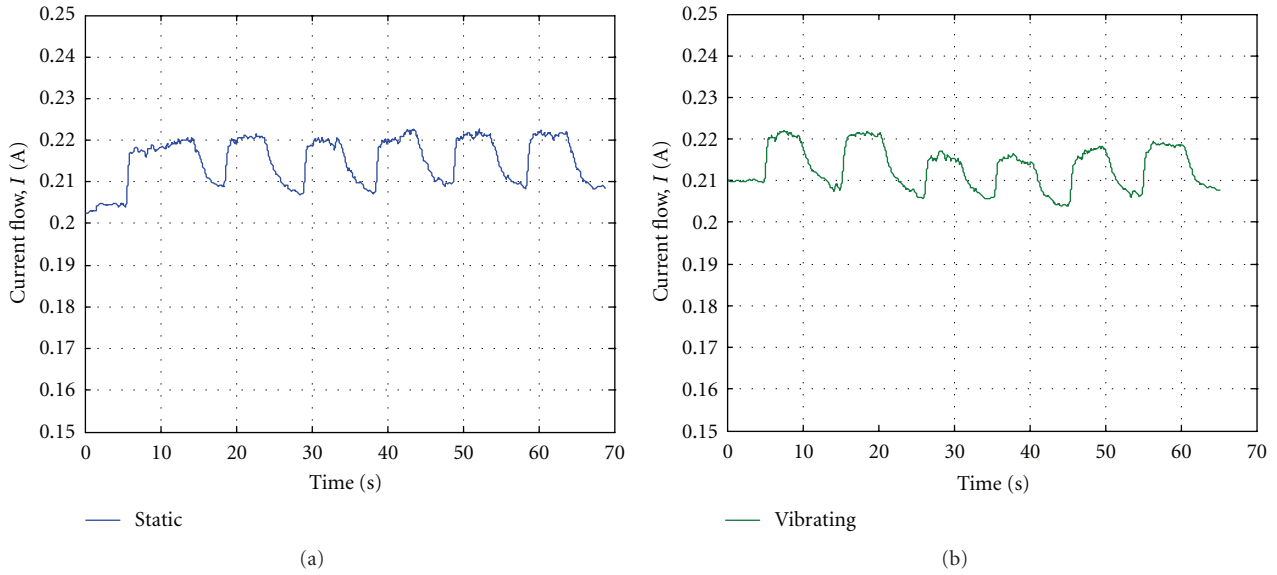


FIGURE 13: Baseline clean NiTiNOL anemometer before dusting.

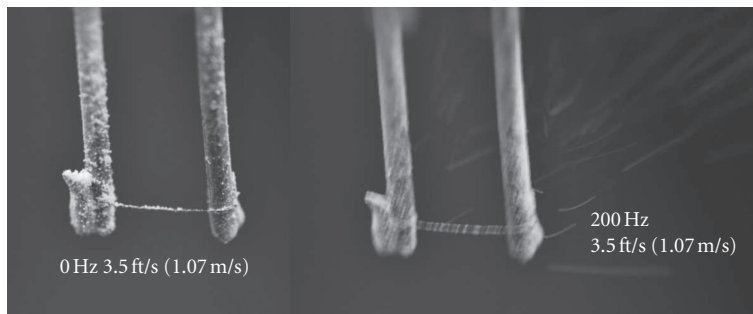


FIGURE 14: NiTiNOL anemometer filament dusted with 5–30  $\mu\text{m}$  particles and under 200 Hz excitation (for photographic reference).

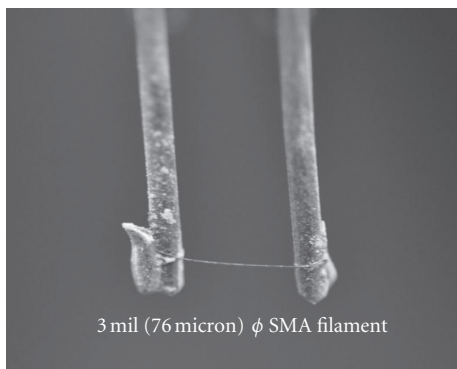


FIGURE 15: Anemometer after cleaning with infra-through ultrasonic vibrations.

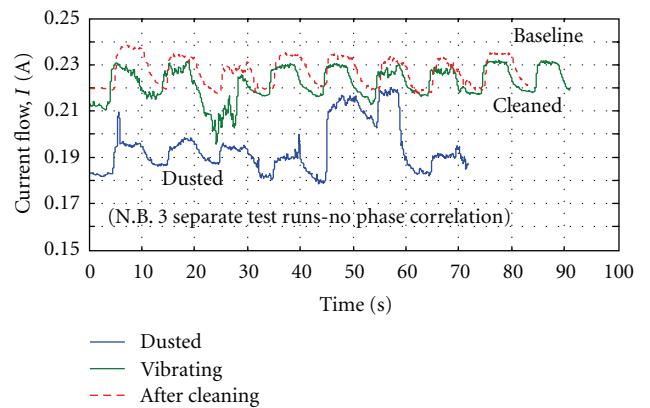


FIGURE 16: Baseline, dirty, and cleaned current flow through anemometer filament.

performance for the anemometer. Each test was conducted in the following manner and order. *Dusted*, *vibrating*, and *after cleaning* refer to the curves in Figures 14, 15, and 16.

(1) *Dusted*: the calibrated 5–30  $\mu\text{m}$  diameter dust was applied and the fan was cycled on and off with out any vibration.

(2) *Vibrating*: the actuator was excited (200 Hz at 7 Volts) and the fan was cycled on and off.

(3) *After cleaning*: the actuator was turned off and the fan was cycled on and off.

Figures 14, 15, and 16 show the quiescent 38  $\mu\text{m}$  diameter NiTiNOL filament suspended between two support posts, covered with calibrated 5–30  $\mu\text{m}$  diameter charged particles. Live testing of the cleaning system was conducted in a 4 m/s airflow. Infrasonic through ultrasonic vibrations of 10–20 kHz clearly rejected electrostatically attached particles as shown in Figures 14, 15 and 16.

Clearly from Figure 16, it has been shown that fouled anemometer filaments generate highly erratic unreliable readings with current flow shifts on the order of 35 mA. Given an anemometry sensitivity level on the order of 400 m/s/A, this represents a signal corruption level of 14 m/s. Infrasonic through ultrasonic cleaning rejected such particulate fouling and resulting signal corruption, leading to restoration of performance levels to within 2% of baseline performance.

#### 4. Conclusions

It has been shown that some of the most advanced microanemometer and acoustic vector sensor (AVS) elements are vulnerable to signal corruption when exposed to typical windblown particles. A statistical analysis of windblown desert sand from the Arabian Peninsula showed that statistically significant percentages of particles ranged from just 1/100th of the diameter of a typical AVS sensor filament to large enough to become lodged between the filaments and even between the filaments and mounting substrate. Wind tunnel tests on 38  $\mu\text{m}$  diameter filaments showed anemometry sensitivities on the order of 400 m/s/A were achieved. These sensitivities were dramatically corrupted when the filament was exposed to 5–30  $\mu\text{m}$  diameter particles which were shown to electrostatically cling to the filament, junctions, and post. In addition to erratic signals due to dusting an erroneous shift resulting in a 14 m/s measurement error appeared due to particulate fouling. An infra-through ultrasonic cleaning system was designed to reject these particles. When energized and swept through a broad frequency range, foulants were expelled from the sensor filaments, restoring sensor performance to within 2% of baseline levels.

#### Acknowledgment

The authors would like to thank the University of Kansas Transportation Research Institute for the continued support and funding of this and related research.

#### References

- [1] D. R. Fulton, P. A. Hawes, and K. S. Lally, "Multiple Acoustic Threat Assessment System," International Patent Application No. PCT/US2009/039909.
- [2] H. E. De Bree, "A perspective on acoustic vector sensors in passive surveillance—real world measurements, algorithms and applications," in *Proceedings of the Aero India*, Bangalore, India, 2009.
- [3] D. Ensminger, *Ultrasonics: Data, Equations, and Their Practical Uses*, vol. 10, CRC Press, Boca Raton, Fla, USA, 2009.
- [4] D. Williams, *Guide to Cleaner Technologies: Cleaning and Degreasing Process Changes*, US Environmental Protection Agency (EPA), Washington, DC, USA, 1994.
- [5] G. K. Nikas, "A mechanistic model of spherical particle entrapment in elliptical contacts," *Proceedings of the Institution of Mechanical Engineers, Part J*, vol. 220, no. 6, pp. 507–522, 2006.

## Research Article

# Static Electric Force and Measurement Principle of Material Constants in Electrostrictive Material

Zhen-Bang Kuang

School of Naval Architecture, Ocean and Civil Engineering, Shanghai Jiaotong University, Shanghai 200240, China

Correspondence should be addressed to Zhen-Bang Kuang, zbkung@mail.sjtu.edu.cn

Received 30 November 2011; Accepted 23 December 2011

Academic Editor: Ma Jan

Copyright © 2012 Zhen-Bang Kuang. This is an open access article distributed under the Creative Commons Attribution License, which permits unrestricted use, distribution, and reproduction in any medium, provided the original work is properly cited.

Electrostrictive materials convert electrical energy into mechanical energy and vice versa. They are extensively applied as intelligent materials in the engineering structures. The governing equations in electrostrictive media under the quasistatic electric field are very important for the measurement of material constants and the research on the strength and function. But some theoretical problems should be further clarified. In this paper, the electric force acting on the material is studied and the complete governing equations will be given. In this paper a possible method to measure electrostrictive coefficients is also discussed.

## 1. Introduction

The measurement method of material constants in an electrostrictive material is somewhat controversial between authors. Shkel and Klingenberg [1] considered that “The ultimate deformation depends on the elastic properties of the fixtures attached to the material (e.g., the electrodes). The (electrostrictive) coefficients  $\gamma_{ijkl}$  are therefore not strictly material parameters, but rather characteristics of the entire system.” Zhang et al. [2] pointed out that “In general in a nonpiezoelectric material such as the polyurethane elastomers investigated, the electric field induced strain can be caused by the electrostrictive effect and also by the Maxwell stress effect. The electrostrictive effect is the direct coupling between the polarization and mechanical response in the material. ... On the other hand Maxwell stress, which is due to the interaction between the free charges on the electrodes (Coulomb interaction) and to electrostatic forces that arise from dielectric inhomogeneities.” Guillot et al. [3] considered that “strictly speaking, the Maxwell stress tensor does not belong to the electrostrictive equations, but that it should be taken into account in the measurements. ... it is possible to factor out its contribution to the total response of the film and therefore to identify the isolated contribution due to the (electrostrictive) tensor only.” Thakur and Singh [4] considered that: “In most of the recent experiments concerning determination of electrostrictive param-

eters in elastic dielectrics, several researchers used incorrect equations without considering the contribution from the edge effect, the shear stress and suitable boundary conditions. This led to wrong predictions of experimental results particularly for materials with high Poisson ratios. Errors in the estimation of induced strains, varying from an underestimation of 202% to an overestimation of 168%, have been pointed out in the case of polycarbonate (PC).” Some material scientists felt puzzled about the objectivity of the electrostrictive coefficients.

In the books of Stratton [5] and Landau and Lifshitz [6], the formula of the stress in an isotropic electrostrictive material is

$$\begin{aligned}\sigma_{ik} &= \frac{\partial g_0}{\partial \varepsilon_{ik}} + \sigma_{ik}^L, \\ \sigma_{ik}^L &= \left(\frac{1}{2}\right)(2\varepsilon - a_1)E_k E_i \\ &\quad - \left(\frac{1}{2}\right)(\varepsilon + a_2)E_m E_m \delta_{ik},\end{aligned}\quad (1)$$

where  $\partial g_0 / \partial \varepsilon_{ik}$  is the stress without the electromagnetic field in the medium. As shown in [7, 8]  $\sigma_{ik}^L$  in this formula is just the pseudo total stress [9, 10] which is the sum of the Maxwell stress and the Cauchy stress introduced by the constitutive equations. In Pao's paper [11], he considered that the expression of the Maxwell stress is not unique and he gave

some different expressions by different authors. McMeeking and Landis [12] considered that “Since there are no experiments that can separate the effects of the Cauchy and Maxwell stresses unambiguously, it is generally more profitable to consider their sum and not to try identify them separately,” “we obviate the need to develop a constitutive theory that is consistent with a pre-determined formulation of the Maxwell stress, as can often be found in the literature on electrostrictive materials. Instead, the constitutive model can be simplified to one that embraces simultaneously the Cauchy, Maxwell, electrostrictive and electrostatic stresses, which in any case cannot be separately identified from any experiment.”

From the above and other literatures we can find that different author has different understanding about the governing equations and the Maxwell stress for the electrostrictive materials. We offered the physical variational principle [7, 8, 13–17] based on the thermodynamics in the nonlinear electroelastic analysis to get the governing equations and get the Maxwell stress naturally. The strength problem in engineering is determined by the Cauchy stress, which is connected with the constitutive equation, and the Maxwell stress is an external effective static Coulomb electric force. In this paper we give a general method to determine the static electric force or the Maxwell stress acting on the material by using the migratory variation of  $\varphi$  in the energy principle. We are sorry that we do not have the ground to do experiments, so in this paper only a possible method to measure electrostrictive coefficients is discussed.

## 2. The Physical Variational Principle

In literatures [7, 8, 13–17] we proposed that the first law of thermodynamics includes two contents: energy conservation law and physical variational principle (PVP), that is,

$$\text{Classical Energy conservation : } \int_V du dV - dw - dQ = 0,$$

$$\text{Classical linear PVP : } \delta\Pi = \int_V \delta u dV - \delta w - \delta Q = 0. \quad (2)$$

We proposed the physical variational principle as a basic principle in the continuum mechanics. From this principle we get the governing equations of the nonlinear electroelastic materials. For this principle with the electric Gibbs function we can simply illustrated as follows.

Under the small deformation the electric Gibbs function or electric enthalpy  $g = U - E_i D_i$ , where  $U$  is the internal energy, can be expanded in the series of  $\boldsymbol{\varepsilon}$  and  $\mathbf{E}$ :

$$g = \left(\frac{1}{2}\right) C_{ijkl} \varepsilon_{ij} \varepsilon_{kl} - \left(\frac{1}{2}\right) \epsilon_{kl} E_k E_l - e_{kij} E_k \varepsilon_{ij} - \left(\frac{1}{2}\right) l_{ijkl} E_i E_j \varepsilon_{kl},$$

$$\begin{aligned} C_{ijkl} &= C_{jikl} = C_{ijlk} = C_{klij}, \\ l_{ijkl} &= l_{jikl} = l_{ijlk} = l_{klij}, \\ e_{kij} &= e_{kji}, \quad \epsilon_{kl} = \epsilon_{lk}. \end{aligned} \quad (3)$$

The constitutive equations are

$$\begin{aligned} \sigma_{kl} &= \frac{\partial g}{\partial \varepsilon_{kl}} = C_{ijkl} \varepsilon_{ij} - e_{jkl} E_j - \left(\frac{1}{2}\right) l_{ijkl} E_i E_j, \\ D_k &= -\frac{\partial g}{\partial E_k} = (\epsilon_{kl} + l_{ijkl} \varepsilon_{ij}) E_l + e_{kij} \varepsilon_{ij} \approx \epsilon_{kl} E_l. \end{aligned} \quad (4)$$

In (3) and (4)  $\boldsymbol{\sigma}$ ,  $\boldsymbol{\varepsilon}$ ,  $\mathbf{D}$ ,  $\mathbf{E}$  are the stress, strain, electric displacement, and electric field, respectively,  $\mathbf{C}$ ,  $\mathbf{e}$ ,  $\boldsymbol{\epsilon}$ ,  $\mathbf{l}$  are the elastic coefficient, piezoelectric coefficient, permittivity, and the electrostrictive coefficient, respectively. Using (4), (3) is reduced to

$$\begin{aligned} g &= \left(\frac{1}{2}\right) C_{ijkl} \varepsilon_{ji} \varepsilon_{lk} + g^e, \\ g^e &= -\left(\frac{1}{2}\right) (D_k E_k + \Delta_{kl} \varepsilon_{lk}), \quad \Delta_{kl} = e_{mkl} E_{mk}, \end{aligned} \quad (5)$$

where  $g^e$  is the part of  $g$  related to the electric field. The value  $\Delta : \boldsymbol{\varepsilon}$  in (5) can be neglected due to its very small. In the electroelastic analysis the dielectric, its environment and their common boundary  $a^{\text{int}}$  consociate a system and should be considered together, because the electric field exists in every material except the ideal conductor. In this paper the variables in the environment will be denoted by a right superscript “env,” and the variables on the interface will be denoted by a right superscript “int.” In the environment (3)–(5) are all held.

Under the assumption that  $\mathbf{u}$ ,  $\varphi$ ,  $\mathbf{u}^{\text{env}}$ ,  $\varphi^{\text{env}}$  satisfy their boundary conditions on their own boundaries  $a_u$ ,  $a_\varphi$ ,  $a_u^{\text{env}}$ ,  $a_\varphi^{\text{env}}$ , and the continuity conditions on the interface  $a^{\text{int}}$ . The physical variational principle with the electric Gibbs free energy is [7, 8, 13–17]:

$$\begin{aligned} \delta\Pi &= \delta\Pi_1 + \delta\Pi_2 - \delta W^{\text{int}} = 0, \\ \delta\Pi_1 &= \int_V \delta g dV + \int_V g^e \delta u_{i,i} dV - \delta W, \\ \delta\Pi_2 &= \int_{V^{\text{env}}} \delta g^{\text{env}} dV + \int_{V^{\text{env}}} g^{e \text{ env}} \delta u_{i,i}^{\text{env}} dV - \delta W^{\text{env}}, \\ \delta W &= \int_V (f_k - \rho \ddot{u}_k) \delta u_k dV - \int_V \rho_e \delta \varphi dV \\ &\quad + \int_{a_\sigma} T_k^* \delta u_k da - \int_{a_D} \sigma^* \delta \varphi da, \\ \delta W^{\text{env}} &= \int_{V^{\text{env}}} (f_k^{\text{env}} - \rho \ddot{u}_k^{\text{env}}) \delta u_k^{\text{env}} dV - \int_{V^{\text{env}}} \rho_e^{\text{env}} \delta \varphi^{\text{env}} dV \\ &\quad + \int_{a_\sigma^{\text{env}}} T_k^{* \text{ env}} \delta u_k^{\text{env}} da - \int_{a_D^{\text{env}}} \sigma^{* \text{ env}} \delta \varphi^{\text{env}} da, \\ \delta W^{\text{int}} &= \int_{a^{\text{int}}} T_k^{* \text{ int}} \delta u_k da - \int_{a^{\text{int}}} \sigma^{* \text{ int}} \delta \varphi da, \end{aligned} \quad (6)$$

where  $\mathbf{f}$ ,  $\mathbf{T}^*$ ,  $\sigma^*$ , are given body force per volume, surface traction per area, and surface electric charge density,  $\mathbf{f}^{\text{env}}$ ,  $\mathbf{T}^{*\text{env}}$ ,  $\sigma^{*\text{env}}$ , and  $\mathbf{T}^{*\text{int}}$ ,  $\sigma^{*\text{int}}$  are also given values in the environment and on the interface, respectively.  $\mathbf{n} = -\mathbf{n}^{\text{env}}$  is the outward normal on the interface of the body.

The variation of the virtual electric potential  $\varphi$  is divided into local variation  $\delta_\varphi\varphi$  and migratory variation  $\delta_u\varphi$ , and the similar divisions in  $\mathbf{E}$ , so we have

$$\begin{aligned}\delta\varphi &= \delta_\varphi\varphi + \delta_u\varphi, & \delta_u\varphi &= \varphi_{,p}\delta u_p = -E_p\delta u_p, \\ \delta E_i &= \delta_\varphi E_i + \delta_u E_i, & \delta_\varphi E_i &= -\delta_\varphi\varphi_{,i}, & \delta_u E_i &= E_{i,p}\delta u_p.\end{aligned}\quad (7)$$

The derivation of  $\delta\mathbf{E}$  is in Appendix A. Finishing the variational calculation finally we get the governing equations:

$$\begin{aligned}S_{jk,j} + f_k &= \rho\ddot{u}_k, & D_{i,i} &= \rho_e, & \text{in } V, \\ S_{jk}n_j &= T_k^*, & \text{on } a_\sigma, & & D_i n_i = -\sigma^*, & \text{on } a_D, \\ \sigma_{ik}^M &= D_i E_k - \left(\frac{1}{2}\right)D_n E_n \delta_{ik}, \\ S_{kl} &= \sigma_{kl} + \sigma_{kl}^M = C_{ijkl}\varepsilon_{ij} - e_{jkl}E_j \\ &\quad - \left(\frac{1}{2}\right)l_{ijkl}E_i E_j + D_i E_k - \left(\frac{1}{2}\right)D_n E_n \delta_{ik},\end{aligned}\quad (8)$$

where  $\sigma_{ik}^M$  is the Maxwell stress and  $S_{kl}$  is the pseudo total stress [9, 10]. In the environment we have

$$\begin{aligned}S_{ij,i}^{\text{env}} + f_j^{\text{env}} &= \rho^{\text{env}}\ddot{u}_j^{\text{env}}, & D_{i,i}^{\text{env}} &= \rho_e^{\text{env}}, & \text{in } V^{\text{env}}, \\ S_{ij}^{\text{env}} n_i^{\text{env}} &= T_j^{*\text{env}}, & \text{on } a_\sigma^{\text{env}}, \\ D_i^{\text{env}} n_i^{\text{env}} &= -\sigma^{*\text{env}}, & \text{on } a_D^{\text{env}}.\end{aligned}\quad (9)$$

On the interface we have

$$\left(S_{ij} - S_{ij}^{\text{env}}\right)n_i = T_j^{*\text{int}}, \quad \left(D_i - D_i^{\text{env}}\right)n_i = -\sigma^{*\text{int}}, \quad \text{on } a^{\text{int}}.\quad (10)$$

The above variational principle requests prior that the displacements, the electric potential satisfy their own boundary conditions and the continuity conditions on the interface, so the following equations should also be added to governing equations:

$$\begin{aligned}u_i &= u_i^*, & \text{on } a_u, & & \varphi &= \varphi^*, & \text{on } a_\varphi, \\ u_i^{\text{env}} &= u_i^{*\text{env}}, & \text{on } a_u^{\text{env}}, & & \varphi^{\text{env}} &= \varphi^{*\text{env}}, & \text{on } a_\varphi^{\text{env}}, \\ u_i &= u_i^{\text{env}}, & \varphi &= \varphi^{\text{env}}, & \text{on } a^{\text{int}}.\end{aligned}\quad (11)$$

Equations (8)–(11) are the governing equations in the electroelastic analysis.

If we introduce the body electric force  $f_k^e$ ,  $f_k^{e\text{env}}$ , and surface electric force  $T_k^e$ ,  $T_k^{e\text{env}}$  in the materials as

$$\begin{aligned}f_k^e &= \sigma_{jk,j}^M, & T_k^e &= \sigma_{jk}^M n_j; \\ f_k^{e\text{env}} &= \sigma_{jk,j}^{M\text{env}}, \\ T_k^{e\text{env}} &= \sigma_{jk}^{M\text{env}} n_j^{\text{env}}.\end{aligned}\quad (12)$$

Then the variational principle equation (6) is reduced to

$$\begin{aligned}\delta\Pi' &= \delta\Pi'_1 + \delta\Pi'_2 - \delta W'^{\text{int}} = 0, \\ \delta\Pi'_1 &= \int_V \delta g dV - \delta W', \\ \delta\Pi'_2 &= \int_{V^{\text{env}}} \delta g^{\text{env}} dV - \delta W'^{\text{env}}, \\ \delta W' &= \int_V (f_k + f_k^e - \rho\ddot{u}_k)\delta u_k dV - \int_V \rho_e \delta\varphi dV \\ &\quad + \int_{a_\sigma} (T_k^* - T_k^e)\delta u_k da - \int_{a_D} \sigma^* \delta\varphi da, \\ \delta W'^{\text{env}} &= \int_{V^{\text{env}}} (f_k^{\text{env}} + f_k^{e\text{env}} - \rho^{\text{env}}\ddot{u}_k^{\text{env}})\delta u_k^{\text{env}} dV \\ &\quad - \int_{V^{\text{env}}} \rho_e^{\text{env}} \delta\varphi^{\text{env}} dV \\ &\quad + \int_{a_\sigma^{\text{env}}} (T_k^{\text{env}*} - T_k^{e\text{env}})\delta u_k^{\text{env}} da \\ &\quad - \int_{a_D^{\text{env}}} \sigma^{\text{env}*} \delta\varphi^{\text{env}} da, \\ \delta W'^{\text{int}} &= \int_{a^{\text{int}}} (T_k^{\text{int}*} + T_k^{e\text{env}} - T_k^e)\delta u_k da \\ &\quad - \int_{a^{\text{int}}} \sigma^{\text{int}*} \delta\varphi da.\end{aligned}\quad (13)$$

In (13) the variations of  $\delta u$  and  $\delta\varphi$  are completely independent, that is, it is not needed to consider the migratory variation  $\delta_u\varphi$ . Equations (8)–(10) are reduced to

$$\begin{aligned}\sigma_{ij,i} + (f_j + f_j^e) &= \rho\ddot{u}_j, & D_{i,i} &= \rho_e, & \text{in } V, \\ \sigma_{ij}n_i &= T_j^* - T_j^{e*}, & \text{on } a_\sigma, & & D_i n_i = -\sigma^*, & \text{on } a_D; \\ \sigma_{ij,j}^{\text{env}} + (f_i^{\text{env}} + f_i^{e\text{env}}) &= \rho^{\text{env}}\ddot{u}_i^{\text{env}}, & D_{i,i}^{\text{env}} &= \rho_e^{\text{env}}, & \text{in } V^{\text{env}} \\ \sigma_{ij}^{\text{env}} n_j^{\text{env}} &= (T_i^{*\text{env}} - T_i^{e\text{env}}), & \text{on } a_\sigma^{\text{env}}, \\ D_i^{\text{env}} n_i^{\text{env}} &= -\sigma^{*\text{env}}, & \text{on } a_D^{\text{env}}, \\ (\sigma_{kl} - \sigma_{kl}^{\text{env}})n_l &= T_k^{*\text{int}} - T_i^e + T_i^{e\text{env}}, \\ D_k n_k - D_k^{\text{env}} n_k &= -\sigma^{*\text{int}}, & \text{on } a^{\text{int}}.\end{aligned}\quad (14)$$

### 3. The Static Electric Force Acting on a Dielectric

*3.1. The Static Electric Force Acting on the Dielectric in a Capacitor.* In any electromagnetic textbook we can find how to determine the static electric force acting on the dielectric in a capacitor consisted of two parallel electrode plates and filled dielectric with permittivity  $\epsilon$ . Assume the length and width of the plates are infinite, the distance  $h$  between two plate electrodes is very small. The electric potential on the upper plate electrode is smaller than that on the lower plate.

Let the coordinate origin be located at its center, the plane  $x_1-x_3$  is parallel, and axis  $x_2$  is perpendicular to the electrode plates. There is no external force on the plate and inside the dielectric and the deformation is small. The electric field inside the dielectric of the capacitor is homogeneous and  $\mathbf{E} = E_2 \mathbf{n}$ ,  $\mathbf{n} = \mathbf{i}_2$  due to that the plates are infinite, where  $E_2 = \varphi/h$ ,  $\varphi$  is the difference of electric potentials between two electrodes. The static electric force acting on electrode plates can be obtained by the energy method.

In this simple case the static electric force can be directly derived from the general equation of the physical variational principle. According to (6) in this case we have

$$\begin{aligned} \delta\Pi &= \delta\Pi_1 + \delta\Pi_2 - \delta W^{\text{int}} = 0, \\ \delta\Pi_1 &= \delta \int_V g dV = h \left[ \sigma_{22} \delta u_{2,2} - D_2 \delta E_2 - \left( \frac{1}{2} \right) E_2 D_2 \delta u_{2,2} \right], \\ \delta\Pi_2 &= 0, \quad \delta W^{\text{int}} = 0. \end{aligned} \quad (15)$$

Give a virtual displacement under the constant electric potential on the electrode plate. It is noted that though  $\varphi$  is constant on the plate, but after virtual displacement  $\varphi$  is changed inside the dielectric. For a fixed  $x$  the change of the electric field due to changed  $\varphi$  is

$$\delta_\varphi E_2 = \frac{\varphi}{(h + \delta h)} - \frac{\varphi}{h} = -\frac{\varphi \delta h}{h^2}, \quad -D_2 \delta E_2 = D_2 E_2 \frac{\delta h}{h}. \quad (16)$$

Due to the electric potential  $\varphi$  on the electrode plate is constant, we have  $\delta_u E_2 = E_{2,p} \delta u_p = 0$ , so  $\delta E_2 = \delta_\varphi E_2$ . Therefore, finally we get

$$\begin{aligned} \delta\Pi &= h \left[ \sigma_{22} \delta u_{2,2} - D_2 \delta E_2 - \left( \frac{1}{2} \right) E_2 D_2 \delta u_{2,2} \right] \\ &= h D_2 \left[ \sigma_{22} \left( \frac{\delta h}{h} \right) + \left( \frac{1}{2} \right) \epsilon E_2^2 \left( \frac{\delta h}{h} \right) \right] = 0 \quad (17) \\ &\Rightarrow T_2 = \sigma_{22} = -\frac{\epsilon E_2^2}{2}. \end{aligned}$$

We can also use the Maxwell stress to derive the force acting on the dielectric directly. According to (10), we have  $(S_{ij} - S_{ij}^{\text{env}})n_i = 0$  or  $T_i = (\sigma_{ij} - \sigma_{ij}^{\text{env}})n_i = -\sigma_{ij}^M n_j$ , where  $\sigma_{ij}^M = 0$  in the electrode is used. In the present case we have  $T_2 = -\sigma_{22}^M = -D_2^2/2\epsilon$ . If the force on the electrode plate is zero, then the static electric force acting on the dielectric is  $-D_2^2/2\epsilon$ , which is identical with that in (17).

In the electric textbooks the derivation is as follows: given the upper plate a virtual displacement  $\delta h$  along  $x_2$ , the electric charge on the electrode plate increases  $\delta q$  due to fixed  $\varphi$ , so the electric source supplies the energy  $\varphi \delta q$ . The energy in the dielectric increases  $\delta(\varphi q/2) = \varphi \delta q/2$  and the remained energy  $\varphi \delta q/2$  is used to overcome the work produced by

the static electric force on the dielectric, that is, for virtual displacement  $\delta u$  we have

$$\begin{aligned} F \cdot \delta u &= \sigma_{22} \delta h = \varphi \delta q - \left( \frac{1}{2} \right) \varphi \delta q = \left( \frac{1}{2} \right) \varphi \delta q \\ &= \left( \frac{1}{2} \right) \varphi \delta(\epsilon E_2) = \left( \frac{\epsilon}{2} \right) \varphi \delta \left( \frac{\varphi}{h} \right) \quad (18) \\ &= -\left( \frac{\epsilon}{2} \right) \left( \frac{\varphi}{h} \right)^2 \delta h \Rightarrow \sigma_{22} = -\left( \frac{\epsilon}{2} \right) E_2^2, \end{aligned}$$

which is identical with that in (17). At least this result partly proves the general theory is correct.

**3.2. The Static Electric Force in General Case.** Though the static electric force acting on dielectric of a capacitor was derived in textbooks from the energy method as shown in above section, but the energy method did not be used to derive the Maxwell stress in the general case.

In the general case the Maxwell stress is introduced by the migratory variations of electric field. So the static electric force from (6) and (13) can be written as

$$\begin{aligned} \delta W^e &= -\delta_u \Pi, \\ \delta_u \Pi &= \int_V g_{,E} \cdot \delta_u E dV + \int_V g^e \delta u_{k,k} dV + \int_V \rho_e \delta_u \varphi dV \\ &\quad + \int_{a_D} \sigma^* \delta_u \varphi da + \int_{V^{\text{env}}} g_{,E}^{\text{env}} \cdot \delta_u E^{\text{env}} dV \\ &\quad + \int_{V^{\text{env}}} g^{e \text{env}} \delta u_{i,i}^{\text{env}} dV + \int_{V^{\text{env}}} \rho_e^{\text{env}} \delta_u \varphi^{\text{env}} dV \\ &\quad + \int_{a_D^{\text{env}}} \sigma^{* \text{env}} \delta_u \varphi^{\text{env}} da + \int_{a^{\text{int}}} \sigma^{* \text{int}} \delta_u \varphi da, \\ \delta W^e &= \int_V f_k^e \delta u_k dV + \int_{a_\sigma} T_k^e \delta u_k da + \int_{V^{\text{env}}} f_k^{e \text{env}} \delta u_k^{\text{env}} dV \\ &\quad + \int_{a_\sigma^{\text{env}}} T_k^{e \text{env}} \delta u_k^{\text{env}} da + \int_{a^{\text{int}}} (T_k^e - T_k^{e \text{env}}) \delta u_k da. \end{aligned} \quad (19)$$

It is easy to prove that  $f_k^e$ ,  $T_k^e$ ,  $f_k^{e \text{env}}$ ,  $T_k^{e \text{env}}$  derived from (19) are identical with that in (12), see Appendix B. If the environment is neglected, then we get

$$\begin{aligned} &\int_V f_k^e \delta u_k dV + \int_{a_\sigma} T_k^e \delta u_k da \\ &= -\left( \int_V g_{,E} \cdot \delta_u E dV + \int_V g^e \delta u_{k,k} dV \right. \\ &\quad \left. + \int_V \rho_e \delta_u \varphi dV + \int_{a_D} \sigma^* \delta_u \varphi da \right). \end{aligned} \quad (20)$$

Using  $\mathbf{D} = D_n \mathbf{n} + D_t \mathbf{t}$  and  $\mathbf{E} = E_n \mathbf{n} + E_t \mathbf{t}$ , and the continuous condition (10) and (11) of the  $\mathbf{D}$ ,  $\mathbf{E}$  on the interface, the Maxwell stress can also be rewritten as

$$\begin{aligned} \mathbf{n} \cdot (\boldsymbol{\sigma} - \boldsymbol{\sigma}^{\text{env}}) &= \tilde{\mathbf{T}}^{*\text{int}}, \\ \tilde{\mathbf{T}}^{*\text{int}} &= \mathbf{T}^{*\text{int}} + \mathbf{n} \cdot (\boldsymbol{\sigma}^M \text{env} - \boldsymbol{\sigma}^M), \\ \mathbf{n} \cdot (\boldsymbol{\sigma}^M \text{env} - \boldsymbol{\sigma}^M) &= \left[ \mathbf{n} \cdot (\mathbf{D}^{\text{env}} \otimes \mathbf{E}^{\text{env}}) - \left( \frac{1}{2} \right) (\mathbf{D}^{\text{env}} \cdot \mathbf{E}^{\text{env}}) \mathbf{n} \right] \\ &- \left[ \mathbf{n} \cdot (\mathbf{D} \otimes \mathbf{E}) - \left( \frac{1}{2} \right) (\mathbf{D} \cdot \mathbf{E}) \mathbf{n} \right] \\ &= \left( \frac{1}{2} \right) [D_n (E_n^{\text{env}} - E_n) - (D_t^{\text{env}} - D_t) E_t] \mathbf{n}, \end{aligned} \quad (21)$$

where  $\mathbf{n}$  is the unit normal, subscripts  $n$  and  $t$  mean the normal and tangential direction respectively; there is no sum on  $n$  and  $t$ . Equation (21) points out that in the case of small strain the boundary surface traction corresponding to the Maxwell stress is along the normal direction.

#### 4. Measurement of Material Constants in Isotropic Electrostrictive Materials

For isotropic materials we have

$$\begin{aligned} C_{ijkl} &= \lambda \delta_{ij} \delta_{kl} + G (\delta_{ik} \delta_{jl} + \delta_{il} \delta_{jk}), \\ I_{ijkl} &= a_2 \delta_{ij} \delta_{kl} + \left( \frac{a_1}{2} \right) (\delta_{ik} \delta_{jl} + \delta_{il} \delta_{jk}), \\ \epsilon_{ij} &= \epsilon \delta_{ij}, \quad e_{kij} = 0. \end{aligned} \quad (22)$$

So (3) and (4) are reduced to

$$\begin{aligned} g &= \left( \frac{1}{2} \right) \lambda \epsilon_{ii} \epsilon_{kk} + G \epsilon_{ij} \epsilon_{ij} - \left( \frac{1}{2} \right) \epsilon E_k E_k \\ &- \left( \frac{1}{2} \right) (a_2 E_i E_i \epsilon_{kk} + a_1 E_i E_j \epsilon_{ij}), \end{aligned} \quad (23)$$

$$\sigma_{kl} = \lambda \epsilon_{ii} \delta_{kl} + 2G \epsilon_{kl} - \left( \frac{1}{2} \right) (a_2 E_i E_i \delta_{kl} + a_1 E_k E_l),$$

$$D_k = \epsilon E_k + (a_2 E_k \epsilon_{mm} + a_1 E_l \epsilon_{kl}) \approx \epsilon E_k,$$

$$\begin{aligned} S_{kl} &= \sigma_{kl} + \sigma_{kl}^M = \lambda \epsilon_{ii} \delta_{kl} + 2G \epsilon_{kl} - \left( \frac{1}{2} \right) (a_2 + \epsilon) E_m E_m \delta_{kl} \\ &+ \left( \frac{1}{2} \right) (2\epsilon - a_1) E_k E_l. \end{aligned} \quad (24)$$

The first formula in (24) is just the usual form of the constitutive equation, where  $a_1$  and  $a_2$  are known as electrostrictive coefficients. From (8)–(11), it is known that solving  $\mathbf{S}$  is easier than solving  $\boldsymbol{\sigma}$ , so in experiments the measured variables usually are  $(\mathbf{S}, \boldsymbol{\epsilon}, \mathbf{E})$ . So that in usual experiments the measured material coefficients are  $2\epsilon - a_1$  and  $a_2 + \epsilon$ . Therefore, when we do experiments we should clearly provide what variables are used. In isotropic materials or

materials without the electromagnetic body couple variables  $\mathbf{S}$ ,  $\boldsymbol{\sigma}$ , and  $\boldsymbol{\sigma}^M$  are all symmetric.

As an example, we discuss the electroelastic field of an isotropic rectangular dielectric with material constants  $\epsilon$ ,  $a_1$ ,  $a_2$ . The length, width and height of the dielectric are  $l$ ,  $b$ , and  $h$ , respectively. Let the coordinate origin be located at its center, the axes are parallel to its edges, the axis  $x_2$  is perpendicular to its middle plane. Assume the electric field in dielectric is homogeneous  $\mathbf{E} = E_2 \mathbf{n}$ ,  $\mathbf{n} = \mathbf{i}_2$  and the dielectric is free from the external force ( $\mathbf{f}, \mathbf{T}^{*\text{int}} = \mathbf{0}$ ).

*4.1. The Surrounding of the Dielectric Is Air.* In the air there is no mechanical stress. On the interface we have

$$E_t^{\text{air}} = E_t, \quad D_n^{\text{air}} = D_n \text{ on interface; or}$$

$$E_1^{\text{air}} = E_1 = 0, \quad E_3^{\text{air}} = E_3 = 0,$$

$$D_2^{\text{air}} = D_2 (\epsilon_0 E_2^{\text{air}} = \epsilon E_2), \quad x_2 = \pm \frac{h}{2}, \quad (25)$$

$$E_1^{\text{air}} = E_1 = 0, \quad E_3^{\text{air}} = E_3 = 0,$$

$$E_2^{\text{air}} = E_2; \quad x_1 = \pm \frac{l}{2}, \quad \text{or} \quad x_3 = \pm \frac{b}{2},$$

where  $n$  and  $t$  mean the normal and tangential directions, respectively. In this case from (8)–(10) we get

$$\begin{aligned} S_{ij,j} &= 0, \quad \text{in } V, \\ (S_{ij} - S_{ij}^{\text{air}}) n_i &= 0, \quad \text{on } a^{\text{int}} \implies \sigma_{ij} = (\sigma_{ij}^M \text{air} - \sigma_{ij}^M)^{\text{int}}, \\ \sigma_{22}^M &= \left( \frac{1}{2} \right) D_2 E_2, \quad \sigma_{11}^M = \sigma_{33}^M = - \left( \frac{1}{2} \right) D_2 E_2, \\ \sigma_{ij}^M &= 0, \quad \text{when } i \neq j; \quad \text{on } a^{\text{int}}, \\ \sigma_{22}^M \text{air} &= \left( \frac{1}{2} \right) D_2^{\text{air}} E_2^{\text{air}}, \quad \sigma_{11}^M \text{air} = \sigma_{33}^M \text{air} = - \left( \frac{1}{2} \right) D_2^{\text{air}} E_2^{\text{air}}, \\ \sigma_{ij}^M \text{air} &= 0, \quad \text{when } i \neq j, \quad \text{on } a^{\text{int}} \implies \\ \sigma_{11} &= \sigma_{33} = - \left( \frac{1}{2} \right) \left[ \left( \frac{\epsilon^2}{\epsilon_0} \right) - \epsilon \right] E_2^2, \\ \sigma_{22} &= \left( \frac{1}{2} \right) \left[ \left( \frac{\epsilon^2}{\epsilon_0} \right) - \epsilon \right] E_2^2. \end{aligned} \quad (26)$$

Using the constitutive equation (24) we get

$$\begin{aligned} - \left( \frac{1}{2} \right) \left[ \left( \frac{\epsilon^2}{\epsilon_0} \right) - \epsilon \right] E_2^2 &= (3\lambda\theta + 2G\epsilon_{11}) - \left( \frac{1}{2} \right) a_2 E_2^2, \\ \left( \frac{1}{2} \right) \left[ \left( \frac{\epsilon^2}{\epsilon_0} \right) - \epsilon \right] E_2^2 &= (3\lambda\theta + 2G\epsilon_{22}) - \left( \frac{1}{2} \right) (a_2 + a_1) E_2^2, \\ - \left( \frac{1}{2} \right) \left[ \left( \frac{\epsilon^2}{\epsilon_0} \right) - \epsilon \right] E_2^2 &= (3\lambda\theta + 2G\epsilon_{33}) - \left( \frac{1}{2} \right) a_2 E_2^2. \end{aligned} \quad (27)$$

4.2. *The Dielectric and Air Are All between Two Parallel Infinite Rigid Electrodes.* In electrodes  $\mathbf{E} = \mathbf{0}$ , so there is no Maxwell stress. In this case from (8)–(10) we get

$$\begin{aligned}
S_{ij,j} &= 0, \quad \text{in } V, \\
(S_{ij} - S_{ij}^{\text{env}})n_i &= 0, \quad \text{on } a^{\text{int}} \implies \sigma_{ij} = [\sigma_{ij}^M \text{env} - \sigma_{ij}^M]^{\text{int}}, \\
\sigma_{22}^M &= \left(\frac{1}{2}\right)\epsilon E_2^2, \quad \sigma_{11}^M = \sigma_{33}^M = -\left(\frac{1}{2}\right)\epsilon E_2^2, \\
\sigma_{ij}^M &= 0, \quad \text{when } i \neq j, \quad \text{on } a^{\text{int}}, \\
\sigma_{22}^{\text{plate}} &= 0, \quad \sigma_{11}^{\text{air}} = \sigma_{33}^{\text{air}} = -\left(\frac{1}{2}\right)\epsilon_0 E_2^2, \\
\sigma_{ij}^{\text{env}} &= 0, \quad \text{when } i \neq j, \quad \text{on } a^{\text{int}} \implies \\
\sigma_{11} &= \sigma_{33} = \left(\frac{1}{2}\right)(\epsilon - \epsilon_0)E_2^2, \\
\sigma_{22} &= -\left(\frac{1}{2}\right)\epsilon E_2^2.
\end{aligned} \tag{28}$$

Using the constitutive equation (24) we get

$$\begin{aligned}
\left(\frac{1}{2}\right)(\epsilon - \epsilon_0)E_2^2 &= (3\lambda\theta + 2G\epsilon_{11}) - \left(\frac{1}{2}\right)a_2 E_2^2, \\
-\left(\frac{1}{2}\right)\epsilon E_2^2 &= (3\lambda\theta + 2G\epsilon_{22}) - \left(\frac{1}{2}\right)(a_2 + a_1)E_2^2, \\
\left(\frac{1}{2}\right)(\epsilon - \epsilon_0)E_2^2 &= (3\lambda\theta + 2G\epsilon_{33}) - \left(\frac{1}{2}\right)a_2 E_2^2.
\end{aligned} \tag{29}$$

In (27) and (29)  $3\theta = \epsilon_{ii}$ . In the discussed cases the third equation in (27) and (29) can be omitted. In experiments we can measure strains from the given electric field. From (27) or (29) or other improved methods we can get electrostrictive coefficients. It is clear that the environment has obviously effect.

The above example is very simple and ideal. The real experimental set is more complex, but from above discussions, we can see that in order to get correct electrostrictive constants in experiments we need consider the entire system including the dielectric medium, its environment and their common boundary.

## 5. Conclusions

In this paper, we discuss the nonlinear electroelastic analysis in the electrostrictive materials by the physical variational principle. Given a general expression of the electric force. Using the governing equation proposed in this paper we give a possible method to correctly measure the electrostrictive coefficients. It is shown that in order to get correct material constants in experiments we need take the correct governing equations and consider the entire system including the dielectric medium, its environment and their common boundary.

## Appendices

### A. The Derivation of $\delta\mathbf{E}$ in (7)

In our previous papers  $\delta\mathbf{E}$  in (7) was directly given, here we shall give a simple derivation.

Assume the variational functional is

$$I = \int_V L(x_i, u_\alpha, u_{\alpha,j}) dV, \tag{A.1}$$

where  $\mathbf{x}$ ,  $\mathbf{u}$ ,  $\mathbf{u}_j$  are the independent variable, dependent variable, and the derivative of the dependent variable, respectively. Assume an infinitesimal transformation

$$\begin{aligned}
x_i &\longrightarrow x'_i = x_i + \delta u_i(x_j, \varphi), \\
\varphi(x_i) &\longrightarrow \varphi'(x'_i) = \varphi(x_i) + \delta\varphi(x_i, \varphi), \\
\delta\varphi &= \varphi'(x'_i) - \varphi(x_i) \\
&= [\varphi(x_i + \delta u_i) + \delta\varphi\varphi(x_i)] - \varphi(x_i) \\
&= \delta_\varphi\varphi + \delta_u\varphi = \delta_\varphi\varphi + \varphi_{,i}\delta u_i.
\end{aligned} \tag{A.2}$$

Noting

$$\begin{aligned}
\frac{\partial x'_i}{\partial x_j} &\approx \delta_{ij} + \frac{\partial \delta u_i}{\partial x_j}, \\
\frac{\partial x_i}{\partial x'_j} &\approx \delta_{ij} - \frac{\partial \delta u_i}{\partial x_j}, \\
j &= \left| \frac{\partial x'_i}{\partial x_j} \right| \approx 1 + \frac{\partial \delta u_i}{\partial x_i},
\end{aligned} \tag{A.3}$$

from (A.2) we get

$$\begin{aligned}
\delta\varphi_{,j} &= \frac{\partial \varphi'(x'_i)}{\partial x'_j} - \frac{\partial \varphi(x_i)}{\partial x_j} \\
&= \frac{\partial [\varphi(x_i) + \delta\varphi(x_i, \varphi)]}{\partial x_k} \frac{\partial x_k}{\partial x'_j} - \frac{\partial \varphi(x_i)}{\partial x_j} \\
&= \frac{\partial \delta\varphi(x_i, \varphi)}{\partial x_j} - \frac{\partial \varphi(x_i)}{\partial x_k} \frac{\partial \delta u_k}{\partial x_j} \\
&= \frac{\partial (\delta_\varphi\varphi + \varphi_{,i}\delta u_i)}{\partial x_j} - \frac{\partial \varphi(x_i)}{\partial x_k} \frac{\partial \delta u_k}{\partial x_j} \\
&= \frac{\partial (\delta_\varphi\varphi)}{\partial x_j} + \frac{\partial (\varphi_{,i}\delta u_i)}{\partial x_j} - \frac{\partial \varphi(x_i)}{\partial x_k} \frac{\partial \delta u_k}{\partial x_j} \\
&= \frac{\partial (\delta_\varphi\varphi)}{\partial x_j} + \frac{\partial (\varphi_{,i})}{\partial x_j} \delta u_i.
\end{aligned} \tag{A.4}$$

Equation (A.4) is identical with  $\delta\mathbf{E}$  in (7) in text.

## B. The Derivation of (19)

From (19) we have

$$\begin{aligned}
\delta_u \Pi &= \int_V g_{,E} \cdot \delta_u E dV + \int_V g^e \delta u_{k,k} dV + \int_V \rho_e \delta_u \varphi dV \\
&+ \int_{a_D} \sigma^* \delta_u \varphi da + \int_{V^{env}} g_{,E}^{env} \cdot \delta_u E^{env} dV \\
&+ \int_{V^{env}} g^e \delta u_{i,i}^{env} dV + \int_{V^{env}} \rho_e^{env} \delta_u \varphi^{env} dV \\
&+ \int_{a_D^{env}} \sigma^{*env} \delta_u \varphi^{env} da + \int_{a^{int}} \sigma^{*int} \delta_u \varphi da \\
&= - \int_V D_i E_{p,i} \delta u_p dV - \int_V \left( \frac{1}{2} \right) D_k E_k \delta u_{j,j} dV \\
&+ \int_V \rho_e \delta_u \varphi dV + \int_{a_D} \sigma^* \delta_u \varphi da - \int_{V^{env}} D_i^{env} \delta_u E_i^{env} dV \\
&- \int_{V^{env}} \left( \frac{1}{2} \right) D_k^{env} E_k^{env} \delta u_{j,j}^{env} dV + \int_{V^{env}} \rho_e^{env} \delta_u \varphi^{env} dV \\
&+ \int_{a_D^{env}} \sigma^{*env} \delta_u \varphi^{env} da + \int_{a^{int}} \sigma^{*int} \delta_u \varphi da \\
&= - \int_V (D_i E_p)_{,i} \delta u_p dV + \int_V (\rho_e - D_{i,i}) \delta_u \varphi dV \\
&- \left( \frac{1}{2} \right) \int_a D_k E_k n_j \delta u_j da + \left( \frac{1}{2} \right) \int_V (D_k E_k)_{,j} \delta u_j dV \\
&+ \int_{a_D} \sigma^* \delta_u \varphi da - \int_{V^{env}} (D_i^{env} E_p^{env})_{,i} \delta u_p^{env} dV \\
&+ \int_{V^{env}} (\rho_e^{env} - D_{i,i}^{env}) \delta_u \varphi^{env} dV \\
&- \left( \frac{1}{2} \right) \int_{V^{env}} D_k^{env} E_k^{env} n_j^{env} \delta u_j^{env} dV \\
&+ \left( \frac{1}{2} \right) \int_{V^{env}} (D_k^{env} E_k^{env})_{,j} \delta u_j^{env} dV \\
&+ \int_{a_D^{env}} \sigma^{*env} \delta_u \varphi^{env} da + \int_{a^{int}} \sigma^{*int} \delta_u \varphi da.
\end{aligned} \tag{B.1}$$

Using (8)–(11), that is,

$$\begin{aligned}
D_i n_i + \sigma^* &= 0, \quad \text{on } a_D, \\
D_{i,i} - \rho_e &= 0, \quad \text{in } V, \\
(D_i - D_i^{env}) n_i &= -\sigma^{*int}, \quad \text{on } a^{int}
\end{aligned} \tag{B.2}$$

and adding terms  $\int_a D_i n_i (E_p \delta u_p + \delta_u \varphi) da = 0$  and  $\int_{a^{env}} D_i^{env} n_i^{env} (E_p^{env} \delta u_p^{env} + \delta_u \varphi^{env}) da = 0$  to (B.1), then (B.1) is reduced to

$$\begin{aligned}
\delta_u \Pi &= - \int_V (D_i E_p)_{,i} \delta u_p dV - \int_V \left( \frac{1}{2} \right) D_k E_k n_j \delta u_j dV \\
&+ \int_V \left( \frac{1}{2} \right) (D_k E_k)_{,j} \delta u_j dV + \int_a D_i E_p n_i \delta u_p da \\
&- \int_{V^{env}} (D_i^{env} E_p^{env})_{,i} \delta u_p^{env} dV \\
&- \int_{V^{env}} \left( \frac{1}{2} \right) D_k^{env} E_k^{env} n_j^{env} \delta u_j^{env} dV \\
&+ \int_{V^{env}} \left( \frac{1}{2} \right) (D_k^{env} E_k^{env})_{,j} \delta u_j^{env} dV \\
&+ \int_{a^{env}} D_i^{env} E_p^{env} n_i^{env} \delta u_p^{env} da \\
&= \int_{a_\sigma} \sigma_{ij}^M n_i \delta u_j da - \int_V \sigma_{ij,i}^M \delta u_j dV \\
&+ \int_{a_\sigma^{env}} \sigma_{ij}^{Menv} n_i^{env} \delta u_j^{env} da - \int_V \sigma_{ij,i}^{Menv} \delta u_j^{env} dV \\
&+ \int_{a^{int}} \sigma_{ij}^M n_i \delta u_j da + \int_{a^{int}} \sigma_{ij,i}^{Menv} \delta u_j^{env} da.
\end{aligned} \tag{B.3}$$

From (19), we know that the work done by the equivalent static electric force is

$$\begin{aligned}
\delta W^e &= \int_V f_k^e \delta u_k dV + \int_{a_\sigma} T_k^e \delta u_k da + \int_{V^{env}} f_k^{eenv} \delta u_k^{env} dV \\
&+ \int_{a_\sigma^{env}} T_k^{eenv} \delta u_k^{env} da + \int_{a^{int}} (T_k^e - T_k^{eenv}) \delta u_k da.
\end{aligned} \tag{B.4}$$

From (B.3) and (B.4), we immediately get (19).

## References

- [1] Y. M. Shkel and D. J. Klingenberg, "Material parameters for electrostriction," *Journal of Applied Physics*, vol. 80, no. 8, pp. 4566–4572, 1996.
- [2] Q. M. Zhang, J. Su, C. H. Kim, R. Ting, and R. Capps, "An experimental investigation of electromechanical responses in a polyurethane elastomer," *Journal of Applied Physics*, vol. 81, no. 6, pp. 2770–2776, 1997.
- [3] F. M. Guillot, J. Jarzynski, and E. Balizer, "Measurement of electrostrictive coefficients of polymer films," *Journal of the Acoustical Society of America*, vol. 110, no. 6, pp. 2980–2990, 2001.
- [4] O. P. Thakur and A. K. Singh, "Electrostriction and electromechanical coupling in elastic dielectrics at nanometric interfaces," *Materials Science- Poland*, vol. 27, no. 3, pp. 839–850, 2009.
- [5] J. A. Stratton, *Electromagnetic Theory*, McGraw-Hill, New York, NY, USA, 1941.
- [6] L. D. Landau and E. M. Lifshitz, *Electrodynamics of Continuum Media*, vol. 8, Pergamon Press, Oxford, UK, 1960.

- [7] Z. B. Kuang, "Some problems in electrostrictive and magnetostrictive materials," *Acta Mechanica Solida Sinica*, vol. 20, no. 3, pp. 219–227, 2007.
- [8] Z. B. Kuang, *Theory of Electroelasticity*, Shanghai Jiaotong University Press, Shanghai, China, 2011.
- [9] Q. Jiang and Z. B. Kuang, "Stress analysis in two dimensional electrostrictive material with an elliptic rigid conductor," *European Journal of Mechanics A*, vol. 23, no. 6, pp. 945–956, 2004.
- [10] Q. Jiang and Z. B. Kuang, "Stress analysis in a cracked infinite electrostrictive plate with local saturation electric fields," *International Journal of Engineering Science*, vol. 44, no. 20, pp. 1583–1600, 2006.
- [11] Y. H. Pao, "Electromagnetic force in deformable continua," in *Mechanics Today*, S. Nemat-Nasser, Ed., Pergamon Press, Oxford, UK, 1978.
- [12] R. M. McMeeking and C. M. Landis, "Electrostatic forces and stored energy for deformable dielectric materials," *Journal of Applied Mechanics*, vol. 72, no. 4, pp. 581–590, 2005.
- [13] Z. B. Kuang, "Some variational principles in elastic dielectric and elastic magnetic materials," *European Journal of Mechanics A*, vol. 27, no. 3, pp. 504–514, 2008.
- [14] Z. B. Kuang, "Some variational principles in electroelastic media under finite deformation," *Science in China, Series G*, vol. 51, no. 9, pp. 1390–1402, 2008.
- [15] Z. B. Kuang, "Internal energy variational principles and governing equations in electroelastic analysis," *International Journal of Solids and Structures*, vol. 46, no. 3-4, pp. 902–911, 2009.
- [16] Z. B. Kuang, "Physical variational principle and thin plate theory in electro-magneto-elastic analysis," *International Journal of Solids and Structures*, vol. 48, no. 2, pp. 317–325, 2011.
- [17] Z. B. Kuang, "Some thermodynamic problems in continuum mechanics," in *Thermodynamics—Kinetics of Dynamic Systems*, J. C. M. Piraján, Ed., InTech Open Access Publisher, Rijeka, Croatia, 2011.

## Research Article

# Active Vibration Control of a Microactuator for the Hard Disk Drive Using Self-Sensing Actuation

Minoru Sasaki,<sup>1</sup> Yoshihiro Inoue,<sup>2</sup> and Hiroyuki Yamada<sup>3</sup>

<sup>1</sup>Department of Human and Information Systems Engineering, Gifu University, 1-1 Yanagido, Gifu 501-1193, Japan

<sup>2</sup>Department of Mechanical and Systems Engineering, Gifu University, 1-1 Yanagido, Gifu 501-1193, Japan

<sup>3</sup>Department of Machines and Metals, Nagoya Municipal Industrial Research Institute, 3-4-41 Rokuban, Atsuta, Nagoya 456-0058, Japan

Correspondence should be addressed to Minoru Sasaki, sasaki@gifu-u.ac.jp

Received 18 November 2011; Accepted 15 January 2012

Academic Editor: Tao Li

Copyright © 2012 Minoru Sasaki et al. This is an open access article distributed under the Creative Commons Attribution License, which permits unrestricted use, distribution, and reproduction in any medium, provided the original work is properly cited.

This paper presents the self-sensing control of a microactuator for hard disk drives. The microactuator uses a PZT actuator pair installed on the suspension assembly. The self-sensing microactuator forms a combined sensing and actuation mechanism. Direct velocity feedback and positive position feedback are used in this paper. Our experimental results show that both strategies are effective in suppressing vibrational modes and successfully demonstrate the feasibility of using a self-sensing actuator on an HDD suspension assembly.

## 1. Introduction

A suspension assembly in a hard disk drive (HDD) is subject to excitation by many disturbances, including the airflow due to the rapidly spinning disks, and noncircular track motion of the head and slider due to resonance in the components. A servo system that can cope with these problems requires a very high servo bandwidth and position error signal sampling frequency. In conventional servo systems, the sampling frequency is limited by data storage efficiency. The desire to more effectively suppress the effect of disturbances has led many researchers to propose the addition of more sensors and actuators. One example which has been proposed is to use a piezoelectric actuator on the suspension in a dual-stage system with one of the two strips as the sensor and the other as the actuator [1, 2]. This, however, reduces the effectiveness of the actuator by half and is not efficient. An alternate approach is to use it as a self-sensing microactuator [3–9], which is the subject of this paper. For dual-stage servo system, the performance of self-sensing actuator systems exceeds that of other vibration compensation systems.

We implemented two active strategies in order to experimentally demonstrate the effectiveness of a self-sensing

system in structural vibration control. The strategies are direct velocity feedback (DVF) and positive position feedback (PPF). DVF, also known as strain rate feedback (SRF) has been used in the active damping of a flexible space structure [10]. In DVF, the structural velocity coordinate is fed back to the compensator and the compensator velocity coordinate multiplied by a negative gain is applied to the structure. DVF has a wide active damping region and can stabilize more than one mode given sufficient bandwidth. In PPF, the structural position coordinate is fed directly to the compensator where a scalar gain is applied and the result sent to the structure [11, 12]. PPF offers quick damping for a particular mode provided the modal characteristics are known. PPF is also easy to implement. Song and Agrawal experimentally demonstrated that it is robust against a varying modal frequency [13]. Pang et al. [14] used the self-sensing technique for active-mode damping in the dual-stage servo system. Chan and Liao [15] used self-tuning adaptive compensation with the self-sensing actuation. We try to demonstrate two active vibration control methods using two types of the sensing signal. This paper is very different from previous publications.

In this paper, we demonstrate the use of these control methods with self-sensing actuators to actively damp

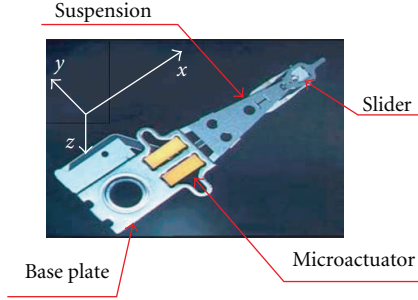


FIGURE 1: Suspension assembly.

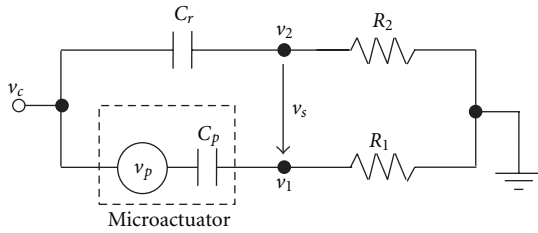


FIGURE 2: CR bridge circuit.

vibrations in an HDD suspension assembly. Experimental results have shown that PPF and DVF control methods are effective in actively increasing damping in an HDD suspension assembly using self-sensing PZT actuators.

## 2. Microactuator for HDD

Figure 1 shows a suspension assembly from a dual-stage HDD servo. A suspension based microactuator uses a PZT actuator pair located between the suspension and the base plate. A slider is installed at the tip of the suspension. When a control voltage is applied to the PZT pair, one of them expands while the other contracts in the  $x$  direction. As a result, the slider moves in the  $y$  direction. The PZT actuator achieves large displacements of the head element by using the length of the suspension as a radius arm. However, the resonance frequency of the suspension limits the servo bandwidth. The configuration of the assembly seems to make it amenable to control using self-sensing actuation. We investigate this in the following sections.

## 3. Self-Sensing Actuation

A piezoelectric self-sensing actuator is a piezoelectric transducer used simultaneously as a sensor and an actuator. The key is capacitance. If the capacitance of a piezoelectric device is known [4], applying the same voltage to a capacitor of the same value and subtracting its electrical response from that of the piezoelectric yields the signal due to the piezoelectric's mechanical response. A bridge circuit using additional resistors and a capacitor is used to obtain the time rate of change of strain (velocity).

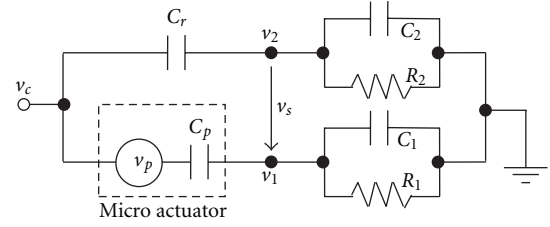


FIGURE 3: CC bridge circuit.

A CR bridge circuit is shown in Figure 2. The difference between the output voltages  $v_1$  and  $v_2$  gives the sensor voltage  $v_s$ . In terms of the Laplace transform, we have

$$V_s(s) = \left\{ \frac{C_p R_1 s}{1 + C_p R_1 s} - \frac{C_r R_2 s}{1 + C_r R_2 s} \right\} V_c(s) + \frac{C_p R_1 s}{1 + C_p R_1 s} V_p(s). \quad (1)$$

If the values of the components are adjusted, so that

$$C_p R_1 = C_r R_2. \quad (2)$$

The first term vanishes, giving us the Laplace transform of the sensor voltage  $V_s$  in terms of the transform of the piezoelectric voltage  $V_p$  as seen in (3):

$$V_s(s) = \frac{C_p R_1 s}{1 + C_p R_1 s} V_p(s). \quad (3)$$

Taking the inverse Laplace transform gives the time domain equation (4):

$$v_s = R_1 C_p \dot{v}_p \quad \left( \text{where } \omega_c \ll \frac{1}{C_p R_1} \right), \quad (4)$$

where the dot indicates the time derivative and  $\omega_c$  is the frequency of the input voltage, and the value of  $C_p$  and  $R_1$  have been chosen to satisfy (4). The charge developed on the sensor can be found from

$$v_s = R_1 C_p k_s \frac{\partial^2 w(l, t)}{\partial x \partial t}. \quad (5)$$

Thus, a distributed piezoelectric sensor with a rate of strain sensing bridge can measure the total angular deflection velocity of the piezoelectric beam at a point  $l$ . The constant  $k_s$  is determined by the size and material of the piezoelectric elements [3–9]. Taking account of the bridge circuit, applied input voltage of the microactuator is

$$V_{\text{piezo}}(s) = V_c(s) - V_1(s) = \frac{1}{1 + C_p R_1 s} V_c(s). \quad (6)$$

The CC bridge circuit corresponding to the self-sensing actuator is shown in Figure 3. An analogous development starts with (7):

$$\begin{aligned} V_s(s) &= V_1(s) - V_2(s) \\ &= \frac{C_p R_1 s}{1 + (C_p + C_1) R_1 s} \{V_c(s) + V_p(s)\} \\ &\quad - \frac{C_r R_2 s}{1 + (C_r + C_2) R_2 s} V_c(s). \end{aligned} \quad (7)$$

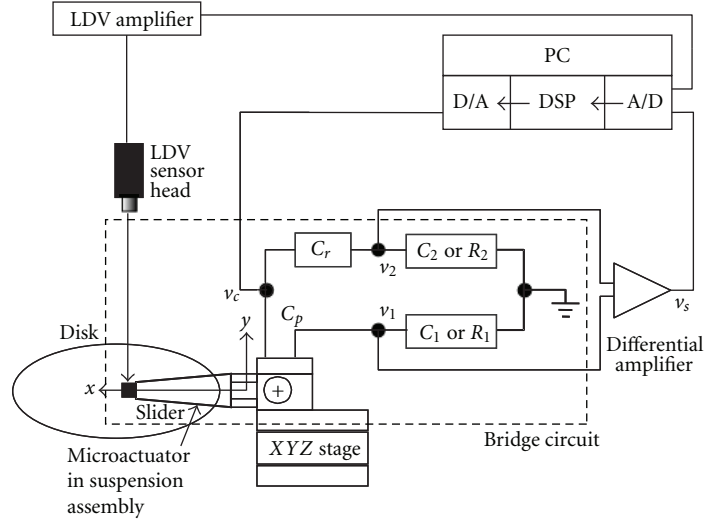


FIGURE 4: Experimental system.

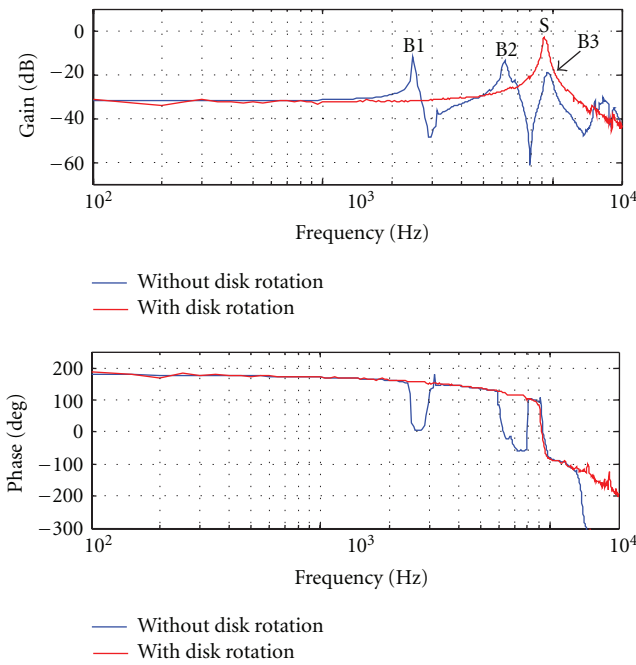


FIGURE 5: Frequency response of the tip displacement.

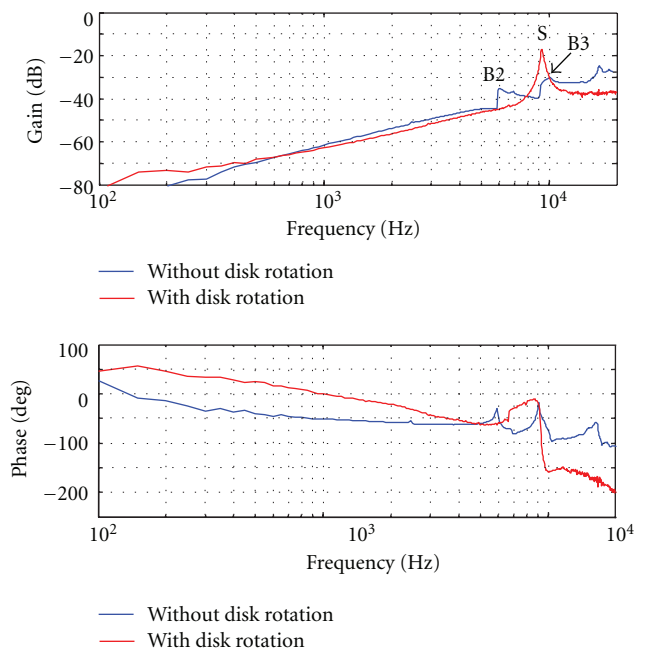


FIGURE 6: Frequency response of the strain rate sensor.

Using the simplifying component values in (8) gives an expression for the Laplace transform of sensor voltage  $V_s$ .

$$\text{If } C_p = C_r, \quad C_1 = C_2, \quad R_1 = R_2, \quad (8)$$

$$V_s(s) = \frac{C_p R_1 s}{1 + (C_p + C_1) R_1 s} V_p(s). \quad (9)$$

Taking the inverse Laplace transform and limiting ourselves to lower frequencies leads to an equation for the input voltage of the actuator (12).

$$v_s = \frac{C_p}{C_p + C_1} v_p \quad (10)$$

when  $\omega_c \geq 1/((C_p + C_1)R_1)$ . The charge developed on the sensor can be found from

$$v_s = \frac{C_p}{C_p + C_1} k_s \frac{\partial w(l, t)}{\partial x}. \quad (11)$$

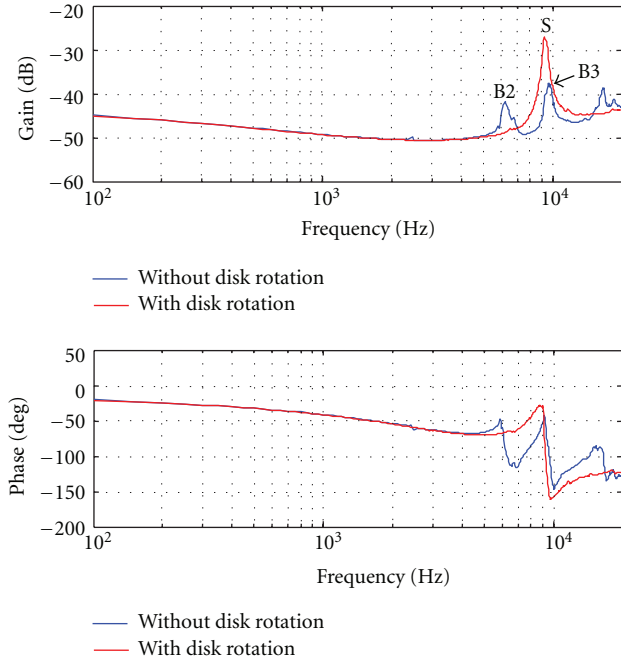


FIGURE 7: Frequency response of the strain sensor signal.

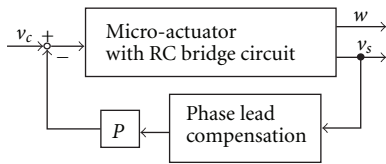


FIGURE 8: Block diagram of the direct velocity feedback control.

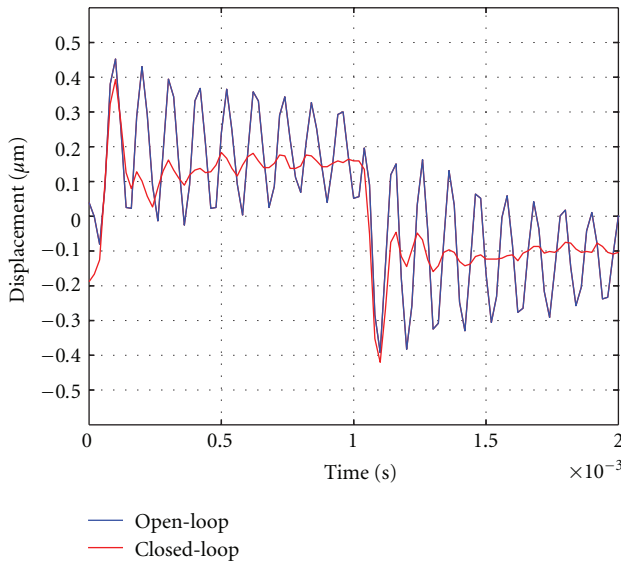


FIGURE 9: Time response of the tip displacement with DVE.

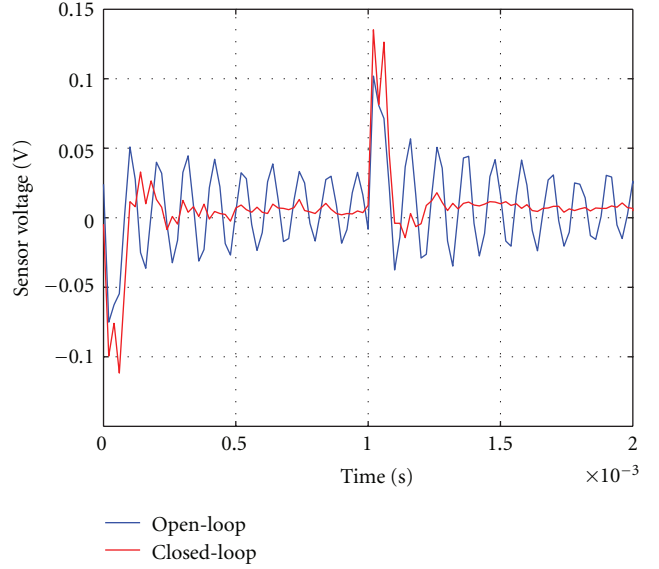


FIGURE 10: Time response of the sensor voltage with DVE.

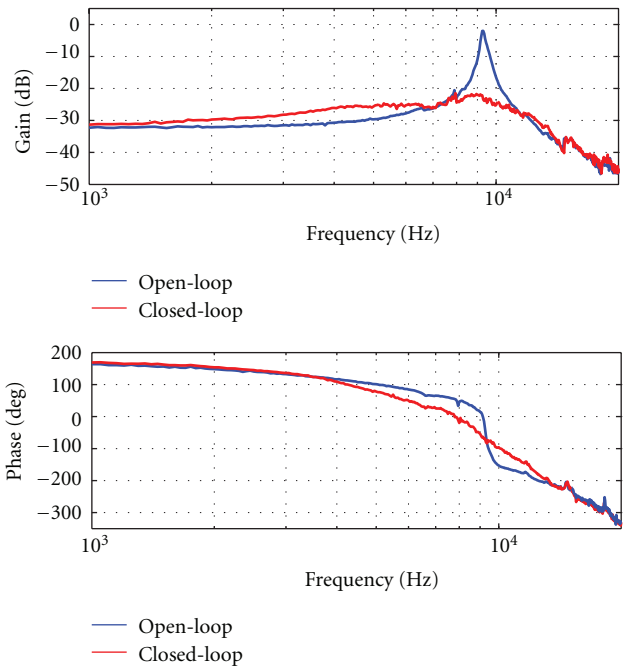


FIGURE 11: Frequency response of the tip displacement with DVE.

Thus a distributed piezoelectric sensor with a strain sensing bridge can measure the total angular deflection of the piezoelectric beam at a point  $l$  [3–9]. Taking account of the bridge circuit, applied input voltage of the microactuator is

$$v_{\text{piezo}} = v_c - v_1 = \frac{C_1}{C_p + C_1} v_c. \quad (12)$$

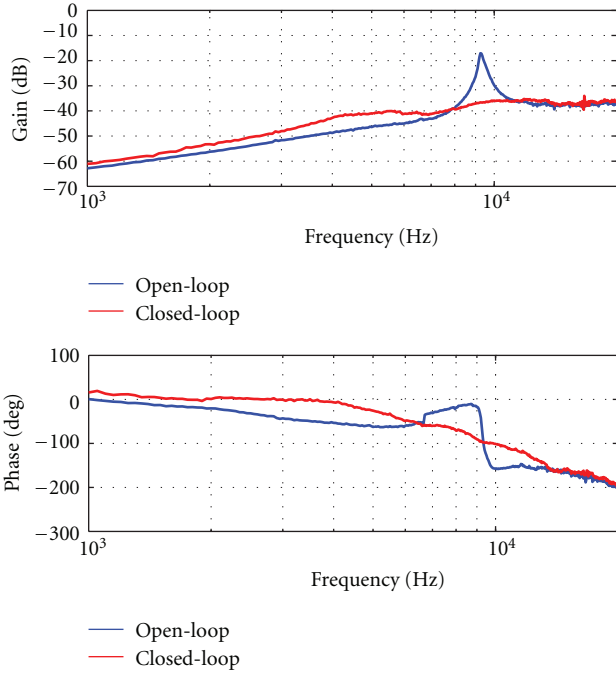


FIGURE 12: Frequency response of the strain rate sensor output voltage with DVF.

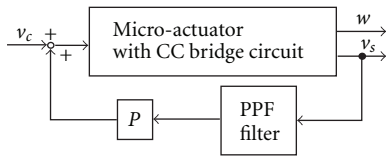


FIGURE 13: Block diagram of the PPF control.

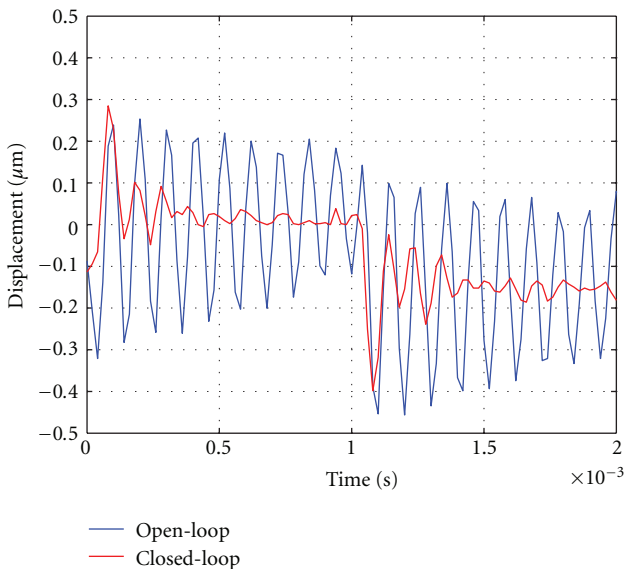


FIGURE 14: Time response of the tip displacement with the PPF control.

### 4. Experimental Setup

Figure 4 shows the setup for our experiments. The experiments were carried out on a spin test stand. An input control voltage is calculated by a DSP every 0.01 millisecond and applied to the bridge circuit through a D/A converter and a piezo driver. Sensor voltage  $v_s$  from the bridge circuit is passed through a differential amplifier and A/D converter to the input of the DSP. For monitoring purpose only, a laser doppler vibrometer (LDV) was used to obtain measurements of tip displacement and velocity.

Figure 5 shows the measured frequency response of the slider tip displacement to an applied control voltage with and without the spinning disk. Figure 6 shows the frequency response of the strain rate sensor. Figure 7 shows the frequency response of strain sensor. In these figures, the red line indicates the response with the spinning disk while the blue line is without the spinning disk. There are four major vibration modes of the suspension assembly while on the spinning disk. There are three suspension bending modes: B1 at 2.7 kHz; B2 at 5.4 kHz, B3 at 9.8 kHz. The fourth major mode is a sway mode: S at 9.2 kHz. The suspension bending modes are vibrations in the vertical direction. The sway mode is the PZT microactuator actuation mode and is a vibration in the horizontal direction. With the disk rotating, the third suspension mode (B3) combines with the sway mode (S). When the experiment is done with a rotating magnetic disk, the suspension modes disappear and the sway mode appears alone as shown in Figure 5.

Corresponding results are shown in Figures 6 and 7, where on the spinning disk, only the sway mode is observed. In these figures, the signals are similar to a velocity signal and a position signal.

### 5. Direct Velocity Feedback Control

Estimating the modal states of a distributed structure in order to apply modal feedback control is difficult. The problem of observation spillover is potentially more serious than the problem of control spillover as it can lead to instability. Hence, a method not requiring modal state estimation is desired. One such method is direct output feedback control where the sensors are collocated with the actuators and a given actuator force is a function of the sensor output at the same point. The self-sensing piezo actuator is a perfect candidate for this control method. DVF is a form of this control method and it stabilizes all vibrational modes.

Figure 8 shows a block diagram of the DVF control system. The microactuator, controlled with collocated velocity feedback giving the strain rate, is unconditionally stable at all frequencies [4]. With the feedback gain at  $P = -60$ , the transfer function for the phase lead compensator is

$$G_c(s) = \frac{s + 809.1}{s + 1.057 \times 10^5}. \tag{13}$$

We implemented real-time DVF on the suspension assembly. Figure 8 shows the actuator input voltage. The input voltage of the actuator is rectangular wave at 5 V in 500 Hz. The DVF controlled time response is compared to

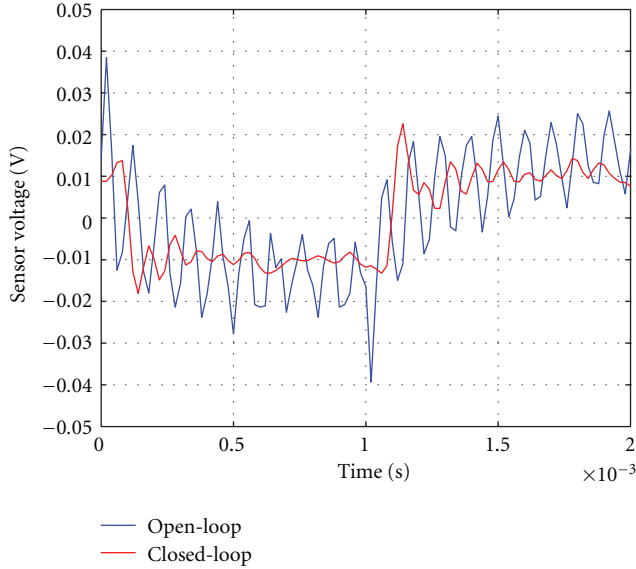


FIGURE 15: Time response of the sensor voltage with the PPF control.

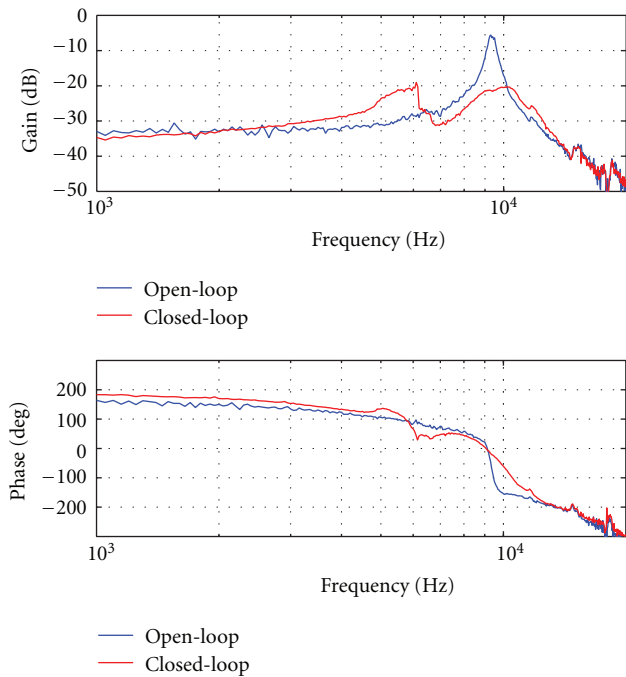


FIGURE 16: Frequency response of the tip displacement with the PPF control.

the vibrations of the uncontrolled system (Figure 9). Under control, suspension assembly vibrations taper off within 0.2 milli seconds of the input signal becoming constant. This is shown in Figure 10. A 20 dB drop in the energy of the sway mode accompanied the damping of the vibrations, as shown in Figures 11 and 12.

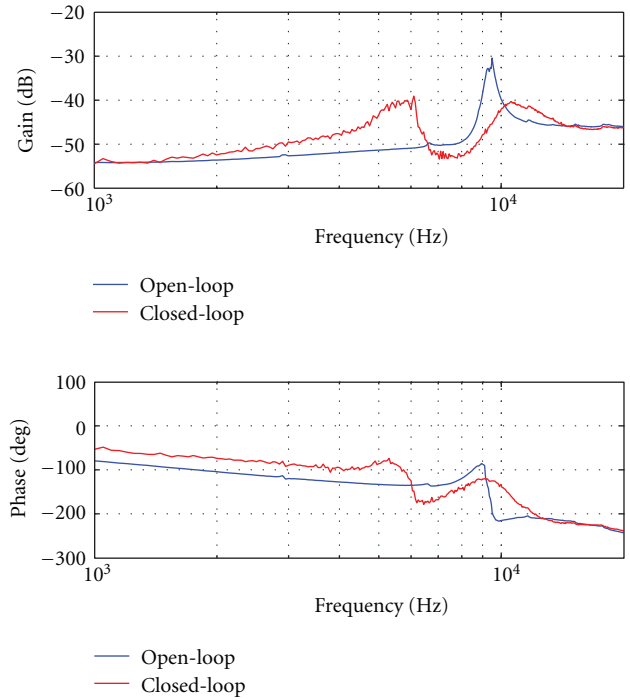


FIGURE 17: Frequency response of the strain sensor output voltage with the PPF control.

## 6. Positive Position Feedback Control

Positive position feedback (PPF) control was first proposed by Goh and Caughey for collocated sensors and actuators. Fanson and Caughey later demonstrated PPF control in space structures. PPF control is done by feeding the structural coordinate directly to compensator where a positive gain is applied before the signal is sent back to the structure. PPF offers quick damping of a particular mode provided the modal characteristics are known. The scalar equation governing a single mode of the vibration of a structure and the PPF controller is

$$\text{PPF filter} = \frac{\omega_f^2}{s^2 + 2\zeta_f \omega_f s + \omega_f^2}, \quad (14)$$

where the natural frequency and the damping ratio of the compensator are  $\omega_f = 7.3$  [kHz],  $\zeta_f = 0.2$ , respectively. The frequency  $\omega_f = 7.3$  [kHz] is slightly lower than the target frequency [12]. A block diagram of the PPF control system appears in Figure 13. It was implemented using the same experiment setup described in Section 4. The mode targeted for control was the sway mode (S) at 9.2 kHz. The control was done in real time with a sampling period of 0.01 milliseconds. Figure 14 shows the uncontrolled and controlled vibrations of the suspension assembly for comparison. Under PPF control, the vibrations damp out within 0.3 milliseconds of the input signal becoming constant. The sensor output from 0 to 2 milliseconds is shown in Figure 15. Under active control, the energy of vibrations drops by 15 dB. PPF control damps down vibrations slightly faster than DVF control.

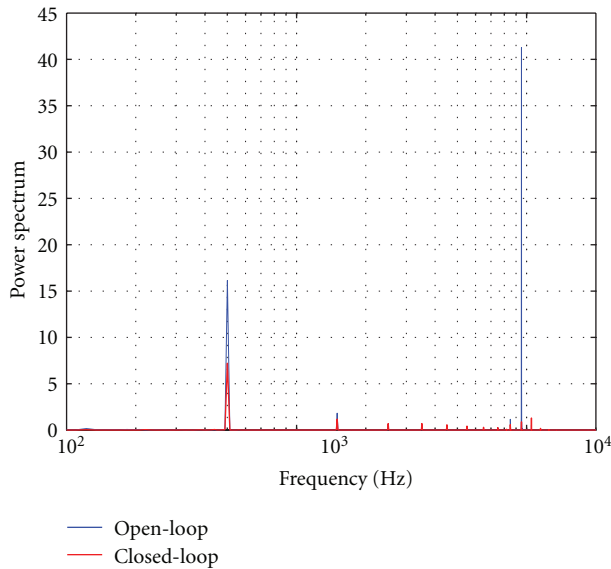


FIGURE 18: Power spectral density comparison of PPF control and without control cases.

With PPF control, maximum damping is achieved when the controller is tuned to the natural frequency of the structure (Figures 16 and 17). As a counterexample, under PPF, the frequency response of tip displacement at 6 kHz increases by 10 dB. However, the power spectrum density comparison in Figure 18 shows no peak at 6 kHz, implying that PPF control does not affect vibrations at that frequency.

## 7. Conclusions

Our experiments successfully demonstrate vibration suppression of a hard drive suspension assembly using signals from a self-sensing actuator by Direct Velocity Feedback (DVF) control and Positive Position Feedback (PPF) control. The self-sensing actuator is a piezoelectric transducer acting simultaneously as sensor and actuator mounted on the suspension itself. The sensor generates an estimate of the strain signal and its derivative. In particular, the DVF method was able to attenuate the suspension assembly's dominant sway mode of vibration by 20 dB. Both DVF and PPF were successful at damping suspension assembly vibrations. Both strategies are good enough for use in real hard disk drives.

## References

- [1] Y. Li, R. Horowitz, and R. Evans, "Vibration control of a PZT actuated suspension dual-stage servo system using a PZT sensor," *IEEE Transactions on Magnetics*, vol. 39, no. 2, pp. 932–937, 2003.
- [2] Y. Li, F. Marcassa, R. Horowitz, R. Oboe, and R. Evans, "Track-following control with active vibration damping of a PZT-actuated suspension dual-stage servo system," in *Proceedings of the American Control Conference*, vol. 3, pp. 2553–2559, Denver, Colo, USA, 2003.
- [3] H. Yamada, M. Sasaki, and Y. Nam, "Control of a micro-actuator for hard disk drives using self-sensing actuator," *International Journal of Applied Electromagnetics and Mechanics*, vol. 24, no. 3-4, pp. 247–259, 2006.
- [4] J. J. Dosch, D. J. Inman, and E. Garcia, "Self-sensing piezoelectric actuator for collocated control," *Journal of Intelligent Material Systems and Structures*, vol. 3, no. 1, pp. 166–185, 1992.
- [5] Y. Nam and M. Sasaki, "Strain rate self-sensing for a cantilevered piezoelectric beam," *KSME International Journal*, vol. 16, no. 3, pp. 310–319, 2002.
- [6] M. Okugawa and M. Sasaki, "System identification and controller design of a self-sensing piezoelectric cantilever structure," *Journal of Intelligent Material Systems and Structures*, vol. 13, no. 4, pp. 241–252, 2002.
- [7] Y. Nam, J. Yoon, and M. Sasaki, "End point motion estimation of a cantilevered piezoelectric beam," *JSME International Journal Series C*, vol. 45, no. 3, pp. 722–729, 2002.
- [8] H. Yamada, M. Sasaki, and Y. Nam, "Active vibration control of a micro-actuator for hard disk drives using self-sensing actuator," *Journal of Intelligent Material Systems and Structures*, vol. 19, no. 1, pp. 113–123, 2008.
- [9] M. Sasaki, K. Fujihara, Y. Nam, S. Ito, and Y. Inoue, "Two-degree-of-freedom control of a self-sensing micro-actuator for HDD," *International Journal of Applied Electromagnetics and Mechanics*, vol. 36, no. 1-2, pp. 159–166, 2011.
- [10] M. J. Balas, "Direct velocity feedback control of large space structure," *Journal of Guidance, Control, and Dynamics*, vol. 2, no. 3, pp. 252–253, 1979.
- [11] C. J. Goh and T. K. Caughey, "On the stability problem caused by finite actuator dynamics in the collocated control of large space structure," *International Journal of Control*, vol. 41, no. 3, pp. 787–802, 1985.
- [12] J. L. Fanson and T. K. Caughey, "Positive position feedback control for large space structures," *American Institute of Aeronautics and Astronautics Journal*, vol. 28, no. 4, pp. 717–724, 1990.
- [13] G. Song and B. N. Agrawal, "Vibration suppression of flexible spacecraft during attitude control," *Acta Astronautica*, vol. 49, no. 2, pp. 73–83, 2001.
- [14] C. K. Pang, G. Guo, B. M. Chen, and T. H. Lee, "Self-sensing actuation for nanopositioning and active-mode damping in dual-stage HDDs," *IEEE/ASME Transactions on Mechatronics*, vol. 11, no. 3, pp. 328–338, 2006.
- [15] K. W. Chan and W. H. Liao, "Self-sensing actuators for adaptive vibration control of hard disk drives," in *Proceedings of the IEEE/ASME International Conference on Advanced Intelligent Mechatronics (AIM '08)*, pp. 665–670, August 2008.

## Research Article

# Comparison of Analog and Digital Self-Powered Systems in Multimodal Vibration Suppression

Shigeru Shimose,<sup>1</sup> Kanjuro Makihara,<sup>2</sup> and Junjiro Onoda<sup>1</sup>

<sup>1</sup>*Institute of Space and Astronautical Science (ISAS), Japan Aerospace Exploration Agency (JAXA), 3-1-1 Yoshinodai, Chuo-Ward, Sagami-hara, Kanagawa 252-5210, Japan*

<sup>2</sup>*Department of Aerospace Engineering, Tohoku University, 6-6-01 Aoba, Aramaki, Aoba-Ward, Sendai 980-8579, Japan*

Correspondence should be addressed to Shigeru Shimose, shimose.shigeru@jaxa.jp

Received 14 December 2011; Accepted 15 January 2012

Academic Editor: Ma Jan

Copyright © 2012 Shigeru Shimose et al. This is an open access article distributed under the Creative Commons Attribution License, which permits unrestricted use, distribution, and reproduction in any medium, provided the original work is properly cited.

This paper compares our analog and digital self-powered systems for vibration suppression, and shows experimental results of multimodal vibration suppression for both self-powered systems. The experimental results are evaluated in light of the damping performance and adaptability under various vibrational conditions. We demonstrate various examples of our innovative vibration suppression method, called “digital self-powered.” Proper status switching of an electric circuit made up of an inductor and a selective switch connected to a piezoelectric transducer attenuates the vibrations. The control logic calculation and the switching events are performed with a digital microprocessor that is driven by the electrical energy converted from the mechanical vibration energy. Therefore, this vibration suppression system runs without any external power supply. The self-powering feature makes this suppression method useful in various applications. To realize an ideal vibration suppression system that is both self-powered and effective in suppressing multimode vibration, sophisticated control logic is implemented in the digital microprocessor. We demonstrate that our digital self-powered system can reduce the vibrational displacements of a randomly excited multimodal structure, by as much as 35.5%.

## 1. Introduction

Vibration control methods are roughly categorized into two groups, that is, active and passive methods [1–4]. Active vibration control methods usually yield high-performance vibration suppression [1, 2]. However, active control systems may become unstable if the control is improperly designed. In addition, active vibration control systems need an external energy supply to suppress vibrations. On the other hand, passive vibration control methods use energy dissipative mechanisms such as dampers, frictional devices, and electric resistors [3, 4]. Because passive approaches do not need an energy supply they are always stable. Passive methods are easier to implement in actual systems than are the more complicated active methods, because they do not need controllers, sensors, or filters. However, in most cases, passive systems do not provide a satisfactory vibration suppression performance. In general, the majority of passive systems suppress vibrations well only in expected situations such as

those regarding natural frequency and temperature. Typical examples of less robustness of frequency alternation are mechanically tuned mass dampers and electrical dynamic vibration absorbers. There are research papers that compare the performance of semiactive and passive systems [5, 6].

We found a new approach to resolve the dilemma between active and passive vibration controls in terms of robustness and suppression performance. The semiactive method is one of the practical answers both to reduce the disadvantages of active systems and to maintain the advantages of passive systems. Many studies of semiactive vibration control methods have been published, and they often use piezoelectric transducers for vibration suppression [7–14]. Some researchers have studied a semiactive approach to suppress vibration by using piezoelectric transducers with switchable circuits [10–14]. Richard et al. [10], Corr and Clark [11], and Onoda et al. [12] proposed the use of an inductive circuit. Depending on the circuit components and

the switching strategies, this approach is called SSDI, LR-switching, RL-shunt, and others. By shunting the transducer in short time, the counter electromotive force that is generated by the inductor and the restored electric charge due to the piezoelectric effect can invert the polarity of the charge stored in it. Accordingly, the stored electrical energy in the transducer is recycled rather than immediately dissipated, and is often called an energy-recycling semiactive method [12]. The energy-recycling semiactive vibration control does not require any external power supply to suppress vibration. The systems without the need for external energy are quite useful for various applications [13, 14] in energy shortage systems and those that require energy saving, such as large space structures, artificial satellites, and isolated lunar bases, all of which are vulnerable to facing long periods without sunlight.

So far, we have developed two types of self-powered vibration controllers: analog [15] and digital [16]. Both types of the controllers do not require external energy. In this paper, we compare our analog [15] and digital self-powered [16] systems for multimodal vibration suppression from the viewpoints of damping performance and adaptability to various vibrational conditions.

## 2. Problem Statements and Research Objectives

The energy-recycling semiactive vibration control does not require any external energy to suppress vibrations. However, switches, switching controllers, and other electric devices contained in the energy-recycling semiactive vibration control devices consume electrical energy. To avoid external power supply, we did not make use of the above devices in the vibration suppression system. Thus, an analog self-powered system using the semiactive technique [15, 17, 18] has been proposed. The ‘‘analog self-powered’’ system is the simplest type among self-powered vibration controllers. This system requires neither an external power supply nor an external control authority. However, analog circuit systems are very awkward in practice and not at all programmable. If the parameters need changing due to system alternations, analog systems cannot deal with such requests. Therefore, to solve the awkwardness and inflexibility issues associated with analog self-powered systems, we investigated ‘‘digital self-powered’’ systems for sophisticated vibration control. Single degree of freedom (SDOF) structural vibration suppression experiments using our ‘‘digital self-powered’’ system indicated that the vibration magnitude dramatically reduced by as much as 79.7% [16]. Moreover, we have attempted to apply our ‘‘digital self-powered’’ system to multimodal structural vibration suppression.

Here, we revealed the experimental performance effectiveness of our proposed analog and digital self-powered systems for multimodal structural vibration suppression control. First, we describe the energy-recycling, semiactive mechanism (switching method for semiactive vibration suppression and the equations of motion for a multimodal structure). Next, an explanation of our self-powered systems is presented. Finally, experimental results are demonstrated in

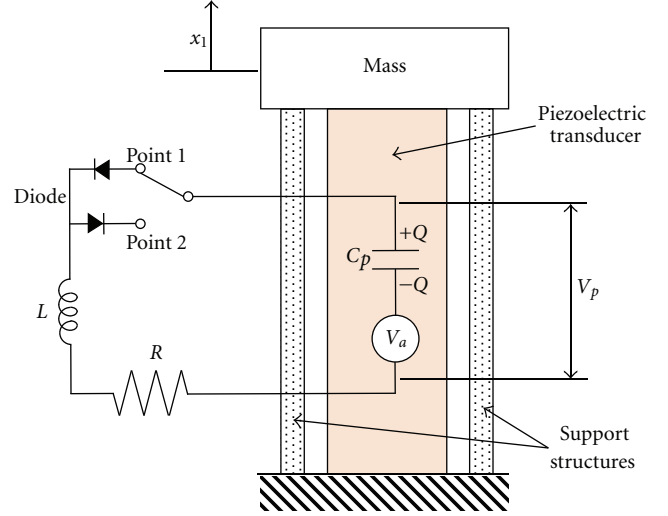


FIGURE 1: SDOF system with switching circuit for energy-recycling.

terms of damping performance under multimodal vibration excitation.

## 3. Theoretical Analysis

**3.1. Switching Method for Semiactive Vibration Suppression.** This section shows the basic idea of the energy-recycling semiactive mechanism that has been reported in [10–12]. However, for a better understanding, a brief explanation is presented using the simple SDOF system shown in Figure 1. The system is composed of a mass, support structures, a piezoelectric transducer, and a switchable inductive circuit. The linear characteristic of the piezoelectric transducer [19] is written as

$$f_p = k_p x_1 - b_p Q, \quad (1)$$

$$V_p = -b_p x_1 + \frac{Q}{C_p}, \quad (2)$$

where  $f_p$  is the applied force,  $x_1$  is the elongation of the piezoelectric transducer,  $Q$  is the electric charge stored in the transducer,  $V_p$  is the piezoelectric voltage across two electric terminals,  $C_p$  is the constant-elongation piezoelectric capacitance, and  $b_p$  is the piezoelectric constant. The piezoelectric transducer is modeled with a voltage generator  $V_a$  and a capacitor  $C_p$ . Here, let us assume that the SDOF system with natural frequency  $\omega$  is vibrating as

$$x_1 = A \sin(\omega t). \quad (3)$$

Active controls can freely change the value of  $Q$  for vibration control. The optimal control charge (defined as  $Q_T$ ) is derived from active control schemes. For instance, the direct velocity feedback control [20] stipulates the control input as

$$Q_T = -F \frac{dx_1}{dt}, \quad (4)$$

where  $F$  is the feedback gain.

In contrast to the abovementioned active controls, our switching system (Figure 1) has only a selective switch to change its electrical state. This is the semiactive method that does not have an external power source and cannot change the value of  $Q$  as expected. Our switching logic is that the selective switch is connected to point 1 or 2 to make the polarity of  $Q$  the same as that of  $Q_T$ . The switching logic [12] is written as follows

$$\begin{aligned} &\text{when } Q_T < 0, \text{ change the switch into point 1,} \\ &\text{when } Q_T \geq 0, \text{ change the switch into point 2.} \end{aligned} \quad (5)$$

We assume that  $Q$  is zero at  $t = 0$ . Equations (1) and (2) indicate that  $V_p$  is negative when  $x_1$  is positive and  $Q$  is zero. While the switch is positioned at point 1, the diode at point 1 prevents the electric current from flowing in the circuit. Consequently  $x_1$  and  $Q$  are zero, and  $V_p$  is  $-b_p A$  just before turning the switch at  $t = \pi/(2\omega)$ . After the switch is connected to point 2 at  $t = \pi/(2\omega)$ , the electric current flows in the inductive circuit. The governing equation of the electric circuit while the current flows is expressed as

$$L\ddot{Q} + R\dot{Q} + \frac{Q}{C_p} = b_p x_1, \quad (6)$$

where  $\omega\sqrt{LC_p} \ll 1$  according to study [12]. We also assume that the electric current stops flowing in a much shorter time than the period of the mechanical vibration. Thus,  $x_1$  can be thought to remain equal to  $A$  during current flow. The values of  $Q$  and  $V_p$  just after the current stops flowing are

$$\begin{aligned} Q &= C_p b_p A (1 + e^{-\zeta\pi}), \quad V_p = b_p A e^{-\zeta\pi}, \\ \zeta &\equiv \frac{R}{2} \sqrt{\frac{C_p}{L}}. \end{aligned} \quad (7)$$

$x_1$  and  $V_p$  and  $Q$  remain constant, because the diodes prevent the current from flowing. At  $t = (3\pi)/(2\omega)$ ,  $x_1$  changes to  $-A$  and  $V_p$  becomes

$$V_p = b_p A e^{-\zeta\pi} + 2b_p A. \quad (8)$$

At this moment, the switch is turned to point 1 according to the control logic (5), and the current starts to flow. After the current flow stops due to the diode at point 1,  $Q$  and  $V_p$  are

$$\begin{aligned} Q &= -C_p b_p A (1 + 2e^{-\zeta\pi} + e^{-2\zeta\pi}), \\ V_p &= -b_p A (2e^{-\zeta\pi} + e^{-2\zeta\pi}). \end{aligned} \quad (9)$$

After many repetitions of switching, the values of  $Q$  and peak voltage converge to

$$\begin{aligned} |Q| &= C_p b_p A \frac{1+\gamma}{1-\gamma}, \quad |V_{\text{Peak}}| = b_p A \left( \frac{1+\gamma}{1-\gamma} + 1 \right), \\ \gamma &\equiv e^{-\zeta\pi}. \end{aligned} \quad (10)$$

Similarly, the dissipated energy  $E_D$  for one cycle is

$$E_D = 4C_p b_p^2 A^2 \frac{1+\gamma}{1-\gamma}. \quad (11)$$

The parameter  $\gamma$  is in direct correlation to the dissipated energy and is called the voltage inversion coefficient. It is defined in [13] as the ratio of voltages after and before the voltage inversion.

#### 4. Equation of Motion of the Multimodal Structure and Controller

For deriving the generalized equations, let us consider an  $l$ -DOF structure with piezoelectric transducers. The equation of motion for the structure with piezoelectric transducers [12] can be written as

$$\mathbf{M}\ddot{\mathbf{u}} + \mathbf{D}\dot{\mathbf{u}} + \mathbf{K}\mathbf{u} = \mathbf{B}_p \vec{Q} + \vec{w}. \quad (12)$$

To express (2) in vector-matrix form, we transform the scalar equation to

$$\vec{V}_p = -\mathbf{B}_p^T \vec{u} + C_p^{-1} \vec{Q}. \quad (13)$$

In modal coordinates, the equation of motion is expressed as

$$\ddot{\xi} + \Xi \dot{\xi} + \Omega \xi = \Phi^T \mathbf{B}_p \vec{Q} + \Phi^T \vec{w}, \quad (14)$$

and the voltage equation is written as

$$\vec{V}_p = -\mathbf{B}_p^T \Phi \vec{\xi} + C_p^{-1} \vec{Q}, \quad (15)$$

where

$$\Phi \equiv [\phi_1, \phi_2, \dots, \phi_l], \quad \Omega \equiv \text{diagonal}[\omega_k^2], \quad (16)$$

$$\Xi \equiv \text{diagonal}[2\zeta\omega_k], \quad (1 \leq k \leq l). \quad (17)$$

Then, (14) and (15) can be transformed into

$$\dot{\vec{z}} = \mathbf{A}\vec{z} + \mathbf{B}\vec{Q} + \mathbf{E}\vec{w}, \quad (18)$$

$$\vec{V}_p = \mathbf{C}\vec{z} + \mathbf{D}\vec{Q}, \quad (19)$$

where

$$\begin{aligned} \vec{z} &\equiv \begin{bmatrix} \vec{\xi}^T, \vec{\xi}^T \end{bmatrix}^T, \quad \mathbf{A} \equiv \begin{bmatrix} 0 & \mathbf{I} \\ -\Omega & -\Xi \end{bmatrix}, \quad \mathbf{B} \equiv \begin{bmatrix} 0 \\ \Phi^T \mathbf{B}_p \end{bmatrix}, \\ \mathbf{C} &\equiv \begin{bmatrix} -\mathbf{B}_p^T & \Phi & 0 \end{bmatrix}, \quad \mathbf{D} \equiv C_p^{-1}, \quad \mathbf{E} \equiv \begin{bmatrix} 0 \\ \Phi^T \end{bmatrix}. \end{aligned} \quad (20)$$

If  $\vec{Q}$  in (18) is regarded as an active control input, the linear quadratic regulator (LQR) control theory [21] specifies that the performance index

$$J \equiv \int_0^\infty (\vec{z}^T \mathbf{W}_1 \vec{z} + \vec{Q}^T \mathbf{W}_2 \vec{Q}) dt \quad (21)$$

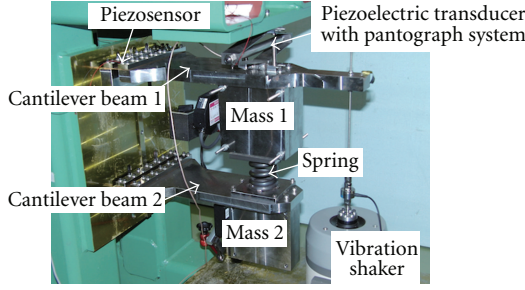


FIGURE 2: Photo of mechanical part in 2-DOF system.

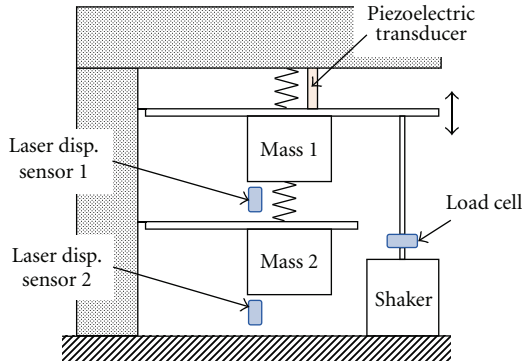


FIGURE 3: Schematic of mechanical configuration of 2-DOF system.

is minimized by

$$\vec{Q} = \vec{Q}_T \equiv -\mathbf{F}\vec{z}, \quad (22)$$

where

$$\mathbf{F} \equiv \mathbf{W}_2^{-1}\mathbf{B}^T\mathbf{P}_1. \quad (23)$$

Here,  $\mathbf{W}_1$  and  $\mathbf{W}_2$  are weighting matrices, and  $\mathbf{P}_1$  is a positive solution of

$$\mathbf{P}_1\mathbf{B}\mathbf{W}_2^{-1}\mathbf{B}^T\mathbf{P}_1 - \mathbf{A}^T\mathbf{P}_1 - \mathbf{P}_1\mathbf{A} - \mathbf{W}_1 = 0. \quad (24)$$

The vector  $\vec{Q}_T$  is an evolved form of the simple scalar in (4). While  $\vec{Q}_T$  can handle multiple transducer systems, the simple scalar form  $Q_T$  can handle only single-transducer system.

## 5. Experimental Configuration

**5.1. Mechanical Experimental System.** A view of the mechanical experiment system is shown in Figures 2 and 3. The mechanical experimental system consists of two masses, a pantograph-type displacement-magnification mechanism, a piezoelectric transducer (PSt 1000/10/200-VS18, Piezomechanik GmbH), piezoelectric sensors, two cantilevered beams, a vibration shaker, and an experimental platform. The displacement-magnification mechanism, attached to the upper beam and upper side of the platform, is used to amplify the displacement.

Figure 4 shows the electrical circuits of the self-powered system. The piezoelectric transducer is connected to the analog self-powered electrical device or the digital self-powered electric device. One piezoelectric sensor is attached to the base of the upper beam. Additional measuring instruments (a laser displacement sensor and load cell) are arranged around the system. These measuring instruments are used only for recording and not for the semiactive feedback control. For the purpose of effective analysis, an equivalent two-DOF spring-mass model is constructed for the experimental system. The natural frequencies of the first and second modes at constant electric charge are 20.3 and 36.6 Hz, respectively. A detailed description of the experimental setup is given in our previous paper [16].

**5.2. Electric Experimental System.** The electrical circuit of the proposed analog self-powered system is shown in Figure 5. This circuit is designed with one energy-recycling section and two peak detection sections. The energy-recycling section has a piezoelectric transducer, inductors, and thyristors. The thyristors work as both a switch and a diode. The peak detection section finds the peak voltage of the piezoelectric transducer.

When the voltage across the piezoelectric transducer  $V_p$  reaches the maximum and starts to decrease, the programmable unijunction transistor PUT1 is automatically turned on, and the charge stored in capacitor C1 flows through the thyristor SCR1 as its gate current. As a result, the thyristor is turned on, and the charge stored in the capacitor of the piezoelectric transducer  $C_p$  flows through the inductor. Because the thyristor prevents the electric current from flowing in the opposite direction, this turning on of the thyristor is equivalent to turning the switch in Figure 1 to point 1. Conversely, when the value of  $V_p$  reaches the minimum and starts to increase, PUT2 is turned on, and subsequently, SCR2 is turned on. This action is equivalent to turning the switch in Figure 1 to point 2. As a result, this analog circuit turns the switch in Figure 1 to point 1 when  $V_p$  is approximately the maximum, and turns the switch to point 2 when  $V_p$  is approximately the minimum. This is equivalent to the switching logic proposed and studied by Richard et al. [10]. This is the simplest design of a self-powered vibration suppression system. However, it is not practical to realize the switching logic for handling a multiple input multiple output (MIMO) system.

Figure 6 shows a diagram of the energy flow and control stream of our digital self-powered system. The energy-harvesting section, comprising four connected diodes, can supply the harvested energy to the digital processor. The energy harvester, with a storage capacitor  $C_S$ , is connected to the piezoelectric transducer to collect vibration energy. The circuit harvests electrical energy in a piezoelectric transducer attached to the vibrating structure, and it supplies energy to the energy harvester and sends the collected energy to the microprocessor. The piezoelectric sensor is attached to the structure and outputs a voltage that is proportional to the upper mass's displacement. It is connected to the analog/digital (A/D) port of the digital processor. All the necessary functions for switching control are built into the

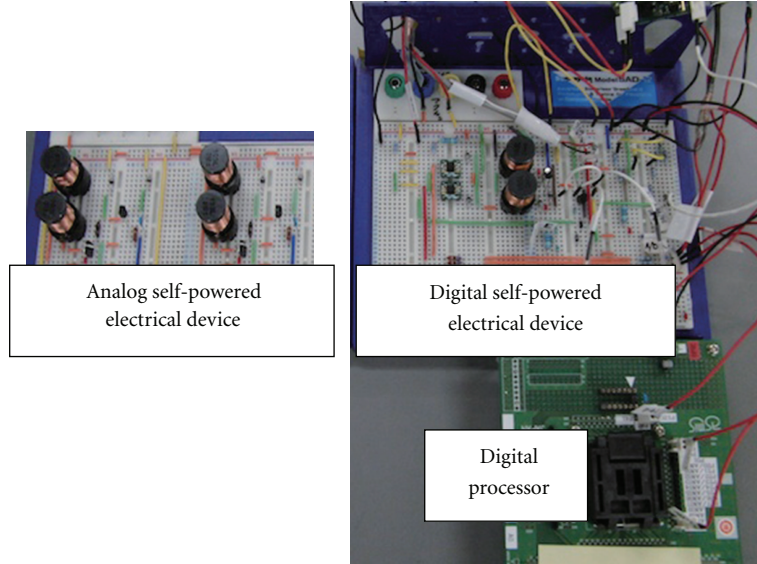


FIGURE 4: Photograph of electrical device in self-powered system.

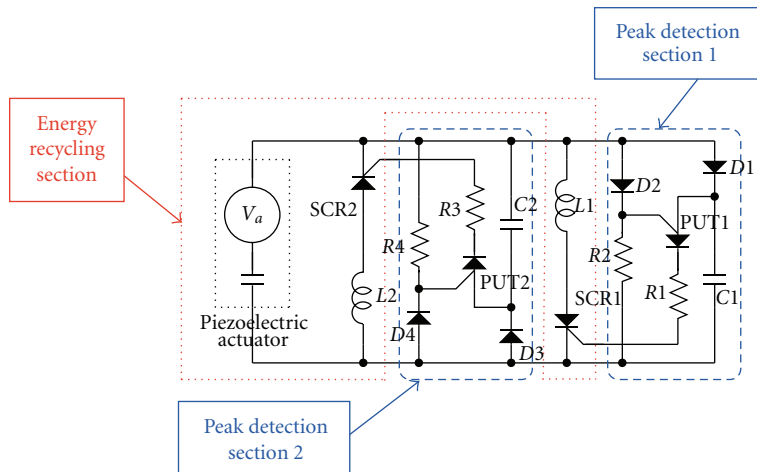


FIGURE 5: Analog self-powered control switching circuit.

digital processor. First, the digital processor activates using the power supplied energy-harvesting section. Second, it collects data pertaining to the structural vibrations from the piezoelectric sensor. Third, it calculates the modal estimation using the Kalman filter. Fourth, it calculates the switching criteria. Fifth, it activates the switch to inverse the voltage polarity of the piezoelectric transducer when the switching criteria polarity shifts. Finally, it monitors the transducer with the shifted voltage polarity that works a transducer to suppress structural vibrations. All of these steps are carried out at 0.5-millisecond intervals.

## 6. Experimental Results

This paper describes three types of vibration suppression experiments using our self-powered systems. Both self-powered systems presented in this paper utilize the same ontroller

and observer designs described in our previous papers [15, 16].

6.1. *Multimodal Sinusoidal Excitation.* In this section, we carried out multimodal sinusoidal vibration suppression experiments using our analog and digital self-powered systems. A function generator creates an input voltage wave and sends it to the vibration shaker. The input wave for the vibration excitation is

$$\alpha \sin(\omega_1 t) + \frac{11}{7} (1 - \alpha) \sin(\omega_2 t), \quad (25)$$

where  $\omega_1$  and  $\omega_2$  are the angular frequencies of the first and second modes, respectively.  $\alpha$  is the modal combination parameter. The excitation with  $\alpha = 1$  means the sinusoidal excitation with frequency  $\omega_1$  of the first mode, and the excitation with  $\alpha = 0$  means the sinusoidal excitation with

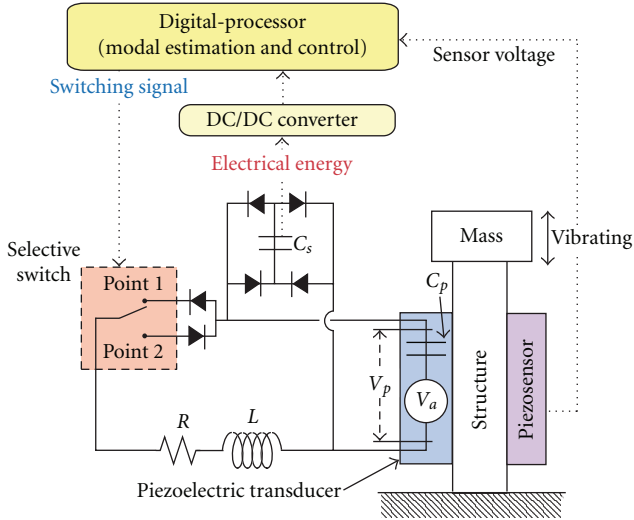


FIGURE 6: Control stream of digital self-powered vibration suppression system.

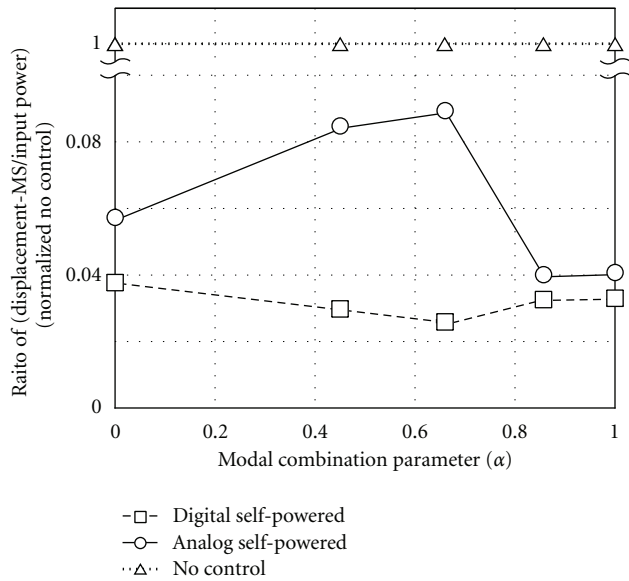


FIGURE 7: Comparison of displacement/input-power for various vibration suppression methods.

frequency  $\omega_2$  of the second mode. The coefficient of the second mode was determined, so that the first and second modal vibrations had the same displacement level.

The comparison between the multimodal sinusoidal excitation experiments with the analog and digital self-powered control systems is shown in Figure 7. The horizontal scale is the multimodal combination parameter, and the vertical scale is the ratio value of the mean square of the combined displacements of masses 1 and 2, divided by the input vibration power. These ratio values are normalized by the value of the no control case. This figure indicates that our digital self-powered control system can suppress all complicated vibrations. In contrast, our analog self-powered

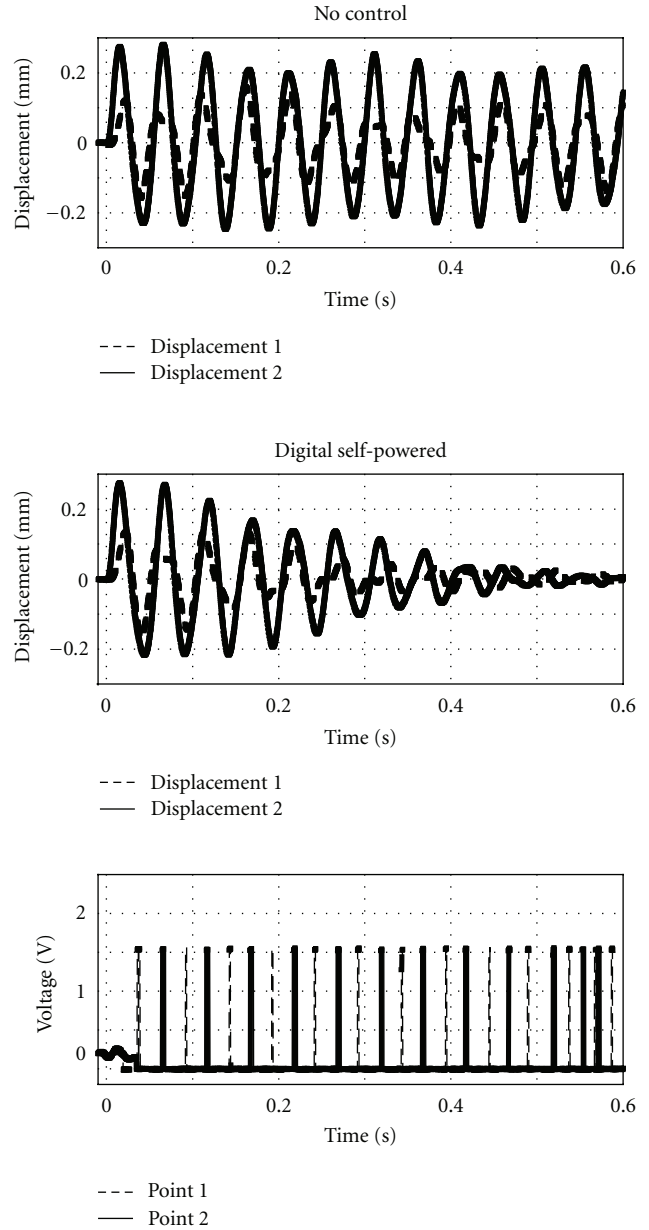


FIGURE 8: Experimental result of displacements under impulsive excitation with digital self-powered control.

control system is less effective when the combination of the two modes is around  $0.4 < \alpha < 0.7$ . This confirms that for suppressing complicated vibrations such as 2-mode vibrations, the digital self-powered system is better than the analog self-powered system.

**6.2. Impulsive Excitation.** We carried out impulse excitation experiments using our analog and digital self-powered systems. The impulse force was applied to mass 2 by an impulse hammer.

Figure 8 shows the displacements of the masses and the switching signal. The top of Figure 8 shows the displacements of masses 1 and 2 with no control. The middle of Figure 8

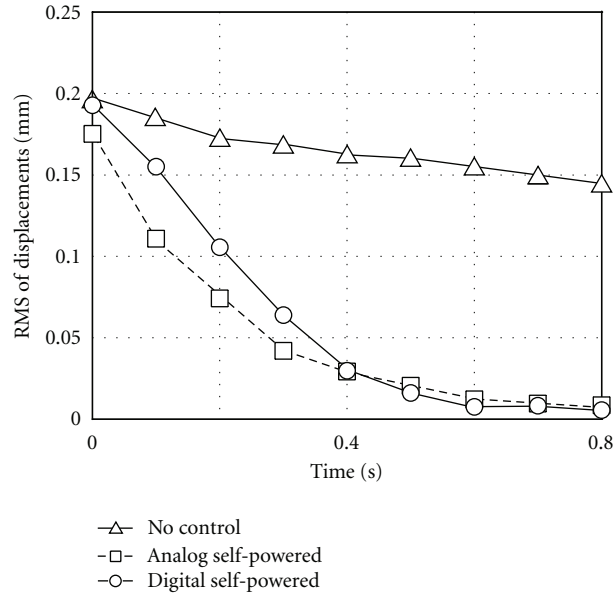


FIGURE 9: Comparison of RMS of displacements under impulsive excitation.

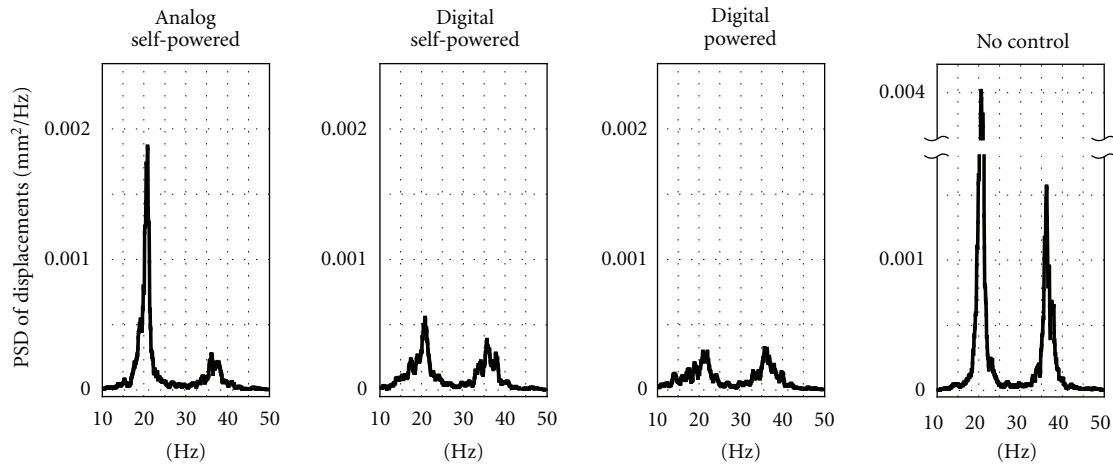


FIGURE 10: Comparison of PSD of displacements under random excitation.

shows the displacements of masses 1 and 2 with digital self-powered control. The bottom of Figure 8 shows the signal voltage of the selective switch. Just after 0.035 seconds of input force, our digital self-powered system started the vibration suppression. At 0.5 s, the magnitude of displacement 2 reduced from 0.215 mm to 0.021 mm, a reduction of 90.4%. These figures indicate that our digital self-powered system has a quick response and can therefore handle impulse dynamics.

Figure 9 shows the comparison between the impulse excitation experimental results of analog and digital self-powered control systems. The horizontal scale is time, and the vertical scale is the root mean square of the combined displacements of masses 1 and 2. During the early period (from 0 to 0.3 s), the analog self-powered system is more effective in vibration suppression than the digital one. This

is quite natural because the digital self-powered system must only store some amount of electrical energy in the storage capacitor until the microprocessor enters the wake-up mode. However, overall, the suppression performances of both analog and digital controls are almost equivalent even for impulsive disturbances.

**6.3. Random Excitation.** In this section, we carried out random vibration suppression experiments using our analog and digital self-powered systems. A function generator creates an input voltage wave and sends it to the vibration shaker. The input wave for random vibration excitation is kept constant in the power spectral density (PSD) value, from 10 to 50 Hz.

Figure 10 shows the comparison of the PSD displacements of masses 1 and 2 under random excitation. The

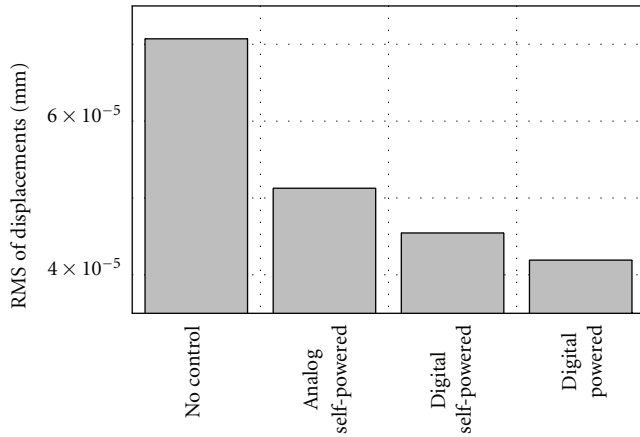


FIGURE 11: Comparison of RMS of displacements under random excitation.

horizontal scale is the frequency, and the vertical scale is the PSD of the displacement. The upper left side of Figure 10 shows the PSD value with analog self-powered control. The upper center of Figure 10 shows the PSD value with digital self-powered control. The upper right side of Figure 10 shows the PSD value with digital powered control. The lower part of Figure 10 shows the PSD value with no control. Unlike our self-powered systems, a digital powered system uses an external power supply for driving the digital processor. These figures indicated that the analog self-powered system could not suppress the first mode. However, the digital self-powered system significantly reduced all modal amplitudes.

Figure 11 shows the comparison of the root mean square of the combined displacements of masses 1 and 2. The experimental results demonstrate that the analog self-powered system reduced the root mean square by 27.6%, the digital self-powered system reduced it by 35.5%, and the digital powered system reduced it by 40.7%. The damping performance of the digital powered system was the most effective. This is quite natural because the digital powered system does not require an energy-harvesting section for driving the digital processor. Thus, these experimental results indicate that the lower the required harvested energy is, the better the damping performance of the digital self-powered system is.

## 7. Conclusions

This paper compared two types (i.e., analog and digital) of self-powered vibration suppression systems by using an energy recycling semiactive method with a piezoelectric transducer. These self-powered systems do not need an external power supply. The analog system comprises only analog electric devices whereas the digital system comprises an electric circuit with a programmable microprocessor.

We carried out several kinds of vibration suppression experiments using our proposed self-powered systems. These experiments clearly indicate that our self-powered systems yield a highly effective damping performance. Furthermore, we demonstrated that the digital self-powered system has

significant advantages over the analog system in dealing with multimodal vibrations. These systems are useful for various applications where energy-saving or energy-shortage concerns exist, such as large-space structures, artificial satellites, and isolated lunar bases, which are all exposed to long periods of no sunlight.

## Acknowledgment

This paper was supported by a Grant-in-Aid for Scientific Research (B) no. 20360386, from the Japan Society for Promotion of Science.

## References

- [1] M. Ahmadian and A. P. DeGiulio, "Recent advances in the use of piezoceramics for vibration suppression," *Shock and Vibration Digest*, vol. 33, no. 1, pp. 15–22, 2001.
- [2] C. Niezrecki, D. Brei, S. Balakrishnan, and A. Moskalik, "Piezoelectric actuation: state of the art," *Shock and Vibration Digest*, vol. 33, no. 4, pp. 269–280, 2001.
- [3] N. W. Hagood and A. von Flotow, "Damping of structural vibrations with piezoelectric materials and passive electrical networks," *Journal of Sound and Vibration*, vol. 146, no. 2, pp. 243–268, 1991.
- [4] S. Y. Wu, "Piezoelectric shunts with a parallel R-L circuit for structural damping and vibration control," in *Proceedings of the Smart Structures and Materials: Passive Damping and Isolation*, vol. 2720 of *Proceedings of SPIE*, pp. 259–269, February 1996.
- [5] D. Hrovat, P. Barak, and M. Rabins, "Semi-active versus passive of active tuned mass dampers for structural control," *Journal of Engineering Mechanics*, vol. 109, no. 3, pp. 691–705, 1983.
- [6] J. Onoda, T. Sano, and K. Kamiyama, "Active, passive, and semiactive vibration suppression by stiffness variation," *AIAA journal*, vol. 30, no. 12, pp. 2922–2929, 1992.
- [7] G. A. Lesieutre, "Vibration damping and control using shunted piezoelectric materials," *Shock and Vibration Digest*, vol. 30, no. 3, pp. 187–195, 1998.
- [8] V. Giurgiutiu, "Review of smart-materials actuation solutions for aeroelastic and vibration control," *Journal of Intelligent Material Systems and Structures*, vol. 11, no. 7, pp. 525–544, 2000.
- [9] W. W. Clark, "Vibration control with state-switched piezoelectric materials," *Journal of Intelligent Material Systems and Structures*, vol. 11, no. 4, pp. 263–271, 2000.
- [10] C. Richard, D. Guyomar, D. Audigier, and H. Bassaler, "Enhanced semi passive damping using continuous switching of a piezoelectric device on an inductor," in *Proceedings of the Smart Structures and Materials: Damping and Isolation*, vol. 3989 of *Proceedings of SPIE*, pp. 288–299, March 2000.
- [11] L. R. Corr and W. W. Clark, "Comparison of low-frequency piezoelectric switching shunt techniques for structural damping," *Smart Materials and Structures*, vol. 11, no. 3, pp. 370–376, 2002.
- [12] J. Onoda, K. Makihara, and K. Minesugi, "Energy-recycling semi-active method for vibration suppression with piezoelectric transducers," *AIAA Journal*, vol. 41, no. 4, pp. 711–719, 2003.
- [13] S. Shimose, K. Makihara, K. Minesugi, and J. Onoda, "Assessment of electrical influence of multiple piezoelectric transducers' connection on actual satellite vibration suppression,"

- Smart Materials Research*, vol. 2011, Article ID 686289, 8 pages, 2011.
- [14] K. Makihara, J. Onoda, and K. Minesugi, "Comprehensive assessment of semi-active vibration suppression including energy analysis," *Transactions of ASME, Journal of Vibration and Acoustics*, vol. 129, no. 1, pp. 84–93, 2007.
  - [15] J. Onoda, "Some advances in energy recycling semiactive vibration suppression," *Advances in Science and Technology*, vol. 56, pp. 345–354, 2008.
  - [16] K. Makihara, S. Takeuchi, S. Shimose, J. Onoda, and K. Minesugi, "Innovative digital self-powered autonomous system for multimodal vibration suppression," *AIAA Journal*. In press.
  - [17] D. Niederberger and M. Morari, "An autonomous shunt circuit for vibration damping," *Smart Materials and Structures*, vol. 15, no. 2, pp. 359–364, 2006.
  - [18] M. Lallart and D. Guyomar, "An optimized self-powered switching circuit for non-linear energy harvesting with low voltage output," *Smart Materials and Structures*, vol. 17, no. 3, Article ID 035030, 2008.
  - [19] B. Jaffe, W. R. Cook Jr., and H. Jaffe, *Piezoelectric Ceramics*, Academic Press, London, UK, 1971.
  - [20] M. J. Balas, "Direct velocity feedback control of large space structures," *Journal of Guidance, Control, and Dynamics*, vol. 2, no. 3, pp. 252–253, 1979.
  - [21] H. Kwakernaak and R. Sivan, *Linear Optimal Control System*, Wiley-Interscience, New York, NY, USA, 1972.

## Research Article

# Modeling Hysteresis with Inertial-Dependent Prandtl-Ishlinskii Model in Wide-Band Frequency-Operated Piezoelectric Actuator

Vahid Hassani, Tegoeh Tjahjowidodo, and Albert D. Soetarto

*Division of Mechatronics & Design, School of Mechanical and Aerospace Engineering, Nanyang Technological University, 50 Nanyang Avenue, Singapore 639798*

Correspondence should be addressed to Vahid Hassani, h\_vhd@yahoo.com

Received 12 November 2011; Accepted 3 January 2012

Academic Editor: Tao Li

Copyright © 2012 Vahid Hassani et al. This is an open access article distributed under the Creative Commons Attribution License, which permits unrestricted use, distribution, and reproduction in any medium, provided the original work is properly cited.

One of the major problems occurring in many technical applications is the presence of the hysteretic behavior in sensors and actuators, which causes a nonlinear relationship between input and output variables in such devices. Since the nonlinear phenomenon of hysteresis degrades the performance of the piezoelectric materials and piezoelectric drive mechanisms, for example, in positioning control framework, it has to be characterized in order to mitigate the effect of the nonlinearity in the devices. This paper is aimed to characterize and model the hysteresis in typical piezoelectric actuators under load-free and preloaded circumstances incorporating the inertial effect of the system. For this purpose, the piezoelectric actuator is modeled as a mass-spring-damper system, which is expressed in terms of a stop operator as one of the essential yet efficient hysteresis operators in the Prandtl-Ishlinskii (PI) model. The reason of utilizing the stop operator in this study is for the sake of control purposes, as the stop operator plays as the inverse of the play operator in the PI model and can be used in a feed-forward controller scheme to suppress the effect of hysteresis in general control framework. The results reveal that this model exhibits better correspondence to the measurement output compared to that of the classical PI model.

## 1. Introduction

Hysteresis is a nonlinear phenomenon that occurs in some types of materials such as piezoceramics, shape-memory alloys, and magnetostrictive actuators. The word “hysteresis” refers to systems that have memory such that similar loops are repeated in each cycle of operation in every dynamical system and, after removal of the force or electrical field, the system does not return to its original location. In this phenomenon, the current output depends also on the history of the input.

The effect of hysteresis nonlinearity can be neglected in some systems. In contrast, ignoring this phenomenon in other types of systems that possess severe hysteresis might create undesirable consequences such as inaccuracy in open loop system, limit cycle, degradation of the tracking performance, and even instability of closed loop system.

To overcome this challenge, some mathematical models, for example, the Preisach model and the PI model, have been proposed to capture the effect of hysteresis in any mechanical

systems. Utilization of the PI model is addressed in many works to characterize the hysteresis due to its simplicity compared to the Preisach model. Wang et al. [1] utilized the classical PI model and neural network approximator to design a robust adaptive control, which ensures that the tracking error is bounded in the presence of unknown hysteresis in a closed-loop system. The generalized PI is proposed for modeling an asymmetric hysteresis in piezoceramic actuators, where a linear function is defined to modify the threshold of the play operator of the model [2]. Krejci and Kuhnen [3] presented a new method of constructing the inverse of the hysteresis model in an analytical form for the system with hysteresis and creep and used the proposed model in a feed-forward controller to mitigate the nonlinearity arisen from the hysteresis. Al Janaideh et al. [4] presented a method to construct the inverse of the generalized PI model to be used in a feed-forward loop cascaded with an adaptive controller to reduce the effect of hysteresis in a piezoelectric actuator, and in another paper, they utilized the generalized PI model to design a robust

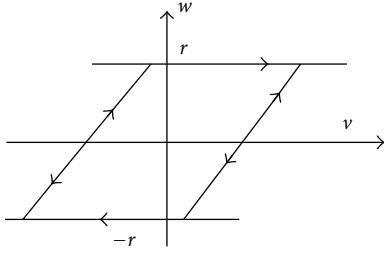


FIGURE 1: Classical stop operator.

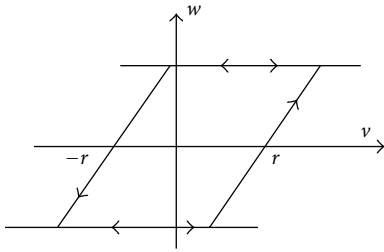


FIGURE 2: Classical play operator.

sliding mode controller to ensure the system stability for smart actuators [5]. A new strategy is introduced by Chen [6] to fuse the PI model with adaptive control techniques, which enhances the global stability of the system.

Various rate-dependent PI models have been proposed to capture the hysteresis in different rate of input or different frequency values of input applied to the piezoelectric actuators. Al Janaideh et al. [7] proposed a new rate-dependent PI model, which utilized logarithmic threshold value and density function in the play operator to characterize the hysteresis of a piezoelectric actuator under dynamically varying input up to 200 Hz. In the paper, they also characterized the hysteresis of a piezoelectric actuator up to 500 Hz and showed that the hysteresis loop gets larger at higher frequencies as well as it generates lower displacement as the frequency is increasing [8]. Kuhnert and Janocha [9] developed a modified PI model to characterize the complex hysteresis in actuators and sensors and presented the inverse of this model in an analytical form. Ang et al. [10] proposed the hysteresis model at low frequencies up to 50 Hz and utilized a linear function relating the slope of the hysteresis loop to input rate applied to the actuator. Subsequently, an advanced model was proposed to characterize the nonlinearity in a piezoelectric actuator under ill-conditioned hysteresis [11]. An adaptive controller was designed to capture the nonlinear effects of the giant magnetostrictive actuator using the PI model to compensate for the hysteresis which was reported by Wang et al. [12]. Goldfarb and Celanovic [13] proposed a rate-independent generalized Maxwell-Slip model for force and positioning control of microrobotic systems. Quant et al. [14] proposed a nonlinear Maxwell-Slip-based model to replace the linear constitutive equations of piezoelectric actuators to

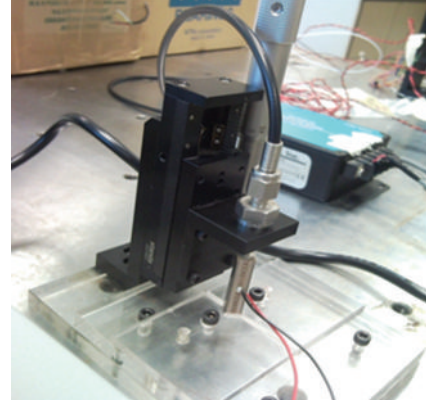


FIGURE 3: Configuration of the experimental setup.

make a comparison between two models. A Maxwell-Slip-based model was proposed to capture the hysteresis in piezoelectric actuator, and the parameters of this model were identified by the linear programming method [15]. Three fitness functions were proposed in terms of the Bouc-Wen model including mass-spring-damper characteristics of piezoelectric actuator, and these functions were minimized using the genetic algorithm method [16]. In other study, piezoelectric actuator was employed as Impact Drive Mechanism, and its model was constructed assuming the system as a spring-mass-damper system, where nonlinearity was modeled using the Bouc-Wen model, and finally the parameters of this system were identified by an adaptive method [17].

In this study, an inertial-dependent model is proposed to overcome the large amount of errors imposed in the modeling with the classical PI model, in particular in capturing the hysteresis at high frequencies as well as high amplitudes of inputs applied to a piezoelectric actuator under load-free and preloaded conditions. As a rate-independent model, it is able to capture the hysteresis at different input magnitudes and frequencies even in the presence of preloading force.

## 2. Classical Prandtl-Ishlinskii (PI) Model

One of the well-known operator-based models, which are used to characterize the hysteresis in piezoceramics and other types of materials, is the classical PI model that utilizes two essential hysteresis operators, namely, the play operator and the stop operator.

**2.1. Stop Operator.** The rate-independent stop operator is illustrated in Figure 1. Conceptually, this operator determines the linear stress-strain ( $w-v$ ) relationship as in the Hook's law, when the stress is less than the yield stress,  $r$  [7]. In analytical form, assume that  $C_m[0, t_E]$  is the space of piecewise monotone continuous functions, a function  $e_r : R \rightarrow R$  is defined by

$$e_r(v) = \min(r, \max(-r, v)) \quad (1)$$

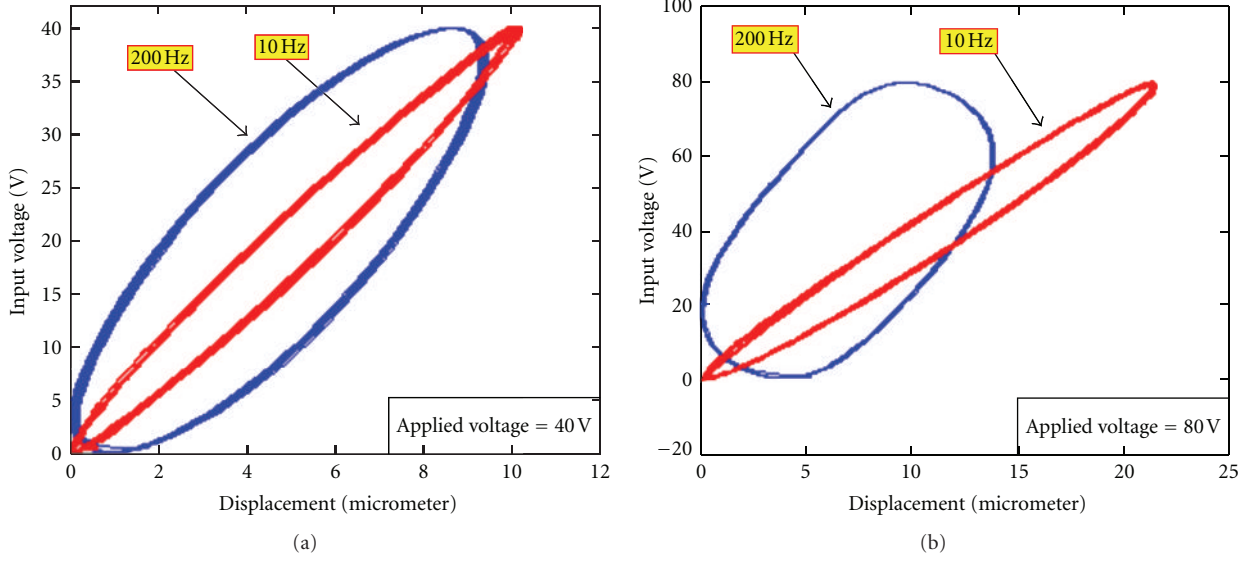


FIGURE 4: Width and slope of the hysteresis curve at different frequencies and input amplitudes for load-free piezoelectric actuator.

with  $r \geq 0$ . For any input  $v(t) \in C_m[0, t_E]$  and any initial value  $\omega_{-1} \in R$ , the stop operator  $E_r$  can be expressed by the following definition:

$$\begin{aligned} E_r[v; \omega_{-1}](0) &= e_r(v(0) - \omega_{-1}), \\ E_r[v; \omega_{-1}](t) &= e_r(v(t) - v(t_i) + E_r[v; \omega_{-1}](t_i)), \quad (2) \\ &\text{for } t_i < t \leq t_{i+1}, \quad 0 < i \leq N - 1, \end{aligned}$$

where  $0 = t_0 < t_1 < \dots < t_N = t_E$  is a part of  $[0, t_E]$ , such that the function  $v$  is monotone on each of the subintervals  $[t_i, t_{i+1}]$ .

**2.2. Play Operator.** The rate-independent play operator is illustrated in Figure 2. This operator implies the reciprocating motion of a piston inside a cylinder with length  $2r$ , where the instantaneous position of center of piston is defined by  $v$  and  $\omega$  as input and output subsequently [7]. In analytical form, for any input  $v(t) \in C_m[0, t_E]$  and  $r \geq 0$ , the play operator is inductively defined by

$$\begin{aligned} F_r[v; \omega_{-1}](0) &= f_r(v(0) - \omega_{-1}), \\ F_r[v; \omega_{-1}](t) &= f_r(v(t), F_r[v; \omega_{-1}](t_i)), \quad (3) \\ &\text{for } t_i < t \leq t_{i+1}, \quad 0 < i \leq N - 1, \end{aligned}$$

where

$$f_r(v, \omega) = \max(v - r, \min(v, \omega)) \quad (4)$$

$\omega_{-1}$  defines the initial state at time  $t = 0$ .

### 3. Inertial-Dependent Prandtl-Ishlinskii (PI) Model

In order to determine the dynamic characteristics of the piezoelectric actuators, the linear constitutive equation has

been proposed [18]. A piezoelectric element can be represented by an element with electrical and mechanical gates in linear form, which is expressed mathematically in (5) disregarding the presence of any nonlinear effects

$$T = C^E S - eE. \quad (5)$$

Since this equation is not involved in the nonlinear phenomenon of hysteresis, it is required to model the nonlinear characteristics of the piezoelectric actuator. For practical applications, engineering variables such as force, speed, electrical current, and voltage are required. In order to simplify the analysis, the strain,  $S$ , stress,  $T$ , and electrical field,  $E$  in (5) are substituted by measurable counterparts, namely, the displacement,  $x$ , force,  $F$ , and voltage,  $U$ , as shown in

$$F = A \cdot U + Zx. \quad (6)$$

Consequently, the constitutive equation can be transformed into the Laplace domain as presented in (7), where  $Z$  represents the mechanical impedance,  $m$  is the equivalent mass of the piezoceramic,  $c$  is the damping factor, and  $k$  is the stiffness of the piezoelectric actuator

$$Z = ms^2 + cs + k. \quad (7)$$

Intuitively, in this model, the piezoelectric actuator is assumed as a mass-spring-damper system. Based on this assumption, basic equation of motion for such systems can be written incorporating with the PI model to take into account the both linear and nonlinear characteristics of the piezoelectric actuator. As a result, the following relationships are proposed in terms of two essential operators of the PI model, namely, the play operator:

$$X = \alpha \cdot V + \beta \cdot F_{P-L} - m_{eq} \frac{d^2 f_{P-O}(V)}{dt^2} - c_{eq} \frac{df_{P-O}(V)}{dt}, \quad (8)$$

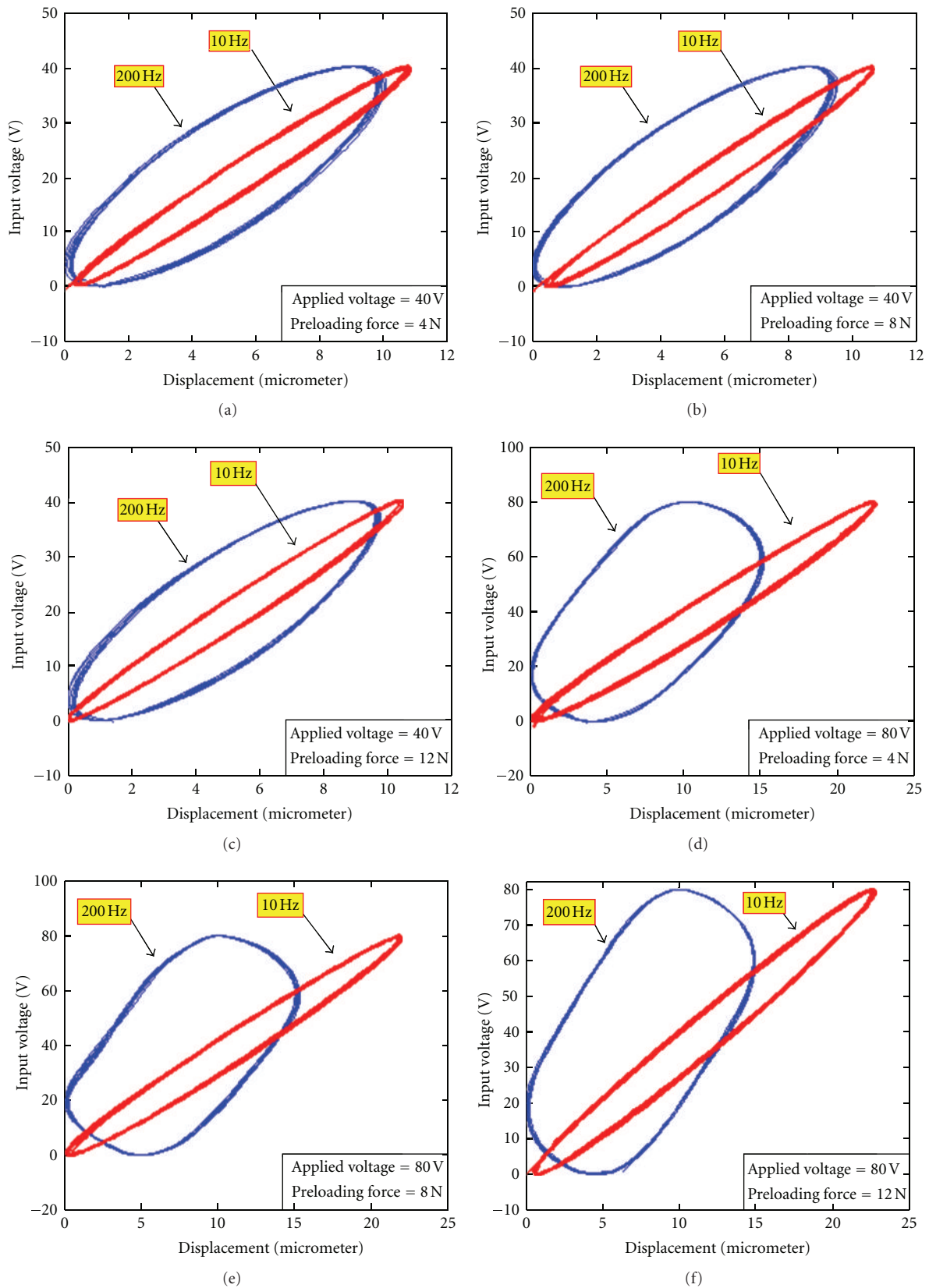


FIGURE 5: Width and slope of the hysteresis curve at different frequencies and input amplitudes for preloaded piezoelectric actuator.

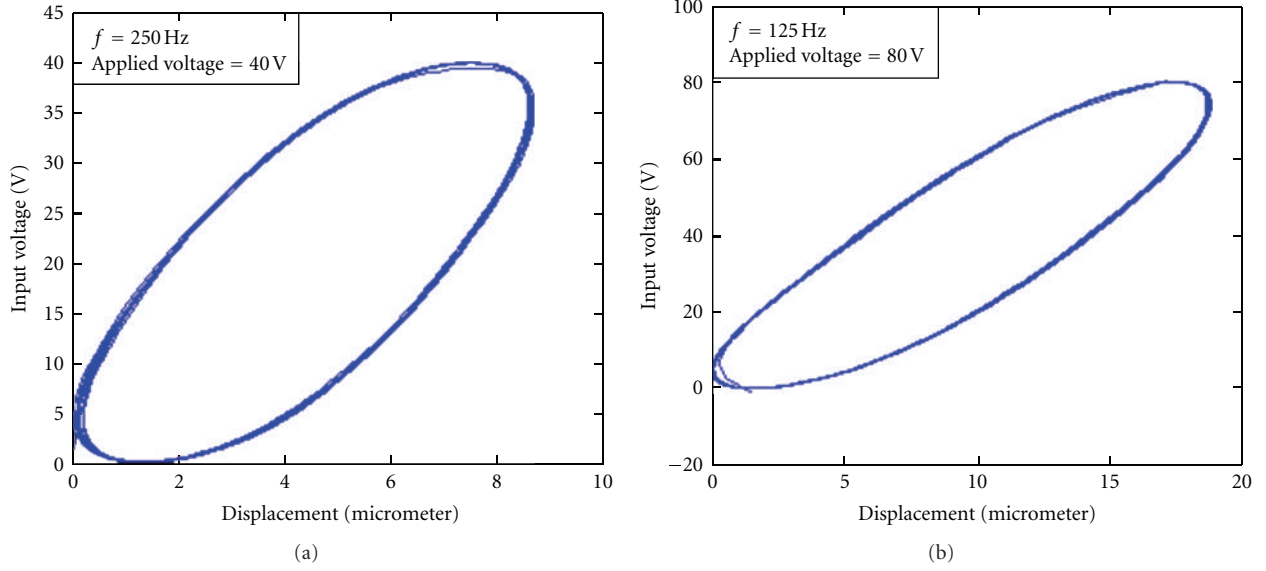


FIGURE 6: Asymmetric hysteresis curve at different frequencies and input amplitudes for load-free piezoelectric actuator.

and inversely in the stop operator, it can be expressed as

$$f_{S.O}(X) = \beta \cdot F_{P.L} - m_{eq} \frac{d^2X}{dt^2} - c_{eq} \frac{dX}{dt} - k_{eq}X, \quad (9)$$

where  $m_{eq}$ ,  $c_{eq}$ , and  $k_{eq}$  are the equivalent mass, damping, and stiffness factors, respectively.  $F_{P.L}$  stands for the preloading force when the piezoelectric actuator is exposed to the preloading condition, which in turn involves two terms of external force and stiffness of the preloading devices which are expressed by  $F_{P.L} = F_{ext} + K_{eq, ext} \cdot x$ . In (8) and (9),  $V$  represents the input voltage applied to the piezoelectric actuator as the input of the play operator and  $X$  represents the desired displacement of the actuator as the input of the stop operator.  $\alpha$  and  $\beta$  stand as correction coefficients of the input voltage in the play operator and the preloading force  $F_{P.L}$ , respectively.  $f_{S.O}(X)$  and  $f_{P.O}(V)$  are subsequently the output of the stop operator and the play operator.

This model takes into consideration two important terms of inertial and damping effects which are shown by  $m_{eq}\ddot{X}$  and  $c_{eq}\dot{X}$ . In the sense of frequency response, these two terms are expressed by  $m_{eq}\omega^2X$  and  $c_{eq}\omega X$ . As a result, these terms are function of frequency, and they vary with variations of the input frequency. Due to this characteristic, the modeling of the hysteresis in piezoelectric actuators is expected to perform better compared to that with the classical PI model.

#### 4. Experimental Set Up

A dedicated set up was built to characterize a piezoelectric actuator experimentally. In this work, the piezoceramic actuator (P-887.90, from PHYSIK Instrument Co.) was used. This actuator provides maximum displacement of  $36 \pm 10\% \mu\text{m}$  at maximum applied voltage of 120 V. The PZT actuator is driven using a power amplifier (E.663, PHYSIK Instrument Co.), which multiplies any input voltage by gain 10 and sends it to the piezoelectric actuator. A capacitive

sensor (CS1, Micro-Epsilon Co. with resolution of 0.75 nm and operating temperature range of  $-50^\circ\text{C}$  to  $200^\circ\text{C}$ ) was utilized to measure the displacement of PZT actuator in terms of voltage (see Figure 3).

#### 5. Experimental Results

In order to characterize the hysteretic behavior of the piezoelectric actuator, two sets of sinusoidal inputs for low-amplitude voltage signal (20 V amplitude with 20 V bias) and high-amplitude voltage signal (40 V amplitude with 40 V bias) were applied to the piezoelectric actuator in load-free and preloading conditions. These sets of input signals were applied at varying frequency ranging from 10 Hz to 200 Hz and different preloading forces of 4 N, 8 N, and 12 N. The reason of selecting different amplitudes besides different frequencies is to analyze the hysteresis characteristic in the piezoelectric actuator in terms of amplitude and frequency variations. Different preload condition on the piezoelectric actuator is also expected to affect the hysteresis characteristics. This motivates the experiment to be conducted at different preloading forces.

Applying two sets of low-amplitude and high-amplitude inputs at different frequencies besides different values of preloading force implies three important aspects in the hysteretic behavior. The first thing, which is observed from this experiment, is attributed to the rate dependency of the hysteresis curve; that is, when the rate of the input voltage is increased, the width of the hysteresis curve is also increasing. Figure 4 shows that the maximum width of the hysteresis at frequency of 200 Hz with low input voltage has become 3.57 times as that of the hysteresis curve at frequency of 10 Hz with the same amount of voltage amplitude. For high amplitude voltage, the width of the hysteresis curve at frequency of 200 Hz has grown up to 4.3 times higher than that of the hysteresis width at frequency of 10 Hz. The

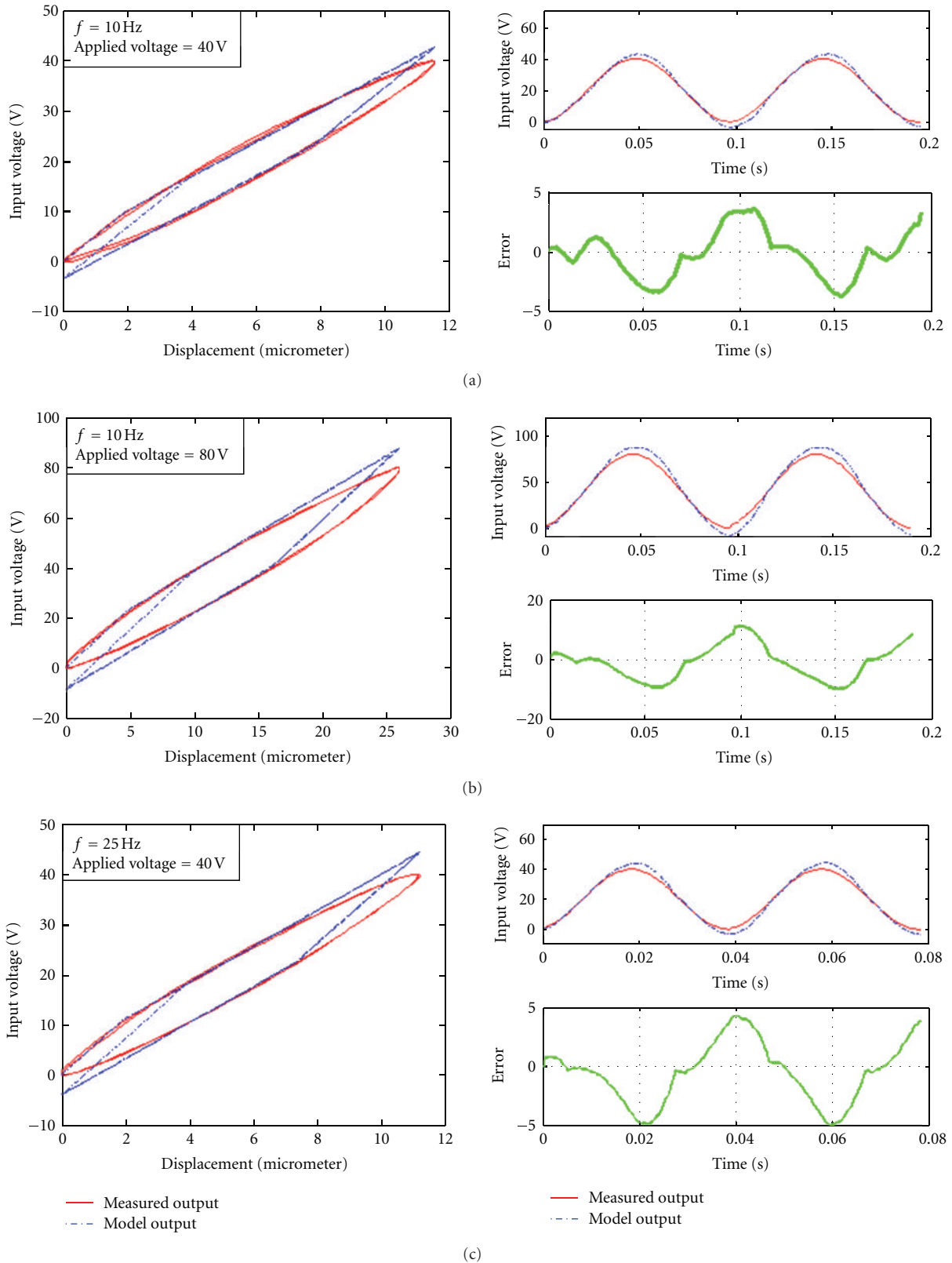


FIGURE 7: Continued.

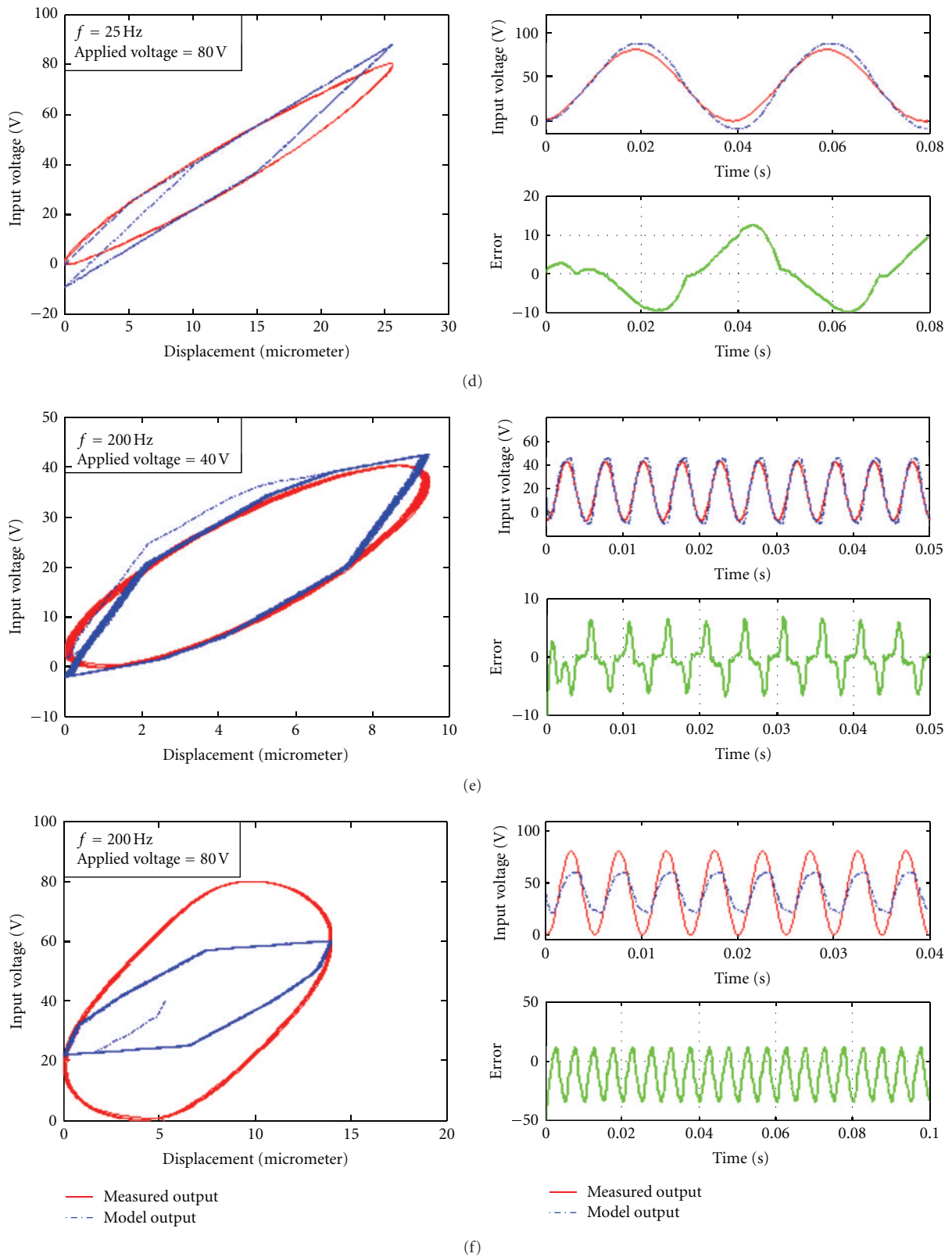


FIGURE 7: The results of modeling with the classical PI for load-free piezoelectric actuator for different input voltage and frequency: (a) 40 V; 10 Hz, (b) 80 V; 10 Hz, (c) 40 V; 25 Hz, (d) 80 V; 25 Hz, (e) 40 V; 200 Hz, (f) 80 V; 200 Hz.

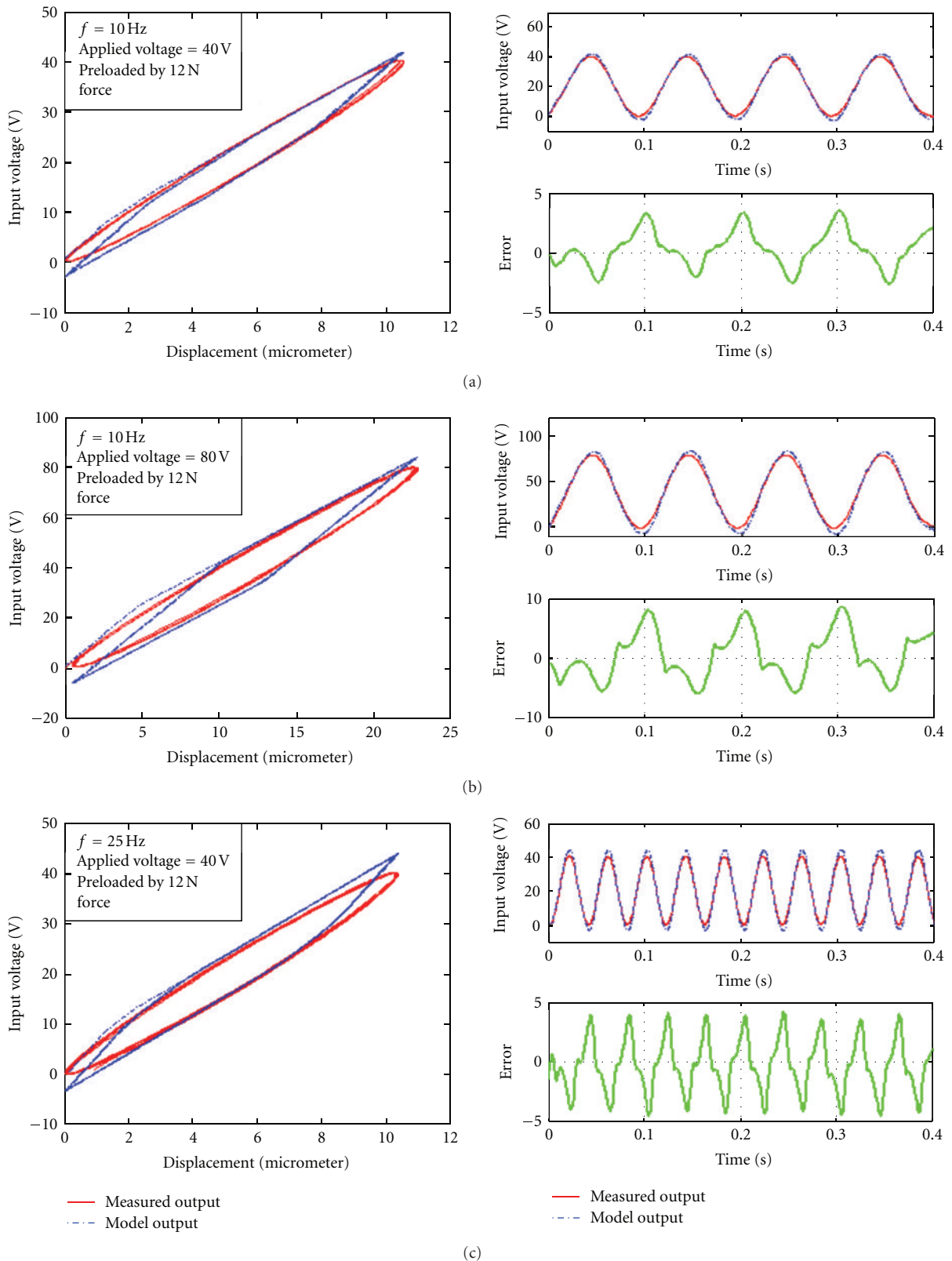


FIGURE 8: Continued.

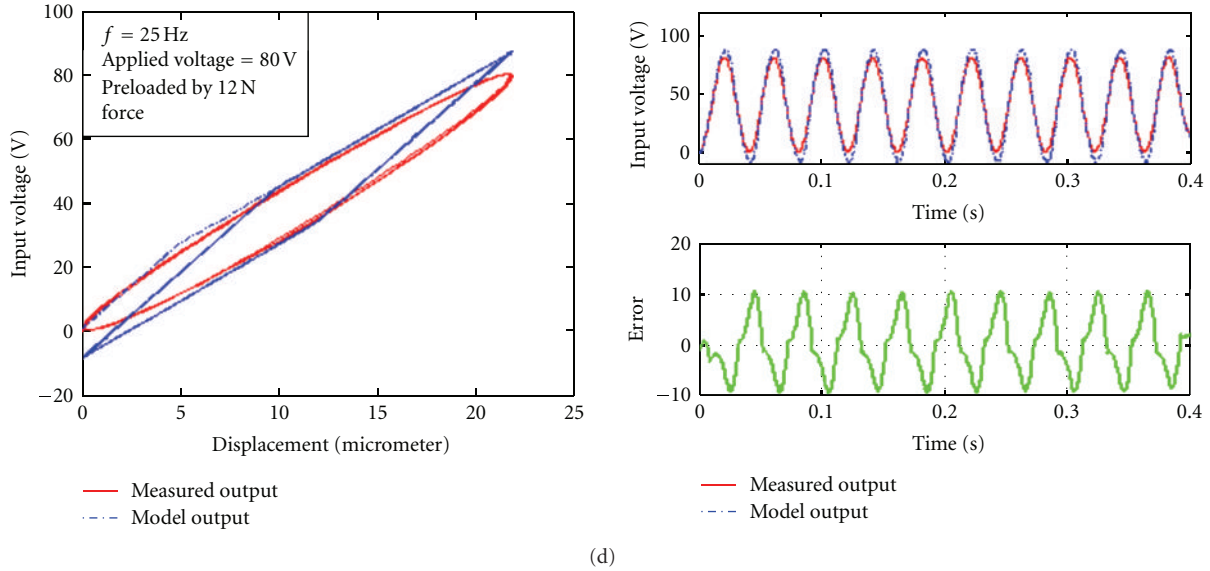


FIGURE 8: The results of modeling with the classical PI for preloaded piezoelectric actuator under 12 N force, for different input voltage and frequency: (a) 40 V and 10 Hz, (b) 80 V and 10 Hz, (c) 40 V and 25 Hz, and (d) 80 V and 25 Hz.

results also show that the maximum width of hysteresis curve is expanded when the magnitude of the applied voltage is increased.

Figure 5 shows the hysteresis obtained from the experiments to characterize the properties of the piezoelectric actuator under preloading condition at three different preloading forces applied to the piezoceramic. From the experiment results using two input signals, the most important thing that can be concluded is that the expansion of the hysteresis curve corresponds to the preloading force. For the case with an input voltage of 40 V and frequency of 200 Hz, the width of the hysteresis is expanded 1.06 times from preloading force of 4 N to preloading force of 12 N. In the case with the input voltage of 80 V and frequency of 200 Hz, this value has shifted up to 1.11 times under preloading force of 4 N in comparison with the preloading force of 12 N. This characterization shows that the intensity of hysteresis is increasing with the preloading forces, and consequently the quantity of maximum displacement of the actuator is also decreasing with increasing preloading force.

The second finding of this experiment is regarding the relationship between the maximum stroke of the actuator and maximum input voltage applied to the actuator. For the case of 40 V input, the maximum stroke of  $10.12 \mu\text{m}$  is obtained at frequency of 10 Hz, and maximum stroke of  $9.454 \mu\text{m}$  is obtained at frequency of 200 Hz. For the case of 80 V input, different values are acquired; meanwhile, the difference between the lowest and the highest stroke of the actuator at frequency of 10 Hz and 200 Hz is larger than that of the case in the 40 V input. These values are subsequently  $21.57 \mu\text{m}$  and  $13.81 \mu\text{m}$  for frequencies of 10 Hz and 200 Hz. The same phenomenon is also observed under the preloading condition.

The third finding observed from this experiment is regarding a tight relationship between amplitude and fre-

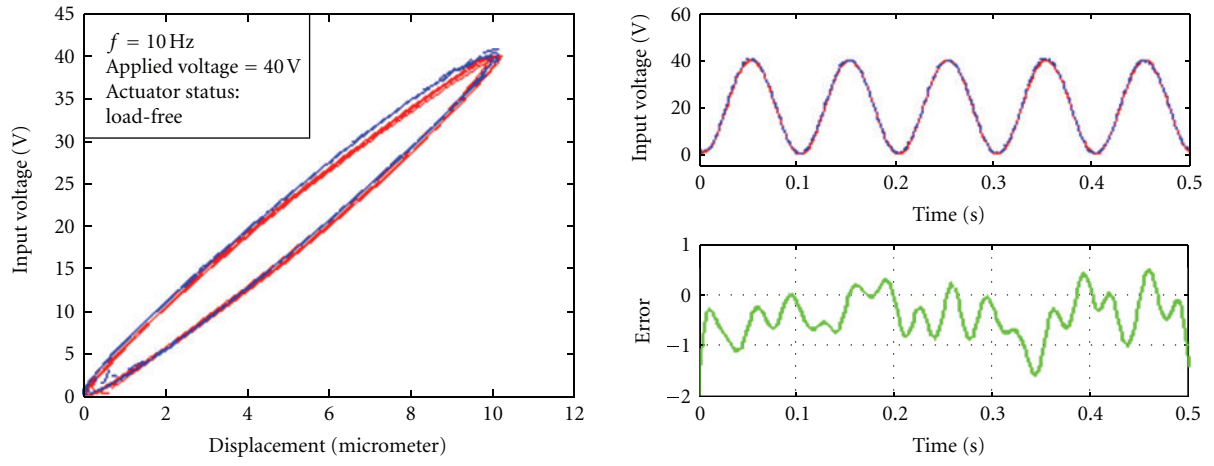
quency in one hand and asymmetrical hysteresis shape and high slope of the hysteresis curve in the other hand. As illustrated in Figures 5 and 6, if the amplitude of the input voltage is increased, the asymmetric hysteresis curve will be formed at low frequencies as compared to application of the low amplitude input, and the slope of the hysteresis curve is also increasing. In the case of the input voltage with magnitude of 80 V, the asymmetric hysteresis curve is obtained at frequency of 125 Hz, while the asymmetric hysteresis is observed at 250 Hz for the lower input amplitude of 40 V.

## 6. Modeling Results

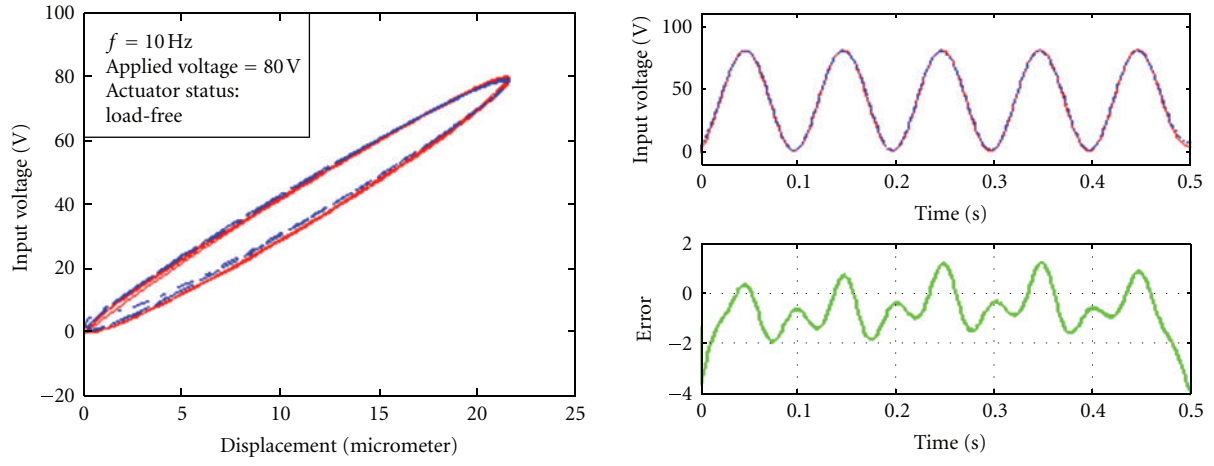
In order to capture the symmetrical hysteresis shapes, which are recorded up to 200 Hz with low-amplitude and high-amplitude voltages, a stop operator was utilized. As described in Section 2, a stop operator plays a role as the inverse of the play operator. The implementation of the stop operator instead of the play operator enables us to use the PI model in a feed-forward loop for positioning control purposes so that it can generate the required control input upon a desired displacement commanded to the control system.

The classical PI model was implemented to characterize the hysteresis in the piezoelectric actuator by utilizing four classical stop operators, in the cases, where the symmetric hysteresis curve takes place. This modeling approach is parameterized by four threshold values of  $r$  and multipliers of  $w$ , where  $r$  adjusts the width and height of the hysteresis and  $w$  adjusts the slope of the hysteresis curve correspondingly. These parameters are optimized upon the minimization of the following cost function:

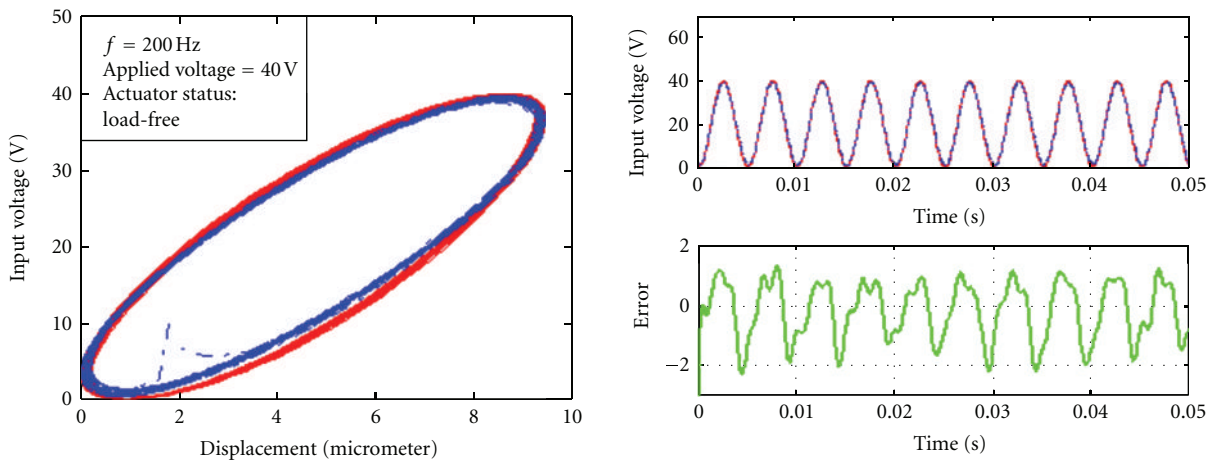
$$J = \sum_{i=1}^n (y_{s.o} - y_m)^2, \quad (10)$$



(a)



(b)



(c)

FIGURE 9: Continued.

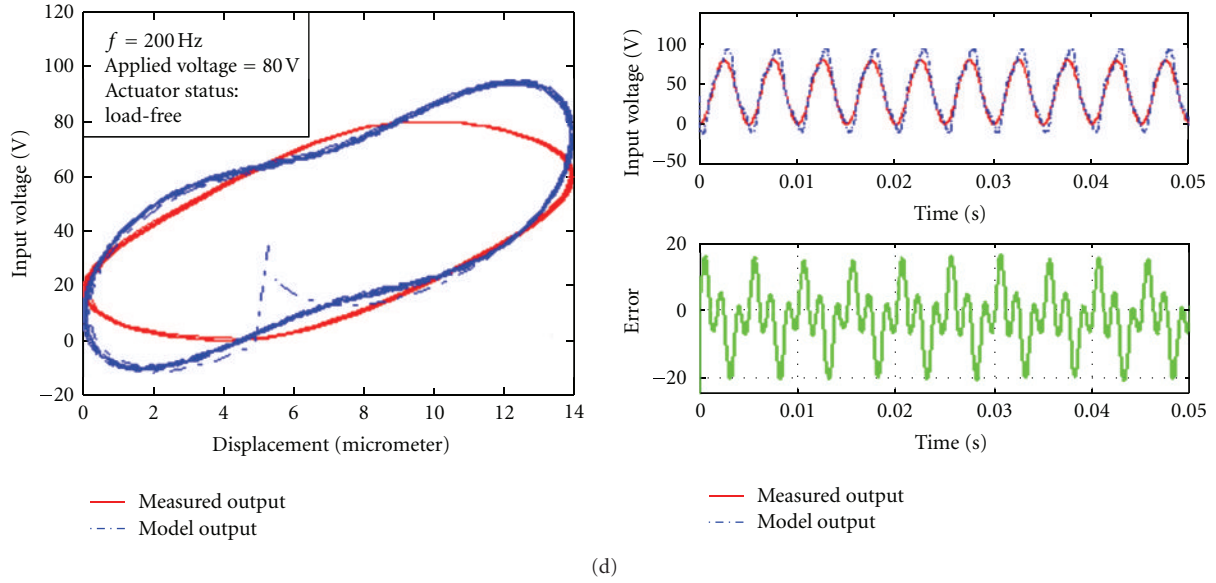


FIGURE 9: The results of modeling with Inertial-dependent PI for load-free actuator with different input voltage and frequency: (a) 40 V and 10 Hz, (b) 80 V and 10 Hz, (c) 40 V and 200 Hz, and (d) 80 V and 200 Hz.

where  $y_{s,O}$  is the output of the stop operator in PI model and  $y_m$  is the actual output which was measured from the experiment and  $n$  is the number of samples. The error minimization problem was solved using the MATLAB optimization toolbox.

As can be seen in Figures 7 and 8 the classical PI model is not capturing the hysteresis pattern satisfactorily, in particular at high frequencies for both cases of the unloaded and preloaded actuator.

In order to overcome the problem, as discussed in the previous section, the inertial-dependent model is introduced, where two important dynamic terms of inertial and damping effects, which are stated by  $m_{eq}\ddot{X}$  and  $c_{eq}\dot{X}$ , are taken into account. In the sense of frequency response, these two terms are expressed by  $m_{eq}\omega^2X$  and  $c_{eq}\omega X$ . Intuitively, the physical aspect of the actuator will also manifest itself in the dynamics of the system. The classical PI model cannot be used solely in characterizing the hysteresis properties of the material. In Figures 7(a) to 7(f), it is shown that the classical PI model cannot capture the hysteresis pattern especially at the turning points, where the major lag occurs between the applied electrical field and actuator displacement. At these points, the PI model generates sharp turning points due to the absence of inertial and damping effects. In order to tackle this discrepancy, inertial-dependent model is implemented to capture the turning points as well as other points of the hysteresis curve with considerable reduction of error as illustrated in Figures 9(a)–9(d). In these figures, the results of simulation from the inertial-dependent PI model are displayed, where the amount of error between the measured output and the output of the inertial-dependent PI model is significantly reduced compared to that from the classical PI model.

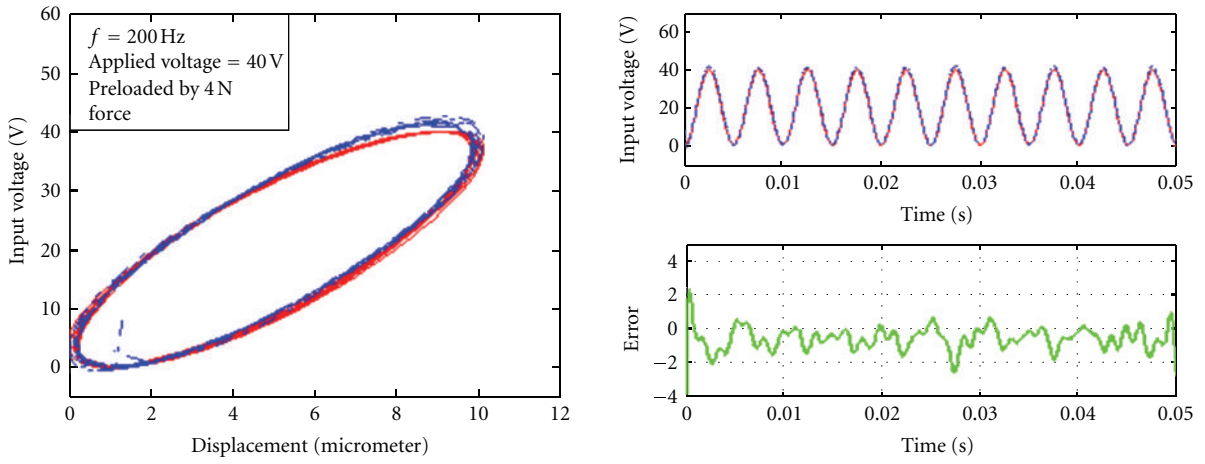
One of the interesting points appears from the characterization of the hysteresis at frequency of 200 Hz with

high-amplitude voltage, where the hysteresis curve starts to skew resulting in an asymmetrical hysteresis. The error in this case seems to be larger compared to the cases at lower frequencies (see Figure 9(d)), which implies that the asymmetric hysteresis is still not incorporated in this model, despite the considerable amount of error that has been reduced in the symmetric hysteresis cases.

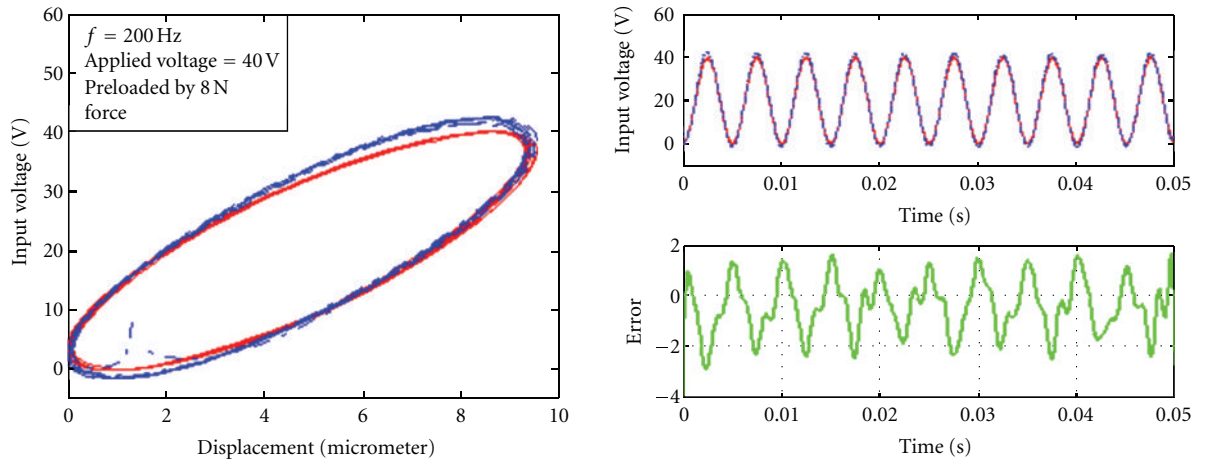
Figure 10 shows the identification results using the inertial-dependent PI model for the piezoelectric actuator under preloading forces of 4 N, 8 N, and 12 N. The first three panels (Figures 10(a)–10(c)) represent the preloading cases for the first applied voltage signal (40 V), where the last three panels are for the case of the second voltage signal (80 V). It can be concluded that this model is also applicable to characterize the piezoelectric actuator under preloading condition with acceptable amount of error by using the inertial-dependent PI model with the consideration of the preloading force,  $F_{P-L} = F_{ext} + K_{eq, ext} \cdot x$ .

The result shows that the introduction of the inertial and damping effect to the classical PI model improves the performance of the model in wide range of operation. As can be seen in Figures 7 and 8, the error between the measured output (voltage) and the actual output is increased from lower frequencies to higher frequencies in the classical PI model. Also, the quantity of the error for high-amplitude voltage is larger than the error for the low-amplitude voltage case. In the inertial-dependent model, not only the amount of error remains low at different amplitudes, but this amount also remains low at different frequency values. As a result, it can be realized that the classical PI model is not capable of characterization of the hysteresis at wide range of frequency solely.

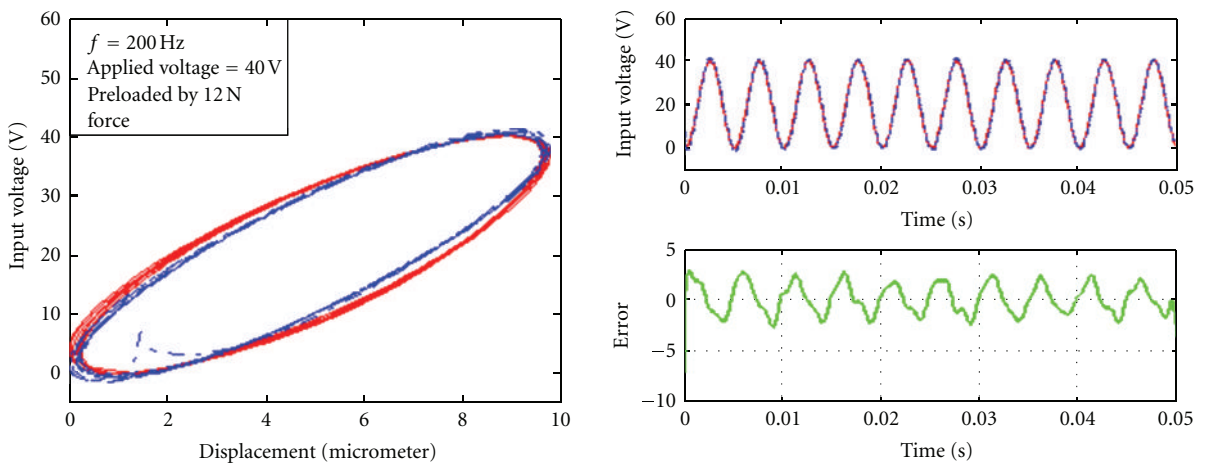
On the other hand, from the simulation at different frequencies with different amplitudes in both preloading and



(a)



(b)



(c)

— Measured output  
- - - Model output

— Measured output  
- - - Model output

FIGURE 10: Continued.

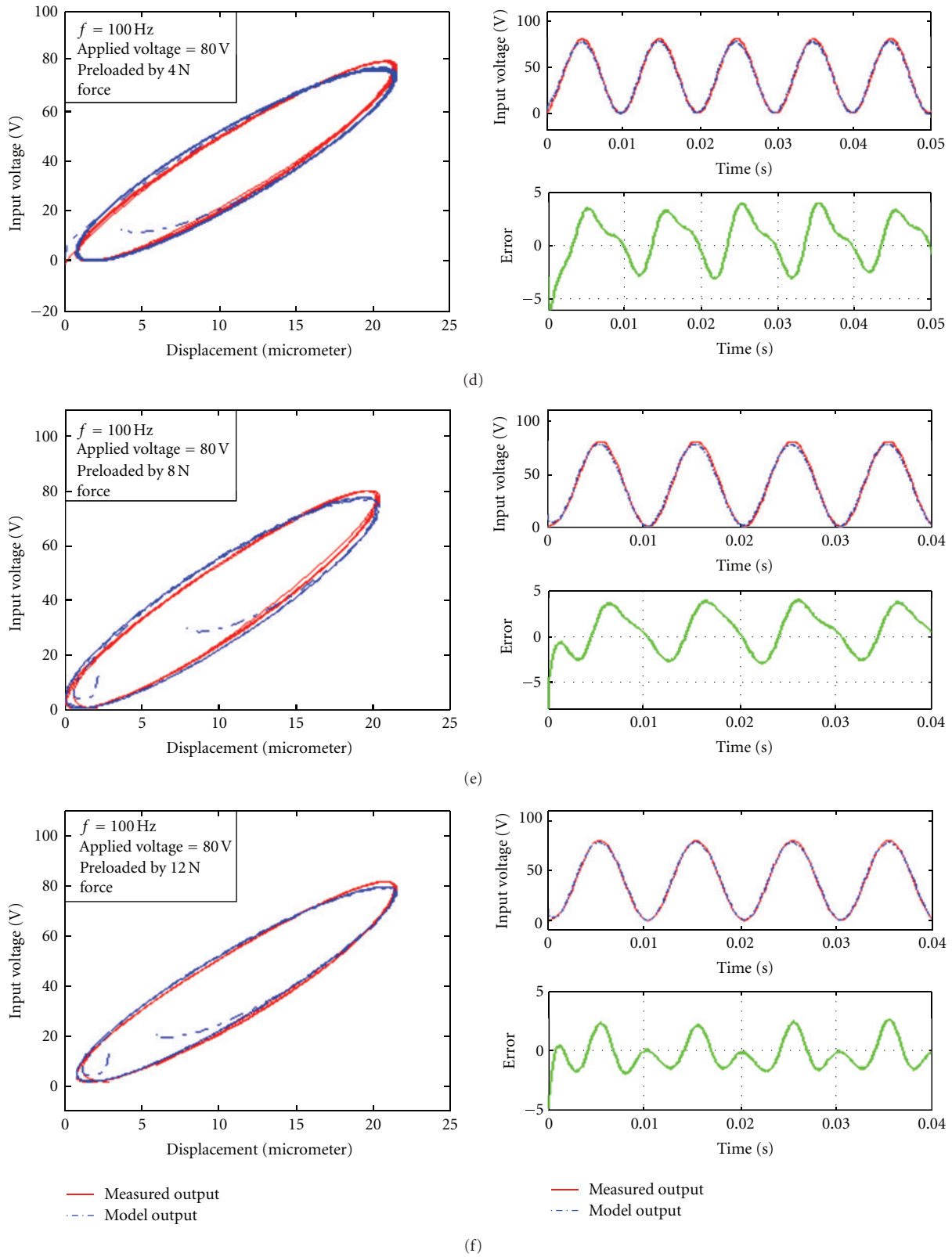


FIGURE 10: The results of modeling with the inertial-dependent PI with different input voltage, frequency, and preload: (a) 40 V; 200 Hz; 4 N, (b) 40 V; 200 Hz; 8 N, (c) 40 V; 200; 12 N, (d) 80 V; 100 Hz; 4 N, (e) 80 V; 100 Hz; 8 N, and (f) 80 V; 100 Hz; 12 N.

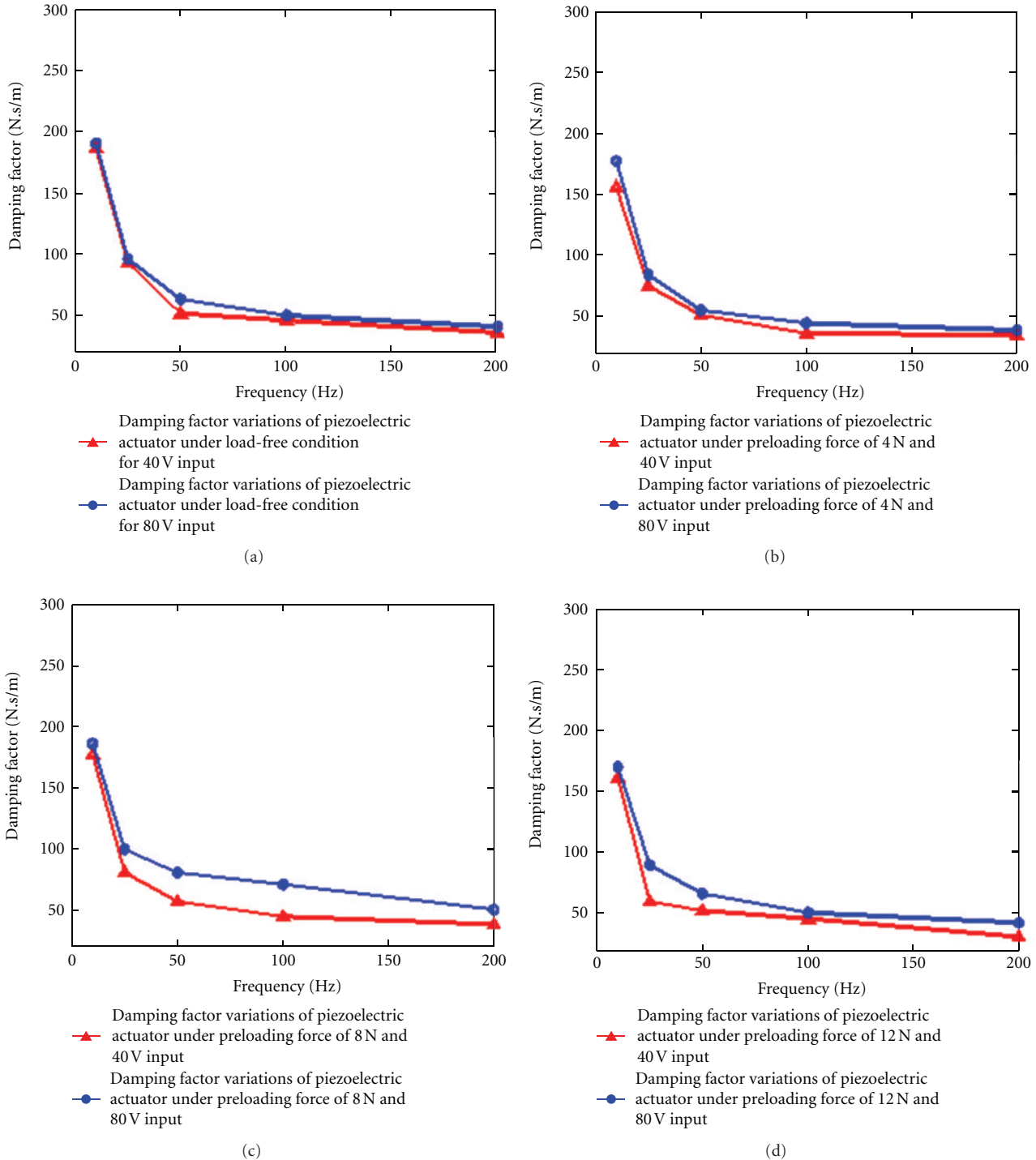


FIGURE 11: Damping factor variations at different frequencies with different amplitudes ( $\blacktriangle$ , low-amplitude voltage, 40 V;  $\bullet$ , high-amplitude voltage, 80 V).

load-free circumstances, the parameter of damping effect is varying as illustrated in Figure 11. As the amplitude goes to higher values for both unloading and preloading conditions, the values of the damping factor shift to the higher values correspondingly, while the variation of the damping factor to the frequency is exponentially decreasing. On the other

hand, in each set of the input voltage imposed to the actuator, the damping factor decreases with increasing the frequency value. This finding could be considered to be a guideline to develop an integrated rate and inertial-dependent model of hysteresis based on the variation of the damping factor versus frequency.

## 7. Conclusion

In this study, the performance of the classical PI model was evaluated using sets of data which incorporate two different magnitudes of the input voltage and varying frequency from 10 Hz to 200 Hz for different preloading conditions. It is shown that the classical Prandtl-Ishlinskii model is unable to characterize the hysteresis in piezoelectric actuators at wide range of frequency and amplitude.

In order to tackle this problem, as the physical aspect of the piezoelectric actuator will manifest itself in the dynamic behavior, the inertial-dependent PI model is proposed to capture the hysteresis at different input amplitudes and frequencies. The proposed model exhibits better performance compared to that of the classical one as implied by the modeling error for wide range of applications. However, moving toward high-frequency applications, the performance of the proposed model is degrading. Incorporating the rate-dependent parameters, for example, as presented by Al-Janaideh et al. [8], to the inertial-dependent model is expected to improve the performance.

## References

- [1] Q. Wang, C. Y. Su, and S. S. Ge, "A direct method for robust adaptive nonlinear control with unknown hysteresis," in *Proceedings of the 44th IEEE Conference on Decision and Control, & the European Control Conference (CDC-ECC '05)*, vol. 1–8, pp. 3578–3583, December 2005.
- [2] M. Al Janaideh, C. Y. Su, and S. Rakehja, "Modeling hysteresis of smart actuators," in *Proceedings of the 5th International Symposium on Mechatronics and Its Applications (ISMA '08)*, Amman, Jordan, May 2008.
- [3] P. Krejci and K. Kuhnen, "Inverse control of systems with hysteresis and creep," *IEE Proceedings-Control Theory and Applications*, vol. 148, no. 3, pp. 185–192, 2001.
- [4] M. Al Janaideh, Y. Feng, S. Rakheja, C. Y. Su, and C. A. Rab-bath, "Hysteresis compensation for smart actuators using inverse generalized prandtl-ishlinskii model," in *Proceedings of the American Control Conference (ACC '09)*, pp. 307–312, St. Louis, Mo, USA, June 2009.
- [5] M. Al Janaideh, Y. Feng, S. Rakheja, Y. Tan, and C. Y. Su, "Generalized Prandtl-Ishlinskii hysteresis: modeling and robust control for smart actuators," in *Proceedings of the 48th IEEE Conference on Decision and Control and 28th Chinese Control Conference*, pp. 7279–7284, 2009.
- [6] X. Chen, "High precision control for piezo-actuated positioners," in *Proceedings of the IEEE International Conference on Mechatronics and Automation (ICMA '09)*, pp. 966–971, Changchun, China, August 2009.
- [7] M. Al Janaideh, S. Rakheja, and C. Y. Su, "Characterization of rate dependent hysteresis of piezoceramic actuators," in *Proceedings of the IEEE International Conference on Mechatronics and Automation (ICMA '07)*, vol. 5, pp. 550–555, Haerbin, China, August 2007.
- [8] M. A. Janaideh, S. Rakheja, and C. Y. Su, "Experimental characterization and modeling of rate-dependent hysteresis of a piezoceramic actuator," *Mechatronics*, vol. 19, no. 5, pp. 656–670, 2009.
- [9] K. Kuhnen and H. Janocha, "Complex hysteresis modeling of a broad class of hysteretic nonlinearities," in *Proceedings of the 8th International Conference on New Actuators*, Bremen, Germany, June 2002.
- [10] W. T. Ang, F. A. Garmon, P. K. Khosla, and C. N. Riviere, "Modeling rate-dependent hysteresis in piezoelectric actuators," in *Proceedings of IEEE/RSJ International Conference on Intelligent Robots and Systems*, pp. 1975–1980, Pittsburgh, Pa, USA, October 2003.
- [11] U.-X. Tan, W. T. Latt, C. Y. Shee, C. N. Riviere, and W. T. Ang, "Feedforward controller of ill-conditioned hysteresis using singularity-free Prandtl-Ishlinskii model," *IEEE/ASME Transactions on Mechatronics*, vol. 14, no. 5, pp. 598–605, 2009.
- [12] X. Wang, Y. Mao, X. Wang, and C. Su, "Adaptive variable structure control of hysteresis in GMM actuators based on Prandtl-Ishlinskii model," in *Proceedings of the 33rd Annual Conference of the IEEE Industrial Electronics Society (IECON '07)*, vol. 1–3, pp. 721–726, Taipei, Taiwan, November 2007.
- [13] M. Goldfarb and N. Celanovic, "Modeling piezoelectric stack actuators for control of micromanipulation," *IEEE Control Systems Magazine*, vol. 17, no. 3, pp. 69–79, 1997.
- [14] M. Quant, H. Elizalde, A. Flores, R. Ramirez, P. Orta, and G. Song, "A comprehensive model for piezoceramic actuators: modelling, validation and application," *Smart Materials and Structures*, vol. 18, no. 12, 2009.
- [15] T. J. Yeh, S. W. Lu, and T. Y. Wu, "Modeling and identification of hysteresis in piezoelectric actuators," *Journal of Dynamic Systems, Measurement and Control-Transactions of the ASME*, vol. 128, no. 2, pp. 189–196, 2006.
- [16] J. L. Ha, Y. S. Kung, R. F. Fung, and S. C. Hsien, "A comparison of fitness functions for the identification of a piezoelectric hysteretic actuator based on the real-coded genetic algorithm," *Sensors and Actuators A*, vol. 132, no. 2, pp. 643–650, 2006.
- [17] J. L. Ha, R. F. Fung, and C. S. Yang, "Hysteresis identification and dynamic responses of the impact drive mechanism," *Journal of Sound and Vibration*, vol. 283, no. 3-5, pp. 943–956, 2005.
- [18] A. Preumont, *Vibration Control of Active Structures, An Introduction*, Kluwer Academic Publishers, Dodrecht, The Netherlands, 2002.

## Research Article

# Fabrication of Simple and Ring-Type Piezo Actuators and Their Characterization

**B. Sahoo and P. K. Panda**

*Materials Science Division, National Aerospace Laboratories, Council of Scientific and Industrial Research, Bangalore 560017, India*

Correspondence should be addressed to P. K. Panda, pkpanda@nal.res.in

Received 22 November 2011; Accepted 3 January 2012

Academic Editor: Tao Li

Copyright © 2012 B. Sahoo and P. K. Panda. This is an open access article distributed under the Creative Commons Attribution License, which permits unrestricted use, distribution, and reproduction in any medium, provided the original work is properly cited.

A piezo multilayered stack of height 10 mm is fabricated using 80  $\mu\text{m}$  thick PZT tapes prepared by tape-casting technique. About 120 layers of thin tapes are dried, screen-printed with Pt-electrode paste, stacked, laminated, and then isopressed to obtain a green multilayered stack. Cofiring of the stack is carried out at 1250°C for 1 h with very slow heating rate (15° per 1 h). The sintered stack is poled at 2 kV per mm in hot (120°C) silicone oil bath for 45 minutes, and free displacement and block force were characterized. The actuator generates free displacement of 10  $\mu\text{m}$  (0.1% strain) and block force of 1427 N at 175 V. In a similar way, a ring-shaped multilayered PZT stack was fabricated; the displacement was measured to be 8  $\mu\text{m}$ . The ring-type actuator is mainly used for fluid flow control in space vehicles.

## 1. Introduction

Piezo actuators/sensors are mainly used for smart applications because of their (i) fast response time, (ii) high frequency response, (iii) precession control, (iv) capability of generating high block force, and so forth [1]. The sensors and actuators with appropriate control unit together form a smart system. Piezo sensors and actuators are used for various applications such as vibration control of aerospace structures, development of smart aeroplane wings, propellant flow control in space vehicles, and fuel flow control in automobile engines. Lead zirconate titanate (PZT) is a well-known piezo material that produces electric charges on application of mechanical stress (as sensor) or undergoes dimensional change when subjected to an electric field (as actuator) [2–6]. For these properties PZT is frequently used for fabrication of multilayered actuators. Ring-type actuator is a special type of actuators exclusively used for flow control purpose. Weight/size reduction of a space instrument or subsystem of a space craft is necessary to save enormous launching cost as well as to increase the mission duration. The reduction in thrust levels for miniaturized spacecraft requires very fine propellant flow rates. Solenoid valves used for flow control are very heavy. Piezo-material-based

microactuators could be best suitable for these applications due to their precision flow control [7] effected by the gradual application of voltage and also due to their low weight.

Therefore, in this study, an effort has been made to fabricate PZT multilayered stack and a ring-type actuator by tape casting technique and block force and displacement were characterized.

## 2. Experimental Procedure

**2.1. Fabrication of Simple Multilayered (ML) Stack.** PZT stacks were fabricated by tape casting method using in-house prepared PZT powders [8]. A well-dispersed PZT slurry was prepared using required amount of PZT powder, organic solvents (methyl ethyl ketone and ethanol), dispersant (Triton), binder, plasticizers, and so forth, by ball milling for 72 hr. The slurry was then filtered and cast on a silicon-coated Mylar sheet using a laboratory tape caster. The thickness of the green tapes is varied between 20  $\mu\text{m}$  and 200  $\mu\text{m}$  by changing the parameters such as the clearance of doctor blade, the casting speed, the viscosity of the slurry. The process flow sheet for fabrication of ML stack by tape casting technique is presented in Figure 1.

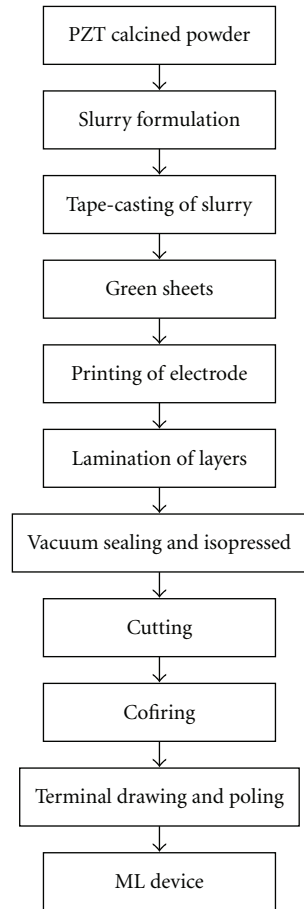


FIGURE 1: Process flow sheet for fabrication of ML stack by tape casting technique.

The green tapes of thickness  $80\ \mu\text{m}$  were dried, cut into required dimensions, screen-printed with platinum electrode paste, and dried. The individual layers are then stacked and laminated one above the other using uniaxial stacking machine. Following the above procedure, a ML stack of height 12 mm (green stage) is fabricated. The stack is then iso-pressed at 30 MPa for 5 min with preheating at  $60^\circ\text{C}$  for 5 min. Binder burnout of the stacks is carried out at  $520^\circ\text{C}$  for 2 hours with very slow heating rate ( $15^\circ$  per 1 h). The cofiring of the stack is done at  $1250^\circ\text{C}$  for 1 h. The stack is leveled to have parallel surface, finished and electrode, and two terminals are drawn by soldering the wires. The photograph of fabricated simple ML stacks is shown in Figure 2. The stack is then poled at  $2\ \text{kV}/\text{mm}$  in hot ( $120^\circ\text{C}$ ) silicone oil bath for 45 minutes, and displacement and block force were characterized.

## 2.2. Fabrication of the Ring Actuator

**2.2.1. Working Principle.** The design of the actuator is mainly used for the flow control of fluid. The ring portion of the actuator in inverted position is glued to a substrate. On application of dc voltage, the active ring stack expands in upward direction and the middle inactive rod attached to the

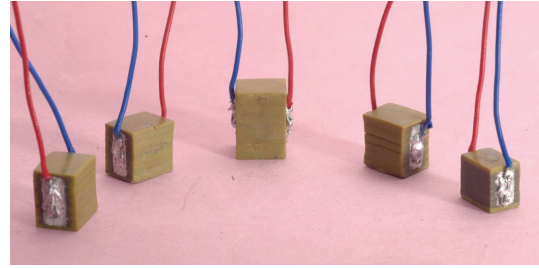


FIGURE 2: Photograph of in house fabricated simple ML stacks.

cap remains as such which produces a gap in between the substrate and the middle rod and facilitates the flow of fluid. A schematic diagram for flow control using this actuator is presented in Figure 3.

**2.2.2. Fabrication.** The ring-type actuator consists of three parts: (i) an active PZT ring stack prepared by 70 layers of annular-shaped (ID = 12 mm, OD = 18 mm) PZT tapes stacked using platinum as internal electrode, (ii) a central cylindrical PZT rod of 8.7 mm diameter fabricated using 80 piezo layers, and (iii) the inactive circular base consisting of 10 piezo layers. The final ring actuator was fabricated by attaching the central rod and active ring stack to the circular PZT base such that a gap is maintained to facilitate the displacement of the active ring actuator. The photograph of the fabricated actuator is presented in Figure 4. The final dimensions of the actuator are (i) height: 12 mm, (ii) internal rod diameter: 8 mm, and (iii) ring diameter: 15.5 mm (outer) and 9.5 mm (internal). The active region of the stack was electrode and poled at  $2\ \text{kV}/\text{mm}$  and, the displacement was measured.

## 3. Results and Discussions

**3.1. Measurement of Displacement and Block Force.** The displacement of fabricated simple ML stack and the ring actuator was measured without application of mechanical load. The actuator is placed on a plane rigid support on top of which the tip of the strain gauge is placed with an initial reading set to zero. A test set-up measurement for displacement of the PZT stack actuators is presented in Figure 5.

The terminals of the actuator are connected to appropriate terminals of a dc source, and the voltage is gradually increased. It is observed that the displacement increases with the increase in voltage and a maximum displacement of  $10\ \mu\text{m}$  and  $8\ \mu\text{m}$  is measured for simple ML stack and ring actuator, respectively. The typical plot of the displacement versus voltage is presented in Figures 6 and 7, respectively.

The simple ML stack is characterized for block force using a block force measuring unit (Figure 8). The actuator is placed on top of a force sensor (load cell) inside the sample holder, and its positive and negative terminals are properly connected to the respective terminals of the voltage source. For measurement of block force, a constant prestress is applied from top of the actuator through 3-4 springs of

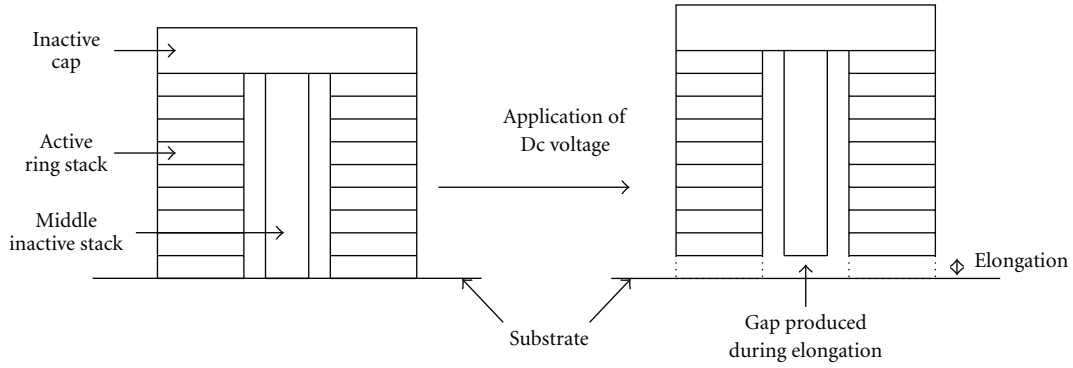


FIGURE 3: Working principle of a ring actuator.

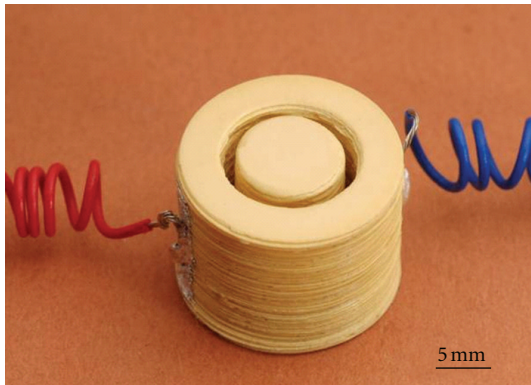


FIGURE 4: Photograph of fabricated ring actuator.

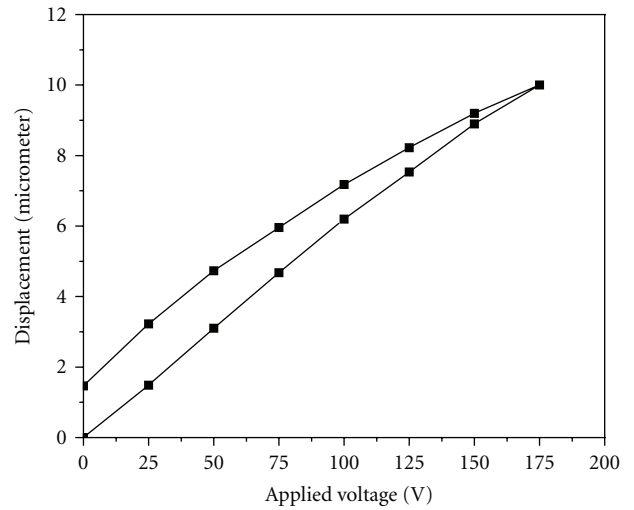


FIGURE 6: Displacement versus voltage graph of simple ML stack.

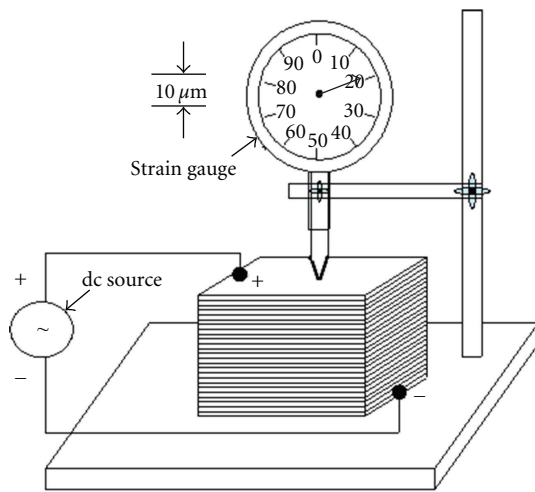


FIGURE 5: A test set up measurement for displacement of the ML stacks.

different stiffness. The actuator observes higher force with the spring having higher stiffness. The values of displacement and force generated by the actuator for all the springs are plotted by block force measurement software. It is observed that a maximum block force of 1427 N is obtained at 175 V.

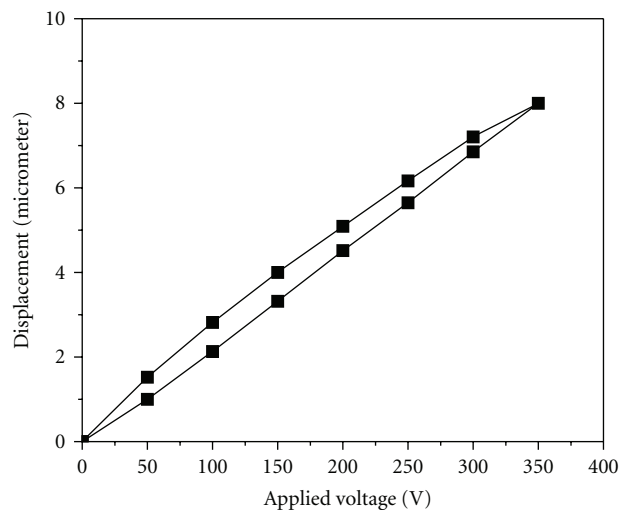


FIGURE 7: Typical plot of the displacement versus voltage of ring actuator.

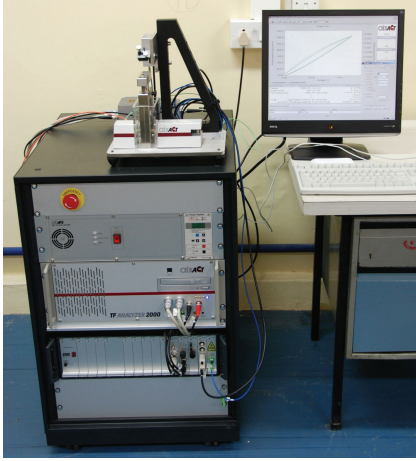


FIGURE 8: Photograph of the block force measurement unit.

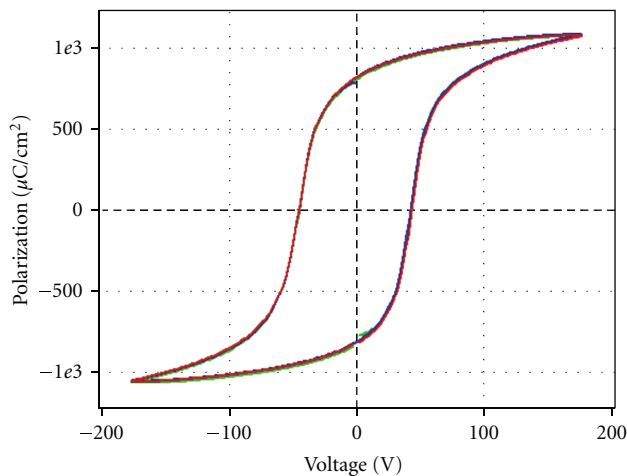


FIGURE 9: Typical hysteresis curve of fabricated ML stack.

The hysteresis of the PZT stack was also measured using the same equipment. The hysteresis curve generated for the PZT stack is shown in Figure 9. It is observed that the remnant polarization ( $P_r$ ) and coercive field ( $E_c$ ) are  $804 \mu\text{C}/\text{cm}^2$  and  $41 \text{ V}$ , respectively.

#### 4. Conclusions

A piezo multilayered stack of height  $10 \text{ mm}$  is fabricated using  $80 \mu\text{m}$  thick PZT tapes prepared by tape casting technique. It generates free displacement of  $10 \mu\text{m}$  ( $0.1\%$  strain) and block force of  $1427 \text{ N}$  at  $175 \text{ V}$ . The remnant polarization ( $P_r$ ) and coercive field ( $E_c$ ) of the stack are found to be  $804 \mu\text{C}/\text{cm}^2$  and  $41 \text{ V}$ , respectively. A special type of ring actuator was fabricated by tape casting technique using in-house-prepared PZT powder. The displacement of the actuator was measured to be  $8 \mu\text{m}$  at  $350 \text{ V}$ . It was observed that the displacement is almost linear to the applied voltage; therefore, the precision control of the fluid flow is expected.

#### Acknowledgments

The authors gratefully acknowledge the Head of Materials Science Division and the Director, NAL, for their encouragement and the support during the course of this study.

#### References

- [1] C. Nizrecki, D. Brei, S. Balakrishnan, and A. Moskalik, "Piezoelectric actuation: state of the art," *Shock and Vibration Digest*, vol. 33, no. 4, pp. 269–280, 2001.
- [2] R. E. Newnham and G. R. Ruschau, "Smart electroceramics," *American Ceramic Society Bulletin*, vol. 75, no. 10, pp. 51–61, 1996.
- [3] G. H. Haertling, "Rainbow ceramics—a new type of ultra-high-displacement actuator," *American Ceramic Society Bulletin*, vol. 73, no. 1, pp. 93–98, 1994.
- [4] R. E. Newnham and G. R. Ruschau, "Smart electroceramics," *Journal of the American Ceramic Society*, vol. 74, no. 3, pp. 463–480, 1991.
- [5] E. F. Crawley and J. de Luis, "Use of piezoelectric actuators as elements of intelligent structures," *AIAA Journal*, vol. 25, no. 10, pp. 1373–1385, 1987.
- [6] K. Uchino, "Advances in ceramic actuator materials," *Materials Letters*, vol. 22, no. 1–2, pp. 1–4, 1995.
- [7] E.-H. Yang, C. Lee, J. Mueller, and T. George, "Leak-tight piezoelectric micro valve for high-pressure gas micro propulsion," *Journal of Microelectromechanical System*, vol. 13, no. 5, pp. 799–807, 2004.
- [8] B. Sahoo, V. A. Jaleel, and P. K. Panda, "Development of PZT powders by wet chemical method and fabrication of multilayered stacks/actuators," *Materials Science and Engineering B*, vol. 126, no. 1, pp. 80–85, 2006.

## Research Article

# Electromechanical and Dynamic Characterization of In-House-Fabricated Amplified Piezo Actuator

P. K. Panda,<sup>1</sup> B. Sahoo,<sup>1</sup> S. Raja,<sup>2</sup> Vijaya Kumar M. P.,<sup>2</sup> and V. Shankar<sup>2</sup>

<sup>1</sup>Materials Science Division, National Aerospace Laboratories, Council of Scientific and Industrial Research, Bangalore 560017, India

<sup>2</sup>Structural Technologies Division, National Aerospace Laboratories, Council of Scientific and Industrial Research, Bangalore 560017, India

Correspondence should be addressed to P. K. Panda, pkpanda@nal.res.in

Received 21 November 2011; Accepted 27 December 2011

Academic Editor: Tao Li

Copyright © 2012 P. K. Panda et al. This is an open access article distributed under the Creative Commons Attribution License, which permits unrestricted use, distribution, and reproduction in any medium, provided the original work is properly cited.

A diamond-shaped amplified piezo actuator (APA) fabricated using six multilayered piezo stacks with maximum displacement of 173  $\mu\text{m}$  at 175 V and the amplification factor of 4.3. The dynamic characterization of the actuator was carried out at different frequencies (100 Hz–1 kHz) and at different AC voltages (20 V–40 V). The actuator response over this frequency range was found neat, without attenuation of the signal. Numerical modeling of multilayered stack actuator was carried out using empirical equations, and the electromechanical analysis was carried out using ABAQUS software. The block force of the APA was 81 N, calculated by electromechanical analysis. This is similar to that calculated by dynamic characterization method.

## 1. Introduction

Lead zirconate titanate (PZT) is a well-known piezo material that produces electric charges on application of mechanical stress (as sensor) or undergoes dimensional change when subjected to an electric field (as actuator) [1–5]. One major drawback of the piezo materials is the low displacement of the order of 0.1–0.15% of the total length; therefore, thick piezo stacks are required even for the moderate-strain requirements. For high-strain requirements wherein the requirement of the strain is in few millimeters, simple multilayer stacks are not suitable. This leads to the development of the various types of high-strain amplified actuators such as hydraulic actuator [6–13], Moonie [14] and Cymbal [15], diamond-shaped actuator, and bow-shaped actuator.

In this study, the details of the fabrication and characterization of a diamond-shaped amplified actuators rare presented. Numerical modeling of multilayered stack actuator and amplified actuator is carried out using empirical equations and the electromechanical analysis using ABAQUS software. The values are correlated to the experimental results.

## 2. Experimental Procedure

**2.1. Preparation of PZT Slurry.** PZT stacks were fabricated by tape-casting method using in-house-prepared PZT powders [16]. A well-dispersed PZT slurry was prepared using required amount of PZT powder, organic solvents (methyl ethyl ketone and ethanol), dispersant (Triton), binder, plasticizers, and so forth, by ball milling for 72 hr. An optimized PZT slurry composition is presented in Table 1. The slurry was then filtered and cast on a silicon-coated Mylar sheet using a laboratory tape caster. The thickness of the green tapes is varied between 20  $\mu\text{m}$  and 200  $\mu\text{m}$  by changing the parameters such as the clearance of doctor blade, the casting speed, and the viscosity of the slurry.

**2.2. Fabrication of Multilayered (ML) Stack.** The green PZT tapes of thickness 80  $\mu\text{m}$  were dried, cut into required dimensions, screen-printed with platinum electrode paste, and dried. The individual layers are then stacked and laminated one above the other using uniaxial stacking machine. Following the above procedure, 6 numbers of identical ML

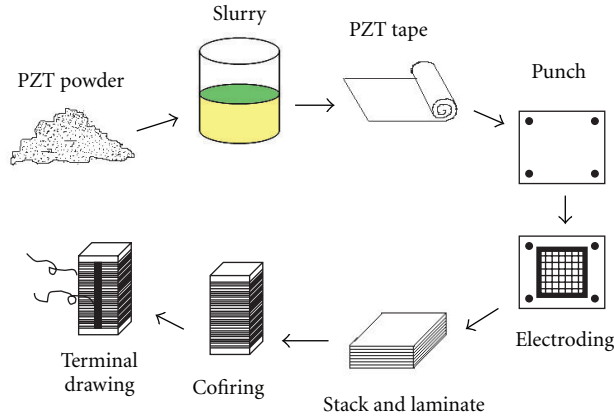


FIGURE 1: Pictorial representation of fabrication procedure of ML stack.

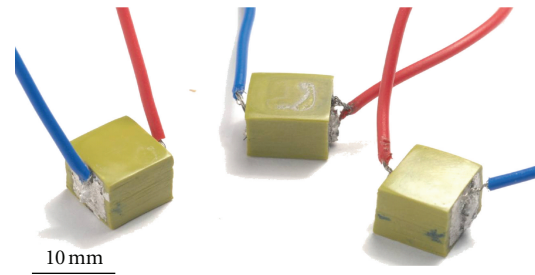


FIGURE 2: Typical picture of fabricated ML stacks.

TABLE 1: Typical PZT slurry composition.

Components	Amounts (%)
PZT powder	65–70
Dispersant	1.25
Solvent	25
Plasticizer	1.75
Binder	2

stacks of height 14 mm (green stage) are fabricated. All the stacks are then isopressed at 30 MPa/5 min with preheating at 60°C/5 min. Binder burnout of the stacks is carried out at 520°C/2 h with very slow heating rate (15°C/1 h). The cofiring of the stacks is done at 1250°C/1 h. The stacks are leveled to have parallel surfaces, finished, and electrode, and two terminals are drawn by soldering the wires. A pictorial representation of fabrication procedure of ML stack is shown in Figure 1. The stacks are then poled at 2 kV/mm in hot silicone oil bath for 45 min, and displacement and block force were characterized. Typical picture of the fabricated ML stack is shown in Figure 2.

**2.3. Fabrication of Al Frame and APA.** An aluminium metal frame of length 60 mm (internal) and height 24 mm (internal) is fabricated. The inside angle of the frame with its mid-

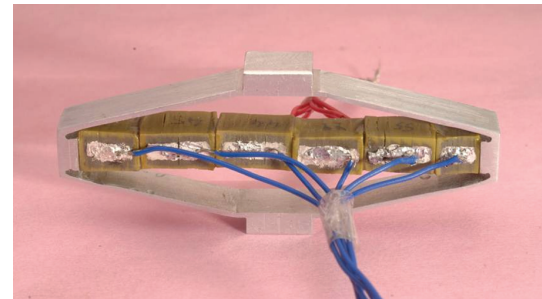


FIGURE 3: A typical picture of fabricated diamond-shaped APA.

dle horizontal line is 15°. All the 6 PZT stacks are then fixed inside the metal frame using a flange in a prestressed condition. The photograph of fabricated diamond-shaped PZT actuator is shown in Figure 3. The weight of the APA is 26.5 g.

### 3. Results and Discussions

**3.1. Displacement and Block Force Measurement.** The individual ML stacks are characterized for displacement and block force using a block force measuring unit. The actuator is placed on top of a force sensor (load cell) inside the sample holder, and its positive and negative terminals are properly connected to the respective terminals of the voltage

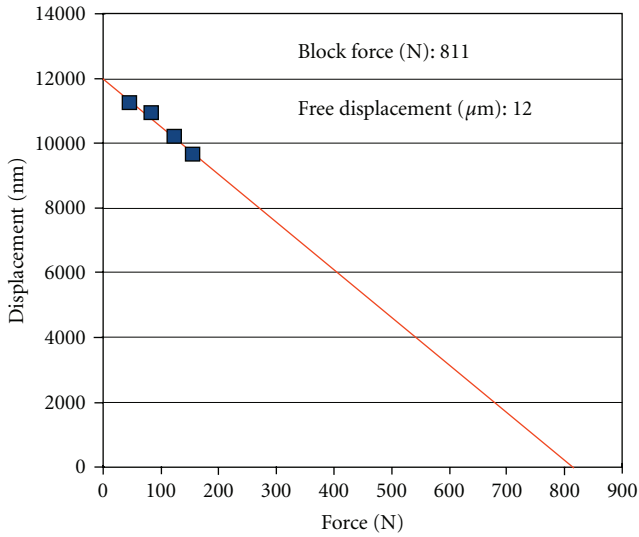


FIGURE 4: Block force versus free displacement graph of ML stack.

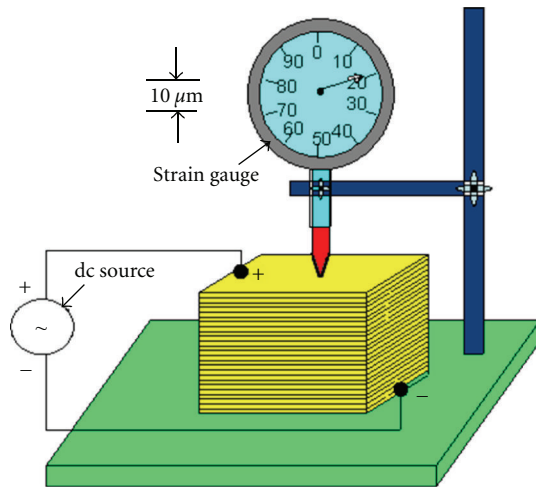


FIGURE 5: Test setup for displacement measurement of the actuators [16].

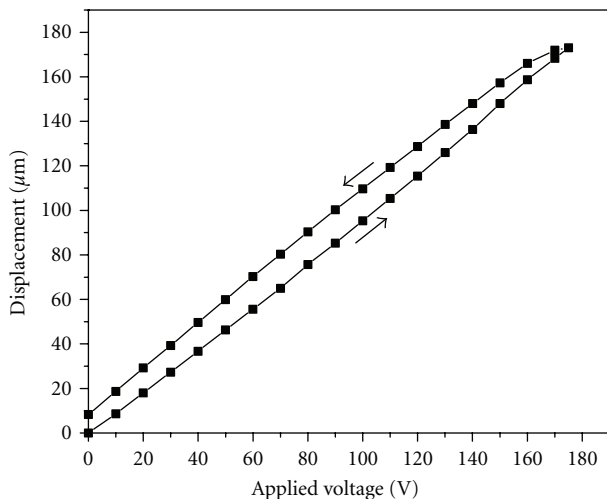


FIGURE 6: Displacement versus voltage graph of APA.

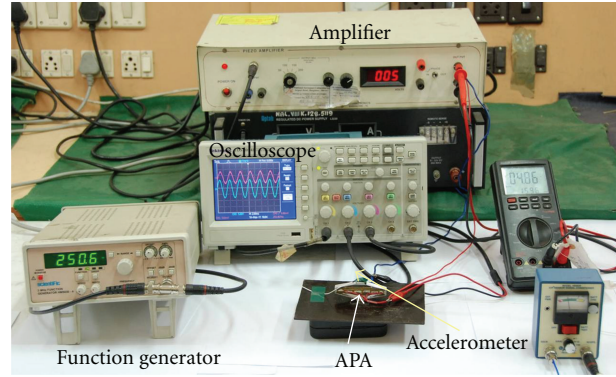


FIGURE 7: Test setup for voltage and frequency characterization of the APA.

source. Displacement of the actuator is measured by a highly sensitive laser interferometer. For measurement of block force, the actuator is prestressed by selecting a suitable spring of specific stiffness. The displacement and the force generated by the actuator for different springs are plotted. The software calculates a linear fit for these points. The block force is determined from the intersection points of the line on X-axis, and the free displacement is measured from its intersection on Y-axis. The graph of displacement versus force is shown in Figure 4.

The displacement characteristics of the APA and assembled ML stacks are measured using a strain gauge. The test setup for displacement measurement of the APA is shown in Figure 5. It is observed that the displacement increases with increase in voltage, and a maximum displacement of  $173 \mu\text{m}$  and  $40 \mu\text{m}$  is measured for APA and assembled ML stacks, respectively, at 175 V. On decreasing the voltage, the displacement curve does not follow the same path and a hysteresis loop is obtained (Figure 6). The amplification factor for diamond-shaped APA is nearly 4.3 times.

**3.2. Dynamic Characterization of Amplified Actuator.** The piezo stack as an electrical load is capacitive in nature. The capacitance of the stack assembly is measured and is around  $2.42 \mu\text{F}$ . This is a useful parameter in the design of electronics actuator amplifier for APA.

**3.3. Characterization of the Actuator at Different AC Signal and Frequency.** For vibration control applications, it is necessary to characterize the dynamic response of the stack at different amplified sinusoidal AC signal and at different frequencies. The dynamic response of APA was carried out at 40 V ( $\pm 20$  V) peak to peak and up to a frequency of 1 KHz. The test setup is shown in Figure 7. A sinusoidal input signal to the stack assembly produces mechanical vibrations on the stack which is coupled to a unit under test (UUT) either to carry out UUT’s resonance search (open loop) or to control UUT’s vibrations (closed loop). For dynamic applications, it is necessary to quantify the acceleration response on the stack assembly with respect to force input to the APA stack assembly at different input voltage levels as well as at different frequencies. A miniature accelerometer

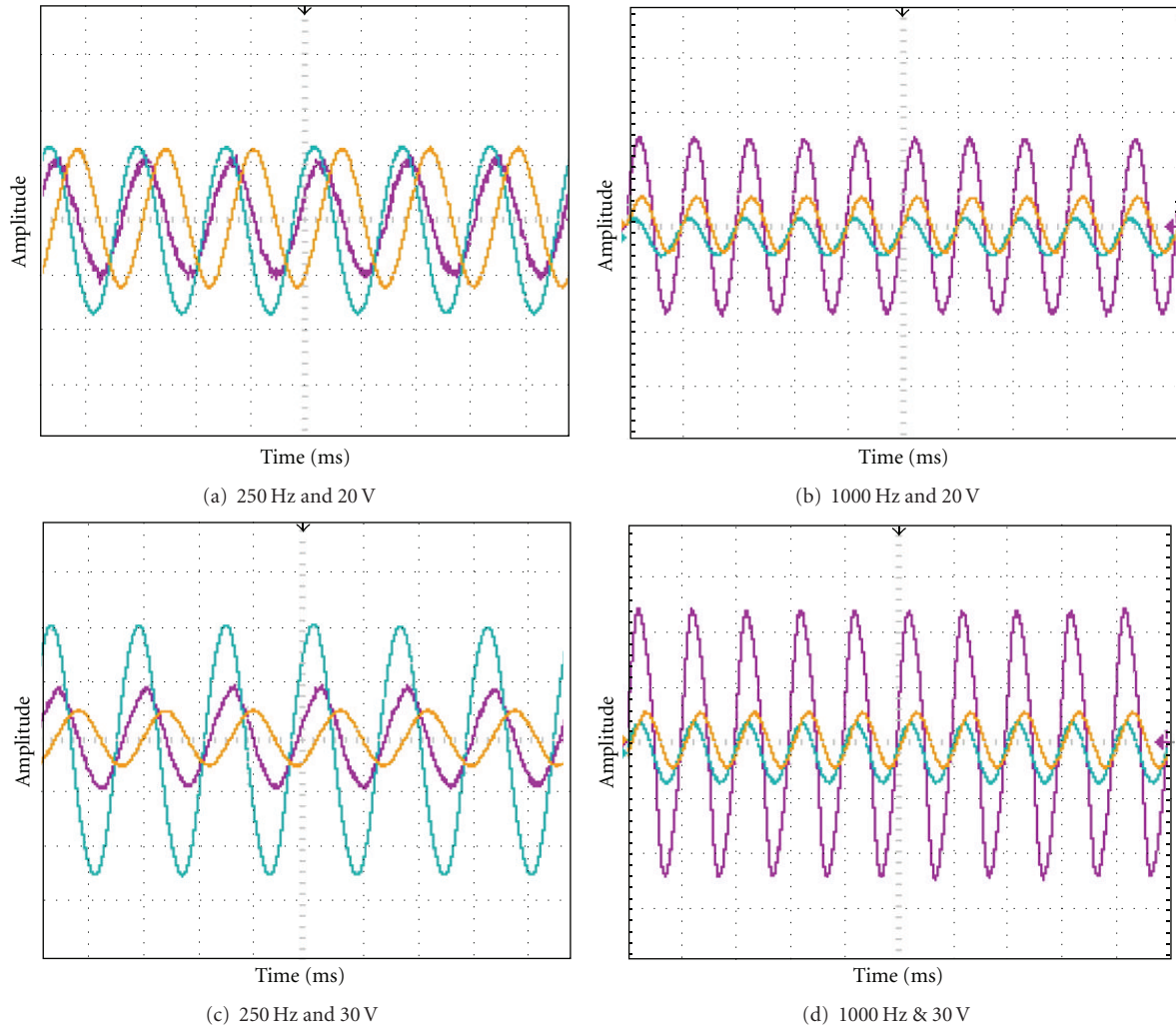


FIGURE 8: Typical plots of actuator response at (a) 250 Hz and 20 V, (b) 1000 Hz and 20 V, (c) 250 Hz and 30 V, and (d) 1000 Hz & 30 V.

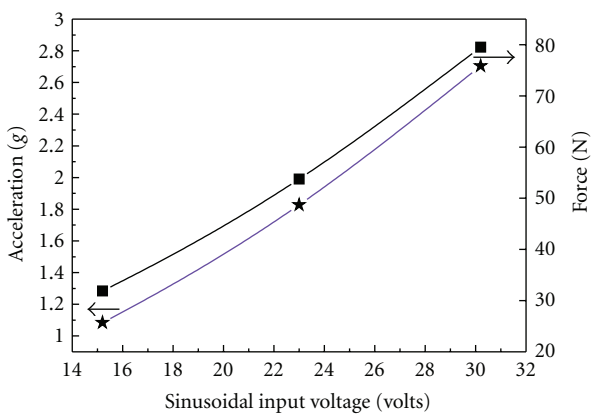


FIGURE 9: Variation of “g” and actuator force versus input voltage.

(with 10.5 mV/g sensitivity and 0.2 g weight) was mounted on the stack followed by its signal conditioning amplifier.

The weight of the APA stack assembly is 26.5 grams. The total weight of the APA stack assembly and accelerometer together is 26.7 grams. Experiments were carried out and measurements were recorded on digital storage oscilloscope at three different sinusoidal input drive voltage levels (20 Vp-p, 30 V p-p and 40 V p-p) to the stack actuator and in the frequency range of 125 Hz to 1 KHz. Typical plots of response of stack at 250 Hz and at 1000 Hz are presented in Figures 8(a)–8(d). From the sensitivity of the accelerometer and the mill volt output produced by the actuator, the acceleration (g) and the force produced by the actuator were calculated. The “g” was 2.7 g/cm<sup>2</sup>, and the force was 81 N at 40 volts, and the variation at different voltage is presented in Figure 9.

**3.4. Numerical Modeling of Multilayered Stack Actuator.** The stack actuators are made up of thin layers of PZT patches, laminated one over the other. Modeling all the thin layers of PZT stack using the piezoelectric solid finite element, available in commercial software is cumbersome. Hence,

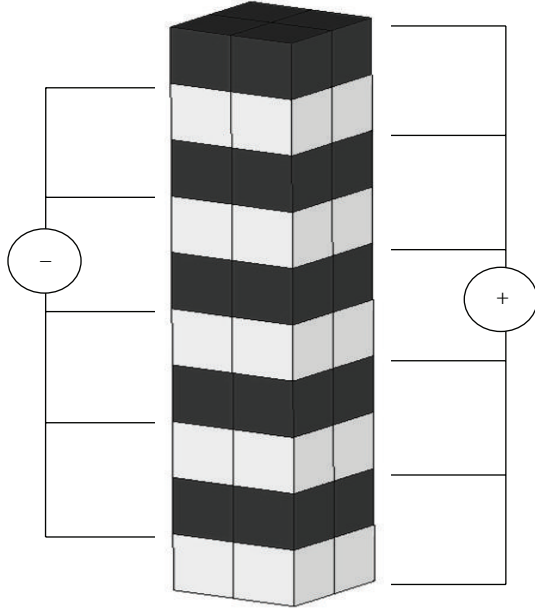


FIGURE 10: Finite-element model of the stack actuator.

TABLE 2: Actuator material properties.

Properties	Data	units
Young's modulus	45	GPa
Piezoelectric constant	$390 \times 10^{-12}$	m/v
Density	7500	kg/m <sup>3</sup>
Poissons ratio	0.22	—

an equivalent model is built from the following empirical relations:

$$\begin{aligned}
 Dx &= n' d'_{33} EV, \\
 E_{33} &= \frac{F'_{\text{block}} t}{d'_{33} A' EV}, \\
 t &= \frac{\text{length of the stack actuator}}{\text{number of layers in the actuator}}, \\
 \phi_{\text{fem}} &= \frac{\text{voltage}_{\text{cal}} \times \text{thickness}_{\text{fem}}}{\text{thickness}_{\text{cal}}},
 \end{aligned} \quad (1)$$

where  $E_{33}$  is Young's modulus,  $d_{33}$  represents piezoelectric strain constant,  $n$  indicates the number of layers,  $EV$  refers to the electric potential across each layer,  $A$  is cross-sectional area of the stack actuator,  $t$  is thickness of each layer,  $\phi_{\text{fem}}$  denotes equivalent electric potential in finite-element method.

**3.5. Finite-Element Modeling of the Stack Actuator.** Assuming 10 piezo layers, each of piezoelectric strain constant ( $390 \times 10^{-12}$  C/N), a finite-element model was created using square cross-section elements to avoid any discrepancy (Figure 10). The two consecutive layers of the finite-element model will have opposite polarity to each other, so as to obtain the extension/compression from all the layers simultaneously

TABLE 3: Characteristics of the actuator (actuator APA).

Description	Data	Units
Displacement	41	$\mu\text{m}$
Blocked force	1450	N
Voltage range	175	V
Height	61.9	mm
Area	$8 \times 6$	mm <sup>2</sup>

TABLE 4: Free deflection and block force of the stack actuator.

Analysis	Displacement ( $\mu\text{m}$ )	Blocked force (N)
APA	41	1450
FEA (ABAQUS)	40.9	1452

(i.e., parallel capacitor configuration). The actuator material properties used for modeling are presented in Table 2. Similarly, the characteristics of the actuator are presented in Table 3.

The actuator is characterized using the stress-strain relation of a coupled electromechanical system

$$\{s\} = [C]\{\varepsilon\} - [C][d]\{E_k\}, \quad (2)$$

where  $C$  is the material stiffness matrices (N/m<sup>2</sup>),  $d$  is the piezoelectric strain constant (m/v),  $E_k$  is the electric field (v/m), and  $\varepsilon$  is the material strain.

**3.6. Electromechanical Analysis Using ABAQUS.** The free deflection and the block force are measured from the electromechanical analysis using ABAQUS. While the free deflection is the actuator deformation when maintained in an unconstrained state with the maximum applied voltage, the block force is the reaction developed by the actuator when maintained in a completely constrained state. The results of the analysis compared with the measured results are presented in Table 4, and the block force and free displacement profile are presented in Figures 11(a) and 11(b).

Figure 12 represents the CAD model of APA, in which the casing is made of aluminum material, and the actuator is placed in between the casing. The aluminum material properties used are Young's modulus  $E = 70$  GPa, density = 2720 kg/m<sup>3</sup>, and Poisson's ratio 0.3.

The weight of the APA is approximately 26.5 grams. Finite-element model of APA is made in Hypermesh and subsequently analyzed for static loading. Further the free vibration analysis is performed using ABAQUS. The static analysis has shown that the casing is safe with a factor of safety 4.7.

**3.7. Piezo Static and Electromechanical Analysis of the APA.** Piezoelectric analysis is carried out with upper and lower pads completely constrained ( $u, v, w = 0$ ) (Figure 13). By applying an equivalent voltage (175 V), the von Mises stress (92 MPa) and the block force are computed (81 N), respectively. Further analysis is done for finding the induced displacement of the APA actuator under unconstrained

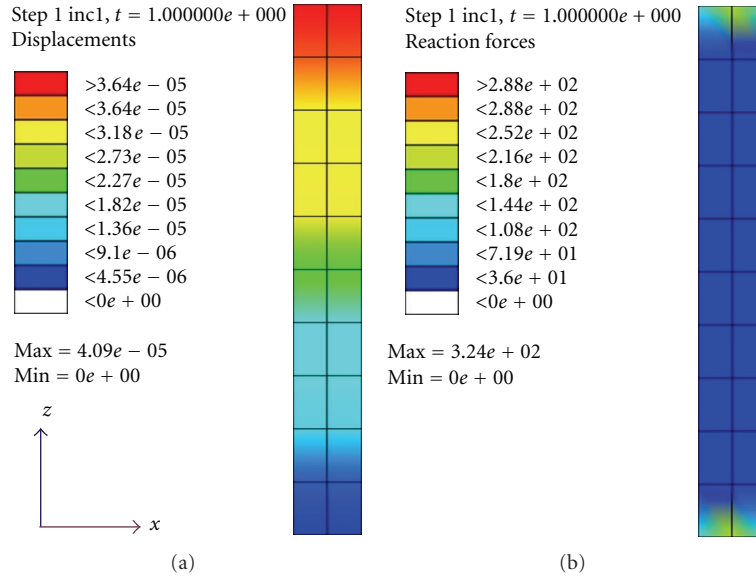


FIGURE 11: (a) Free displacement and (b) block force measurement using FEA.

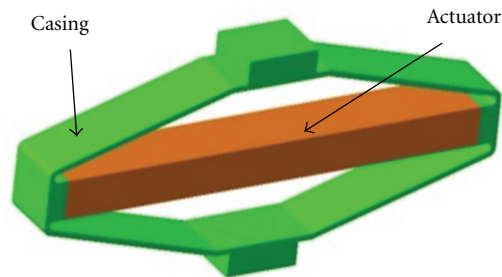


FIGURE 12: CAD model of the APA.

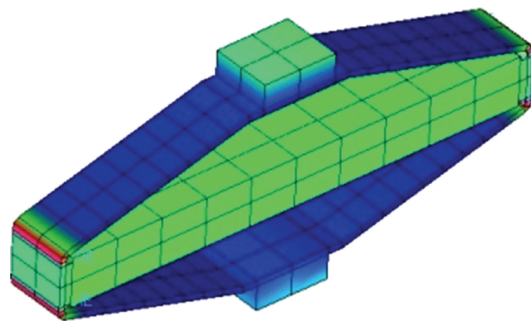


FIGURE 13: Pzeio static analysis APA actuator.

state ( $148 \mu\text{m}$ ). The result is presented in Figure 14. Similarly for different actuator voltages, the free deflections are computed, at actuator level as well as for the APA. The results are presented in Table 5 for different voltage configurations.

#### 4. Conclusions

A diamond-shaped APA was successfully fabricated by designing suitable metal frame and using 6 multilayered PZT stacks. The APA produces displacement of  $173 \mu\text{m}$  with

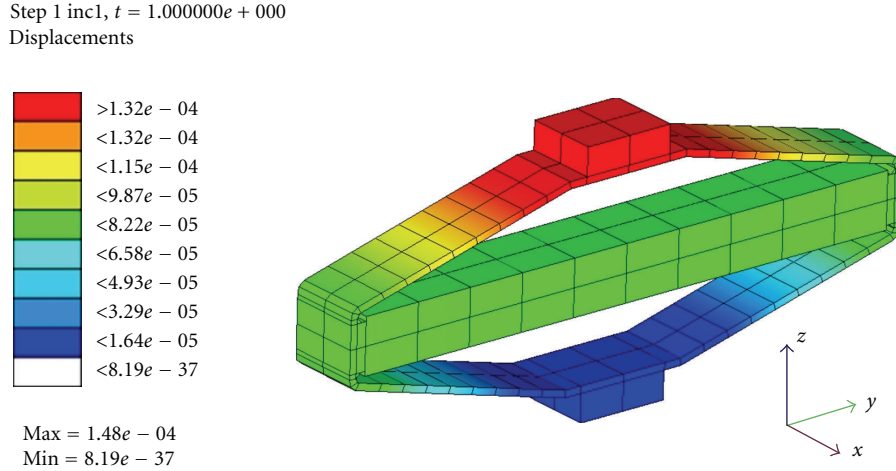


FIGURE 14: Electromechanical analysis of APA.

TABLE 5: Displacement values of APA.

Actuator Voltage (V)	Equivalent numerical voltage (V)	ABAQUS-free Displacement of actuator ( $\Delta x$ ) $\mu\text{m}$	ABAQUS-APA Displacement ( $\mu\text{m}$ )
175	5250	40.9	148
160	4800	37.4	135
140	4200	32.8	118
120	3600	28.1	102
100	3000	23.4	84.6
80	2400	18.7	67.7
60	1800	14	50.8
40	1200	9.38	33.8
20	600	4.68	16.9
0	0	0	0

displacement amplification of 4.3 times. The actuator was subjected to different frequencies and different AC voltages. The performance was found very well over the frequency range without attenuation of the signal. Both the waveforms, namely, input to the stack actuator and accelerometer output, is showing no distortion thereby indicating the stack actuator assembly is behaving linearly. The equivalent numerical modeling of APA was built, and electromechanical analysis was carried out. The induced displacement obtained was  $148 \mu\text{m}$  for the maximum operational voltage. The actuator free displacement and block force were also computed to be  $40.9 \mu\text{m}$  and  $1450 \text{ N}$ , respectively. The maximum von-Mises stress estimated is  $92 \text{ MPa}$ , which gives a factor of safety of 4.7, and block force generated is  $81 \text{ N}$ . The block force of the APA was  $81 \text{ N}$ , calculated by electromechanical analysis. This is similar to that calculated by dynamic characterization method.

### Acknowledgments

The authors gratefully acknowledge Mr. M. K. Sridhar, Head, Materials Science Division, and Dr. A. R. Upadhya, Director, NAL, for their encouragement and the support during the course of this study. The authors also thank Mr. Chandraiah, project assistant, for his help in preparation of PZT tapes.

### References

- [1] R. E. Newnham and G. R. Ruschau, "Smart electroceramics," *American Ceramic Society Bulletin*, vol. 75, no. 10, pp. 51–61, 1996.
- [2] G. H. Haertling, "Rainbow ceramics-a new type of ultra-high-displacement actuator," *American Ceramic Society Bulletin*, vol. 73, no. 1, pp. 93–98, 1994.
- [3] R. E. Newnham and G. R. Ruschau, "Smart electroceramics," *Journal of the American Ceramic Society*, vol. 74, no. 3, pp. 463–480, 1991.
- [4] E. F. Crawley and J. De Luis, "Use of piezoelectric actuators as elements of intelligent structures," *AIAA Journal*, vol. 25, no. 10, pp. 1373–1385, 1987.
- [5] K. Uchino, "Advances in ceramic actuator materials," *Materials Letters*, vol. 22, no. 1-2, pp. 1–4, 1995.
- [6] J. Juuti, K. Kordás, R. Lonnakko, V. P. Moilanen, and S. Leppävuori, "Mechanically amplified large displacement piezoelectric actuators," *Sensors and Actuators A*, vol. 120, no. 1, pp. 225–231, 2005.
- [7] C. Niezrecki, D. Brei, S. Balakrishnan, and A. Moskalik, "Piezoelectric actuation: state of the art," *The Shock and Vibration Digest*, vol. 33, no. 4, pp. 269–280, 2001.
- [8] A. Dogan, Q. Xu, K. Onitsuka, S. Yoshikawa, K. Uchino, and R. E. Newnham, "High displacement ceramic metal composite actuators (moonies)," *Ferroelectrics*, vol. 156, no. 1, pp. 1–6, 1994.
- [9] L. Denghua, F. Daining, W. Lina, J. Weijun, and J. Meijian, "Cymbal piezocomposites for vibration accelerometer applications," *Integrated Ferroelectrics*, vol. 78, no. 1, pp. 165–171, 2006.

- [10] M. Joshi and S. Priya, "Piezo-bow-high displacement and high blocking force actuator," *Integrated Ferroelectrics*, vol. 82, no. 1, pp. 25–43, 2006.
- [11] H. Zhou and B. Henson, "Analysis of a diamond-shaped mechanical amplifier for a piezo actuator," *International Journal of Advanced Manufacturing Technology*, vol. 32, no. 1-2, pp. 1–7, 2007.
- [12] B. Watson, J. Friend, and L. Yeo, "Piezoelectric ultrasonic micro/milli-scale actuators," *Sensors and Actuators A*, vol. 152, no. 2, pp. 219–233, 2009.
- [13] X. Li, J. S. Vartuli, D. L. Milius, I. A. Aksay, W. Y. Shih, and W. H. Shih, "Electromechanical properties of a ceramic d," *Journal of the American Ceramic Society*, vol. 84, no. 5, pp. 996–1003, 2001.
- [14] Y. Sugawara, K. Onitsuka, S. Yoshikawa, Q. Xu, R. E. Newnham, and K. Uchino, "Metal-ceramic composite actuators," *Journal of the American Ceramic Society*, vol. 75, no. 4, pp. 996–998, 1992.
- [15] J. F. Fernández, A. Dogan, J. T. Fielding, K. Uchino, and R. E. Newnham, "Tailoring the performance of ceramic-metal piezocomposite actuators, "cymbals"," *Sensors and Actuators A*, vol. 65, no. 2-3, pp. 228–237, 1998.
- [16] B. Sahoo, V. A. Jaleel, and P. K. Panda, "Development of PZT powders by wet chemical method and fabrication of multi-layered stacks/actuators," *Materials Science and Engineering B*, vol. 126, no. 1, pp. 80–85, 2006.

## Research Article

# Damping Analyses of Structural Vibrations and Shunted Piezoelectric Transducers

**Saber Mohammadi and Akram Khodayari**

*Mechanical Engineering Department, Razi University, 6714967346 Kermanshah, Iran*

Correspondence should be addressed to Saber Mohammadi, [saberm7@yahoo.com](mailto:saberm7@yahoo.com)

Received 17 November 2011; Accepted 7 December 2011

Academic Editor: Tao Li

Copyright © 2012 S. Mohammadi and A. Khodayari. This is an open access article distributed under the Creative Commons Attribution License, which permits unrestricted use, distribution, and reproduction in any medium, provided the original work is properly cited.

Piezoelectric transducers in conjunction with appropriate electric networks can be used as a mechanical energy dissipation device. Alternatively, undesired mechanical energy of a structure could be converted into electrical energy that can be dissipated through a shunt network in the form of Joule heating. This paper presents an experimental method to calculate damping energy in mechanical systems. However, the mathematical description of damping mechanism is much more complicated, and any process responsible for the occurrence of damping is very intricate. Structural and piezoelectric damping are calculated and analysed in the case of pulse switching or SSDI semiactive vibration control technique. This technique which was developed in the field of piezoelectric damping consists in triggering the inverting switch on each extremum of the piezoelectric voltage which induces an increase of the electromechanical energy conversion.

## 1. Introduction

Vibration damping is one of the manifestations of mechanical energy dissipation related to motion in mechanical systems. Damping processes have been studied for a long time. Damping forces are small compared to the other interactions in a mechanical system and yet their mathematical description remains much more complicated. Actually, any process responsible for the occurrence of damping is very intricate and the knowledge of it is insufficient. Sometimes just changing the system's stiffness or mass to alter the resonance frequencies can reduce the unwanted vibration as long as the excitation frequencies do not change. But in most cases, the vibrations need to be dissipated using damping materials or devices that are tuneable with vibration.

Several methods have been investigated in case of vibration damping. These methods have the forms of passive, semiactive, and active treatments which can be used for sound/vibration cancellation. Active control involves the use of active elements (actuators) along with sensors and controllers (analogue or digital) to produce an out-of-phase actuation to cancel the disturbance causing the noise/vibration [1]. All other methods that do not include

a real-time active algorithm can be grouped under the passive control option. Passive damping refers to energy dissipation within the structure by add-on damping devices. Viscous dampers (dashpots), viscoelastic damping, tuned-mass dampers, dynamic absorbers, and shunted piezoelectric dampers are the mechanisms of passive vibration control. The most common types of passive damping treatments of viscoelastic materials were described by Rao [2]. Tuned dampers are the reactive devices which used to oscillation damping at a particular resonant frequency. It consists of an inertia element, a compliant/resilient element, and an energy dissipating element. The inertial, resilient, and dissipative elements in such devices are: mass, spring and dashpot. Depending on the application, these devices are sized from a few grams to many tons. They attract the vibration energy of the target mode and dissipate it as heat through the action of its dashpot.

Electronic damping using piezoelectric ceramics (Piezo-Shunt) is less temperature sensitive and more tuneable compared with viscoelastic damping treatments. In this damping technique, the mechanical energy of the structure is converted to electrical energy by piezoelectric material. The electrical energy, in turn is dissipated, as heat, in an electrical

shunt circuit. These methods are interesting because they do not rely on any operative energy as in active control. They consist in the drive of a few solid-state switches (i.e., MOSFET transistor) requiring very few power and, in general, are simple to implement. Pulse switching damping technique [3–7] which is implemented in this paper consists in leaving the piezo elements in open-circuit except during very brief period of time where the electric charge is either suppressed in a short circuit or inverted on an inductance.

Many various terms are used to represent vibration damping. These representations merely indicate the mathematical model used to represent the physical mechanism of damping that is still not clearly understood for many cases [8, 9]. The purpose of this paper is the practical measurement of damping energy which is the vital problem in vibrating systems. The effects of piezoelectric damping and structural damping are observed experimentally and compared with each other. At the following, the damping behaviors in low and high values of deformation are studied. In order to analyse the vibration damping, a multimodal structure equipped with piezoelectric elements wired on a pulse switching cell is experimented.

## 2. Energy Analyses and Energetic Considerations

In vibration analyses, it is concerned with damping in terms of system response. The loss of energy from the oscillatory system results in the decay of free vibration amplitude. In steady-state forced vibration, the loss of energy is balanced by the energy which is supplied by the excitation. Energy dissipation is usually determined under conditions of cyclic oscillations. The energy dissipated per cycle due to a damping force  $F_d$  is computed from the general equation [8]

$$W_d = \oint F_d du, \quad (1)$$

where  $u$  is the displacement. On the other hand, experiments by several investigators [8] indicate that for most structural metals (such as steel), the energy dissipated per cycle (*structural damping*) proportional to the squared of the vibration amplitude and independent of the frequency over a wide frequency range. Then energy dissipated by structural damping may be written as [10]

$$W_d = \alpha_d u_{\max}^2, \quad (2)$$

where  $\alpha_d$  is a constant independent of the frequency of harmonic oscillation and  $u_{\max}$  is the amplitude of vibration. Material in cyclic stress exhibits a stress-strain relation characterized by a hysteresis loop. The cyclic dissipated energy is proportional to the hysteresis loop area. Consequently, the energy balance equation based on hysteresis loop can be deduced. The following is an equation of motion of a vibrating system

$$\ddot{u} = F_i(u, \dot{u}) + F_e(t), \quad (3)$$

where  $F_i(u, \dot{u})$  and  $F_e(t)$  correspond to internal and external forces per unit mass, respectively. The external and the internal loops (hysteresis loops) can be then described by

$$F_e = F_e(u), \quad F_i = F_i(u). \quad (4)$$

We can write down the following relationship between them:

$$F_i(u) = \ddot{u}(u) - F_e(u). \quad (5)$$

Owing to this relationship we, can convert the external loop into an internal one by subtracting the values corresponding to the external loop from acceleration dependent on displacement. Multiplying (5) by  $du = \dot{u} dt$  enables one to obtain the infinitesimal work done by exciting forces. Integrating over the entire period leads to

$$\int_0^T F_i[u(t)]\dot{u}(t)dt = \int_0^T \ddot{u}(t)\dot{u}(t)dt - \int_0^T F_e[u(t)]\dot{u}(t)dt. \quad (6)$$

The first integral on the right-hand side of (6) equals zero for periodic motion. Hence, we can derive the following well-known formula:

$$L_i = L_e, \quad (7)$$

which say that dissipated energy is equal to the work done by external forces [11, 12].

The experimental sample in this paper is a cantilever beam equipped with piezoelectric patches wired on a pulse switching cell (Figure 1) [13].

The total outgoing current from the piezoelectric patches using their constitutive equations can be calculated as [14, 15]

$$I = \sum_{i=1}^N \alpha_i \dot{q}_i - C_p \dot{v}, \quad (8)$$

where  $C_p$  is the capacitance of the piezoelectric elements. In general, the piezoelectric patches are wired together in parallel. Multiplying each term of (8) by the voltage and integrating over the time shows that the converted energy is the sum of the electrostatic energy stored on the piezoelectric elements and the energy absorbed or dissipated by the electrical device as

$$E_t = \sum_{i=1}^N \alpha_i \int_0^t \dot{q}_i v_i dt = \frac{1}{2} C_p v^2 + \int_0^t v I dt. \quad (9)$$

In the case of pulse switching technique, an electric circuit is connected to the piezoelectric elements. This circuit can be used for dissipating energy from the system or energy recovery or for both of them. It consists of a switching device in parallel with the piezoelectric elements. The current in the switching device is always zero except during the voltage inversion that takes place at each switch trigger. At each inversion, the energy extracted from the piezoelement is equal to the difference in the electrostatic energy on the piezoelectric elements before and after the voltage inversion

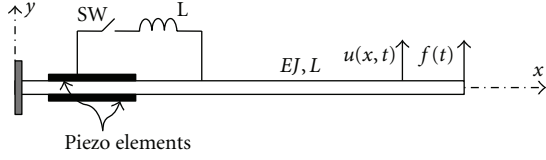


FIGURE 1: Cantilever beam where  $u(x,t)$  is the beam deflection along the transverse direction ( $y$ ) and  $f(t)$  is the excitation force.

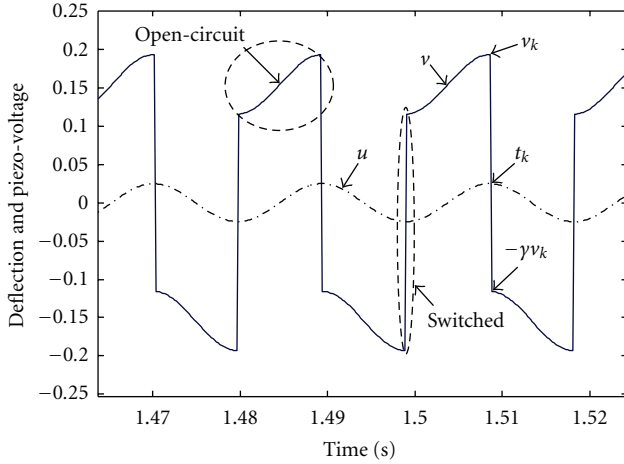


FIGURE 2: Strategy of pulse switching technique.

jump (Figure 2). The energy dissipated in the switching device is then given by

$$\int_0^t vI dt = \frac{1}{2} C_p \sum_k v_k^2 (1 - \gamma^2), \quad (10)$$

where  $v_k$  is the piezoelectric voltage just before the  $k$ th inversion and  $\gamma$  is the inversion coefficient.

There are two types of damping: material damping (structural) and system damping. Material damping is the damping inherent in the material, while system damping includes the damping at adds damper devices to the system (such as, piezoelectric material), in addition to material damping. By calculating damping energy (7) in the case of forced harmonic vibration during a time period for controlled and uncontrolled cases, respectively, the piezoelectric damping can be calculated. Among to the methods of damping measurement of a vibrating system, attenuation [11] is the other parameter to describe the vibration damping as

$$\text{Attenuation} = 20 \log \left( \frac{(u_{\max})_c}{(u_{\max})_{\text{unc}}} \right), \quad (11)$$

where  $(u_{\max})_c$  and  $(u_{\max})_{\text{unc}}$  are the maximum amplitude of displacement in controlled (structure with piezo elements) and uncontrolled cases, respectively.

### 3. Experimental Results

Experimental setup considered is a steel beam equipped with piezoelectric inserts. This structure corresponds to the

TABLE 1: Characteristics of the experimental structure.

Plate material	Steel
Plate dimensions (free)	$180 \times 90 \times 2 \text{ mm}^3$
Piezoelectric material	P189
Number of piezo elements	12 (on each face)
Piezo elements position	10 mm from the clamping end
Piezo elements dimensions	$10 \times 30 \times 0.3 \text{ mm}^3$
Open-circuit resonance frequency	56.48 Hz
Inversion coefficient $\gamma$	0.6

description given in Table 1. The proposed control strategy is implemented using a laboratory PC-based real-time DSP controller environment. Either the voltage or the deflection signals are sampled by the board as input data. According to the proposed method, the switch trigger is generated by the digital output of the control board, connected on a pulse switching device as described in [5]. The displacement sensor used is a simple piezoelectric insert collocated with the main inserts. The sensor thickness and material are similar to the control insert and generates, therefore, the same open-circuit voltage. Control strategy programming and implementation is done using the Matlab/Simulink software environment and dSPACE Real-Time Workshop for real-time computing and input/output control. Excitation of the beam is obtained using an electromagnet driven using an audio amplifier, by a harmonic excitation generated by the dSPACE board.

In practice, to measure the energy dissipated per cycle, using the concept of (7), the procedure is rather straightforward. For a cantilever beam with applied  $f(t)$  at its free-end, this energy loss is given by the integral over a complete cycle in the case of harmonic excitation as

$$E_f = \int_0^T f(t) \dot{u} dt, \quad (12)$$

where  $T$  is the cycle's period. This integration can be estimated by using  $Z$  data points separated by  $\Delta t$  seconds, so that digital summation over  $Z - 1$  data points replaces the continuous integral. Thus (12) leads to

$$E_f = \frac{1}{n} \int_0^{nT} f(t) \dot{u} dt = \frac{\Delta t}{n} \sum_{i=1}^{Z-1} (f \dot{u})_i, \quad (13)$$

where  $n$  is the number of cycles. Therefore, by multiplying generated force in the dSPACE board to the free-end measured velocity by the laser sensor and dSPACE step time  $\Delta t$  for the  $Z$  captured data points during  $n$  cycle, the dissipated energy from (13) can be calculated during a time period. Piezoelectric damping energy is equal to the difference between controlled and uncontrolled cases.

Figure 3 shows the variations of capture (displacement sensor) signal amplitude versus the excitation force amplitude in controlled and uncontrolled cases, respectively. The curves slope indicate the influence coefficient (inverse of stiffness) at the point that in which excitation force is applied (It should be mentioned that the capture signal is an image of the free-end deflection of beam; it has

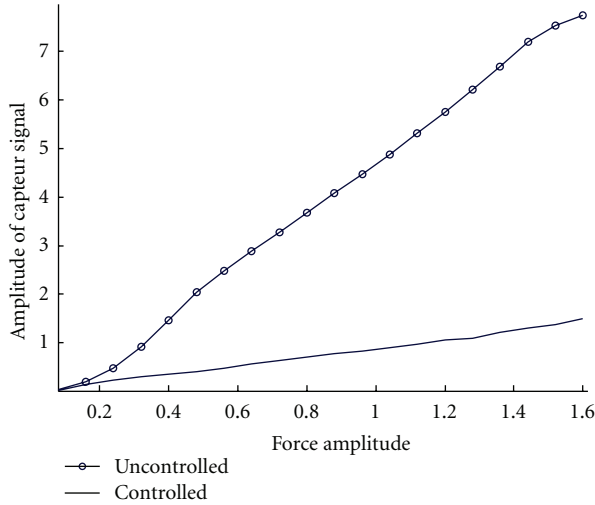


FIGURE 3: Variations of the capture signal amplitude versus the force amplitude in controlled and uncontrolled cases.

placed at the clamped end of beam that in which the bending moment is maximum and consequently the capture voltage (piezoelement deformation) and free-end deflection are maximum. Indeed, computations have been made using the image of deflection given by the collocated piezoelectric deflection sensor.). Damping effect increases gradually with increase of force amplitude which is more evident in controlled case because of the piezoelectric damping. Piezoelectric effect is too little in small deformations. The vertical distance between these two curves show the effect of piezoelectric damping. Since the structural damping is the same in controlled (piezo elements) and uncontrolled cases, the difference of curves slope is just the one caused by the piezoelectric damping. In high deformations (force amplitude  $> 1.4$ ), the curves tend to be parallel with each other. It is mentioned that the maximum damping caused by piezoelectric elements was limited and have its ultimate value. After the ultimate value, the curves rise similarly with increase of force amplitude. In this case, the additional injected energy to the system only increases the amplitude of vibration in two cases (controlled and uncontrolled) proportionally. In this figure, the excitation frequency is equal to the first resonant frequency of the beam (Table 1).

Figure 4 shows the variations of capture signal attenuation versus the force amplitude. From the figure, the decreasing of the attenuation was limited. The minimum attenuation (ultimate value) is about  $-10$  dB. It is observed that after the ultimate value the curve rise slowly with increase of force amplitude. In this case, structural damping is more predominant than piezoelement damping (It is proportional to the square of vibration amplitude, (2)). Also, the excitation frequency is the first resonant frequency (Table 1).

Figure 5 indicates the variations of periodical damping energy versus the square of capture signal amplitude. Damping energy in controlled case increases faster than one in uncontrolled case with increase of capture signal amplitude.

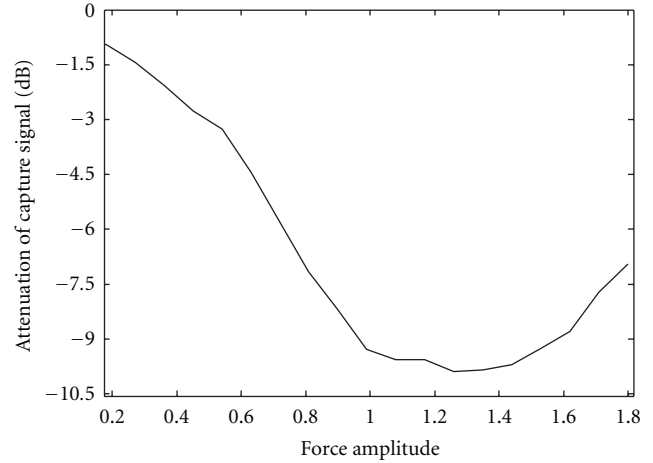


FIGURE 4: Variations of the capture signal attenuation in dB versus the force amplitude.

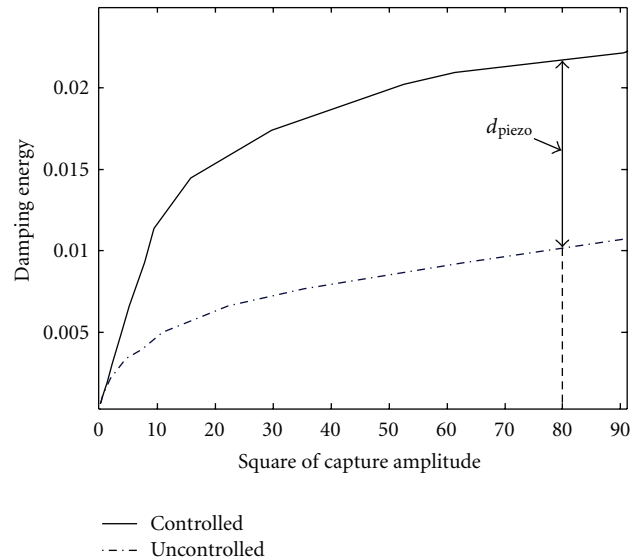


FIGURE 5: Variations of damping energy versus the square of capture signal amplitude.

Therefore, the curve slope in controlled case is more than the one in uncontrolled case up to the value of 60. After that, the structural damping is more predominant, and piezoelectric damping reaches its ultimate value. Then, two curves are approximately parallel (with distance  $d_{\text{piezo}}$ ). It can be concluded that (2) holds true only for high values of structural deformation (The curves slope are constant in high deformations). Also, the values of  $\alpha_d$  are the same for the two cases (controlled and uncontrolled) and are just as the one for structural damping. Piezoelectric effect increases damping only more than uncontrolled case equal  $d_{\text{piezo}}$ . Thus as (2) is relevant to structural damping, this equation for controlled case is

$$W_d = \alpha_d u_{\max}^2 + d_{\text{piezo}}. \quad (14)$$

The slope of these curves gives the value of  $\alpha_d$  and is approximately equal to 0.026.

#### 4. Conclusions

This paper showed an experimental method to calculate the damping energy in mechanical system. However, the mathematical description of damping mechanism is much more complicated and any process responsible for the occurrence of damping is very intricate and the knowledge of it is insufficient. Structural damping and piezoelectric damping for pulse switching semiactive nonlinear control technique have been calculated and analysed. Pulse switching control technique is interesting for structural damping applications because it presents simultaneously good damping performances, a good robustness, and very low power requirements. Finally, it is important to consider that this technique is simple enough to be self-powered. Piezoelectric damping will increase with increase of force amplitude but its maximum value was limited and has its ultimate value.

#### Acknowledgments

The authors would like to thank Professor D. Guyomar and Professor C. Richard from LGEF-INSA for their kind help.

#### References

- [1] D. Niederberger, A. Fleming, S. O.R. Moheimani, and M. Morari, "Adaptive multi-mode resonant piezoelectric shunt damping," *Smart Materials and Structures*, vol. 13, no. 5, pp. 1025–1035, 2004.
- [2] M. D. Rao, "Recent applications of viscoelastic damping for noise control in automobiles and commercial airplanes," *Journal of Sound and Vibration*, vol. 262, no. 3, pp. 457–474, 2003.
- [3] A. Badel, *Récupération d'énergie et contrôle vibratoire par éléments piézoélectriques suivant une approche non linéaire*, Ph.D. thesis, Ecole Doctorale de l'Université de Savoie, 2005.
- [4] D. Guyomar and A. Badel, "Nonlinear semi-passive multi-modal vibration damping: an efficient probabilistic approach," *Journal of Sound and Vibration*, vol. 294, no. 1-2, pp. 249–268, 2006.
- [5] C. Richard, D. Guyomar, D. Audigier, and G. Bassaler, "Enhanced semi passive damping using continuous switching of a piezoelectric device on an inductor," in *Smart Structures and Materials*, vol. 3989 of *Proceedings of SPIE*, pp. 288–299, San Diego, Calif, USA, 2000.
- [6] C. Richard, D. Guyomar, D. Audigier, and G. Ching, "Semi passive damping using continuous switching of a piezoelectric device," in *Smart Structures and Materials*, vol. 3672 of *Proceedings of SPIE*, p. 104, San Diego, Calif, USA, 1998.
- [7] L. R. Corr and W. W. Clark, "A novel semi-active multi-modal vibration control law for a piezoceramic actuator," *Journal of Vibration and Acoustics, Transactions of the ASME*, vol. 125, no. 2, pp. 214–222, 2003.
- [8] W. T. Thomson, *Theory of Vibration with Applications*, Prentice-Hall, Upper Saddle River, NJ, USA, 1981.
- [9] L. Meirovitch, *Elements of Vibrations Analyses*, McGraw-Hill, New York, NY, USA, 1986.
- [10] L. Meirovitch, *Analytical Methods in Vibrations*, The Macmillan Company, New York, NY, USA, 1967.
- [11] Z. Osinski, *Damping of Vibrations*, A.A. Balkema, Rotterdam, The Netherlands, 1998.
- [12] Z. Osinski, "Hysteresis loops of the vibrating system," *Machine Dynamics Problems*, vol. 5, 1993.
- [13] D. Guyomar, C. Richard, and S. Mohammadi, "Semi-passive random vibration control based on statistics," *Journal of Sound and Vibration*, vol. 307, no. 3–5, pp. 818–833, 2007.
- [14] A. Khodayari, A. Ahmadi, and S. Mohammadi, "On physical realization of the wireless semi active real time vibration control based on signal statistical behavior," *Sensors and Actuators, A*, vol. 167, no. 1, pp. 102–109, 2011.
- [15] S. Mohammadi, *Semi-passive vibration control using shunted piezoelectric materials and harvesting energy*, Ph.D. thesis, INSA, Lyon, France, 2007.

## Research Article

# Redirection of Lamb Waves for Structural Health Monitoring

W. H. Ong and W. K. Chiu

*Department of Mechanical and Aerospace Engineering, Monash University, Clayton, VIC 3800, Australia*

Correspondence should be addressed to W. H. Ong, wern.ong@monash.edu

Received 31 August 2011; Accepted 7 October 2011

Academic Editor: Tao Li

Copyright © 2012 W. H. Ong and W. K. Chiu. This is an open access article distributed under the Creative Commons Attribution License, which permits unrestricted use, distribution, and reproduction in any medium, provided the original work is properly cited.

Currently, structures are designed without structural health monitoring (SHM) in mind. It is proposed that SHM should be addressed at the design stage of new structures. This paper explores the benefit which can be gained from such considerations. The scope encompasses Lamb-wave-based SHM and a given fatigue critical location (FCL). Optimization is performed using specialised ray tracing. A case study is carried out using a specimen that simulates a hard-to-inspect region in a fuel vent hole in wings structures of aircraft. This work will report on the potential use of the focussing of stress wave to improve detectability of defect in this hard-to-inspect location. Following optimization, results are produced numerically and experimentally. The results revealed sensitivity to damage is nearly doubled while minimum detectable damage size is significantly decreased. As a result, this study brings together an assortment of specialised tools to form a workflow ready for implementation.

## 1. Introduction

Propagating Lamb-wave-based structural health monitoring methodologies have been widely reported to be convenient and efficient in detecting fatigue cracks in metallic structures [1, 2] and disbonds and delaminations in composite structures [3]. The propagating characteristics of Lamb waves in metals [4] and multilayered materials [5] are well documented. An attractive feature of this stress-wave-based method of structural health monitoring is that it can be used in “hard-to-reach” areas because the actuators and the sensors required can be bonded onto the structure. This is commonly known as “insitu structural health monitoring” (ISHM). The investigators of this project are amongst the many others who have contributed to the development of the Lamb-wave-based method of ISHM.

Many authors have published on optimizing and improving probability of detection (POD) and damage sensitivity. However, the works published have been focused on topics such as sensor placement, sensor selection, frequency selection, data capture, and data analysis. Such topics indicate that the structure itself is not included as a part of the optimization. SHM is not a part of the design process, rather an afterthought. A successful SHM friendly structure can be

designed with less tolerance and therefore less material and weight. Consequently, the weight gained from implementing SHM systems can be offset.

A variety of tools acquired over former years have been applied to this problem. Ray tracing specialised in propagating Lamb waves has been used to redirect waves. Laser vibrometry and FEA are used to acquire displacement fields caused by Lamb waves. Damage quantification techniques described in (1) by Ong and Chiu [6] have been used to evaluate the efficacy of the structural alterations:

$$\text{Scatter}(x, y) = \frac{\sum_{t=0}^{n_t} |u_k(x, y, t) - u_0(x, y, t)|}{n_t}, \quad (1)$$

where  $n_t$  is the number of time steps used,  $u_k$  is the displacement field of the damaged specimens and  $u_0$  is the displacement field of the flawless specimen.

A structure representing an aircraft wing spar with flange and riser has been chosen to demonstrate the benefits of wave redirection. The specimen is shown in Figure 1. Often aircraft utilize wet wings loaded with fuel; this will require a fuel vent hole to be drilled into the spar creating a stress concentration leading to fatigue cracks. Additionally, sensors cannot be placed on the riser due to the presence of fuel.

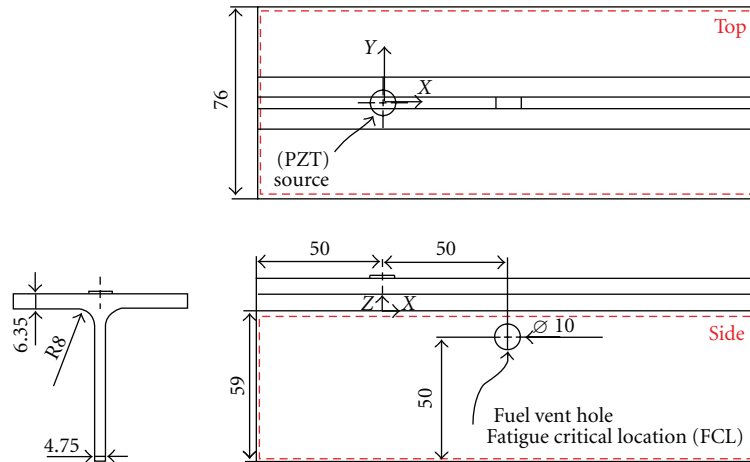


FIGURE 1: Original specimen configuration.

The condition conducive to crack growth will be a tension loading in the marked  $x$  direction. This loading leads to cracks propagating perpendicular to the direction of load. Therefore, an upward (towards flange) crack and downward crack form on the fuel vent hole. The upward crack can be detected through multiple means including bulk wave and Lamb wave ultrasonics since the location has line of sight with the external facing flange. However, the line of sight with the downward crack is blocked by the fuel vent hole making the area hard to inspect. Hence, this specimen has been chosen to demonstrate wave redirection as another approach to improvement of damage detection.

Three studies performed sequentially will be presented here. The first step will be modelling the specimen with a ray tracing tool. This tool has the ability to solve the propagation of Lamb waves and present the wavefront in a clear and precise style allowing the user to determine exactly where the waves are going. Due to the simplicity of the method and equations involved, the simulations are solved in seconds allowing instant feedback and facilitation of iterative design of wave guides. The second step will be to test the design in finite element analysis (FEA) in order to assess the efficacy of the modifications made and confirm the predicted wave propagation in ray tracing. The final step is experimental testing of the design which provides confirmation that all the modelling performed is correct and the concept is proven and solid.

## 2. Modification for Wave Redirection

The original specimen is an aluminium T beam consisting of a 4.75 mm thick web (labelled “side”) and 6.35 mm flange (labelled “top”) as shown in Figure 1. The fuel vent hole is located on the side 50 mm above the bottom of the web. The focus of this work will be to detect damage in the FCL under the fuel vent hole. This 10 mm diameter hole is typical in aircraft structures and gives rise to stress concentrations. Lamb wave generation is handled by a piezoelectric transducer (PZT) placed on the top surface.

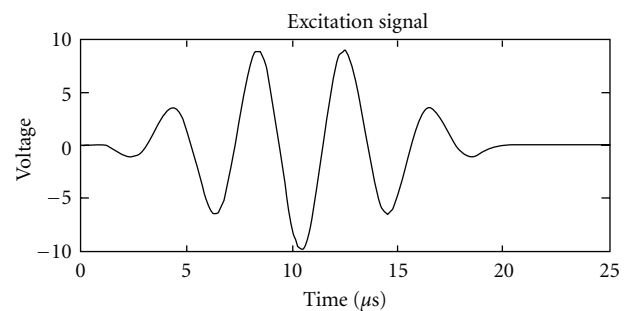


FIGURE 2: Hanning windowed 5-cycle sine wave excitation signal. Centre frequency set at 240 kHz.

Placement of PZTs is constrained to the top surface as the side surface will be immersed in fuel. Therefore, it will be preferable to enhance the sensitivity to damage when the receiver is placed along the top surface. The chosen excitation signal is a 240 kHz 5-cycle Hanning windowed sine wave as shown by Figure 2. The centre frequency was chosen due to resonances in the actuation system which improve the signal to noise ratio.

The modifications done to optimise SHM detectability focuses on the redirection of Lamb waves towards the fatigue critical location (FCL). In this case, the FCL is the hole drilled into the T beam for fuel flow in an aircraft. A circular reflector has been cut into the free edge of the T beam to direct the Lamb waves emitted from the PZT to the FCL. The shape was arrived at through application of ray tracing which allowed for the trial and error of many positions, sizes, and shapes. The process is described in greater detail in the ray tracing section.

An obvious problem arising from Figure 3 is the new stress concentration created by the removal of material to form the Lamb wave focusing reflector. However, the study presented here is a demonstration of concept and is not a suggestion of drastic design change. Instead, it

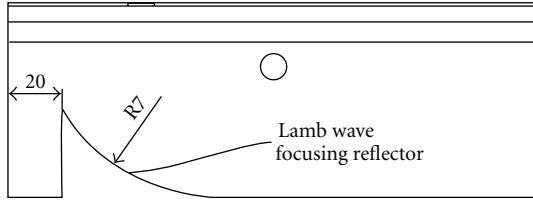


FIGURE 3: Modified specimen optimized for damage detection at FCL.

is recommended that existing cutouts and geometry be optimized for SHM rather removing more material.

Detection has been attempted on a 5 mm downward cut placed at the hole. The damage detection technique is based on the windowed scatter/difference calculations performed in a previous paper [6]. This case study demonstrates the need to have an array of specially developed tools available to optimise a structure. The scattered field calculation allows for detection of changes in the structure (such as damage) and the corresponding location for optimal detection. Ray tracing is used for fast and concise optimization of Lamb wave direction, while FEA can validate these optimizations without fabrication of a specimen.

### 3. Ray Trace Study

**3.1. Method.** A simple ray trace program was written in MATLAB to model Lamb wave propagation. Details and verification of the modelling technique have been published by Ong and Chiu [7]. A key difference between ray tracer used for light rays and the one presented here is the time stepping algorithm used. Typically, in the field of modelling light, the rays are solved until a set number of bounces are reached or the rays exit the work area. This results in a fast solution which solves the completed path of a ray without consideration to the transit of the rays. In the case of Lamb wave propagation in solids, the Lamb waves will never exit the workspace. Consequently, the rays will always be in transit as they are bounded within the solid. Additionally, the evolution and propagation of the rays are important; consequently, the temporal dimension has importance. As a result, the ray tracing program steps through time the same way a transient FEA simulation is done. Group velocities determine how fast the rays travel with respect to time while changes in phase velocities determine the bending of rays (refraction) at thickness change interfaces. This is calculated using Snell's law shown in (2). Reflection is assumed to be governed by (3):

$$\frac{c_1}{c_2} = \frac{\sin(\theta_1)}{\sin(\theta_2)}, \quad (2)$$

where  $c$  and  $\theta$  theta are the phase velocity and direction of propagation, respectively. While subscripts 1 and 2 represent the entry and exit wave.

$$\theta_i = \theta_r. \quad (3)$$

The side surface was chosen for ray trace modelling as this is the side which hosts the reflector and the FCL. 18 rays

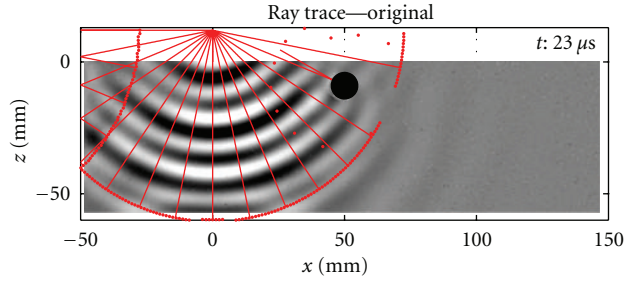


FIGURE 4: Ray trace overlaid on displacement field captured by laser vibrometer. In addition to ray lines, 180 points were emitted to form a visualization of the wavefront.

were emitted downward from the PZT location where it was assumed Lamb waves would propagate in a radial direction despite having to go through the top surface. Effects from the 6.35 mm thick flange have been assumed negligible. The validity of this assumption is demonstrated by the agreement between the experimental wavefront and ray trace predicted wavefront, as shown in Figure 4. Constant duration time steps were set at 0.2  $\mu$ s providing a sample rate of 5 MHz, which will be identical to FEA performed later.

**3.2. Results.** As described earlier, the approach taken to enhancing detection of damage is to redirect Lamb wave energy. A reflector placed on the bottom edge is used for this task. The specimen was modelled in the ray trace software which gave instant feedback about the propagation of Lamb waves. This feedback was used in deciding the size and location of the reflector.

Figure 5 shows 3 models which have been solved by the ray trace software. In Figure 5(a), the original specimen has been included for comparison, showing how the waves propagate omnidirectionally. By observation, there is no direct line of sight between the FCL located at the bottom of the fuel vent hole and the PZT source. This means all the wave energy arriving at the FCL is done so through reflection (attenuated by distance and radial spread).

In Figure 5(b), a circular-shaped reflector was added to the ray trace model in the form of a boundary representing a cutout to be performed in the physical specimen. The size (radius) and location of the reflector were manipulated until the waves were focused at the desired location (FCL). Distance travelled by the reflected waves is not significantly altered; therefore, attenuation from distance is roughly the same. However, the radial spread of wave energy is converted to a gathering of energy at the focal point of the reflector. This energy will result in more reliable and sensitive detection of damage in the FCL.

Figure 5(c) shows the "FCL focus offset" model which has been included to demonstrate how the reflector parameters were arrived at. The design process was iterative through trial and error enabled by the high-speed solutions provided by ray tracing. The model which has its reflector offset 10 mm to the right shows the final step in iterative design before reaching optimal configuration. Sensitivity to geometry when trying to redirect energy is also revealed.

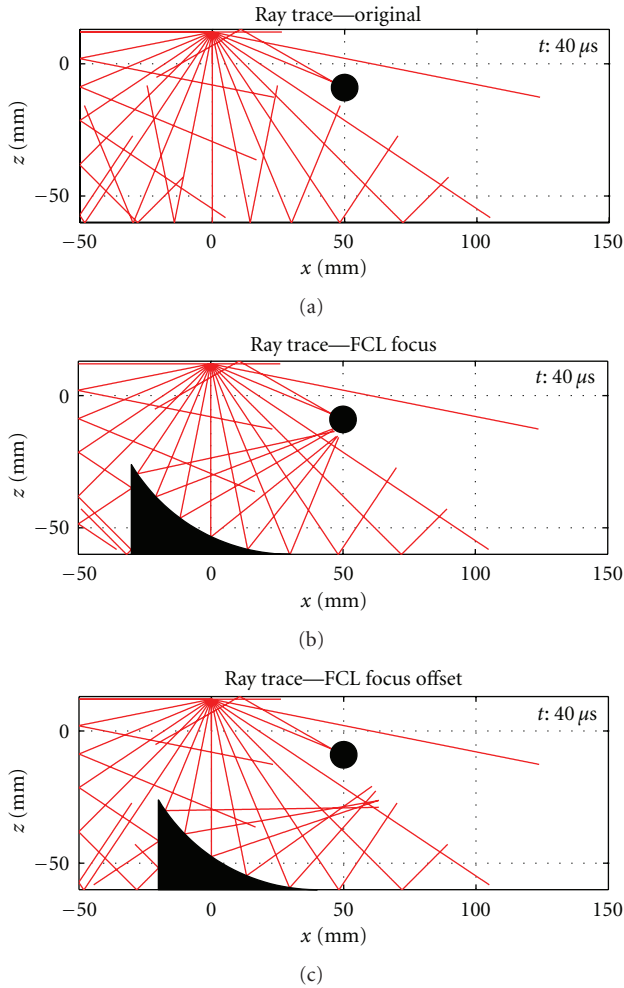


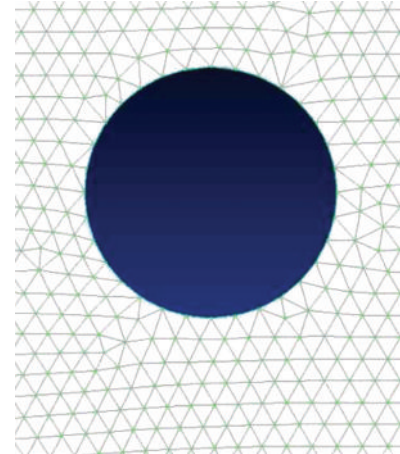
FIGURE 5: Ray trace snapshots.

When a reasonable focus has been achieved the dimensions are saved for use in experimental and FEA studies. This case is shown in Figure 5(b).

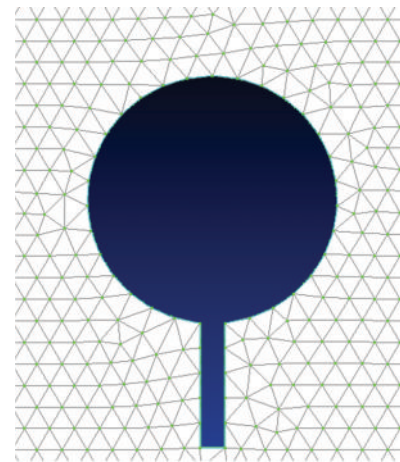
## 4. Numerical Study

**4.1. Finite Element Setup.** The specimen is modelled in 3D using tetrahedral elements. Commercially available Femap pre-/postprocessor is used in modeling, while solving is done in NEiNastran. Only out-of-plane displacements are saved to remain consistent with laser vibrometry. Further post-processing is carried out in MATLAB to convert and analyse the displacement fields from the model. From this stage, the out-of-plane displacement field is identical in format to that acquired from laser vibrometry used in experimental study.

Damage was introduced by performing a Boolean subtraction to replicate the saw used in experimental studies. A  $5 \times 1$  mm rectangle is subtracted from the FCL as shown in Figure 6. A mesh spacing of 1 mm is used in all models. Given the A0 mode will have the highest spatial frequency (approximately 640 rad/m), this mesh spacing gives a node to wavelength ratio of 9.82. Propagating stress waves are



(a) Undamaged



(b) Damaged

FIGURE 6: Fuel vent holes.

solved using the transient dynamic/time history solver. A time step is set to be 0.2  $\mu$ s. The total time record calculated is 100 microseconds. This time record was selected to be long enough for the wave packet to travel downstream, towards the edges of specimen.

In this computational study, the size of the actuation region on the model is identical to the PZT used in experimental study. The excitation scheme used to produce a Lamb wave caused by the low-profile PZT is similar to that described by Constantin et al. [8]. Figure 7 shows the 2 types of input forces placed on the FE geometry. The plane of the plate is described by the X-Y plane, and the Z axis is out-of-plane and perpendicular to the plate.

**4.2. Results.** Displacement fields were solved for 4 models. Flawless and damaged models were made in the T beam's original and modified form. Equation (1) is applied to the flawless and damaged displacement fields to create the scattered field. The displacement fields were analysed for a suitable time window which the waves affected by the defect

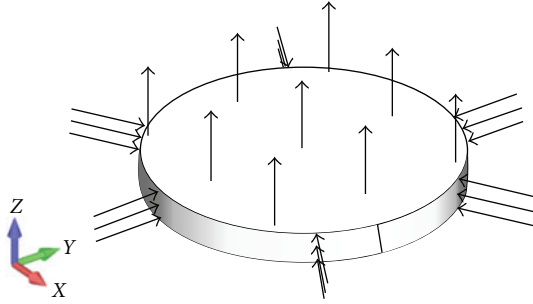


FIGURE 7: Excitation scheme employed in FEA.

TABLE 1: Comparison of sensitivity to damage before and after modification.

	Improvement (FEA)
Original: maximum scatter on top surface (nm)	1.18
Modified: maximum scatter on top surface (nm)	2.02
Percentage improvement (%)	71.2

would propagate to the flange. The window chosen for this is between 50–85  $\mu$ s.

The side-by-side comparison is shown in Figure 8 and displays obvious benefits from the addition of the reflector. Scatter intensities are visibly larger in the modified specimen for the same damage size, indicating that sensitivity to damage has been improved.

In the original specimen, the area sensitive to damage is located on the opposite side of the T-beam ( $x = 100$  mm). Therefore, in order to achieve acceptable detectability a second sensor must be placed in that vicinity, in a similar fashion to the pitch-catch arrangement used in traditional ultrasonics. However, the modified specimen reveals a very sensitive area where the PZT actuator has already been located. As the time window for excitation (0–20  $\mu$ s) and time window for reception (50–85  $\mu$ s) do not clash it is highly probable that a single transducer can be used for transmission and reception, thereby saving weight and cost.

The improvement can be measured more quantitatively by measuring scatter intensity at feasible points of detection. As explained earlier, placement of sensors is constrained to the top surface due to the presence of fuel in a wet wing. Therefore, only sensitive locations on the top surface will be used to gauge sensitivity to damage in the FCL.

Table 1 summarises the improvement in defect detectability when monitoring the top surface. A significant (71%) increase in sensitivity to damage is observed when comparing the modified design to the original. This demonstrates that the directed and precisely focused energy at the FCL is advantageous in detection of damage.

## 5. Experimental Study

5.1. *Lamb Wave Transmission and Reception.* Transmission was achieved using piezoelectric transducers (PZT), while

the Lamb waves were received using a laser vibrometer. A movable table allows positioning of the laser’s scan point. This simple concept can be visualised in Figure 9. If the scan is repeated thousands of times across the entire specimen a complete displacement field can be captured. A rig enabling this has been assembled for Lamb wave imaging shown in Figure 9.

Laser vibrometry has been a key tool to aid comprehension and understanding of Lamb waves as shown by Staszewski et al. [9] and Rajic and Rosalie [10]. A laser is used to detect Lamb wave displacements in a specimen rather than a PZT. This noncontact approach is more precise and consistent due to the removal of coupling mediums and the pin point accuracy of the laser. The major advantage of this technique is the speed and potential for automation due to the noncontact operation.

A low-profile PZT is used,  $10 \times 1$  mm in diameter and thickness, respectively. It is produced using “Pz26” material sourced from Ferroperm. Coupling to the specimen is done by Araldite epoxy, while the electrical connections to the PZT are taken care of by conductive copper adhesive strips. This is done in order to maintain a low-profile and avoid heat stress involved with soldering. Figure 9 demonstrates an example.

An excitation signal was generated comprising of sine waves enclosed in a Hanning window function. A resonant frequency of 240 kHz was chosen for this. This helped combat the notorious signal to noise ratios associated with laser vibrometers. Furthermore, 32 ensemble averages are taken to further reduce noise. The PZT was excited through a Krohn-Hite model 7602 broadband amplifier set to deliver peak-to-peak amplitude of 50 V. Out of plane displacement is detected by a Polytec OFV 505 laser vibrometer. Input (displacement) and output (excitation) data is sampled at 10 and 4 MHz, respectively. These rates are the maximum allowed by the National Instruments PCI-6115 data acquisition card. Motion is taken care of by a computer control X-Y table equipped with stepper motors. The ratio of the table is 5000 steps per mm providing 0.0002 mm resolution.

The rig has been programmed to collect data in a zigzag pattern to minimise wasted motion. The data is then rearranged to form a grid such that a complete image of the plate displacement field can be formed. Scan points on our rig are set to 1.5 mm spacing giving a point density of 1 point per 2.25 mm<sup>2</sup>. This is a great increase in density compared to the 1 point per 15.71 mm<sup>2</sup> (420 points over 110  $\times$  60 mm) reported by Staszewski et al. [11]. Consequently, our resolution is much higher.

Figure 10 shows the fabricated specimens. They have been made with the dimensions specified in the ray trace model. The T beam has been cut from an aluminium extrusion. A computer numerically controlled (CNC) milling machine was used to cut the reflector using the dimensions from the ray tracing study.

5.2. *Results.* In order to maintain consistency and allow for comparison, the parameters such as time window of 50–85  $\mu$ s selected in the FEA study have been retained in the experimental study. Damage detection has been attempted

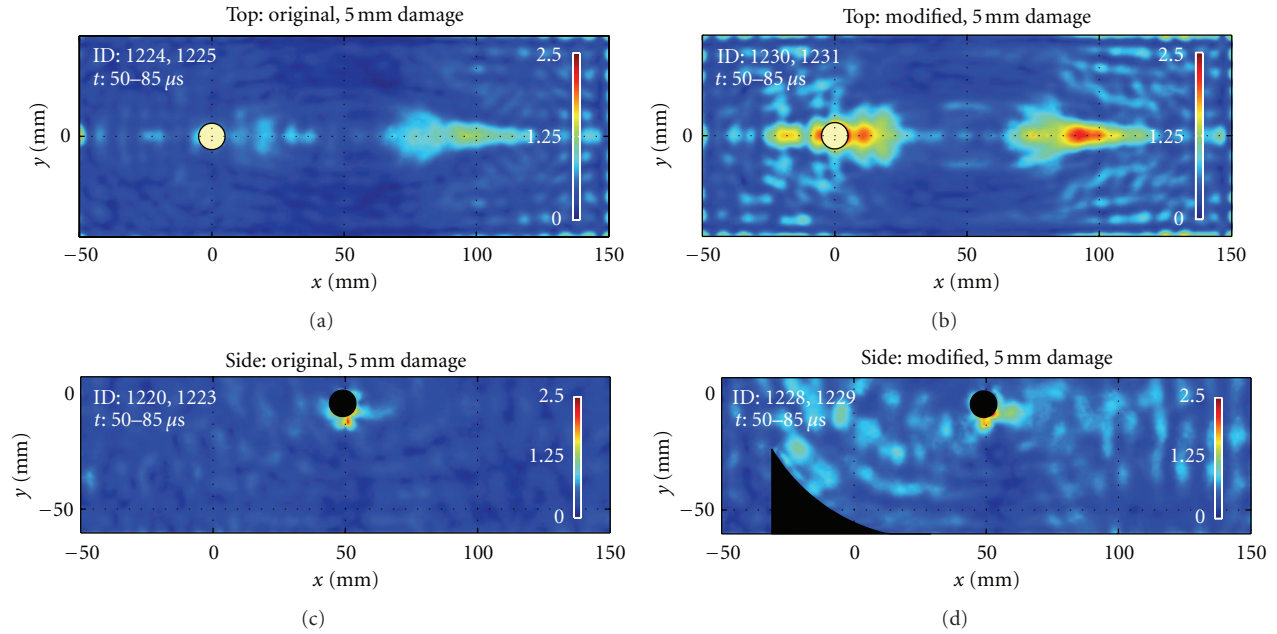


FIGURE 8: Scatter plots predicted by FEA before and after modification.

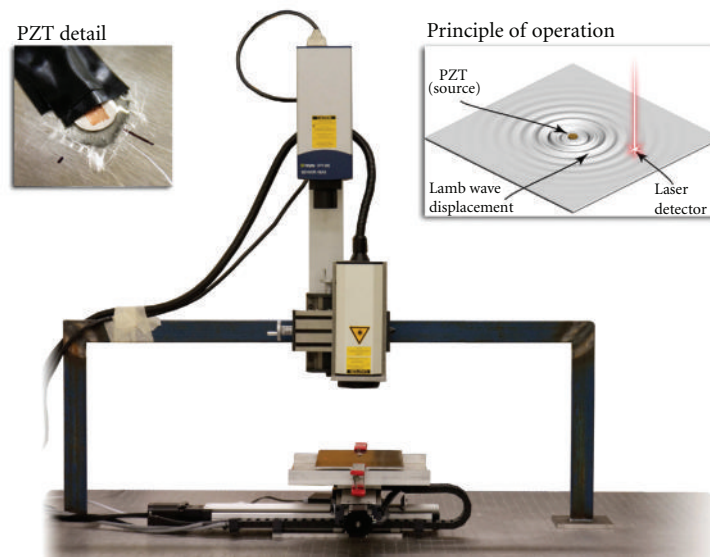


FIGURE 9: Laser vibrometry rig.



FIGURE 10: Photo of fabricated specimens.

on 1 mm damage. Figures 11(a)–11(d) show the resulting scatter field given this damage size. Although only the

top surface is available for sensor placement, both surfaces have been scanned and presented as the side surface is important for greater comprehension. Both sides of the original specimen display almost no signs of the 1 mm damage, making it undetectable.

The modified specimen yields a superior sensitivity to the 1 mm damage as shown in Figures 11(b) and 11(d). Large amounts of scatter are revealed by the side scan, which are not present in the original specimen. Consequently, a high-sensitivity is implied; however, only the results on the top edge of the side scan ( $z = 0$  mm) are relevant to the top

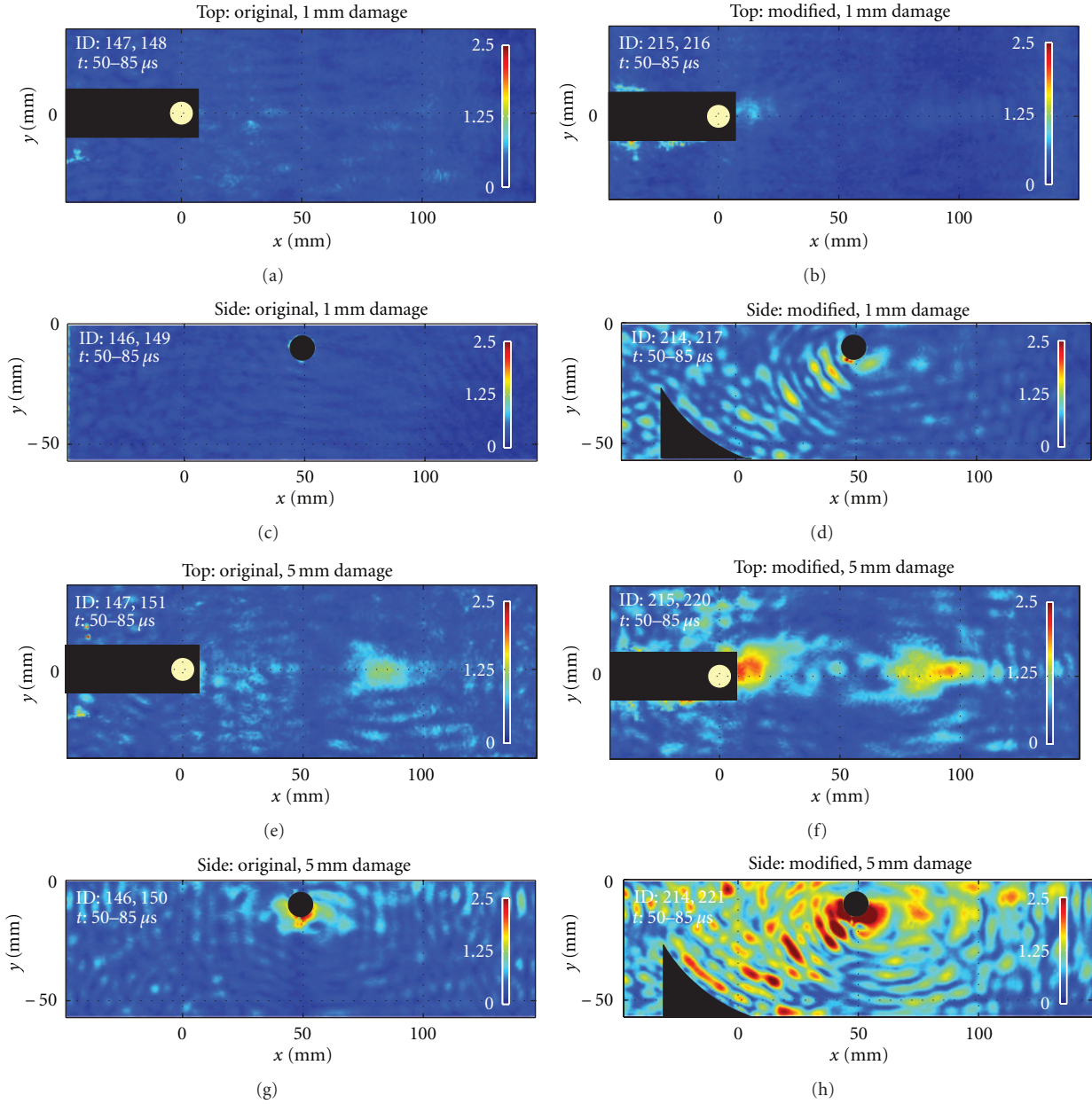


FIGURE 11: Scatter plots generated from experimental scans before and after modification.

surface used in detection. Along this edge, the sensitivity is greatest when  $x < 0$  mm; however, this area cannot be analysed due to the supporting lead wires for the PZT blocking the laser. The right half of the specimen ( $x > 50$  mm) shows small amounts of scatter, this leaves an area between  $x = 0$  mm, to  $x = 50$  mm as the best possibility for damage detection. Figure 11(b) confirms a location ( $x = 10$  mm,  $y = 0$  mm) as the location of highest sensitivity.

This indicates that the modified specimen not only redirects the incident waves towards the defects but also focuses the reemitted waves from the defect towards the top surface where the PZT resides. It is highly likely that higher sensitivities would be achieved where the PZT actuator is

placed; however, it is not possible to scan this area. Despite this the arrangement is similar to the pulse-echo setup used in classical ultrasonics [12]. Hence, interrogation of the structure can be performed with a single PZT given the right hardware.

Figures 11(e)–11(h) show the results when 5 mm of damage has been introduced. At 5 mm, the damage can be detected in both original and modified specimens. However, a much higher sensitivity to the damage is observed in the modified specimen. The location of highest sensitivity remains the same for the modified specimen, whereas the original specimen did not have a location. The increase to 5 mm damage length gives rise to a high-sensitivity location

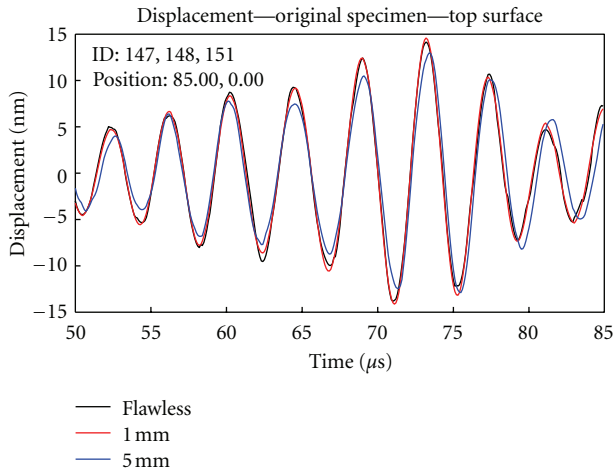


FIGURE 12: Displacement at maximum sensitivity location on original specimen.

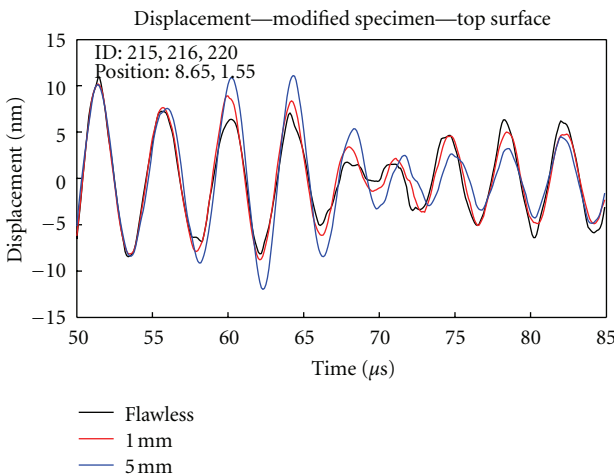


FIGURE 13: Displacement at maximum sensitivity location on modified specimen.

on the right side of the original specimen ( $x = 85$  mm,  $y = 0$  mm).

Table 2 summarises and quantifies the results from this section. As in the numerical study, the maximum scatter in the top surfaces were compared to measure the improvement gained by modifying the specimen. The experiments reveal a 76% and 62% improvement for the 1 and 5 mm damages, respectively. These figures are in line with the improvement predicted by the numerical study.

The displacement time series in Figures 12 and 13 demonstrate sensitivity of the Lamb wave response to damage in greater detail. The location of maximum scatter and sensitivity on the top surface are used in plotting the displacement time series. In the case of the original specimen, this position is ( $x = 85$  mm,  $y = 0$  mm) while this is located at ( $x = 8.65$  mm,  $y = 1.55$  mm). The original specimen shows very little deviation from the flawless waveform. This makes it impossible to discriminate the response to 1 mm damage from that of a flawless specimen. Conversely, the

TABLE 2: Comparison of sensitivity to damage before and after modification.

	Improvement (experimental)	
Cut size (mm)	1	5
Original: maximum scatter on top surface (nm)	0.5 (noise)	1.283
Modified: maximum scatter on top surface (nm)	0.88	2.076
Percentage improvement (%)	76.0	61.8

modified specimen shows a significantly different response from flawless even at 1 mm damage size indicating a greater sensitivity to damage.

## 6. Conclusions

This work has proposed a different approach to SHM, in which the structure becomes another parameter to optimize. This new parameter has been optimized through ray tracing to arrive at a design which redirects Lamb wave energy towards the desired inspection area which is placed in a hard to-reach-location. Using FEA to confirm the efficacy of the method, it was determined that around 70% improvement in sensitivity could be achieved from optimization. Following the numerical study, an experimental study confirmed the improvement. Additionally, the 1 mm defect could only be detected by the modified specimen. This improvement in detectability is highly desirable in low tolerance structures.

It has been noted that the modification presented here would not be practical due to the amount of material removal inhibiting the structure from carrying its original load. However, the specimen is only used as a demonstration of the optimization concept. The concept is expected to be implemented on existing boundaries rather than making new ones. An example of such a specimen is shown in work by Weller and McDonald [13]. The F-111 wing pivot has stiffeners which have an existing taper which may be optimized for Lamb wave redirection.

## Acknowledgment

The authors wish to acknowledge the financial support provided by USAF AOARD-09-4036.

## References

- [1] B. C. Lee and W. J. Staszewski, "Modelling of Lamb waves for damage detection in metallic structures: Part I. Wave propagation," *Smart Materials and Structures*, vol. 12, no. 5, pp. 804–814, 2003.
- [2] N. Rajic, S. C. Galea, and W. K. Chiu, "Autonomous detection of crack initiation using surface-mounted piezotransducers," *Smart Materials and Structures*, vol. 11, no. 1, pp. 107–114, 2002.
- [3] Y. L. Koh and W. K. Chiu, "Numerical study of detection of disbond growth under a composite repair patch," *Smart Materials and Structures*, vol. 12, no. 4, pp. 633–641, 2003.

- [4] I. A. Viktorov, *Rayleigh and Lamb Waves: Physical Theory and Applications*. Ultrasonic Technology, Plenum Press, New York, NY, USA, 1967.
- [5] M. Castaings and B. Hosten, "Guided waves propagating in sandwich structures made of anisotropic, viscoelastic, composite materials," *Journal of the Acoustical Society of America*, vol. 113, no. 5, pp. 2622–2634, 2003.
- [6] W. H. Ong and W. K. Chiu, "Damage quantification in plates using lamb waves," in *Proceedings of the Australasian Congress on Applied Mechanics*, Perth, Australia, 2010.
- [7] W. H. Ong and W. K. Chiu, in *Proceedings of the Asia Pacific Workshop on Structural Health Monitoring*, Tokyo, Japan, 2010.
- [8] N. Constantin, S. Sorohan, M. Găvan, and V. Raetțchi, "Efficient and low cost PZT network for detection and localization of damage in low curvature panels," *Journal of Theoretical and Applied Mechanics*, vol. 49, no. 3, pp. 685–704, 2011.
- [9] W. J. Staszewski, B. C. Lee, L. Mallet, and F. Scarpa, "Structural health monitoring using scanning laser vibrometry: I. Lamb wave sensing," *Smart Materials and Structures*, vol. 13, no. 2, pp. 251–260, 2004.
- [10] N. Rajic and S. C. Rosalie, *A Feasibility Study into the Active Smart Patch Concept for Composite Bonded Repairs*, Defence Science and Technology Organisation, Melbourne, Australia, 2008.
- [11] W. J. Staszewski, B. C. Lee, and R. Traynor, "Fatigue crack detection in metallic structures with Lamb waves and 3D laser vibrometry," *Measurement Science and Technology*, vol. 18, no. 3, pp. 727–739, 2007.
- [12] NASA Ultrasonic Testing of Aerospace Materials.
- [13] S. Weller and M. McDonald, *Stress Analysis of the F-111 Wing Pivot Fitting*, Defence Science and Technology Organisation, Melbourne, Australia, 2000.

## Research Article

# A Surface Acoustic Wave Ethanol Sensor with Zinc Oxide Nanorods

**Timothy J. Giffney, Y. H. Ng, and K. C. Aw**

*Department of Mechanical Engineering, The University of Auckland, Auckland 1142, New Zealand*

Correspondence should be addressed to K. C. Aw, k.aw@auckland.ac.nz

Received 7 October 2011; Accepted 29 November 2011

Academic Editor: Tao Li

Copyright © 2012 Timothy J. Giffney et al. This is an open access article distributed under the Creative Commons Attribution License, which permits unrestricted use, distribution, and reproduction in any medium, provided the original work is properly cited.

Surface acoustic wave (SAW) sensors are a class of piezoelectric MEMS sensors which can achieve high sensitivity and excellent robustness. A surface acoustic wave ethanol sensor using ZnO nanorods has been developed and tested. Vertically oriented ZnO nanorods were produced on a ZnO/128° rotated Y-cut LiNbO<sub>3</sub> layered SAW device using a solution growth method with zinc nitrate, hexamethylenetriamine, and polyethyleneimine. The nanorods have average diameter of 45 nm and height of 1 μm. The SAW device has a wavelength of 60 μm and a center frequency of 66 MHz at room temperature. In testing at an operating temperature of 270°C with an ethanol concentration of 2300 ppm, the sensor exhibited a 24 KHz frequency shift. This represents a significant improvement in comparison to an otherwise identical sensor using a ZnO thin film without nanorods, which had a frequency shift of 9 KHz.

## 1. Introduction

Sensing of ethanol vapour has important applications in industry and society. At high temperatures (200°C to 300°C) zinc oxide absorbs ethanol vapour, causing a significant change in conductivity [1, 2] and also leading to a change in mass. This change in properties can be used to create an ethanol sensor.

Surface acoustic wave (SAW) sensors are a class of piezoelectric MEMS sensor which can achieve high sensitivity and excellent robustness. Since their discovery by Rayleigh in 1885 [3] surface acoustic waves have been extensively researched. The energy of a surface acoustic wave is concentrated within several wavelengths of the surface [4, 5]. For this reason, the propagation characteristics of surface acoustic waves are highly sensitive to any change in the properties of the surface on which they travel.

Due to the sensitivity of SAW devices to small changes in mass loading and surface conductivity, SAW devices have been extensively studied as gas sensors [6–8]. A typical SAW gas sensor uses an interdigital transducer (IDT) to generate a surface acoustic wave in a piezoelectric substrate. The surface acoustic wave propagates along a delay line coated in some

material which absorbs the target gas. A second IDT at the end of the delay line is then used to transduce the SAW to an electrical signal. Absorption of gas onto the sensing layer causes a change in the propagation velocity of the surface acoustic wave, resulting in a shift in the resonant frequency of the device.

The majority of existing SAW gas sensors have used thin film sensing layers, with limited surface area. The application of nanostructured sensing layers, such as ZnO nanorods can potentially lead to improved sensing performance due to increased surface area. Promising results for SAW sensors using ZnO nanorods for hydrogen gas sensing [9, 10] and UV light detection [11] have been reported, although there have been few direct comparisons between the performance of these sensors and the performance of sensors using the same materials in thin film form.

## 2. Design and Fabrication

**2.1. Sensor Design.** The ZnO nanorod ethanol sensor was fabricated on a 128° rotated Y-cut LiNbO<sub>3</sub> substrate. LiNbO<sub>3</sub> offers excellent surface acoustic wave performance due to

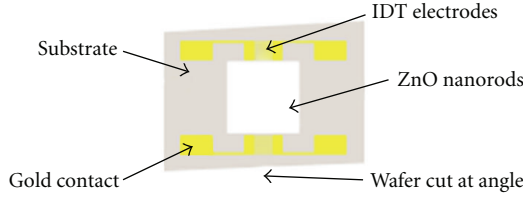


FIGURE 1: Sensor layout.

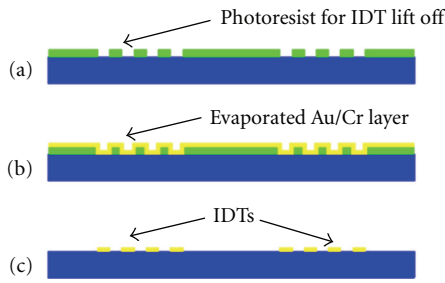


FIGURE 2: Fabrication process for SAW delay line.



FIGURE 3: Micrograph of fabricated IDT section.

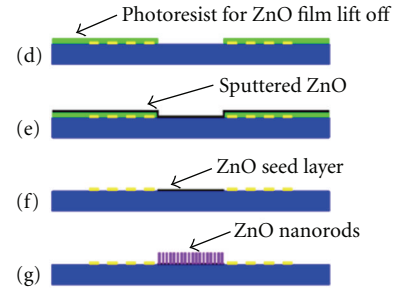


FIGURE 4: Fabrication process for ZnO nanorod layer.

the high-electromechanical-coupling coefficient ( $k_2 = 4.5\%$ ) and low attenuation at high temperature [12].

The overall layout of the sensor is shown in Figure 1. Two interdigital transducers (IDTs), each consisting of 50 electrode pairs, are separated by a 12 mm delay line. The width of each IDT electrode and the spacing between the edges of adjacent IDT electrodes are  $15\ \mu\text{m}$ . The length of the IDT electrodes is 3 mm. The IDTs are oriented on the wafer so that SAW propagation is along the  $x$ -direction of the crystal. As shown in Figure 1, the substrate is cut at an angle to the SAW propagation direction to minimize reflections from the substrate edge on the side of the IDT away from the delay line [13].

The  $15\ \mu\text{m}$  electrode width and spacing result in the fundamental mode having a wavelength of  $60\ \mu\text{m}$ . The measured centre frequency of the devices at room temperature was 66 MHz. By the equation  $v = f\lambda$ , this implies a propagation velocity of  $3960\ \text{ms}^{-1}$ .

**2.2. Fabrication Process.** The metal electrodes and contacts were formed on the  $\text{LiNbO}_3$  wafer using a lift-off technique. The process used is illustrated in Figure 2.

AZ nLOF 2070 photoresist was spin-coated on the wafer and patterned (a). A 20 nm chromium layer followed by a 100 nm gold layer was then thermally evaporated (b) and the photoresist removed (lift-off process) to form the IDTs and contacts (c). A section of a fabricated IDT is shown in Figure 3.

The ZnO thin film and nanorods were produced only in the delay line of the device. The fabrication process used to deposit the ZnO thin film and grow the ZnO nanorods is summarized in Figure 4.

A photoresist layer was spin-coated and patterned with a window covering the delay line of the sensor (d). A 100 nm ZnO layer was then deposited by sputtering from a ZnO ceramic target (e). In order to obtain a good quality film, the

DC sputtering was carried out at a pressure of 2.7 Pa, in an atmosphere with 80% argon and 20% oxygen. The current used was 0.25 A DC. The photoresist was then removed in acetone, leaving the ZnO thin film, which serves as a seed layer for nanorod growth (f). Finally, the ZnO nanorods were produced by a solution growth technique [14] (g). The devices were suspended ZnO-side-down in a sealed bottle containing a solution of zinc nitrate, hexamethylenetriamine, and polyethyleneimine in deionized water. The sealed bottle was then incubated in a laboratory oven at  $95^\circ\text{C}$  for 4 hours, after which the substrates were removed from the solution, rinsed with  $95^\circ\text{C}$  DI water, and allowed to air-dry at room temperature. The growth parameters were selected to give a uniform layer of predominantly vertical nanorods which adhered well to the substrate. Nanorods produced by this method are shown in Figure 5. The nanorods formed are vertical and well defined, with average diameter  $45\ \text{nm}$  and height  $1\ \mu\text{m}$ .

**2.3. Measuring System.** The ethanol sensors produced were characterized using general purpose laboratory equipment controlled from the computer, as illustrated in Figure 6. An Agilent 33250A function generator was programmed to apply an excitation voltage to one IDT of the sensor. The magnitude and phase of this waveform, and of the waveform from the second IDT, were monitored using an Agilent 6102A DSO.

The propagation velocity of surface acoustic waves in  $\text{LiNbO}_3$  is temperature dependent. The absorption of ethanol onto ZnO nanorods is also temperature sensitive [15]. Therefore, in order to detect low concentrations of ethanol vapour, the sensor temperature must be tightly controlled. A platinum thin film resistance thermometer on the substrate was used to monitor the operating temperature of the device during measurement. For characterization, the sensor was heated using a laboratory hot plate. Testing of sensitivity to

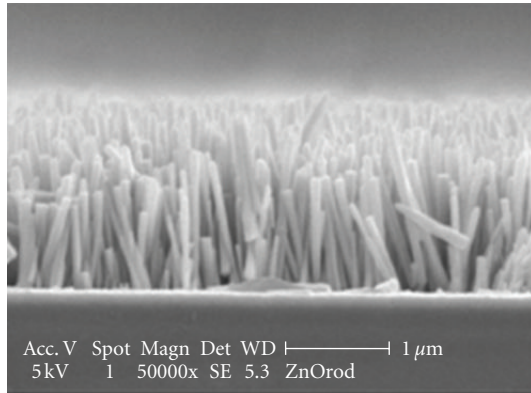


FIGURE 5: SEM image of ZnO nanorods.

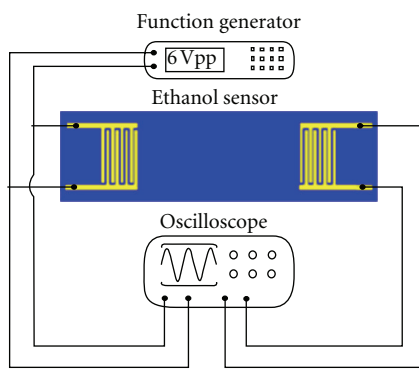


FIGURE 6: Equipment configuration for measurements.

ethanol was performed with the sensor in a sealed chamber, in which the heated sensor could be alternately exposed to a known concentration of ethanol and flushed with air to allow adsorbed ethanol to desorb from the ZnO layer.

### 3. Results

The response of the SAW ethanol sensor using ZnO nanorods to a known concentration of ethanol was measured. In order to demonstrate that the ZnO nanorods provided a benefit for ethanol sensing, the shift in the frequency response of the sensor with nanorods was compared with that of an otherwise identical device with the sputtered ZnO thin film, but lacking the ZnO nanorod layer. In the oscillator configuration commonly used for SAW gas sensors, the oscillation frequency is determined by the frequency at which the phase shift around the loop is some integer multiple of  $2\pi$  [16]. Therefore, the results presented are given in terms of the phase shift between the wave input to one IDT of the sensor and the wave received at the second IDT, after propagating through the nanorod layer.

The effect of 2300 ppm ethanol on the phase shift of a sample with nanorods at 270°C is presented as Figure 7. Results under the same conditions for a sample without nanorods are shown in Figure 8. It was noted that the shape of the phase response for the sensor with nanorods differed

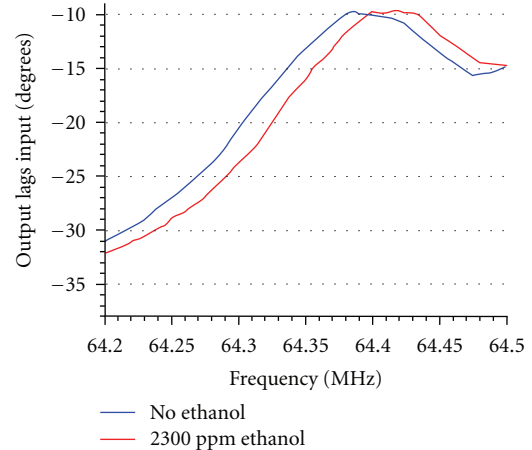


FIGURE 7: Effect of 2300 ppm ethanol on phase shift of sample with nanorods at 270°C.

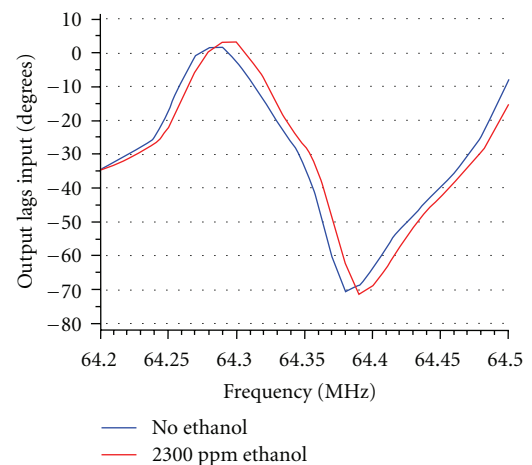


FIGURE 8: Effect of 2300 ppm ethanol on phase shift of sample without nanorods (with only ZnO thin film) at 270°C.

from that of the sensor with nanorods. This was attributed to increased mechanical damping caused by the nanorod layer.

The maximum frequency offset between the phase response plot obtained with air in the chamber and the phase response obtained with 2300 ppm ethanol in air in the chamber was 24 KHz for the sensor with ZnO nanorods. In comparison, the maximum frequency offset under these conditions with ZnO thin film only was 9 kHz. The 24 kHz frequency shift obtained for the sample with ZnO nanorods subjected to 2300 ppm ethanol, expressed as a fraction of the 64.3 MHz frequency where this shift occurred, is 370 ppm. In comparison, the fractional frequency shift for the sample without ZnO nanorods was 140 ppm.

The sensor's response time is estimated by measuring the phase shift between the input and output signal at a particular frequency (64.37 MHz) as shown in Figure 9. A 2.5 mL of ethanol was vaporized at approximately 340 s. The sensor took approximately 200 s to reach its maximum phase shift at 640 s. The phase shift remains at approximately  $-15.1^\circ$  for another 200 s before it starts to recover. From

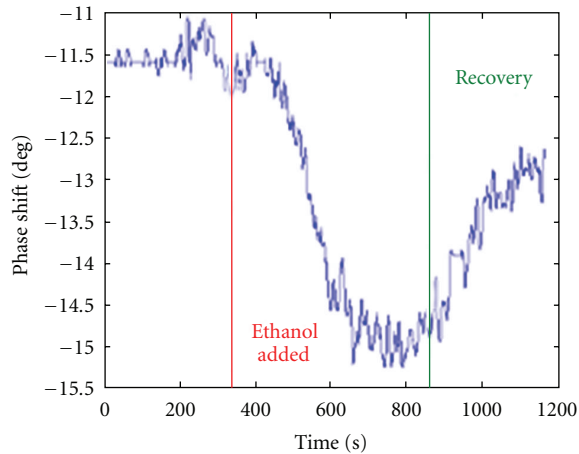


FIGURE 9: The response of the sensor.

Figure 9, the sensor seems to take a longer time to recover. After waiting for approximately 240 s, the sensor has yet to fully recover to its initial phase shift. It is believed that at higher temperature, the response and recovery time could be shortened but this requires further investigation. Nevertheless, we have demonstrated that the use of nanorods increased the sensitivity of the sensor.

#### 4. Conclusions

A novel surface acoustic wave ethanol sensor using ZnO nanorods was developed and tested. The change in frequency response that occurred when the sensor was exposed to ethanol was measured and compared to that of a sensor using a ZnO thin film only. The SAW ethanol sensor with ZnO nanorods demonstrated a frequency shift of 24 kHz in response to 2300 ppm ethanol at 270°C, a significant improvement over the 9 kHz shift of the sensor without nanorods. The application of a nanorod sensing layer is a promising technique to improve the sensitivity of surface acoustic wave gas sensors, albeit the long response and recovery time.

#### References

- [1] Q. Wan, Q. H. Li, Y. J. Chen et al., "Fabrication and ethanol sensing characteristics of ZnO nanowire gas sensors," *Applied Physics Letters*, vol. 84, no. 18, pp. 3654–3656, 2004.
- [2] G. Heiland, "Homogeneous semiconducting gas sensors," *Sensors and Actuators*, vol. 2, pp. 343–361, 1981.
- [3] Rayleigh, "On waves propagated along the plane surface of an elastic solid," *Proceedings of the London Mathematical Society*, vol. 1, supplement 1–17, pp. 4–11, 1885.
- [4] R. White, "Surface elastic waves," *Proceedings of the IEEE*, vol. 58, no. 8, pp. 1238–1281, 1970.
- [5] A. Mamishev, K. Sundara-Rajan, F. Yang, Y. Du, and M. Zahn, "Interdigital sensors and transducers," *Proceedings of the IEEE*, vol. 92, no. 5, pp. 808–845, 2004.
- [6] A. D'Amico, A. Palma, and E. Verona, "Surface acoustic wave hydrogen sensor," *Sensors and Actuators*, vol. 3, pp. 31–39, 1982.
- [7] Y. J. Lee, H. B. Kim, Y. R. Roh, H. M. Cho, and S. Baik, "Development of a SAW gas sensor for monitoring SO<sub>2</sub> gas,"

*Sensors and Actuators A: Physical*, vol. 64, no. 2, pp. 173–178, 1998.

- [8] R. A. McGill, V. K. Nguyen, R. Chung et al., "The "NRL-SAWRHINO": a nose for toxic gases," *Sensors and Actuators B: Chemical*, vol. 65, no. 1, pp. 10–13, 2000.
- [9] F. C. Huang, Y. Y. Chen, and T. T. Wu, "A room temperature surface acoustic wave hydrogen sensor with Pt coated ZnO nanorods," *Nanotechnology*, vol. 20, no. 6, Article ID 065501, 2009.
- [10] A. Z. Sadek, W. Wlodarski, Y. X. Li et al., "A ZnO nanorod based layered ZnO/64° YX LiNbO<sub>3</sub> SAW hydrogen gas sensor," *Thin Solid Films*, vol. 515, no. 24, pp. 8705–8708, 2007.
- [11] W. S. Wang, T. T. Wu, T. H. Chou, and Y. Y. Chen, "A ZnO nanorod-based SAW oscillator system for ultraviolet detection," *Nanotechnology*, vol. 20, no. 13, Article ID 135503, 2009.
- [12] J. Hornsteiner, E. Born, G. Fischerauer, and E. Riha, "Surface acoustic wave sensors for high-temperature applications," in *Proceedings of the 1998 IEEE International Frequency Control Symposium*, pp. 615–620, May 1998.
- [13] W. Soluch, "Design of SAW delay lines for sensors," *Sensors and Actuators A: Physical*, vol. 67, no. 1, pp. 60–64, 1998.
- [14] P. Hari, M. Baumer, W. D. Tennyson, and L. A. Bumm, "ZnO nanorod growth by chemical bath method," *Journal of Non-Crystalline Solids*, vol. 354, no. 19–25, pp. 2843–2848, 2008.
- [15] B. B. Rao, "Zinc oxide ceramic semi-conductor gas sensor for ethanol vapour," *Materials Chemistry and Physics*, vol. 64, no. 1, pp. 62–65, 2000.
- [16] H. Wohltjen, "Mechanism of operation and design considerations for surface acoustic wave device vapour sensors," *Sensors and Actuators*, vol. 5, no. 4, pp. 307–325, 1984.

## Research Article

# Local Fatigue Evaluation in PZT Thin Films with Nanoparticles by Piezoresponse Force Microscopy

**B. S. Li**

*Material and Reliability, ASMPT, Singapore 768924*

Correspondence should be addressed to B. S. Li, [bsli@asmpt.com](mailto:bsli@asmpt.com)

Received 28 June 2011; Accepted 22 August 2011

Academic Editor: Tao Li

Copyright © 2012 B. S. Li. This is an open access article distributed under the Creative Commons Attribution License, which permits unrestricted use, distribution, and reproduction in any medium, provided the original work is properly cited.

Lead zirconate titanate (PZT) thin films with the morphotropic phase boundary composition ( $Zr/Ti = 52/48$ ) have been prepared using a modified diol-based sol-gel route by introducing 1–5 mol% barium titanate (BT) nanoseeds into the precursor solution on platinumized silicon substrates (Pt/Ti/SiO<sub>2</sub>/Si). Macroscopic electric properties of PZT film with nanoparticle showed a significant improvement of ferroelectric properties. This work aims at the systematic study of the local switching polarization behavior during fatigue in PZT films with and without nanoparticles by using very recent developed scanning piezoelectric microscopy (SPM). We show that the local fatigue performance, which is characterized by variations of local piezoloop with electric cycles, is significantly improved by adding some nanoseeds. It has been verified by scanning electron microscope (SEM) that the film grain morphology changes from columnar to granular structure with the addition of the nanoseeds. On the other hand, the existence of Pt<sub>x</sub>Pb transition phase, which existed in interface at early crystallization stage of pure PZT thin film, deteriorates the property of the interface. These microstructures and the interfaces of these films significantly affect the electrons injection occurred on the interfaces. The domain wall pinning induced by injected electrons and the succeeding penetration into the films is discussed to explain the fatigue performance.

## 1. Introduction

Lead zirconate titanate (PZT) thin film has been a good candidate for application in ferroelectric materials in nonvolatile ferroelectric random access memory (FERAM) due to its excellent ferroelectric properties [1, 2]. One prerequisite property of PZT thin films for ferroelectric devices is the microscopic perfection of the polarization switching, defined as the symmetric switching between two opposite polarization states. The occurrence of polarization fatigue, which is the decrease of polarization during repeated electrical pulses, has been an obstacle for full commercialization of the PZT thin films, especially for applications of PZT thin films on Pt electrode coated substrates. As such, extensive studies have been carried out to disclose the microscopic fatigue nature in PZT thin films [3–10]. Oxygen vacancies, which are very easy to form during crystallization process and the most mobile point defects in perovskite material like PZT, are deemed to be a major factor in fatigue. Scott et al. argued that the transition of oxygen vacancies into two-dimensional planar arrays is a fatigue mechanism in perovskite ferroelectrics

[3, 5]. Park and Chadi investigated atomic relaxations around oxygen-vacancy defects in ferroelectric perovskite PbTiO<sub>3</sub> through first-principles pseudopotential total energy calculations [6]. The atomic relaxations around oxygen vacancies may result in a tail-to-tail polarization and thus favor the charge trapping and domain pinning. Lupascu and Rabe directly observed point defect clustering in perovskite ferroelectrics during cyclic electrical pulses [7]. It seems, from these data, that the redistribution of the point defect (mainly oxygen vacancies) plays a crucial role in fatigue mechanism. However, there are some arguments against this opinion which are summarized in [8]:

- (1) Doping is always used to control the oxygen vacancy concentration, but the experimental results on the effect of doping of PZT films on fatigue are contradictory.
- (2) The activation energy which corresponds to the temperature dependence of the fatigue rate (0.05 eV) is much smaller than the typical one of the oxygen vacancy mobility in perovskites (1 eV).

Considering the above arguments, one may draw the conclusion that in fatigue mechanism, the crucial contributing factor was not the redistribution of the oxygen vacancies. Studies reveal that charge carriers could also influence fatigue. An apparent polarization attenuation exists in PZT and BaTiO<sub>3</sub> when ultraviolet illumination is used to generate electron and hole pairs [9]. When a sample is fatigued, electrons and holes injected from the electrodes into the ferroelectric film can be trapped at deep levels and immobilized producing as a simple charged defect [8]. These defects associated with the bound charges of the domain walls pin the reorientation of the domains during fatigue. Cillessen et al. demonstrated an electron injection model occurred in near-electrode region [10]. According to this model, the coercive field of the film will increase if the near-electrode electron injection is present. Du and Chen observed improvement of fatigue performance in PZT films when using P type silicon as the top electrode, and they attributed the improved fatigue endurance to absence of the electron penetration [11]. These findings demonstrate that electrons injection during fatigue plays a very important role in the fatigue performance of PZT films.

In our previous work [12, 13], a novel approach to improve microstructure and decrease the processing temperature of PZT films on Pt/Si by sol-gel was developed. This approach introduced small amounts of perovskite nanoparticles into the precursor, and the films prepared by seeded precursor show not only improved microstructure and ferroelectric properties, but also fatigue endurance. Our results show that an alternative to improve the fatigue endurance by adding nanoseeds into the films has been found. However, systematic studies on the seeding effect on fatigue performance at a nanoscale level have not been conducted yet, and the mechanism of this improvement remains to be discovered.

It should be noted that the fatigue mechanisms mentioned only consider the variations in macroscopic hysteresis loops before and after fatigue. In fact, this characterization could not define the microscopic fatigue performance and possible imprint along polarization axis well. Recently, piezoforce microscopy (PFM) has been intensively used to study the domain variations in ferroelectrics due to its significant advantage for monitoring domain features and ability for investigating local piezoresponse with piezoloop [14]. Furthermore, compared with macroscopic hysteresis loops, the microscopic piezoloop may well define the imprint phenomenon along the polarization axis due to its displacement-dependent nature. In contrast, this kind of imprint cannot be detected in macroscopic measurements of ferroelectric polarization, because an arbitrary integration constant is used in the polarization measurement [15]. Therefore, in this work, PFM is utilized to analyze the local fatigue performances in three kinds of PZT ferroelectric thin films. The electron injection [16] and the succeeded domain pinning by the penetrated electrons were investigated in microregion by piezoloops. The diverse domain pinning processes in these films during fatigue were reported here, and a possible explanation was suggested.

## 2. Experimental Procedure

The PZT precursor solution was prepared according to the stoichiometric formula Pb(Zr<sub>0.52</sub>Ti<sub>0.48</sub>)O<sub>3</sub>. No excess lead was added. The starting reagents were lead acetate trihydrate, titanium diisopropoxide bisacetylacetonate, and zirconium acetylacetonate. A 0.4 M stock solution was used for the PZT thin-film deposition. The viscosity of the solutions with and without seeds was adjusted to 0.012 Pa s.

Ultra fine barium titanate (BT) powders (20 ~ 80 nm) were used as seeds. BT seed powder was prepared by a direct hydrolysis synthesis in which titanium alkoxide mixed into barium hydroxide solution at 90°C. Perovskite phase was directly formed after drying the powder at room temperature. The BT powder was milled and dispersed with a suitable solvent and dispersant (Dispex A40; Allied Colloids, Ltd-ammonium salt of a polycarboxylic acid) for 5 h using a vibrator mill. The suspension of BT seeds was mixed with the PZT precursor sol according to certain ratios. The weight ratios of BT seeds in PZT sol were 1% and 5%, respectively. The sol was processed with vigorous stirring and followed by a 20 min ultrasonic treatment. The stability of the PZT suspension sols was measured with a rheometer.

PZT films were deposited on Pt/Ti/SiO<sub>2</sub>/Si multilayered substrates by dip-coating. The substrate was dipped and withdrawn from the precursor sol at a constant rate of 0.17 cm/s. The resulting wet films were dried on a hot plate at 300°C for 1 min to remove residual organics. After deposition of four layers, the films were fired at 550°C for 30 min in air. The PZT thin films with 1 wt% and 5 wt% BT seeds are briefly called PZT-BT1 and PZT-BT5, respectively. The thickness of these films were about 400 nm. The stoichiometry and the interfaces quality of the films were studied by Rutherford back scattering (RBS) spectrometry using a He<sup>+</sup> beam at 1.6 MeV.

Surface morphology and domain structure inspection of the films was performed via so-called piezoforce microscopy (PFM) that relies on a local reverse piezoelectric effect exhibited by the film's surface. A modified commercial atomic force microscope (Multimode, Nanoscope IIIA, Digital Instruments) was used in the experiment to record synchronously two different features: topography and piezoresponse. A conductive Ti (1st layer) and Pt (2nd layer) coated tip cantilever (NSC14/Ti-Pt, MikroMasch) system was used for the application of external voltages and for effective piezocoefficient ( $d_{\text{eff}}$ ) measurements. The first harmonics of the cantilever vibration was detected under an ac voltage (3 V, 50 kHz) was applied between the grounded tip and the bottom electrode. In the piezoresponse image, domains with opposite polarization exhibit different contrast. Dark regions (hereafter referred to as negative domains) correspond to domains with polarization oriented towards the substrate, and bright regions (positive domains) refer to domains with polarization point at the free surface of the film. The local piezoelectric hysteresis loops (piezoloops) before and after fatigue were measured on a fixed point inside an unambiguous domain. The tip was put on the relative flat area to avoid the interference caused by  $d_{31}$  and  $d_{15}$  vibration. The loop acquisition consisted of applying a dc voltage,  $V_{\text{dc}}$ , for a short time

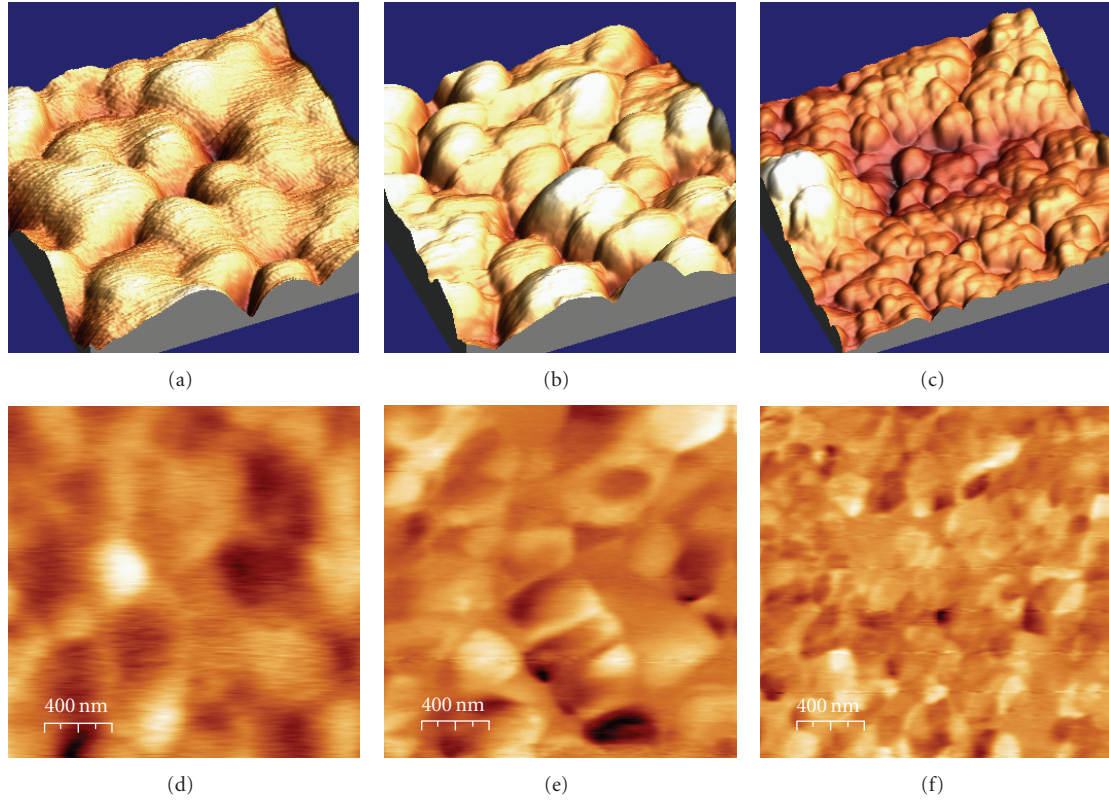


FIGURE 1: Topographic images of PZT films without seeds (a), with 1% BT seeds (b), with 5% seeds (c), and corresponding piezoresponse images (d), (e), and (f) in three kinds of PZT thin films. The scale bar in topographic image is same as that in piezoresponse one.

( $\approx 1$  s) and measuring the actual remanent piezoelectricity when the dc voltage was reduced to zero for each piezoelectric measurement. The voltage was swept by 1 V increments in the range  $-20 \text{ V} < V_{\text{dc}} < +20 \text{ V}$ . The frequency and amplitude of electric field for fatigue is 50 kHz and 2 times of the corresponding coercive field, respectively.

### 3. Results and Discussions

Typical topography and piezoresponse images of three kinds of films are shown in Figure 1. Among these PZT films, pure PZT film shows the lowest surface roughness, while PZT-BT5 film presents the roughest one. The rms roughnesses are 2.01 nm, 4.93 nm, and 7.33 nm for PZT, PZT-BT1, and PZT-BT5 films, respectively. As suggested in [16], there were pyrochlore residue phase forming a uniform cover on PZT films. This may be the reason why the grains and the domain populations did not correlate each other.

It is also shown in Figure 1 that these films possessed different grain sizes. From the results, as addition of 1 wt% BT seeds did not result in a significant change in grain size, whereas a significant decreased in grain size was observed in PZT-BT5 film. Theoretically, nanoparticles added in the film can act as nucleation centers to favor crystallization process. Compared to the pure PZT films heated under the same conditions, the extent of crystallization of the perovskite structure was much higher [13]. The smaller grain in PZT-BT5 film is due to the presence of excessive nucleation center,

which will increase the nucleation density and, therefore, to smaller grains.

**3.1. Static Fatigue Studies.** Figure 2 shows the piezoloops after different fatigue cycles in these films, which were measured consecutively for each film. The tip was immovable during the fatigue process, so it was briefly called “static fatigue”. For pure PZT film, square-like piezoloop were observed when the measuring electric field was applied on the virgin film. There was an aggravation of the pinched shape to some degree with increasing of the fatigue switching cycles. After the  $3 \times 10^8$  switching cycles, the ferroelectric behavior was entirely suppressed, and any expected correlation between the piezoresponse and the voltage applied disappeared, especially in the up polarized state. This illustrates that there were pinned domains in PZT film, because the domain size distribution during the growth process determined the hysteresis loop shape. Since a large ac field was applied in the fatigue experiment, the interior component of the PZT film was excited [17]. Thus, the pinned area was not just beneath the tip and localized in one domain. This might extend deep into the film due to the highly inhomogeneous and large electric field during fatigue experiment.

Note that PFM response has crystallographic dependence, which was dominated by  $d_{33}$  value [18]. The relation between the coercive field and off-axis orientation of the grain could be approximately evaluated with [19]:

$$EP \cos(\theta) = A, \quad (1)$$

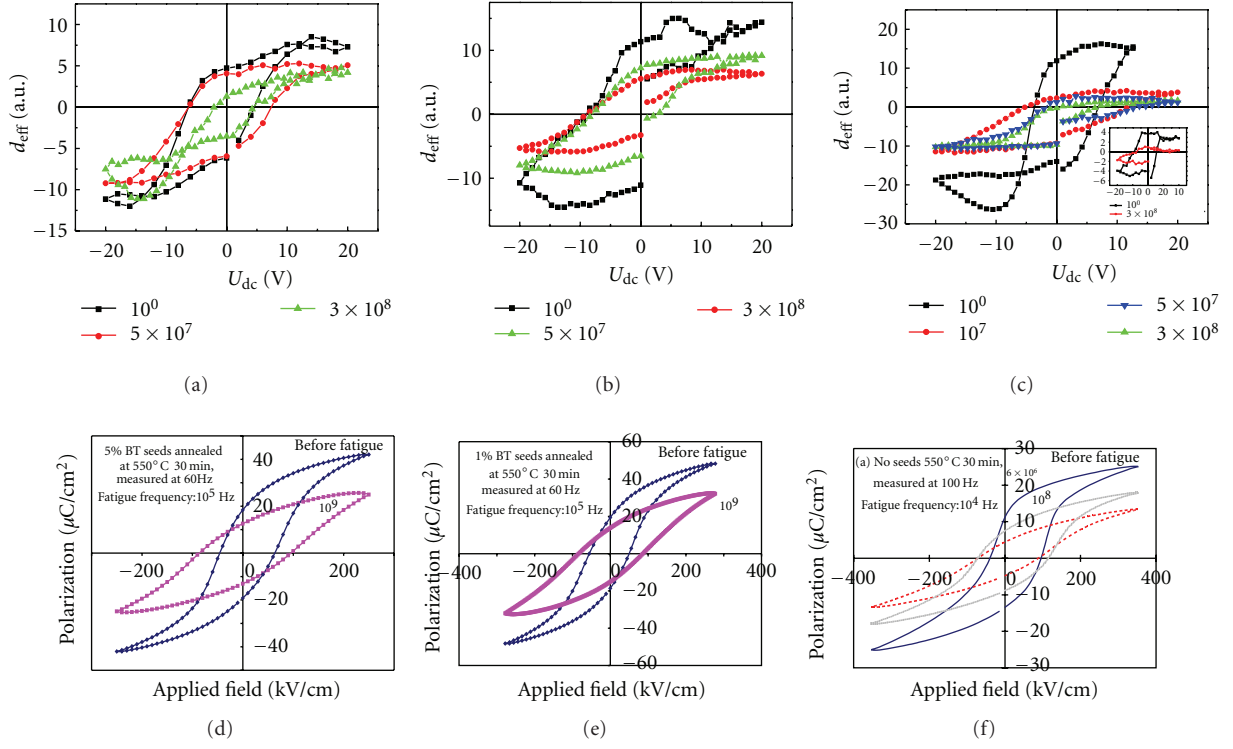


FIGURE 2: Local (upper) and macroscopic (lower) piezoloops obtained in different PZT films of different fatigue cycles. (a) PZT-BT5 thin film, (b) PZT-BT1 film, and (c) PZT film. Inset in (c) shows variation of the piezoloops with electric cycles in PZT sample which is annealed in nitrogen at 600°C for 30 minutes.

where  $E$  is electric field,  $P$  is polarization,  $\theta$  is off-axis angle and  $A$  is a constant. Therefore, coercive field is expected to increase with the increase of off-axis angle, while polarization decreases to guarantee the product to be a constant. In present, it is obvious that increase of the coercive voltage (or decrease of the polarization) cannot be attributed to an off-axis orientation of the grain, since the product of coercive field and polarization significantly decreased after long-term fatigue cycles. Thus, this shows that the fatigue mechanism indeed involved a pinning process around domains. This is also an indication that under the probing location, the domain walls became clamped, inhibiting the growth of opposite domains so that a higher field was required to partly switch the domain into the opposite state. The slope of the piezoloop near the coercive field had a significant decrease, which indicates a difficult nucleation and expansion of the new domain.

Comparison of the loops in Figure 2(c) shows that the piezoloop presents apparent imprint after fatigue. It seemed that there was almost no positive displacement in PZT film after severe fatigue. During the measuring of piezoloop, it was believed that the switching begins with the nucleation of reverse domain seeds just underneath the tip. The newly growing domain then expanded to an equilibrium size reach to some depth in the film. The piezoelectric displacement can be expressed in the following way [20]:

$$d_{\text{eff}} = \frac{1}{V_{\text{ac}}} \int_0^t d_{33} E_z dz = \frac{d_{33}}{V_{\text{ac}}} \left[ \int_0^l E_z dz - \int_l^t E_z dz \right] \quad (2)$$

$$= \frac{d_{33}}{V_{\text{ac}}} [V(0) - 2V(l)],$$

where  $V(0)$  is the potential on the surface and  $V(l)$  is the potential at the domain boundary. For the spherical model  $V(l) \sim V(0)R/(R+l)$  [20], where  $R$  is contact radius,  $l$  is the distance from the center of the contact area. The surface potential  $V(0) = V_{\text{tip}} = V_{\text{dc}} + V_{\text{ac}} \cos(\omega t)$ . Then, the piezoelectric displacement is proportional to surface potential. Thus, the imprint of piezoloop can be explained by considering the large decrease of the  $V_{\text{dc}}$ . It is highly probable that this decrease is caused by injection of electrons from the tip. The possible mechanism for electron injection is a thermoionic injection of negative charge carriers (electrons) through the tip, as described with [21]

$$J = AT^2 \exp\left(-\frac{\phi}{KT}\right), \quad (3)$$

where  $A$  and  $K$  are the Richardson and Boltzmann constants,  $T$  is the temperature, and  $\phi$  is the effective barrier for electron injection. In other words, the increase in temperature along the fatigue process brings about an increase in current density, which will simultaneously decrease the effective barrier

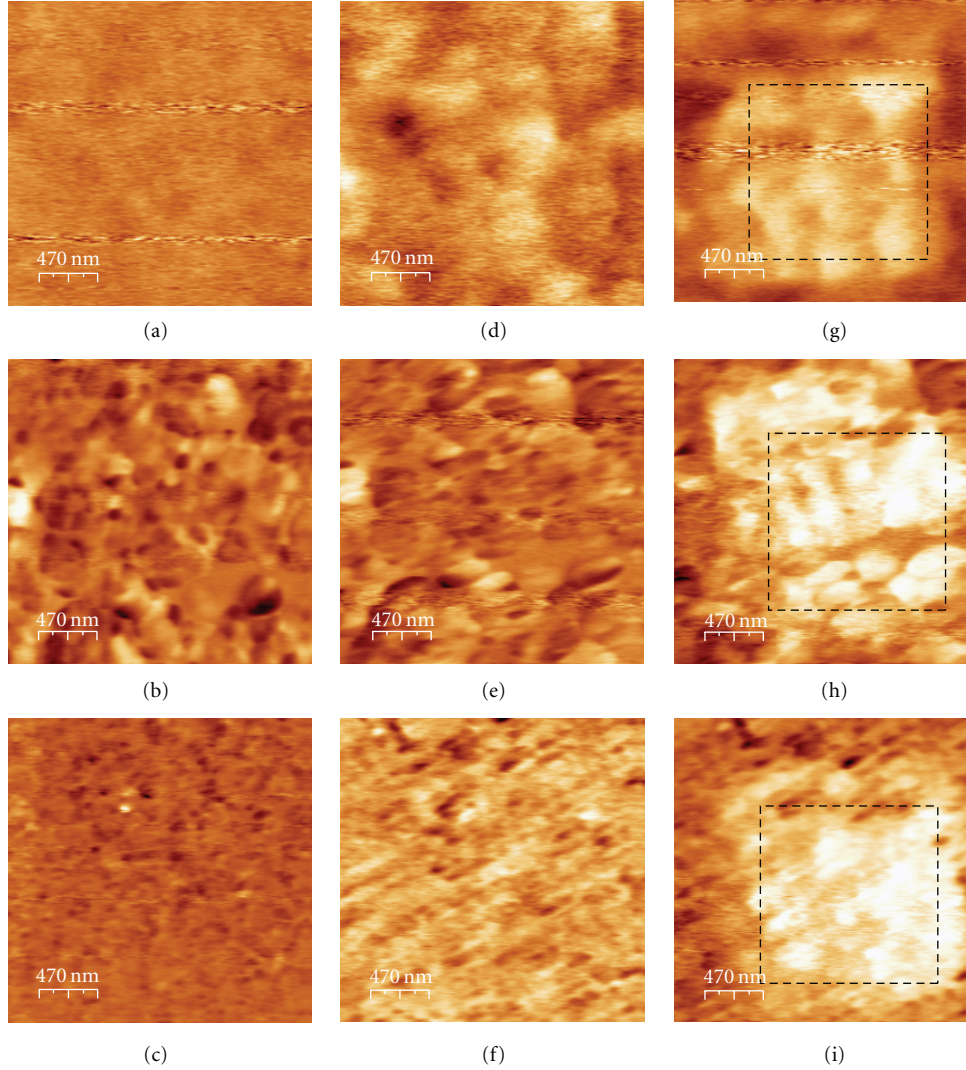


FIGURE 3: Piezoresponse images of the PZT series films. (a) ~ (c) are piezoresponse images for PZT, PZT-BT1, and PZT-BT5 as-deposited films, respectively; (d) ~ (f) show piezoresponse images on fatigued PZT series films; (g) ~ (i) show corresponding poling effects on these films. The black frame represents poling area produced by moving the cantilever while applying a positive 20 V<sub>dc</sub> voltage. Unswitchable domains appear as dark color.

height  $\phi$ . As a result, the electrons ejected from tip may screen applied voltage and greatly decrease the V<sub>dc</sub> of the PZT film as a reverse bias voltage, resulting in a strong imprint in piezoloop of PZT film. The mechanism for electron penetration may come from the high field induced by unscreened embryo domains, which is probably expressed by Fowler-Nordheim tunneling as [22]

$$J = C_{FN} E_{bc}^2 \exp \left[ -\frac{4\sqrt{2}m^*(q\phi_b)^{3/2}}{3q\xi E_{bc}} \right], \quad (4)$$

where  $C_{FN}$  is the Fowler-Nordheim coefficient which depends on the barrier height  $\phi_B$  and the the electron effective mass  $m^*$  at the interface. Under such a high tunneling current, the penetration of the charge can be expected especially near the nucleation sites.

Comparing the piezoloops shown in Figures 3(a), 3(b), and 3(c), an apparent difference in loop shapes after fatigue was observed. After  $3 \times 10^8$  fatigue cycles, the pinched degree for seeded films was much more alleviated as compared with unseeded PZT film. The slopes of the piezoloop near the coercive field for seeded films decreased moderately, which indicates that the domains in the area just under the tip were not largely frozen. It implied that there were different fatigue processes between seeded and unseeded films.

Some authors have suggested oxygen vacancy migration or accumulation near the film electrode will result in electrical fatigue [3, 5, 6]. To verify the role of oxygen vacancies in fatigue course, the PZT sample was annealed in nitrogen atmosphere for half an hour. The oxygen vacancies could not be compensated by ambient oxygen during cooling process, resulting in the distortion of the oxygen octahedron which would deteriorate the ferroelectric properties. As shown in

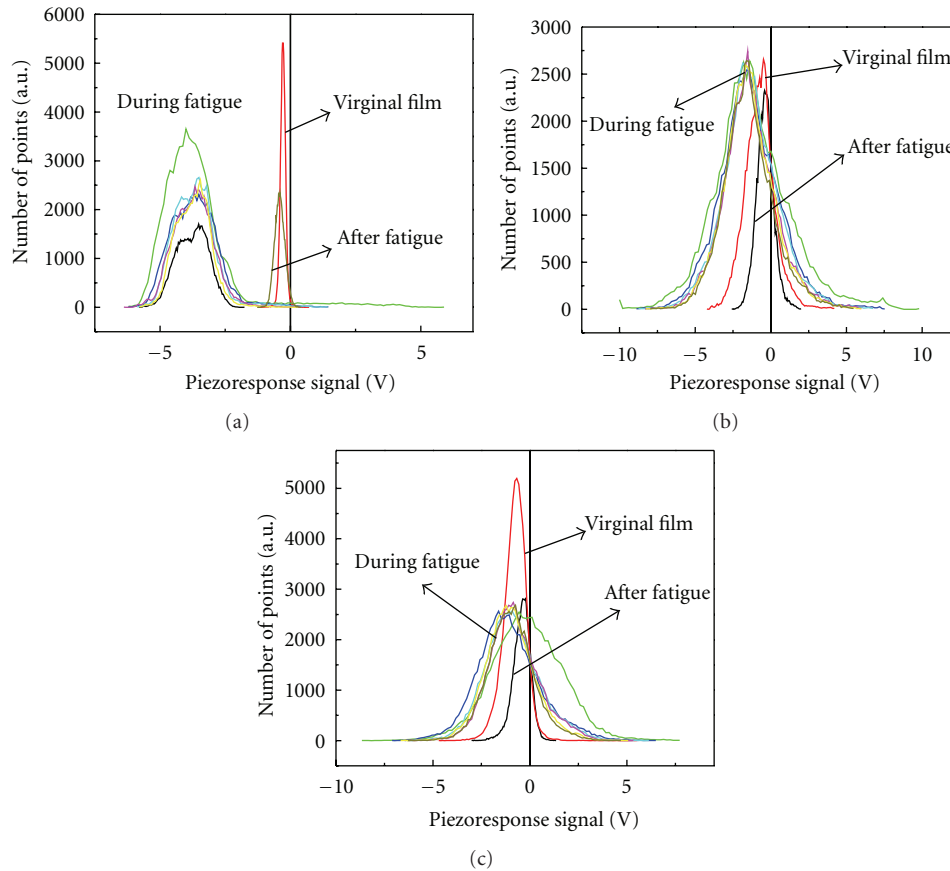


FIGURE 4: Piezoelectric histograms of three kinds of PZT films. Three types of histograms about virginal film, during fatigue and after fatigue, are shown, respectively, in (a) PZT, (b) PZT-BT1, and (c) PZT-BT5 films.

the inset of Figure 2(c), the remnant polarization of nitrogen-processed sample before fatigue decreased to one-third of the virginal sample. After  $3 \times 10^8$  electrical cycles, the fatigued loop of this sample was severely pinched, but from the normalized viewpoint, it is unlikely that the oxygen vacancies play a key role in the fatigue mechanism.

**3.2. Dynamic Scanning Fatigue Studies.** To further investigate the fatigue effect in these PZT films, a further experiment was carried out. A  $2.35 \times 2.35 \mu\text{m}^2$  square area was scanned for 6 cycles (about 50 minutes) by a conductive tip on which high voltage was applied to induce repeated polarization switching. We briefly call this mode scanning fatigue, which parallels the standing fatigue as presented earlier in Figure 3. The scanning fatigue mode is equivalent to the application of  $5 \times 10^3$  electrical pulses to each pixel on surface of the film. After the fatigue operation, a new cantilever was used to study the same original sample area. Then, a smaller area inside the original fatigued area was poled with high positive voltage to observe the domain pinning in the fatigued area. These results are shown in Figure 3. It is noticed that pure PZT film shows a considerable change in the piezoresponse pattern of the fatigued area, while PZT films with BT nanoparticles maintained their domain distributions. The right column of Figure 3 shows the piezoresponse images of these films, where a positive  $20 V_{\text{dc}}$  voltage was applied through the

scanning tip to induce reorientations on the corresponding fatigued area. For pure PZT film, it is obvious that some of the domains could not be reoriented and still exhibit its original piezoelectric signals. This is a strong indication that there were domains pinning around these regions [23]. In the case of the PZT films, with nanoparticles, the area of un-switchable region was much smaller as compared to PZT film and further for PZT-BT5 film, the domain populations inside the black frame could even be switched freely.

The piezohistograms of these films in as-deposited, during-fatigue, and after-fatigue states obtained from corresponding PFM images are shown in Figure 4. It is complex to analyze the during-fatigue piezoresponse image due to an intricate domain switching case which is involved into it. Theoretically, when we consider the first harmonic piezoresponse during domain switching as a sine ac signal is used, the amplitude of piezoelectric displacement will present two same segments corresponding to one period of the ac signal. Thus, the whole first harmonic signal acquired from upper layer of the measured object should be zero. In fact, some signal strength must be present due to a highly inhomogeneous electric field beneath the tip. However, we preferably consider that this first harmonic signal results from the piezoelectric contribution at deeper region just beneath the upper one in the surface.

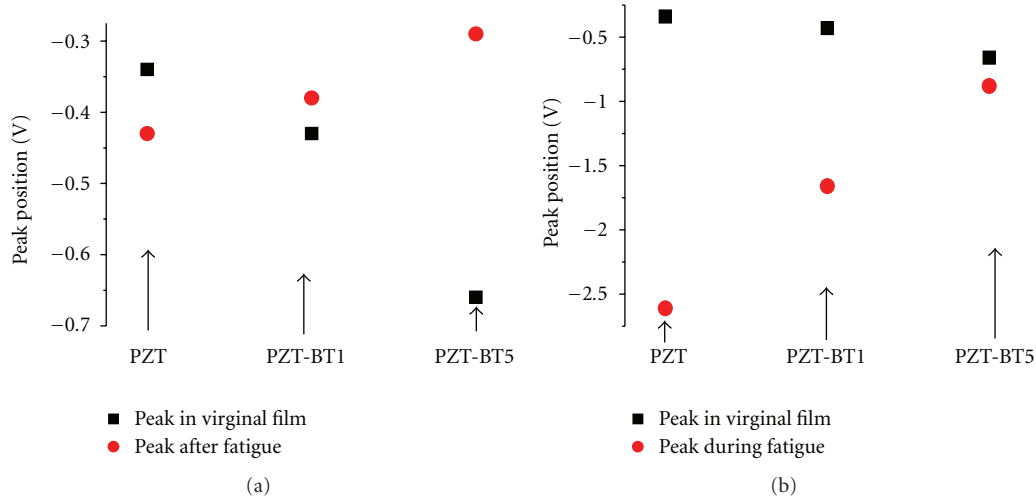


FIGURE 5: Peak offset in corresponding histogram between (a) virginal film and after-fatigue film, (b) virginal film and during-fatigue film.

Generally, piezohistogram describes statistical distribution of domain population and provide a tangible reference for domain orientation. The peak of a piezohistogram refers to the most probable domain configuration, and its width indicates possible number of domain variations. The height of the curve is highly width-dependent, because the number of events is closely related to span of the interval. So, we ignore the variation of height in these histograms. Analysis of piezohistograms for virgin films reveals that these PZT films exhibit self-polarization effect. It is due to the strong built-in field near the bottom electrode formed by the trapped electrons and ionic defects near the film-bottom electrode interface [24]. This effect produced an additional internal electric field with a determinate direction, inducing mainly downward domains in this area, as shown in Figure 4. Furthermore, a large offset of the piezohistogram is observed for pure PZT film when a large ac voltage is applied to excite domain switching. In contrast to the pure PZT film, the PZT films with nanoparticles have smaller offset even almost zero for PZT-BT5 film in that moment as shown in Figure 4(c). After application of electric cycles, the pure PZT film shows a negative offset, which indicates that its self-polarization will be strengthened. On the contrary, films with nanoparticles present small positive offsets as shown in Figures 4(b) and 4(c). Then, alleviation in their self-polarization can be expected.

Concerning sol-gel-derived PZT films, the presence of built-in bias field near bottom electrode can result in self-polarization. It is both probable that the injected electrons come from bottom electrode or from tip, and these two types of electrons induce reverse effect for self-polarization [24]. The results in Figure 5 follow that the aggravation of the self-polarization during fatigue probably results from the injection of electrons from the bottom electrode. It should be noted that the aggravation degree is different for these films. After the fatigue process ended, opposite offset shown in Figure 5(a) implies that the injected electrons are trapped

in different region. For pure PZT film, they are located near the bottom electrode, and for films with nanoparticles, they stay near the surface.

To investigate the effect of injected electrons on switching character, piezoloops for PZT and PZT-BT5 films was carried out before and after scanning fatigue as shown in Figure 6. Comparison of these two kinds of films reveals the scanning fatigue cause opposite shifts in the vertical direction. It also implies that charges are in different interface, resulting in opposite bias field. We find that this result is in good agreement with [23] measured on fatigue effect in PZT film [23].

We suggest that film microstructure may be responsible for the fatigue performance. In our previous work [13], detailed crystallization processes for these PZT films were described. For PZT films with nanoparticles, nucleation occurs at the surface of the bottom electrode, at the seed surfaces, and at the top film surface, which brings about a higher degree of perovskite crystallinity but a less orientated texture, that is, granular structure. For pure PZT film, the nucleation takes place only at the surface of the bottom electrode. Then, columnar structure can be expected.

The change of film grain morphology from granular to columnar may have an effect on the fatigue performance in seeded and unseeded films. Generally, grain boundaries act as current pass, and as a result, injected electrons may vanish faster in films with lots of grain boundaries. Thus, the injected electrons will not pin the domain reorientations in films with the addition of nanoparticles. Therefore, good fatigue endurance is present in films with nanoparticles rather than pure PZT film. It is interesting to note that this suggestion is not in well consistent with the results in the reference [25], in which greater polarization fatigue for a granular PZT film was reported.

We further suggest that the inferior fatigue performance in unseeded film is closely related to early crystallization process. When the pure PZT film was pyrolyzed at 400°C for 5 min, at the Pt/PZT interface, a  $Pt_xPb$  interlayer

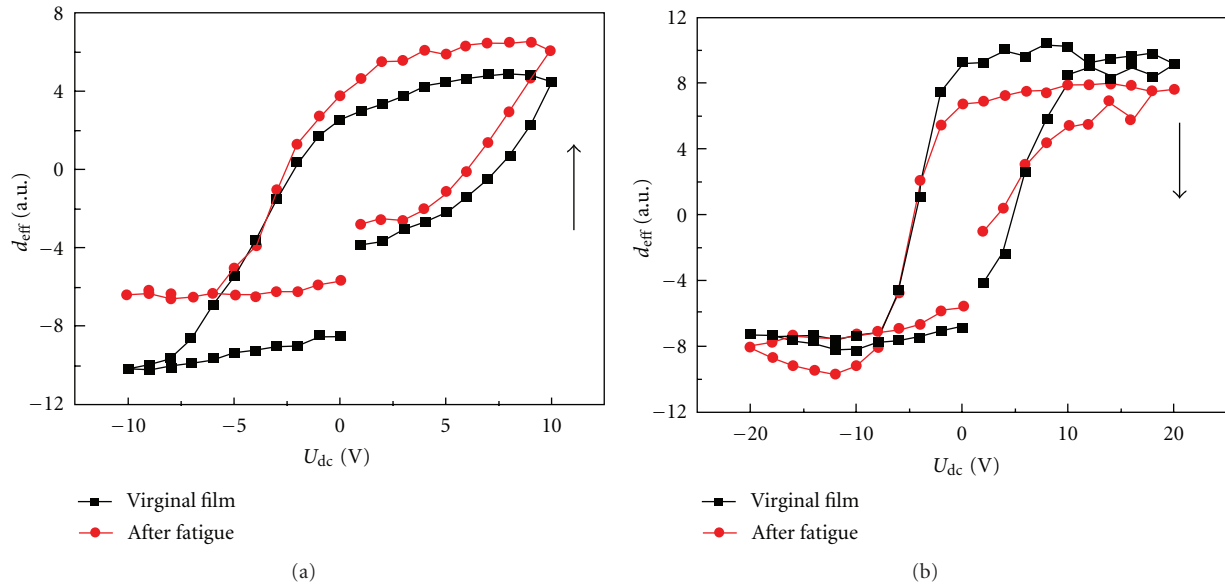


FIGURE 6: Variations of Piezoloop after fatigue for (a) unseeded and (b) seeded films.

was observed even though it disappeared in later period [13]. For seeded films pyrolyzed under the same conditions, the  $Pt_xPb$  interlayer was reduced or not observed when seeds content increased to 5%. Furthermore, there was evidence that the morphology of  $Pt_xPb$  interlayer for PZT film was continuous while it was intermittent for PZT films with nanoparticles. Disappearance of the interlayer implies that the location with such a transition phase is prone to transform into heterogeneity which is easy to be penetrated by injected electrons. Besides this, electrons are more difficult to vanish in pure PZT film than in PZT films with nanoparticles so that the injected electrons are easy to pin the domain reorientation in pure PZT film. We believe that these are the reasons behind the inferior fatigue performance for pure PZT film. The possible incomplete compensation of depolarization field [7] did not to influence the electron injection, since we found in another experiment that static fatigue showed no frequency dependence.

#### 4. Conclusions

In summary, we have demonstrated that polarization fatigue of PZT films depends on the addition of nanoseeds with piezoresponse force microscopy. Piezoresponse images and related piezoloops reveal that seeded films possess better fatigue endurance. We suggest that the film morphology and the microstructure of the bottom interface play key roles in the evolution of the fatigue. Formation of the continuous  $Pt_xPb$  interlayer in interface may damage the intactness of the bottom electrode although the interlayer disappears in latter crystallization. These areas probably act as the pipeline for penetration of the electrons, and the fatigue endurance degrades with the combinations between mobile carriers and these electrons. In addition, the fatigue performance may also be affected by film microstructure which will evolve

from columnar to granular growth with the addition of nanoseeds.

#### Acknowledgment

The author would like to acknowledge sample preparation and some experimental results done at University of Avero.

#### References

- [1] J. F. Scott and C. A. Paz De Araujo, "Ferroelectric memories," *Science*, vol. 246, no. 4936, pp. 1400–1405, 1989.
- [2] G. H. Haertling, "Ferroelectric ceramics: history and technology," *Journal of the American Ceramic Society*, vol. 82, no. 4, pp. 797–818, 1999.
- [3] M. Dawber and J. F. Scott, "A model for fatigue in ferroelectric perovskite thin films," *Applied Physics Letters*, vol. 76, no. 8, pp. 1060–1062, 2000.
- [4] J. F. Scott, C. A. Araujo, B. M. Melnick, L. D. McMillan, and R. Zuleeg, "Quantitative measurement of space-charge effects in lead zirconate-titanate memories," *Journal of Applied Physics*, vol. 70, no. 1, pp. 382–388, 1991.
- [5] J. F. Scott and M. Dawber, "Oxygen-vacancy ordering as a fatigue mechanism in perovskite ferroelectrics," *Applied Physics Letters*, vol. 76, no. 25, pp. 3801–3803, 2000.
- [6] C. H. Park and D. J. Chadi, "Microscopic study of oxygen-vacancy defects in ferroelectric perovskites," *Physical Review B*, vol. 57, no. 22, pp. R13961–R13964, 1998.
- [7] D. C. Lupascu and U. Rabe, "Cyclic cluster growth in ferroelectric perovskites," *Physical Review Letters*, vol. 89, no. 18, pp. 187601/1–187601/4, 2002.
- [8] A. K. Tagantsev, I. Stolichnov, E. L. Colla, and N. Setter, "Polarization fatigue in ferroelectric films: basic experimental findings, phenomenological scenarios, and microscopic features," *Journal of Applied Physics*, vol. 90, no. 3, pp. 1387–1402, 2001.
- [9] W. L. Warren, D. Dimos, B. A. Tuttle, and D. M. Smyth, "Electronic and ionic trapping at domain walls in  $BaTiO_3$ ," *Journal*

- of the American Ceramic Society, vol. 77, no. 10, pp. 2753–2757, 1994.
- [10] J. F. M. Cillessen, M. W. J. Prins, and R. M. Wolf, “Thickness dependence of the switching voltage in all-oxide ferroelectric thin-film capacitors prepared by pulsed laser deposition,” *Journal of Applied Physics*, vol. 81, no. 6, pp. 2777–2783, 1997.
- [11] X. Du and I. Chen, “Model experiments on fatigue of Pb ( $Zr_{0.53}Ti_{0.47}$ )O<sub>3</sub> ferroelectric thin films,” *Applied Physics Letters*, vol. 72, p. 1923, 1998.
- [12] A. Wu, P. M. Vilarinho, I. M. Miranda Salvado, and J. L. Baptista, “Seeding studies in PZT thin films,” *Materials Research Bulletin*, vol. 33, no. 1, pp. 59–68, 1998.
- [13] A. Wu, P. M. Vilarinho, I. Reaney, and I. M. Miranda Salvado, “Early stages of crystallization of sol-gel-derived lead zirconate titanate thin films,” *Chemistry of Materials*, vol. 15, no. 5, pp. 1147–1155, 2003.
- [14] A. L. Kholkin, S. V. Kalinin, A. Roelofs, and A. Gruverman, “Review of ferroelectric domain imaging by Piezoresponse Force Microscopy,” in *Scanning Probe Microscopy: Electrical and Electromechanical Phenomena at the Nanoscale*, S. Kalinin and A. Gruverman, Eds., Springer, New York, NY, USA, 2006.
- [15] M. Alexe, C. Harnagea, D. Hesse, and U. Gösele, “Polarization imprint and size effects in mesoscopic ferroelectric structures,” *Applied Physics Letters*, vol. 79, no. 2, pp. 242–244, 2001.
- [16] S. Bühlmann, E. Colla, and P. Muralt, “Polarization reversal due to charge injection in ferroelectric films,” *Physical Review B*, vol. 72, no. 21, Article ID 214120, 7 pages, 2005.
- [17] G. Arlt, D. Hennings, and G. De With, “Dielectric properties of fine-grained barium titanate ceramics,” *Journal of Applied Physics*, vol. 58, no. 4, pp. 1619–1625, 1985.
- [18] E. L. Colla, I. Stolichnov, P. E. Bradely, and N. Setter, “Direct observation of inversely polarized frozen nanodomains in fatigued ferroelectric memory capacitors,” *Applied Physics Letters*, vol. 82, no. 10, pp. 1604–1606, 2003.
- [19] X. H. Du, U. Belegundu, and K. Uchino, “Crystal orientation dependence of piezoelectric properties in lead zirconate titanate: theoretical expectation for thin films,” *Japanese Journal of Applied Physics, Part 1*, vol. 36, no. 9, pp. 5580–5587, 1997.
- [20] S. V. Kalinin, A. Gruverman, and D. A. Bonnell, “Quantitative analysis of nanoscale switching in SrBi<sub>2</sub>Ta<sub>2</sub>O<sub>9</sub> thin films by piezoresponse force microscopy,” *Applied Physics Letters*, vol. 85, no. 5, pp. 795–797, 2004.
- [21] A. Wu, P. M. Vilarinho, V. V. Shvartsman, G. Suchaneck, and A. L. Kholkin, “Domain populations in lead zirconate titanate thin films of different compositions via piezoresponse force microscopy,” *Nanotechnology*, vol. 16, no. 11, pp. 2587–2595, 2005.
- [22] E. Bouyssou, P. Leduc, G. Guégan, and R. Jérésian, “Leakage current conduction in IrO<sub>2</sub>/PZT/Pt structures,” *Journal of Physics*, vol. 10, no. 1, pp. 317–320, 2005.
- [23] X. J. Lou, M. Zhang, S. A. T. Redfern, and J. F. Scott, “Local phase decomposition as a cause of polarization fatigue in ferroelectric thin films,” *Physical Review Letters*, vol. 97, no. 17, Article ID 177601, 2006.
- [24] A. Gruverman, O. Auciello, and H. Tokumoto, “Nanoscale investigation of fatigue effects in Pb(Zr,Ti)O<sub>3</sub> films,” *Applied Physics Letters*, vol. 69, no. 21, pp. 3191–3193, 1996.
- [25] A. Gruverman, B. J. Rodriguez, R. J. Nemanich, and A. I. Kingon, “Nanoscale observation of photoinduced domain pinning and investigation of imprint behavior in ferroelectric thin films,” *Journal of Applied Physics*, vol. 92, no. 5, p. 2734, 2002.